



In-situ identification of marine organisms using high frequency, wideband ultrasound

Pham, An Hoai; Lundgren, Bo; Stage, Bjarne; Jensen, Jørgen Arendt

Publication date:
2013

Document Version
Publisher's PDF, also known as Version of record

[Link back to DTU Orbit](#)

Citation (APA):

Pham, A. H., Lundgren, B., Stage, B., & Jensen, J. A. (2013). In-situ identification of marine organisms using high frequency, wideband ultrasound. Kgs. Lyngby: Technical University of Denmark (DTU).

DTU Library Technical Information Center of Denmark

General rights

Copyright and moral rights for the publications made accessible in the public portal are retained by the authors and/or other copyright owners and it is a condition of accessing publications that users recognise and abide by the legal requirements associated with these rights.

- Users may download and print one copy of any publication from the public portal for the purpose of private study or research.
- You may not further distribute the material or use it for any profit-making activity or commercial gain
- You may freely distribute the URL identifying the publication in the public portal

If you believe that this document breaches copyright please contact us providing details, and we will remove access to the work immediately and investigate your claim.

In-situ identification of marine organisms using high-frequency, wideband ultrasound

An Hoai Pham

September 13, 2012

Section for Management Systems, National Institute of Aquatic Resources
& Center for Fast Ultrasound Imaging, Department of Electrical Engineering
Technical University of Denmark

SUBMITTED IN PARTIAL FULFILLMENT OF THE
REQUIREMENTS FOR THE DEGREE OF
DOCTOR OF PHILOSOPHY
AT
THE TECHNICAL UNIVERSITY OF DENMARK
SEPTEMBER 2012

Signature of Author

THE AUTHOR RESERVES OTHER PUBLICATION RIGHTS, AND NEITHER THE THESIS NOR EXTENSIVE EXTRACTS FROM IT MAY BE PRINTED OR OTHERWISE REPRODUCED WITHOUT THE AUTHOR'S WRITTEN PERMISSION.

THE AUTHOR ATTESTS THAT PERMISSION HAS BEEN OBTAINED FOR THE USE OF ANY COPYRIGHTED MATERIAL APPEARING IN THIS THESIS (OTHER THAN BRIEF EXCERPTS REQUIRING ONLY PROPER ACKNOWLEDGEMENT IN SCHOLARLY WRITING) AND THAT ALL SUCH USE IS CLEARLY ACKNOWLEDGED.

© Copyright by An Hoai Pham 2012
All Rights Reserved

Contents

Preface	iii
Acknowledgments	v
Abstract	vii
Resumé (dansk)	ix
List of Abbreviations	xi
1 Introduction	1
1.1 State of the art	1
1.2 Preliminary results	2
1.3 Scope and Aim of study	4
1.4 Contributions	5
1.5 The dissertation	5
2 Empirical ultrasound backscatter in the MHz frequency range from fish	7
2.1 Materials and method	8
2.1.1 Setup of the measurements	8
2.1.2 Data processing	10
2.2 Results	11
2.3 Discussion	16
2.4 Conclusions	23
3 Simulation of ultrasound images of fish from CT images	25
3.1 Objective of Study	25
3.2 Summary of Papers	26
3.2.1 Materials and methods	26
3.2.2 Results	29
3.2.3 Discussion	33
4 Fish species discrimination using range profiles in the MHz frequency range	35
4.1 Objective of Study	35
4.2 Summary of Papers	35
4.2.1 Materials	36
4.2.2 Results	37

4.2.3	Discussion	41
5	Conclusions	47
5.1	Future developments	48
	Bibliography	48
	List of Figures	59
	List of Tables	61
A	Articles in Journals	63
A.1	Shadow effects in simulated ultrasound images derived from computed tomography images using a focused beam tracing model	65
A.2	Fish species discrimination using range profiles in the MHz frequency range	77
B	Articles in Conference Proceedings	107
B.1	Simulation of ultrasound backscatter images from fish	108
B.2	Simulation of shadowing effects in ultrasound imaging from computed tomography images	119
B.3	Ultrasound backscatter from free-swimming fish at 1 MHz for fish identification	124
C	Other Results	127
C.1	Range profiles of three cods for the study presented in chapter 2	127
C.2	Range profiles of a cod and a saithe for the study presented in chapter 2	131
C.3	Range profiles of a saithe and two cods for the study presented in chapter 2	136
C.4	Average cross section images of a saithe and a cod for the study presented in chapter 2	146
C.4.1	Average cross section images of the saithe fish2	146
C.4.2	Average cross section images of the cod fish3	150
C.5	Data of some other measurements of the study presented in chapter 4	153

Preface

It has been almost four years since I applied for the project to try to identify fish in the sea. When I read the announcement, my first impression of the project was that this would be a good project. I would work with many electronic systems, travel around, and do a lot of experiments in a beautiful sea full of fish. I would get on a boat, go out to the sea outside of Copenhagen, put the systems down into the water and soon after know what kinds of fish are there near the boat. Maybe even meet a beautiful mermaid passing by?

Time flies. I worked six months as a research assistant to investigate possibilities and opportunities as well as to make a plan for the project, and three years and three months as a Ph.D. candidate to put the plan into action. Although reality is not always what I thought it would be, it has been a really interesting project and good results have been obtained.

My time as a Ph.D. student has been spent taking part in survey cruises at sea, looking for fish samples, arranging places for experiments, arranging logistics, preparing electronic devices, building new systems, and doing experiments. More time has been spent taking courses, reading literature, being a teaching assistant, and going to conferences. And even more time has been spent developing a method for simulation, running simulations, processing experiment data, interpreting data, and writing articles. I never met a mermaid.

It has been really enjoyable and a great experience to work with underwater sound as well as medical ultrasound imaging. The work in the Ph.D. study was carried out at the National Institute of Aquatic Resources, Technical University of Denmark both in Copenhagen and Hirtshals, Denmark, as well as at the Center for Fast Ultrasound Imaging, Department of Electrical Engineering, Technical University of Denmark. The work has been supervised by Senior scientist Bjarne Stage, Senior Scientist Bo Lundgren, and Professor Dr. Techn. Jørgen Arendt Jensen.

I hope you will enjoy reading this dissertation.

An Hoai Pham
September 13, 2012

Acknowledgments

A Ph.D. project full of possibilities and opportunities is ending. I have had the pleasure of working with many nice, interesting, and professional people whom I would like to thank.

First of all I would like to thank Senior Scientist Bjarne Stage, my main supervisor, who introduced me to the world of underwater sound, taught me image processing and gave many valuable comments for the experiments and results.

I would also like to thank Senior Scientist Bo Lundgren, my supervisor, who helped me a lot with the *ex-situ* experiments and the articles and joined many interesting discussions on the results of the work, and Professor Dr. Techn. Jørgen Arendt Jensen, my supervisor, who has provided me with a very good learning and working environment, given me a chance to work with medical ultrasound imaging and provided valuable comments on the experiments, simulations, data processing as well as the articles. It has been a great opportunity for me to be a member of the Center for Fast Ultrasound Imaging (CFU).

My thanks also go to Head of section, J. Rasmus Nielsen, who gave me an opportunity to join a brilliant section in the National Institute of Aquatic Resources (DTU-Aqua) and gave me advice on how to solve problems of my experiments.

A special thanks to my colleagues at CFU and Copenhagen University Hospital, Rigshospitalet: Martin Christian Hemmsen for helping me with the ultrasound scanner and simulation of ultrasound images; Mads Møller Pedersen for helping me with the CT scan; Jens Munk Hansen for programming as well as many interesting discussions; David Baek, Iben Kraglund Holfort, Yigang Du, Marie Sand Enevoldsen, Michael Johannes Pihl, Ye Li, Joachim Rasmussen, Peter M. Hansen, Morten Fischer Rasmussen, and Mette Funding La Cour for numerous discussions, inputs, talks and pleasant travels.

Other special thanks to Stina Bjørk Stenersen Hansen and Karl-Johan Staehr at DTU-Aqua, John Fleng Steffensen at the Marine Biological Laboratory, Biological Institute, University of Copenhagen for providing fish samples and teaching me how to handle them in experiments, Tina Bock Pedersen and Flemming Dalsgaard at the Department of Radiology, Copenhagen University Hospital, Rigshospitalet for the CT scanning of fish, and last but not least to Henrik Flintegaard and the helpful staff at the North Sea Oceanarium, Hirtshals, Denmark for providing me with very good facilities for the *ex-situ* experiments.

Furthermore, thanks to Henrik Larsen, Elna Sørensen and Nina Kjaergaard at CFU and Lis Vinther at DTU-Aqua for their always very kind help.

I would also very much like to thank my family for their faith in me, their support, and for

always being there for me, and all my friends in Denmark as well as in Viet Nam who have been supportive and encouraged me to keep up the good work.

This work is sponsored by a grant from the Globalization project of the Technical University of Denmark.

Abstract

Reliable remote fish identification would be an important improvement in resource management as well as in commercial fishing. Optical and acoustical methods could be used either in combination or separately. However, the acoustical methods have better detection ranges than any known optical methods. Conventional acoustical methods use frequencies in the range of 10 to 500 kHz and give reasonable estimations of size distribution, if the species is known, but can only significantly support the determination of the actual species, if there are only a few known species available. It is expected that higher frequencies and broader bandwidths than used until now will give more information useful for fish species identification.

The objective of this Ph.D. study has been to develop a method to investigate the possibility of *in-situ* identification of fish with high-frequency, wideband ultrasound. The approach was to build a 1 MHz wideband single-element transducer system to obtain range profiles of fish, and to do fish species identification by comparing measured range profiles with libraries of reference range profiles as it is done in some radar systems used to identify aircraft. To do this, it is also necessary to investigate the properties of ultrasound backscatter of fish in the MHz frequency range to help the interpretation of the range profiles. Three case studies were investigated in this Ph.D. study.

The first case study was to investigate the ultrasound backscatter of fish in the MHz frequency range using empirical methods. Measurements using a BK Medical ultrasound scanner equipped with a dedicated research interface were performed on a saithe (*Pollachius virens*) and three cods (*Gadus morhua*) at different frequencies as well as angles between the center line of the transducer beams and the fish bodies. The frequencies are 2, 3.5, and 6 MHz. The angles are -30° , -15° , 0° , 15° , and 30° . The results show that even though there are variations, a scan of the ultrasound backscatter along a fish of a specific species contains patterns that are characteristic for that species. This is true at all frequencies in the low MHz range. The part of a fish that contributes most is not necessarily the swimbladder as the results indicate that in the low MHz frequency range bone structures, and skin surfaces are more important.

The second case study was to develop a method to generate simulated ultrasound images from computed tomography images to build simulated ultrasound range profiles of fish. It can be observed from the first case study that shadow effects are normally pronounced in ultrasound images, so they should be included in the simulation. In this study, a method to capture the shadow effects has been developed, which makes the simulated ultrasound images appear more realistic. The method using a focused beam tracing model gives diffuse shadows that are similar to the ones observed in measurements on real objects.

The last case study was to do measurements of ultrasound range profiles of free-swimming

fish using a 1 MHz wideband single-element transducer system. The portable system consists of a Reson TC3210 1 MHz single-element transducer, a BlueView P900-2250 dual-frequency multi-beam sonar, and three Oregon ATC9K cameras on a fixture. The positions, orientations, and lengths of the fish were estimated by three-dimensional image analysis, while species were identified manually from the video sequences. *Ex-situ* experiments were performed on fish that have swimbladder (cod, European sea bass (*Dicentrarchus labrax*), gilthead sea bream (*Sparus aurata*), and Atlantic horse mackerel (*Trachurus trachurus*)) as well as on fish that do not have swimbladder (Atlantic mackerel (*Scomber scombrus*)). There are indications that the variations in the range profiles seem to have some unique details to discriminate between species like mackerel and sea bream. In some cases the range profiles also indicate whether the head or the tail is closest to the transducer. It has also been shown that the surface areas of the fish are the most important elements that decide how much energy is backscattered in the low MHz frequency range.

In conclusion, the ultrasound backscatter from fish in the MHz frequency range was investigated empirically as well as by simulation and the 1 MHz wideband single-element transducer system was developed. The results data from the *ex-situ* experiments in a large aquarium tank presented in the last case study can be considered comparable to data obtained in *in-situ* experiments in a calm shallow sea area. The single-element transducer system can therefore be considered ready for preliminary *in-situ* experiments. Hereby the main objectives of the Ph.D. study have been reached.

Resumé (dansk)

Formålet med dette Ph.D. projekt har været at udvikle en metode til at undersøge muligheden for *in-situ* identifikation af fisk med højfrekvent, bredbåndet ultralyd. Fremgangsmåden var at bygge et 1 MHz bredbåndet målesystem med en enkeltstrålet transducer til at opsamle ekkoprofiler fra fisk, og at forsøge identificere fiskearter ved at sammenligne målte ekkoprofiler med referenceekkoprofiler, på lignende måde som nogle radarsystemer bruges til at identificere fly. Derfor er det også nødvendigt at undersøge, hvordan ultralyd reflekteres af fisk i det lave MHz-frekvensområde, for at kunne fortolke variationerne i ekkoprofilerne. Tre casestudier blev gennemført i dette Ph.D. undersøgelse.

Resultaterne af det første casestudie viser, at selvom der er variationer, indeholder et scan af ultralydsreflektionen langs en fisk af en specifik art mønstre, der er karakteristiske for denne art. Den del af fisken, der bidrager mest er ikke nødvendigvis svømmeblæren, men resultaterne tyder på, at i det lave MHz-frekvensområde er knoglestrukturer, og hudoverflader vigtigere.

En simulationsmetode, der gengiver skyggeeffekter i ultralydsbilleder mere realistisk, er blevet udviklet i det andet casestudie. Metoden bruger en model med fokuserede lydstråler i stedet for parallelle stråler. Det giver diffuse skygger, der bedre ligner dem, der observeres ved målinger på virkelige objekter.

Det sidste casestudie gjaldt målinger af ultralydsekkoprofiler af fritsvømmende fisk ved hjælp af det førnævnte 1 MHz målesystem. Der er tegn på, at variationerne i ekkoprofilerne indeholder nogle unikke detaljer som gør det muligt at skelne mellem arter som makrel og guldbrasen. I nogle tilfælde kan ekkoprofilerne også angive, om hovedet eller halen nærmest transduceren. Det ser ud til at overfladearealerne af fisken er de vigtigste elementer, der bestemmer, hvor meget lydenergi, der reflekteres i det lave MHz frekvensband.

List of Abbreviations

List of Abbreviations

AUV	Autonomous underwater vehicles
CFU	Center for Fast Ultrasound Imaging
CT	Computed tomography
DIDSON	Dual-frequency identification sonar
DTU-Aqua	National Institute of Aquatic Resources of the Technical University of Denmark
HU	Hounsfield unit
IEEE	Institute of Electrical and Electronics Engineers
PC	Personal computer (chapter 2) / portable computer (chapter 4)
POE	power over Ethernet
RF	Radio frequency
ROV	Remotely operated vehicles
SD	secure digital
SPIE	the international society for optics and photonics
US	ultrasound

List of some of the Symbols

α	the angle between the fish and the transducer center beam (chapter 2 & 3) the angle between the center line of the Reson transducer (UT) and the center line of the Blueview sonar (S) (chapter 4)
x	the RF line number (chapter 2) an axis parallel to the line between cameras C2 and C3 (chapter 4)
y	the image number in a recording (chapter 2)
z	the sample number in a RF line (chapter 2) an axis away from the Reson transducer (chapter 4)

Introduction

Reliable remote fish identification would be an important improvement both when doing resource management and commercial fishing. If a fisheries scientist can identify the species and size of marine organisms *in-situ*, time consuming and costly sampling of the organisms can be reduced. If a fisher could know the species composition of a fish aggregation prior to catching the fish, some unwanted by-catches could be avoided.

Current practice for fish *in-situ* identification in both fisheries and fisheries research is based on echo sounders and sonars operating in the frequency range 18 - 500 kHz (typical range 5000 - 100 m) [1]. By comparing the strength of the backscattered signals at a number of discrete frequencies a crude species identification can be performed. The sensors are usually mounted in the hull of a vessel or a towed body at constant depth and thus needs a range corresponding to the distance to the fish of interest. The use of high-frequency (above 500 kHz) acoustic sensors and optical sensors would be useful to improve measuring resolution. But in most practical cases, the use of these sensors would give a limited range because high-frequency sound or light is strongly attenuated by seawater (acoustical high-frequency sensor typically range 10 - 30 m, optical sensor typically range 0.5 - 10 m). During fisheries surveys reliable species identification can therefore currently only be performed by catching the marine organisms in nets such as trawls and perform the identification on board the vessel. But trawling is time consuming. The vessel must stop to set out the trawl gear and then trawling must continue for a period (often 0.5 - 1 hour) at reduced speed compared to normal survey speed. After recovery of the trawl, the fish samples must be sorted into groups of species and groups by length by measurements on board. If the water mass contains several layers of different targets, in principle, all layers should be sampled by different trawl hauls. This is normally not possible due to constraints on survey time, which will introduce uncertainty in the results of a survey. During the last decade new sensor platforms such as remotely operated vehicles (ROV), autonomous underwater vehicles (AUV) and high speed towed bodies have become widely used [2–11]. By using this type of platform the sensors can be detached from the hull of the vessel and moved close to the organisms of interest. This allows the introduction of short range high resolution sensors.

1.1 State of the art

It is usually not possible to get reliable information about fish aggregations such as species and size distribution with the conventional methods before the fish has been caught. It may lead to misjudging the available fish stocks and wasteful use of living resources. Therefore, better methods to identify the fish before they are caught are needed. The acoustic fish identifica-

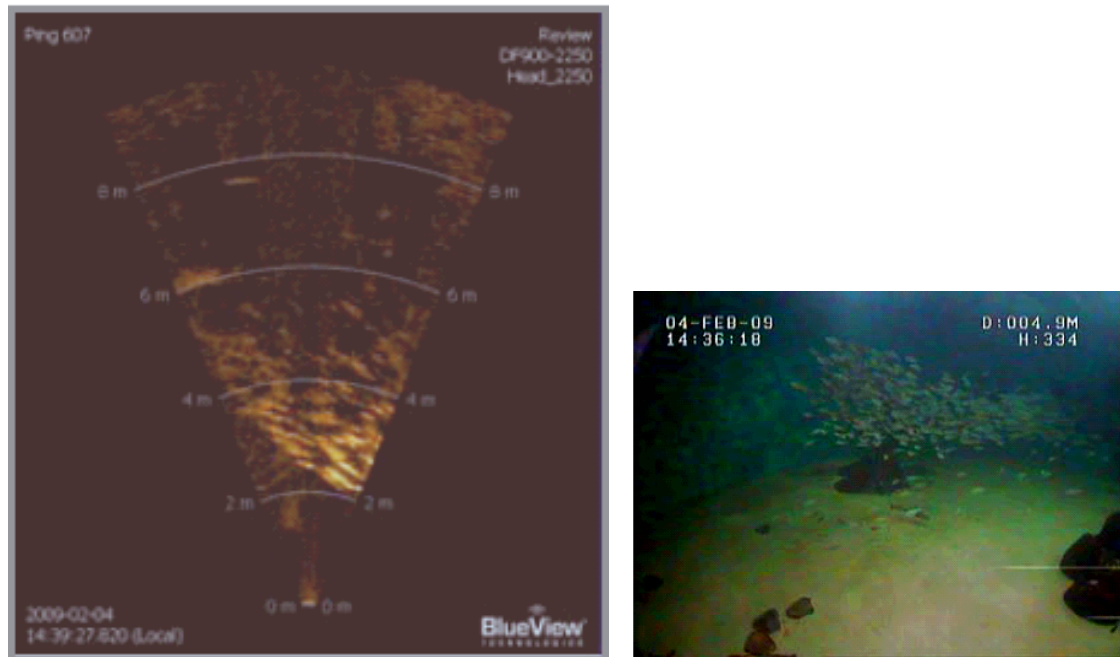
tion methods mentioned above are already in use, and they have better detection ranges than any known optical methods. There is still no well-established method to reliably distinguish between fish species at large distances. Several investigations have been made to improve existing methods in the literature. Efforts have been made to extract as much useful information as possible from the acoustic signal and increase the accuracy of this information. Most investigations are either measuring the backscatter from a single fish or are directed towards measuring the backscatter from aggregations of fish, as well as doing multi-frequency measurements. In some experiments the fish were immobilized, anesthetized and tied to a fixture as described in [12–19]. The fixture could be rotated and the information about the orientation of the fish could be derived from the fixture orientation. Single-element transducers were used to get the target strength from the fish for different orientations of the fish. In other experiments, a net was used to limit an area where fish swam free [20–22]. In addition to single-element transducers, cameras were used in stereo configuration to estimate the orientation of the fish. Then the target strength of the fish as a function of frequency was obtained for many different orientations of the fish. Drawbacks of these approaches were that the fixture or net interfered with the backscatter signals from the fish and that the net limited the mobility of the fish. Other groups have performed experiments on free-swimming fish without a net to avoid this drawback [2, 4, 11, 23–29]. All of those experiments followed the target strength approach and were performed in the frequency range well below 1 MHz except the work of Jaffe and Roberts [18].

Recently, with the development of the platforms for sensors, new approaches to use transducers in the MHz frequency range and wider bandwidths have been applied. Many groups have used multi-beam sonars, such as a dual-frequency identification sonar (DIDSON) to identify fish species [3, 6, 9, 30, 31]. The device gives a two dimensional ultrasound image for each ping and the size, orientation and the position of the fish can be derived from the images. The drawback of this approach is that the commercial sonars usually do not provide access to raw data, but only amplitude, and not the phase. This means that full information about the backscatter of fish cannot be obtained. Experience has shown that bladder shape and orientation of the fish are two of the parameters that have the strongest influences on the reflected sound from fish. However, it is very difficult to obtain results especially on the bladder shape because it is invisible from outside the fish. The bladder shape has been investigated using X-ray technique and then used to predict scattering properties. A possible way to take advantage of the information about the scattering properties is to use an underwater high-frequency ultrasonic system similar to those used in medical diagnosis fields [3, 6, 9, 30, 31].

1.2 Preliminary results

The National Institute of Aquatic Resources of the Technical University of Denmark (DTU-Aqua) performs fish population surveys every year. In order to investigate the possibility of tracing and identifying fish with high resolution, an underwater remote control package was purchased. The package includes an ROV equipped with underwater cameras and a Blueview multi-beam sonar with 900 kHz and 2.25 MHz center frequencies. The performance of the ROV was tested in the North Sea Oceanarium in Hirtshals, Denmark in February 2009. A typical image from the sonar is shown in Fig. 1.1(a). A photo taken by the front-camera of the ROV at the same time with the sonar image is shown in Fig. 1.1(b). As indicated in Fig. 1.1(a) and 1.1(b) the sonar as well as the front-camera were directed towards a fish school.

As can be seen, fish echoes are clearly visible in the sonar image. The shape of the fish is shown



(a) An image from the Blueview sonar on the ROV (2.25 MHz and 2 to 10 m range) (b) An image from camera on the ROV

Figure 1.1: Images from the sonar and front camera on the ROV captured at the same time

approximately, but there is no available technique to actually identify the fish from the sonar image. If one had knowledge about the expected ultrasound backscatter signals from different kinds of fish, it might be possible to process the echoes to identify the type of fish.

In order to investigate the possibility to develop methods to predict the ultrasound backscatter signals from some specific types of fish, an *in-vitro* experiment was performed by my colleagues from DTU-Aqua at the Center for Fast Ultrasound Imaging (CFU), Department of Electrical Engineering, Technical University of Denmark. The fish species used for the experiment were a blue whiting (*Micromesistius poutassou*) and a cod (*Gadus morhua*) and they were scanned with a medical ultrasound scanner with a 12 MHz ultrasound transducer. The photos of the blue whiting and the cod are presented in Fig. 1.2(a) and Fig. 1.2(b). The ultrasound images of the blue whiting and the cod are presented in Fig. 1.3(a) and Fig. 1.3(b).

It is easy to see the differences between the two fish species in the ultrasound images. Differences occur due to differences in structures like bones or swimbladder. If the acoustic properties of these structures are known, it would, in principle, be possible to predict the shape of the function describing the backscatter signal from a fish insonified by an ultrasound pulse from any direction. The function describing the amplitude and phase of the backscatter signals can be called range profiles. But during the ultrasound scans the fish was only insonified dorsally (from the back) by sound beams perpendicular to its length axis. Due to high attenuation, not all parts inside the fish are insonified. This means that ultrasound range profiles in perpendicular directions are not enough to identify free-swimming fish. Ultrasound scans from many different angles and combining the data could improve the chances of acquiring the required information, but it would take a lot of time. It would be useful to develop a simulation method to estimate the distribution of acoustical properties in fish and run the simulation to generate the range profiles from many different directions.



Figure 1.2: Photos of the fish

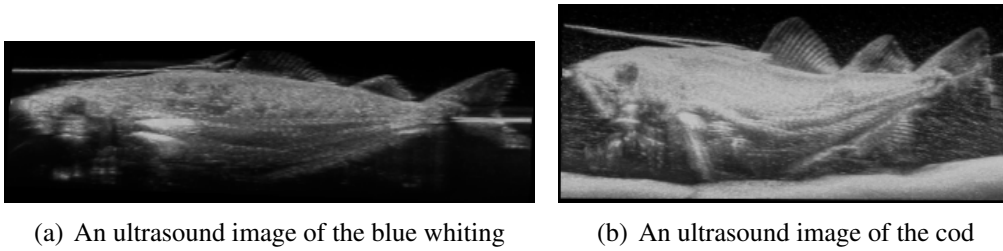


Figure 1.3: Ultrasound images of the fish scanning at 12 MHz using a BK Medical Viking ultrasound scanner

1.3 Scope and Aim of study

It was expected that using higher frequencies and broader bandwidths than used until now would give more information useful for the identification of fish species. The initial objective of the study was to investigate the information content of echoes from fish at ranges up to at least 30 m with a single-element transducer in the MHz range. One possible approach would be to build libraries of reference range profiles of fish as it is done in some radar systems used to identify aircraft as described in [32]. However, a suitable system to acquire acoustic range profiles of fish is not commercially available. Therefore, it was decided to start a study with the purpose of developing a cost-effective, reliable method for species discrimination using a high-frequency, wideband ultrasound system with a single-element transducer as a continuation of the work from Lundgren and Nielsen [21, 22]. There are three case studies. One of them is to build such a system and study the empirical range profiles of fish recorded by the system. The preparation for the identification is to build a library of empirical range profiles for known orientations of each fish species and then use modeling to predict the range profiles from other orientations. Because the frequency used in the system is in the MHz frequency range, it is also necessary to investigate characteristics of ultrasound backscatter in the MHz frequency range of fish. This can be achieved by either measuring the backscattered ultrasound field using empirical methods or calculating the field using simulation based on knowledge of the internal structure of the fish. Some preliminary results of measuring ultrasound backscatter from free swimming fish using a sonar on a ROV as well as ultrasound scan images of fish at 12 MHz are presented in Section 1.2. The effort required to obtain the empirical results indicates that it is necessary to support the empirical measurements with simulation methods to obtain a complete picture of the sound fields from a fish. The other two case studies would be on empirical measurements and simulations of ultrasound backscatter in the MHz frequency range from fish, respectively.

1.4 Contributions

On the path of achieving these goals of the studies a number of articles in journals as well as conference proceedings have been written.

Articles in Journals

1. **An Hoai Pham**, Bo Lundgren, Bjarne Stage, Mads Møller Pedersen, Martin Christian Hemmsen, Michael Bachmann Nielsen, and Jørgen Arendt Jensen, "Shadow effects in simulated ultrasound images derived from computed tomography images using a focused beam tracing model", published in *Journal of the Acoustical Society of America*, vol. 132, no. 1, pp. 487-497, 2012.
2. **An Hoai Pham**, Bo Lundgren, Bjarne Stage, and Jørgen Arendt Jensen, "Fish species discrimination using range profiles in the MHz frequency range", submitted to *IEEE Journal of Oceanic Engineering* in September 2012.
3. **An Hoai Pham**, Bo Lundgren, Bjarne Stage, and Jørgen Arendt Jensen, "Empirical ultrasound backscatter in the MHz frequency range from fish", draft version, to be submitted to *Canadian Journal of Fisheries and Aquatic Sciences* in 2012.

Articles in Conference Proceedings

1. **An Hoai Pham**, Bjarne Stage, Martin Christian Hemmsen, Bo Lundgren, Mads Møller Pedersen, Tina Bock Pedersen, and Jørgen Arendt Jensen, "Simulation of ultrasound backscatter images from fish", published in *Proceedings of SPIE*, 2011, 7961-796152(1-10).
2. **An Hoai Pham**, Bjarne Stage, Bo Lundgren, Martin Christian Hemmsen, Mads Møller Pedersen, and Jørgen Arendt Jensen, "Simulation of shadowing effects in ultrasound imaging from computed tomography images", published in *Proceedings of IEEE International Ultrasonics Symposium*, 2011, pp. 1411 -1414.
3. **An Hoai Pham**, Bo Lundgren, Bjarne Stage, and Jørgen Arendt Jensen, "Ultrasound backscatter from free-swimming fish at 1 MHz for fish identification", abstract accepted as poster presentation and will be published in conference Proceedings, *IEEE International Ultrasonics Symposium* in October 2012.

1.5 The dissertation

The following consists of three main chapters (2 - 4) presenting the work on the three case studies mentioned in Section 1.3, a conclusion with remarks about future developments, and appendixes including all the papers as well as more detailed data from the case studies. Two of the three main chapters are written as summaries of the respective papers. Therefore, all papers in Appendix A and B are integral parts of the corresponding chapters and should be read as well to acquire all details.

Chapter 2 is a draft version of a paper to be submitted to *Canadian Journal of Fisheries and Aquatic Sciences*. The chapter presents a case study on empirical ultrasound backscatter in the MHz frequency range from fish. Measurements were performed on fish using medical ultrasound scanner. The center frequency of the transmit pulse of the transducer were in the 2 to 10 MHz frequency range. The measurements were performed for different angles between the fish and the transducer beams. The detailed data set of the measurements is available in Appendix C.

Chapter 3 describes a case study to develop a method to simulate ultrasound images of fish from computed tomography (CT) images. The method is based on the ultrasound beam tracing method, which is then refined into the ultrasound focused beam tracing method in the case study. The papers summarized in this chapter are placed in Appendix A.1, B.1, and B.2.

Chapter 4 presents a case study on efforts to do fish species discrimination using range profiles in the MHz frequency range. A single-element transducer system was developed and is used to measured range profiles of free-swimming fish. The measurements were performed not only on single fish but also on schools of fish. The papers summarized in this chapter are placed in Appendix A.2 and B.3.

Chapter 5 presents conclusions of the thesis as well as considerations for future developments.

Empirical ultrasound backscatter in the MHz frequency range from fish

This chapter is a draft version of a paper to be submitted in 2012. The name of the paper is:

1. **An Hoai Pham**, Bo Lundgren, Bjarne Stage, and Jørgen Arendt Jensen, "Empirical ultrasound backscatter in the MHz frequency range from fish", to be submitted to *Canadian Journal of Fisheries and Aquatic Sciences* in 2012.

In order to develop a proper method for fish species discrimination, the understanding of ultrasound backscatter from fish is necessary. Many groups have been doing research on this topic with empirical methods as well as simulations. Using a Kirchhoff-ray mode scattering model, it is said that echo amplitudes from fish are largely dependent on the presence or absence of a swimbladder [33]. Hence, the swimbladder is usually considered the most important part for fish species discrimination. In many investigations [4, 14, 16, 17, 34], fish were first scanned using X-ray to find the shapes, sizes, and orientations of the swimbladders. Then fish were fixed to tethers underwater and ultrasound backscatter signals from them were recorded. The experiments were performed with different angles between the fish and the transducer beams as well as at different transducer frequencies. The transmitted signals were simulated killer whale echolocation signals with center frequencies in the range 50 - 200 kHz. The recorded signals were used to calculate target strength or relative amplitude as a function of frequency and angle. The investigations [4, 14, 16, 17, 33, 34] focused only on the amplitude of the received signals, but to take the phase signature of the signals into account Barr et al. performed simulations and *in-situ* experiments on fish [35]. The transducer frequency was 38 kHz and a gas filled swimbladder model was used for the simulations.

However, there are fish that do not have swimbladder, namely Atlantic mackerel. Gorska et al. investigated backscatter from Atlantic mackerel both with modeling and the use of field data [36, 37]. The transducer frequencies were in the range from 18 to 364 kHz. The results are, that at higher frequencies back scattering is dominated by contributions from the back bone of the fish.

There are groups that also use other approaches. Sun et al. performed *in-vitro* experiments on fish [13]. They built a 220 kHz focused sonic scanner with a focal distance of 10 cm. The axis of the fish was placed 10 cm from the transducer during measurements. They wanted to get a detailed structure of the fish, which was needed to construct a Huygen's scatterer acoustic model of fish. They measured how the peak amplitude of backscatter sound varied along the length of the fish. The results show that the swimbladder gave about 80% of the scattered energy for one fish species but only about 20% for another fish species. The experiments were

performed using only one transducer frequency and only one angle between the fish bodies and the transducer beam. In another investigation, Jech et al. performed experiments to determine acoustic backscattering cross sections of fish [38]. The fish were insonified at 120, 200, and 420 kHz. They conclude that the results support the idea that knowledge of fish orientation in the field is important and that the effect of orientation becomes more significant at higher frequencies.

The abovementioned experiments were performed at frequencies well below 1 MHz. In this case study the final goal is to investigate the possibility to do fish species discrimination in the low MHz frequency range; therefore, there is a need to know the ultrasound backscattering of fish in this frequency range. A suitable 1 MHz single-element transducer system was not available at the time of the investigation and a commercial medical ultrasound imaging system was used instead. The measurements were performed on fish for different transducer center frequencies as well as different angles between the fish body and the transducer center beam. The hypotheses for the measurements are:

- The ultrasound backscatter of a specific species contains patterns that are characteristic for that species.
- The characteristic backscatter patterns of one species are different from those of another species.
- This is true at all frequencies in the low MHz range.
- The part of a fish that contribute most to the ultrasound backscatter in the MHz frequency range is not necessarily the swimbladder.
- The measurement procedure can be used to produce empirical ultrasound range profiles for fish identification for directions other than those measured, as mentioned in Section 1.3.

The procedure and results of the measurements as well as a discussion are presented in the following sections.

2.1 Materials and method

This experiment is a continuation of previous work performed at CFU by colleagues, as mentioned in Section 1.2. The measurements were again performed at CFU. Live fish were provided by the Marine Biological Laboratory, Biological Institute, University of Copenhagen, Helsingør, Denmark. The fish were anaesthetized with a deadly dose 10 minutes before the measurements.

2.1.1 Setup of the measurements

The setup of the measurements is presented in Fig. 2.1 and Fig. 2.2. A fish was held underwater in a small aquarium by 1 mm diameter nylon strings. At the bottom of the aquarium, there was a pad made of vibration absorbing material to reduce the reverberation in the aquarium. A convex array transducer was positioned above the fish and held by an angle adjustment

device. A convex array transducer was chosen, because it has a wider field of view than a linear array transducer and can image a whole slice of the fish. The transducer was connected to a BK Medical Profocus 2202 ultrasound scanner (BK Medical, Herlev, Denmark) equipped with a dedicated research interface connected to a personal computer (PC) through an X64-CL Express camera link interface (Dalsa, Waterloo, ON, Canada). The angle adjustment device was mounted on a mechanical linear scanner, controlled by a manual control pad.

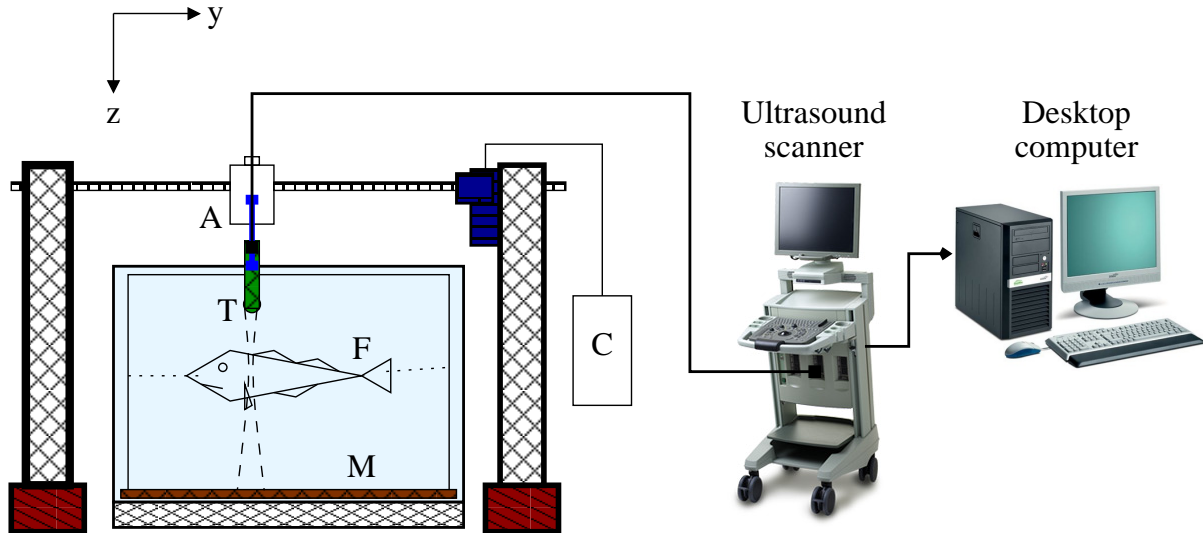


Figure 2.1: Setup of the measurements. *M* is a pad made of vibration absorbing material. *F* is a fish. *T* is a convex array transducer. *A* is an angle adjustment device. *C* is a controller for the mechanical scanner to move the transducer in the direction along the fish.

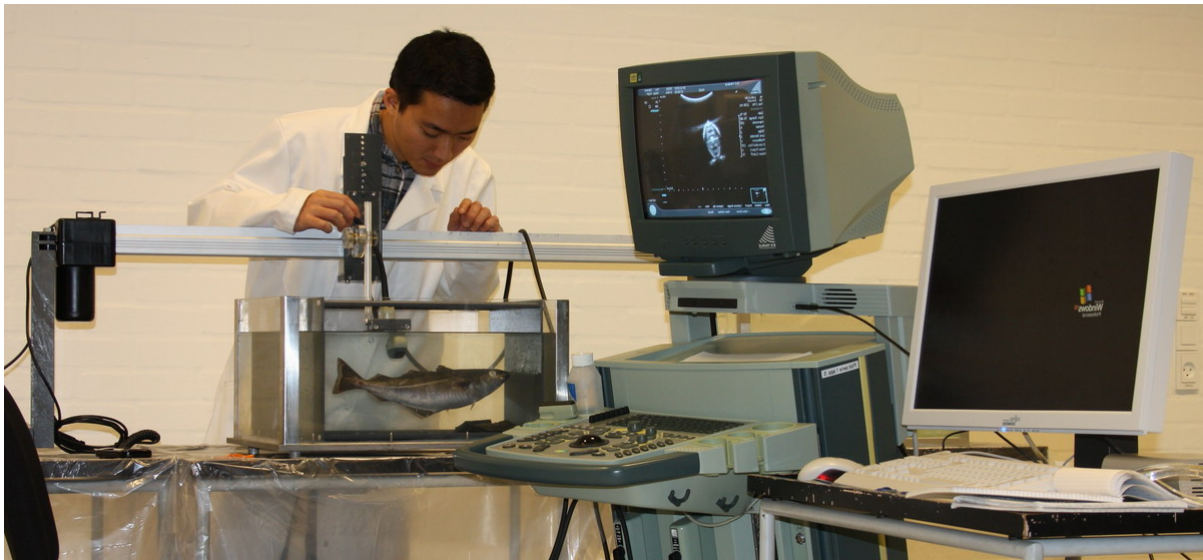


Figure 2.2: A photo of the setup for the measurements.

In each measurement, the transducer was moved along the fish from head to tail by using the mechanical scanner. The angle between the fish and the transducer center beam was selected using the angle adjustment device (Fig. 2.3). The ultrasound images were recorded both as video image data and as digitally beamformed radio frequency (RF) echo data sampled at 40 MHz. The video data were initially stored on the ultrasound scanner and later downloaded. The

RF data were saved on the PC using the program CFU GRABBER [39]. The original program could only save up to 1.4 gigabytes at a time. It was modified for the measurements in this study so that up to 3 gigabytes could be saved at a time, which made it possible to cover larger sections of a fish. One recording consists of two or three sections including several hundred ultrasound slice images.

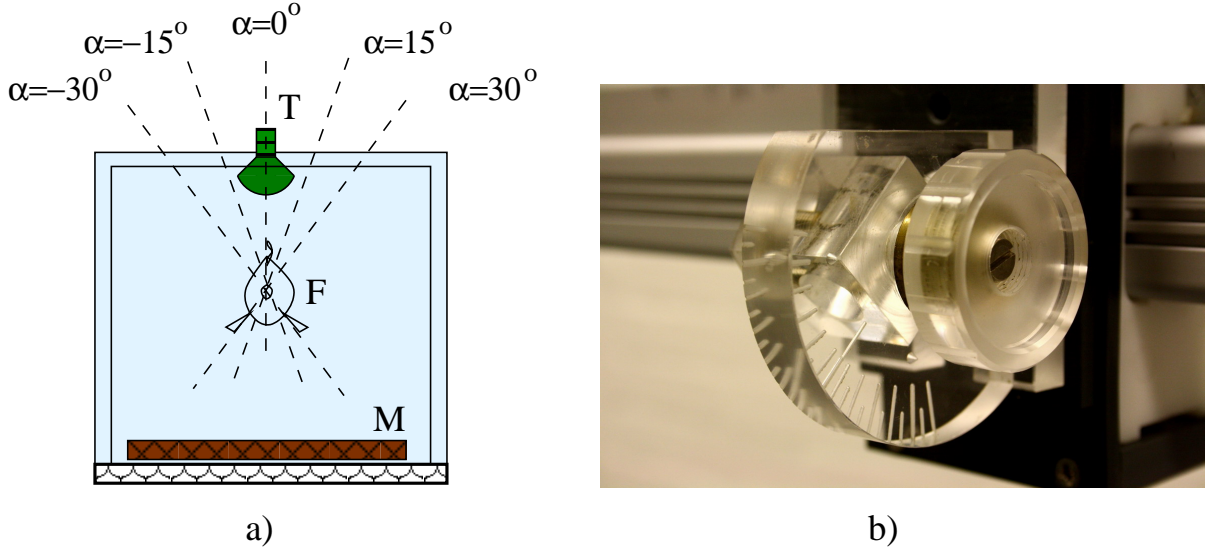


Figure 2.3: Adjustment of angle α between the fish and the transducer center beam. M is the pad made of vibration absorbing material. F is a fish. T is the convex array transducer. A cross section of the fish and different angle adjustments (a). The angle adjustment device (b).

2.1.2 Data processing

Matlab was used to process the RF data, and video data were used only as backups or for a quick overview of the results. Each recording corresponds to a fixed value of the angle α . The convex array transducer transmits a fan of beams. The image field is a sector with a total angle β , which consists of $n = 384$ RF scan lines which from now on will be called RF lines. There are m samples in a RF line and k ultrasound images in one recording. To explain the processing of the data, the coordinate system is defined as:

- y axis is the axis along the length of the fish. It is perpendicular to the imaging plane of the transducer. y is the image number in a recording.
- xz is in the imaging plane of the transducer.
- x is the RF line number.
- z is the sample number in an RF line.

A sample point $r(z, x, y)$ is the value of the RF signal at sample number z , RF line number x , image number y . In order to investigate the ultrasound backscatter of a slice of fish as a function of range, range profiles will be calculated by

$$R(z, y) = \frac{1}{n} \sum_{x=1}^n r(z, x, y) \quad (2.1)$$

where $R(z, y)$ is the average of sample points for the same image number and range.

The envelop detection method is then applied using the $hilbert()$ function (Signal Processing Toolbox, Matlab) then the $abs()$ functions is applied to generate the intensity range profiles

$$I(z, y) = abs(hilbert(R(z, y))) \quad (2.2)$$

Energy distribution of ultrasound backscatter along the y axis from the fish is obtained by averaging all the data points in each intensity range profile

$$E(y) = \frac{1}{m - z_0 + 1} \sum_{z=z_0}^m I(z, y) \quad (2.3)$$

where z_0 is the start data point in z direction corresponding to the first usable sample point in the fish.

The ultrasound images of the fish are also divided into three groups: the ultrasound images for the head of fish, the body of fish, and the tail of fish. The head of the fish has the most complicated bone structure. The body of the fish has the most complicated soft tissue structures, namely the intestines and the swimbladder. For each group of images an average cross section image of the fish is calculated

$$R_{ac}(z, x) = \frac{1}{k_b - k_a + 1} \sum_{y=k_a}^{k_b} r(z, x, y) \quad (2.4)$$

$$I_{ac}(z, x) = abs(hilbert(R_{ac}(z, x))) \quad (2.5)$$

where k_a to k_b are the image numbers.

2.2 Results

Ultrasound measurements were performed on four fish. The transducer center frequencies were 2.5, 3.5, and 6 MHz. Fish1 is a cod with a length of about 26 cm and a pop-up right eye. Fish2 is a saithe (*Pollachius virens*) with a length of about 32.5 cm. Fish3 is a cod with a length of about 29 cm. Fish4 is also a cod with a length of about 33.5 cm. Photos of the fish are presented in Fig. 2.4. A list of figures showing the results is presented in Table 2.1. Energy distribution curves of the backscatter from fish are presented as function of normalized length. Each energy distribution is log compressed and normalized to the local maximum value in the distribution. The length of each fish is normalized to its maximum length so that the results from fish with different lengths can be compared. The value 0 corresponds to the head and 1 to the tail of the fish. The energy distribution curves are discussed in this section. The intensity range profiles are presented as range profile maps in Appendix C for reference.

Comparisons of energy distributions from the three cods are presented in Fig. 2.5. The transducer center frequency is 6 MHz. The values of the scanning angle α are 0° , 30° , and -30° . There are three dorsal fins in a cod. The last dorsal fin and the tail appeared clearly in the distribution curves positioned from 0.65 to 1 of the normalized length. The position of the second dorsal fin from 0.45 to 0.65 of the normalized length can also be seen in the energy distribution curves even though it is not very clear for fish1. Maximum values of the energy appear at about

Table 2.1: A list of figures for an overview of the results

Measurements	α [degree]	$E(y)$ (normalized log compressed)	$I(z,y)$ [dB]
3 cods, 6 MHz			
	0	Fig. 2.5a	Fig. C.1
	30	Fig. 2.5b	Fig. C.2
	-30	Fig. 2.5c	Fig. C.3
a cod + a saithe, 6MHz			
	0	Fig. 2.6a	Fig. C.4
	30	Fig. 2.6b	Fig. C.5
	-30	Fig. 2.6c	Fig. C.6
	15	Fig. 2.7a	Fig. C.7
	-15	Fig. 2.7b	Fig. C.8
a saithe and 2 cods 6MHz, 3.5 MHz, 2.5 MHz			
fish 2	0	Fig. 2.8a	Fig. C.9
fish 3		Fig. 2.9a	Fig. C.12
fish 4		Fig. 2.10a	Fig. C.15
fish 2	30	Fig. 2.8b	Fig. C.10
fish 3		Fig. 2.9b	Fig. C.13
fish 4		Fig. 2.10b	Fig. C.16
fish 2	-30	Fig. 2.8c	Fig. C.11
fish 3		Fig. 2.9c	Fig. C.14
fish 4		Fig. 2.10c	Fig. C.17
		$I_{ac}(z,x)[dB]$	$I_{ac}(z,x)[dB]$
a saithe (fish2) and a cod (fish 3)			
head (2.5 MHz)	0	Fig. 2.12a, b	
body (2.5 MHz)	0	Fig. 2.12c, d	
tail (2.5 MHz)	0	Fig. 2.13	
fish2, 2.5 MHz	30, -30		Fig. C.18
fish2, 3.5 MHz	0, 30, -30		Fig. C.19
fish2, 6 MHz	0, 30, -30		Fig. C.20
	15, -15		Fig. C.21
fish3, 2.5 MHz	30, -30		Fig. C.22
fish3, 3.5 MHz	0, 30, -30		Fig. C.23
fish3, 6 MHz	0, 30, -30		Fig. C.24



a) fish1 _ a cod with a pop-up right eye



b) fish2 _ a saith



c) fish3 _ a cod



d) fish4 _ a cod

Figure 2.4: Photos of four fishes used for the measurements.

0.3 to 0.4 of the normalized length. In case of fish1, a maximum value of the energy also appears at about 0.175 of the normalized length. The energy distributions from about 0.1 to 0.65 of the normalized length appear complicated. The data for the cod fish4 are only available up to about 0.8 of the normalized length due to some mistakes in the measurements.

Fig. 2.6 and 2.7 present comparisons of the energy distributions between the cod fish1 and the saithe fish2 to see if the backscatter characteristics of one species are different from the characteristics of another species. The center frequency of the transducer is 6 MHz, and the values of the angle α are 0° , 30° , -30° , 15° , and -15° . The data of a part of the head of the saithe fish2 are not available, also due to mistakes in the measurements. The dorsal fins of the saithe do not appear clearly in the distribution curves. The transition from the head to the body of the saithe can be seen as a local minimum in the distribution curves at about 0.2 in the normalized length. The energy distribution curves of the saithe appear smoother than the curves of the cod fish1 in the region 0.2 to 0.8 of the normalized length. The maximum value of the energy distribution of the saithe appears at about 0.3 to 0.4 of the normalized length.

To observe if the characteristics of the backscatter remain the same for different frequencies in the MHz, comparisons between energy distributions of the backscatter in measurements with different transducer center frequencies are performed. The comparisons are presented in Fig. 2.8, 2.9, and 2.10. The transducer center frequencies are 6, 3.5, and 2.5 MHz. The discrepancies among the energy distribution curves are little for most of them. The shapes of the curves for all the fish are very similar for different transducer center frequencies. There are few significant discrepancies, namely at about 0.8 to 1 of the normalized length in Fig. 2.8a, and 0 to 0.2 of the normalized length in Fig. 2.10b.

The energy distributions of the backscatter only give estimations of backscatter energy along the fish. It is still not clear which parts of the fish contribute to the backscatter. In the frequencies well below 1 MHz, it is usually the swimbladder that contributes the most. In this study

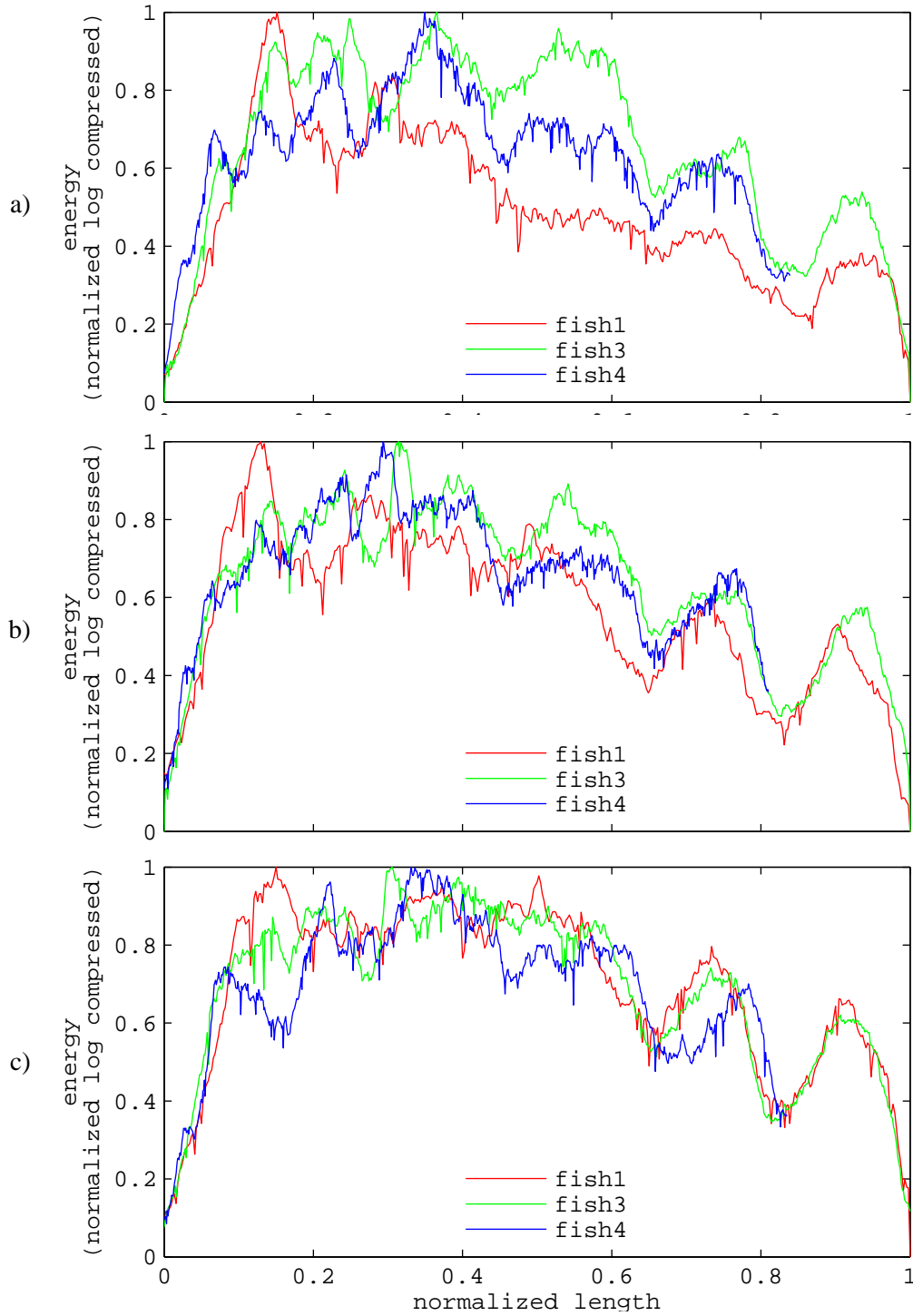


Figure 2.5: Energy distributions of the three cods fish1, fish3, fish4. The length of the fish is normalized to the total length of the fish. The transducer center frequency is 6 MHz. The values of the angle α are 0° (a), 30° (b), and -30° (c).

the range profile maps and the cross section images will be used to investigate backscatter from different regions of the fish. Examples of the range profile maps and the average cross section images are presented in Fig. 2.11, 2.12, and 2.13. Only results corresponding to the transducer frequency of 2.5 MHz are presented here as 2.5 MHz is the lowest available center frequency and is close to 1 MHz, the transducer center frequency of the desired single-element transducer

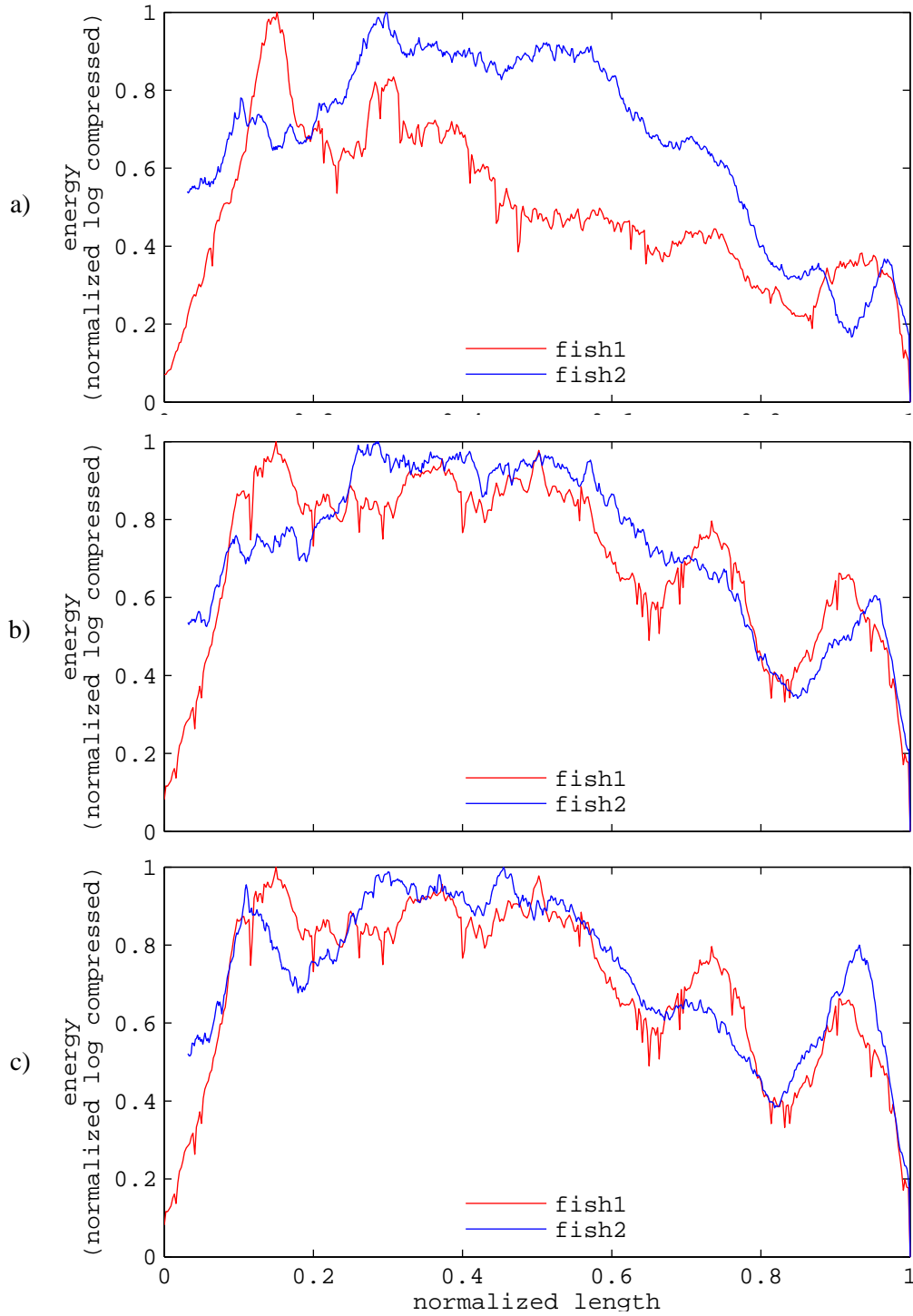


Figure 2.6: Energy distributions of the cod fish1, and the saithe fish2. The length of the fish is normalized to the total length of the fish. The transducer center frequency is 6 MHz. The values of the angle α are 0° (a), 30° (b), and -30° (c).

system. More examples corresponding to other transducer center frequencies as well as different fish can be found in Appendix C, but conclusions drawn from them are not significantly different. Fig. 2.11 shows that the bone and skin structures of the fish are the structures contribute with higher echoes than the other structures. The swimbladder is not visible at all in the range profile map of the saithe in Fig. 2.11a. There is a very bright region where the swim-

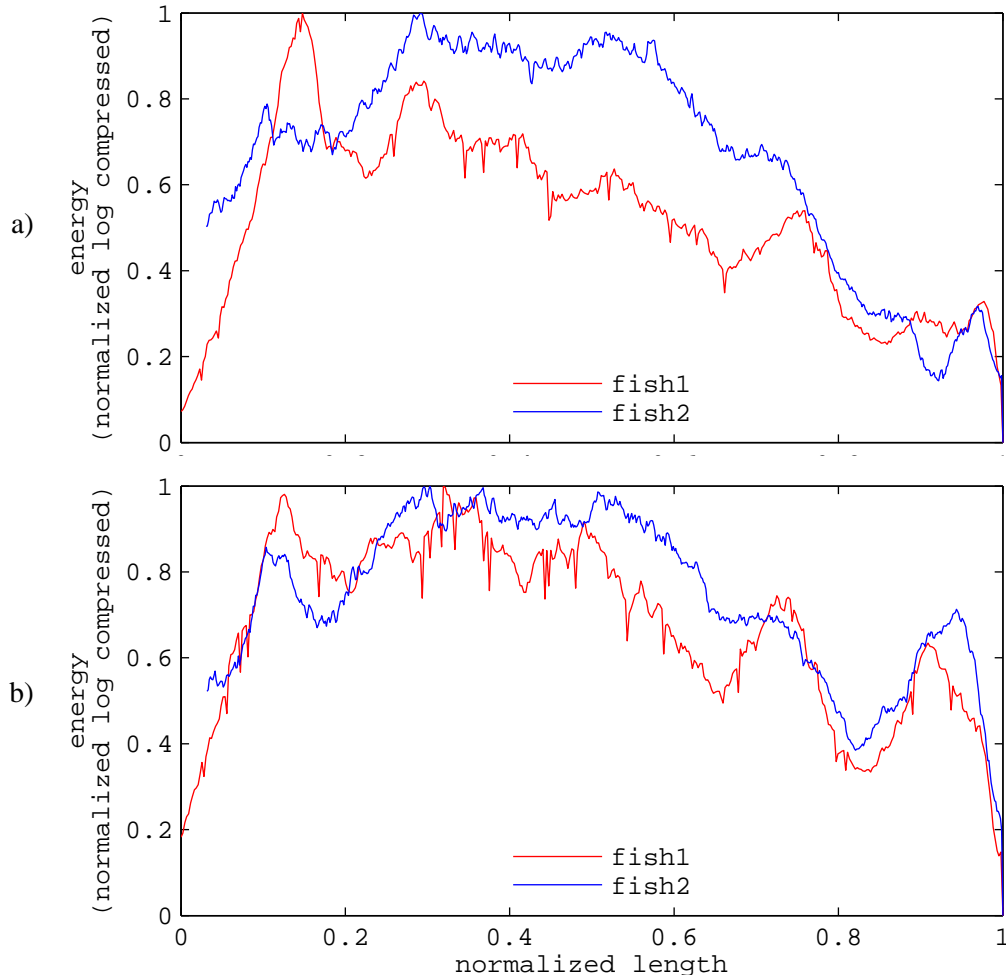


Figure 2.7: Energy distributions of the cod fish1, and the saithe fish2. The length of the fish is normalized to the total length of the fish. The transducer center frequency is 6 MHz. The values of the angle α are 15° (a), and -15° (b).

bladder may be located in the cod in Fig. 2.11b. More details of the backscatter can be seen from the average cross section images in Fig. 2.12 and 2.13. It is clear from Fig. 2.12d that the bright region is due mostly to the bone structures of the cod. Shadow effects appear behind the bone regions in the images. The regions closer to the transducer are brighter than the other regions. Because of the shadow effects it is difficult to get signals from the whole fish.

2.3 Discussion

Using the normalized length, it is possible to compare the results of backscatter from different fish with different lengths. The energy distribution curves of the cods at about 0.65 to 1 of the normalized length are very similar. Because the last dorsal fins, the anal fins, and the tails of the fish contribute significantly to the backscatter energy, the relative size and position of the fish fins are similar for different sizes of fish, and the tissue structure of the tail part is relatively simple (Fig. 2.4, Fig. 2.5). The shapes of the other fins of the cods vary. Some of them are fully opened, some are closed, some are straight, and some are bent. The bone structure of the head and the tissue structure of the body of the fish are complicated, especially the intestines.

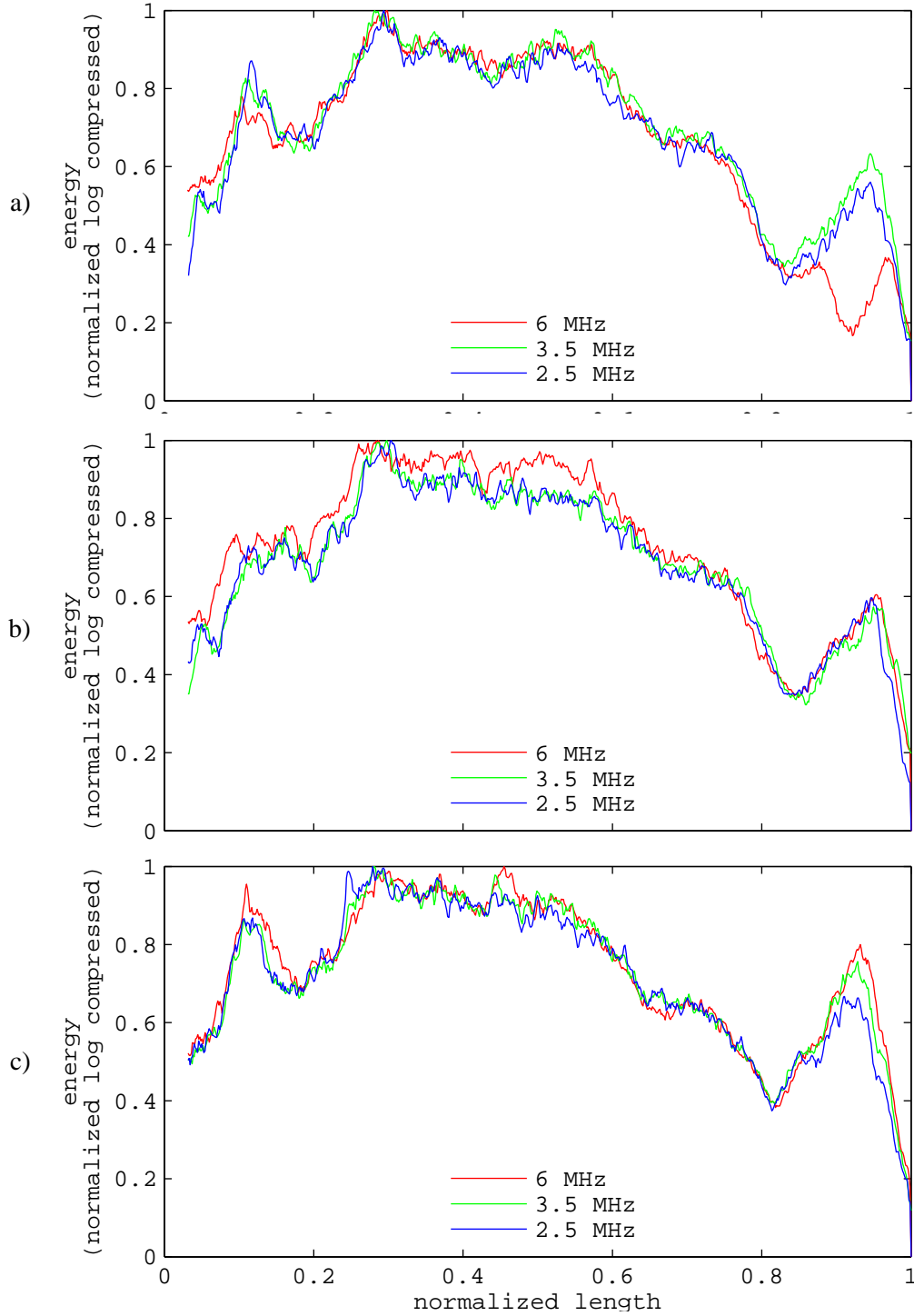


Figure 2.8: Energy distributions of the saithe fish2. The length of the fish is normalized to the total length of the fish. The transducer center frequencies are 6, 3.5, and 2.5 MHz. The values of the angle α are 0° (a), 30° (b), and -30° (c).

Because of all of that, the energy distribution curves from 0 to 0.65 of the normalized length vary somewhat.

The angle α also contributes to the variation of the energy distributions. For example, the energy distribution curve from 0.3 to 0.8 of the normalized length of fish1 for $\alpha = 0^\circ$ is smoother

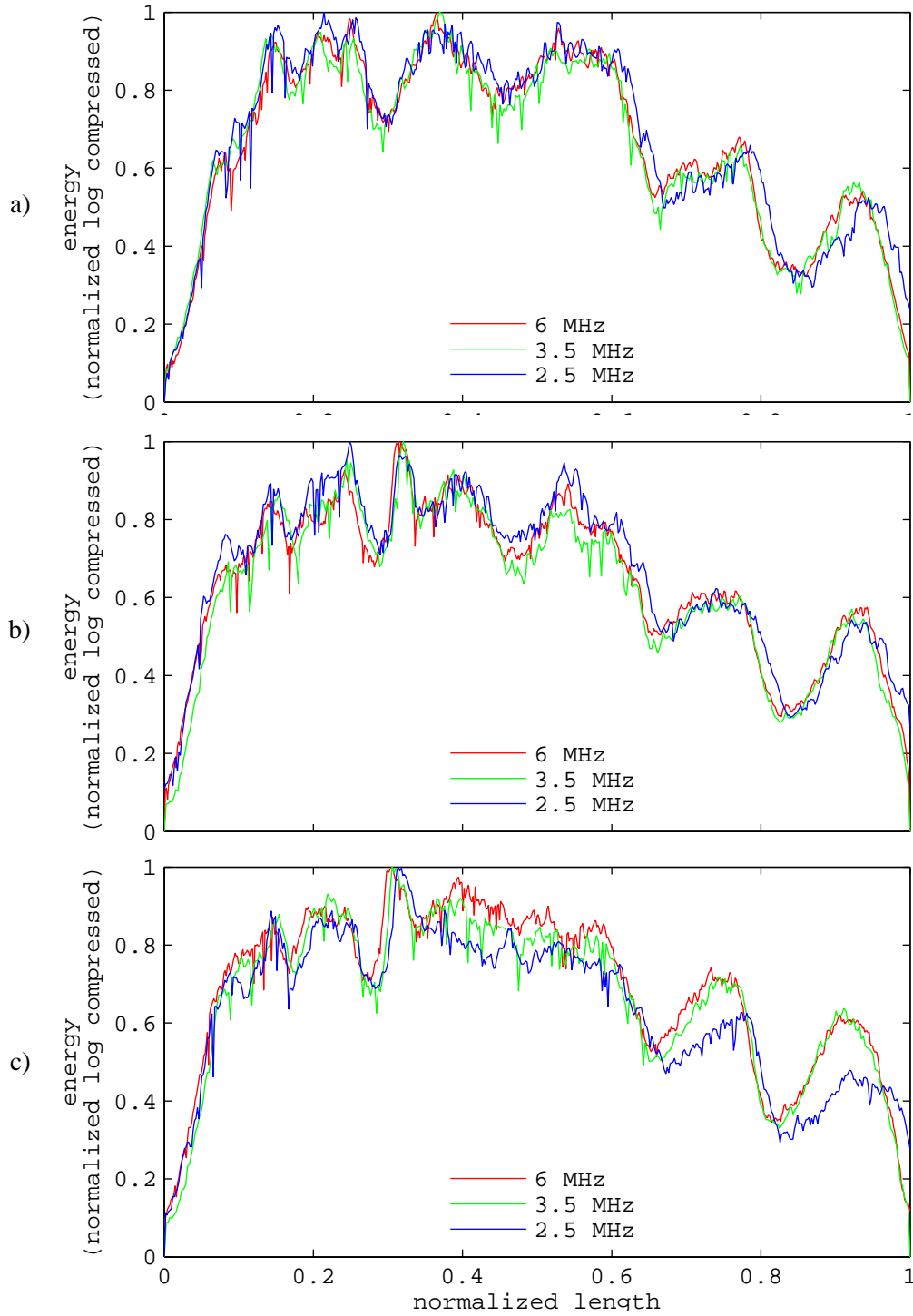


Figure 2.9: Energy distributions of the cod fish3. The length of the fish is normalized to the total length of the fish. The transducer center frequencies are 6, 3.5, and 2.5 MHz. The values of the angle α are 0° (a), 30° (b), and -30° (c).

than the corresponding curve for $\alpha = 30^\circ$ (Fig. 2.5). However, the angle α has little effect on an abnormal maximum value in the energy distribution curves of fish1 that appears at about 0.175 of the normalized length, a position corresponding to the pop-up right eye of fish1. The damage to the eye happened while the fish was still alive. The composition of the eye may have changed making backscattering from the eye stronger than normal. The position outside

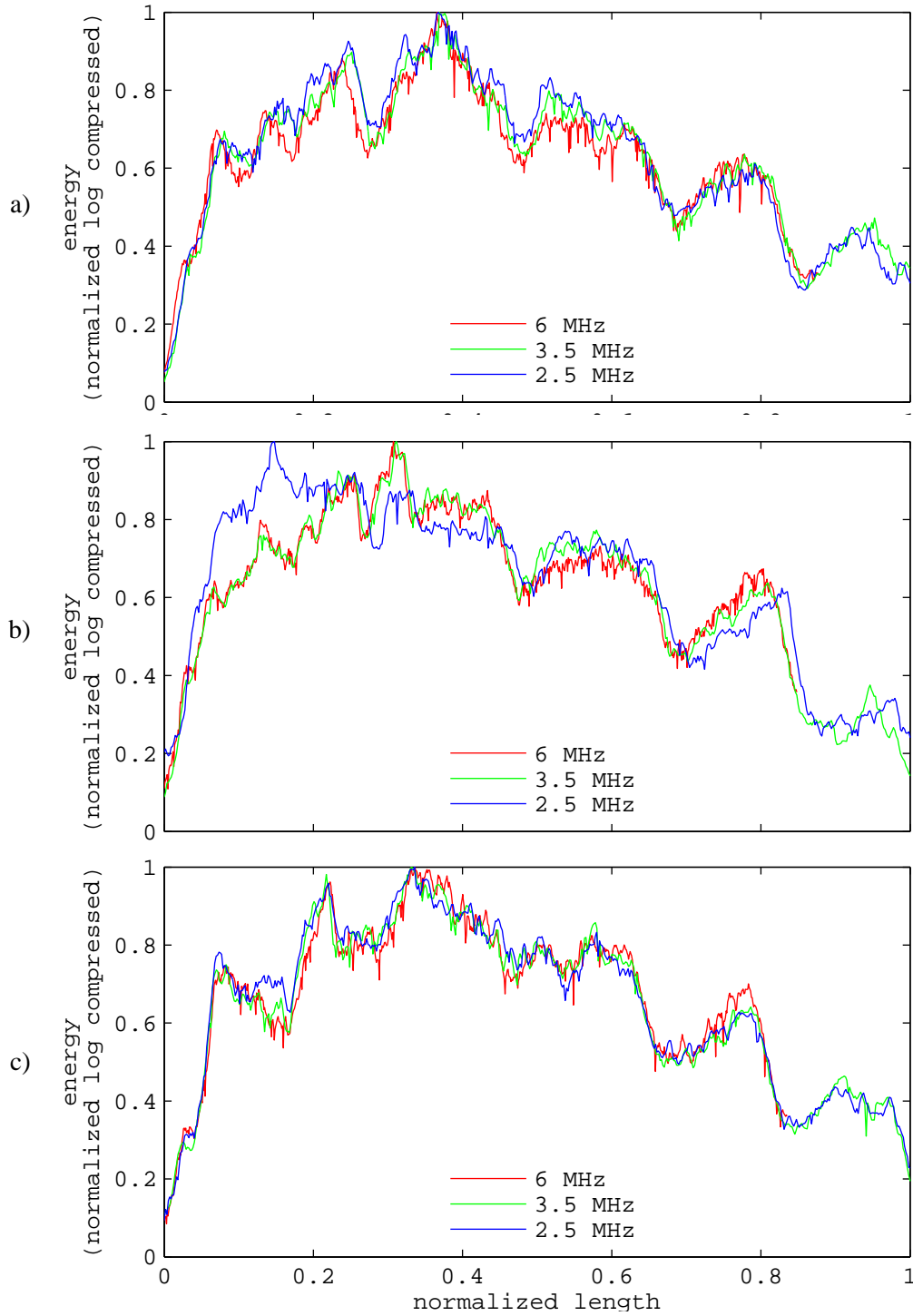


Figure 2.10: Energy distributions of the cod fish4. The length of the fish is normalized to the total length of the fish. The transducer center frequencies are 6, 3.5, and 2.5 MHz. The values of the angle α are 0° (a), 30° (b), and -30° (c).

the head may also increase the scattering strength. This should be taken into account in fish species discrimination as this phenomenon can also occur for live fish in the sea.

The discrimination may be possible if there are differences in characteristics of the backscatter from species to species. There are several similar characteristics on the energy distribution

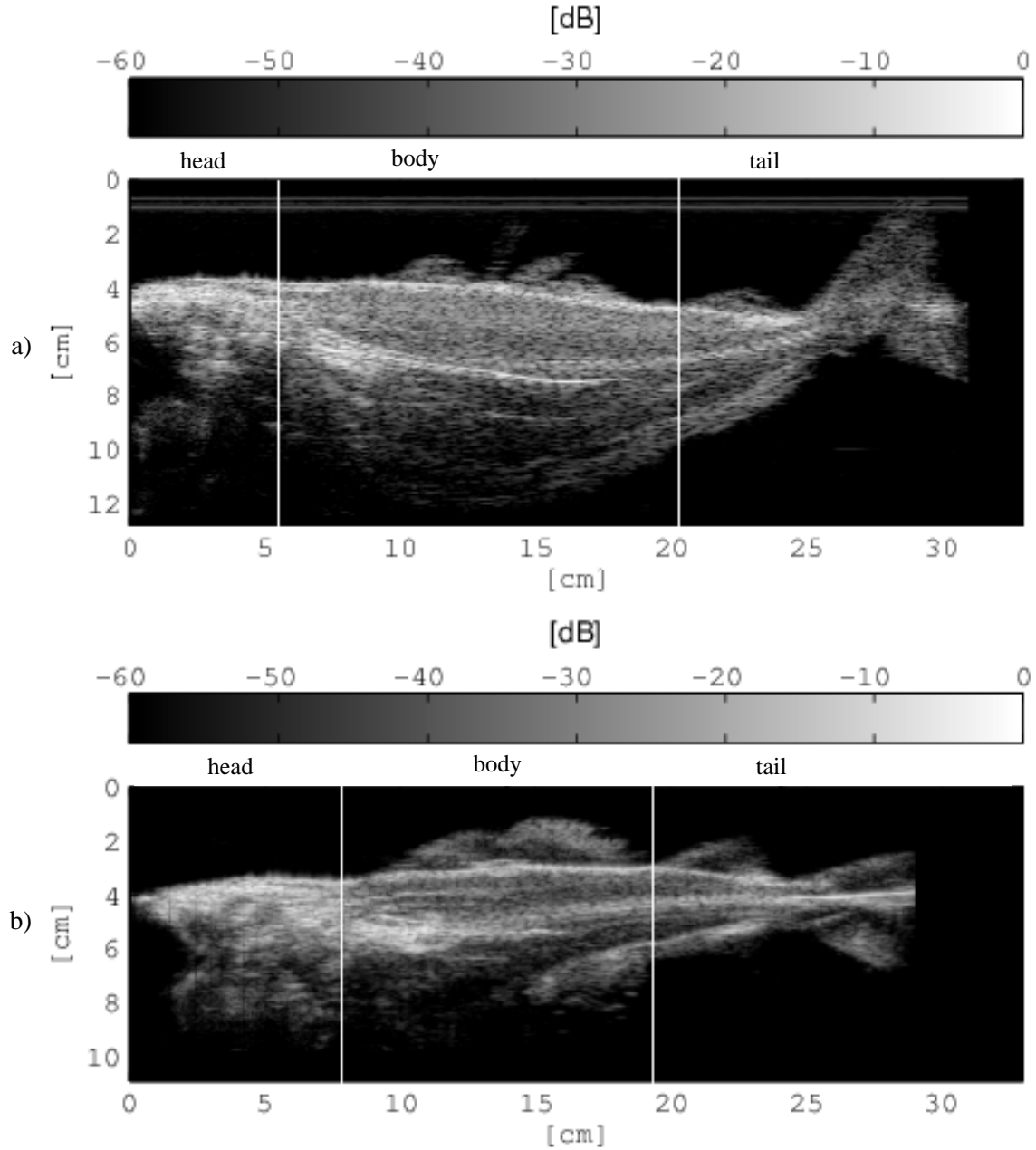


Figure 2.11: Range profile maps in the yz plane of the saithe fish2 (a), and the cod fish3 (b). The transducer center frequency is 2.5 MHz. The angle α is 0° . The vertical white lines are to mark the limits between different parts of the fish.

curves for the saithe and the three cods (Fig. 2.5 and 2.6). The head of the fish appears from 0 to about 0.2 of the normalized length, the body from about 0.2 to 0.8, and the tail fin from about 0.8 to 1. The last local minimum of the curves is usually a transition position between the body and the tail of the fish. A transition between the head and the body is not as clear as the transition between the body and the tail. So are there any differences in backscatter from a cod and a saithe? In the body region at about 0.2 to 0.8 of the normalized length, the energy distribution curve of the saithe appear smoother than the curves of the cods, because the ratios of the sizes of the fins and the size of the body of a saithe are smaller than the same ratios of a cod. There are at least three local maxima in the curves of the cods, whereas the local maxima

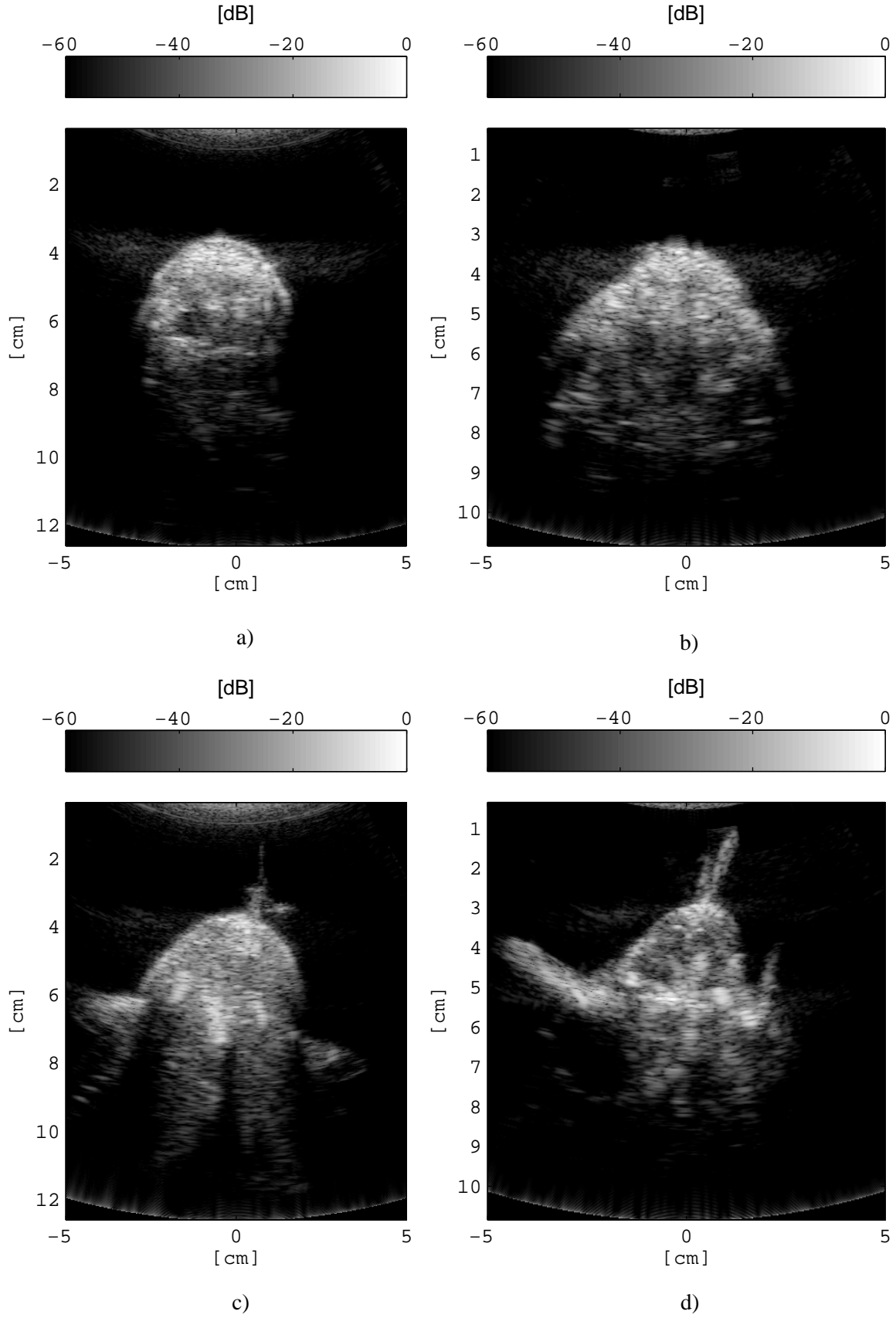


Figure 2.12: Average cross section images of different parts of the fish. The transducer center frequency is 2.5 MHz. The angle α is 0° . The head of the saithe fish2 (a), the head of the cod fish3 (b), the body of the saithe (c), and the body of the cod (d).

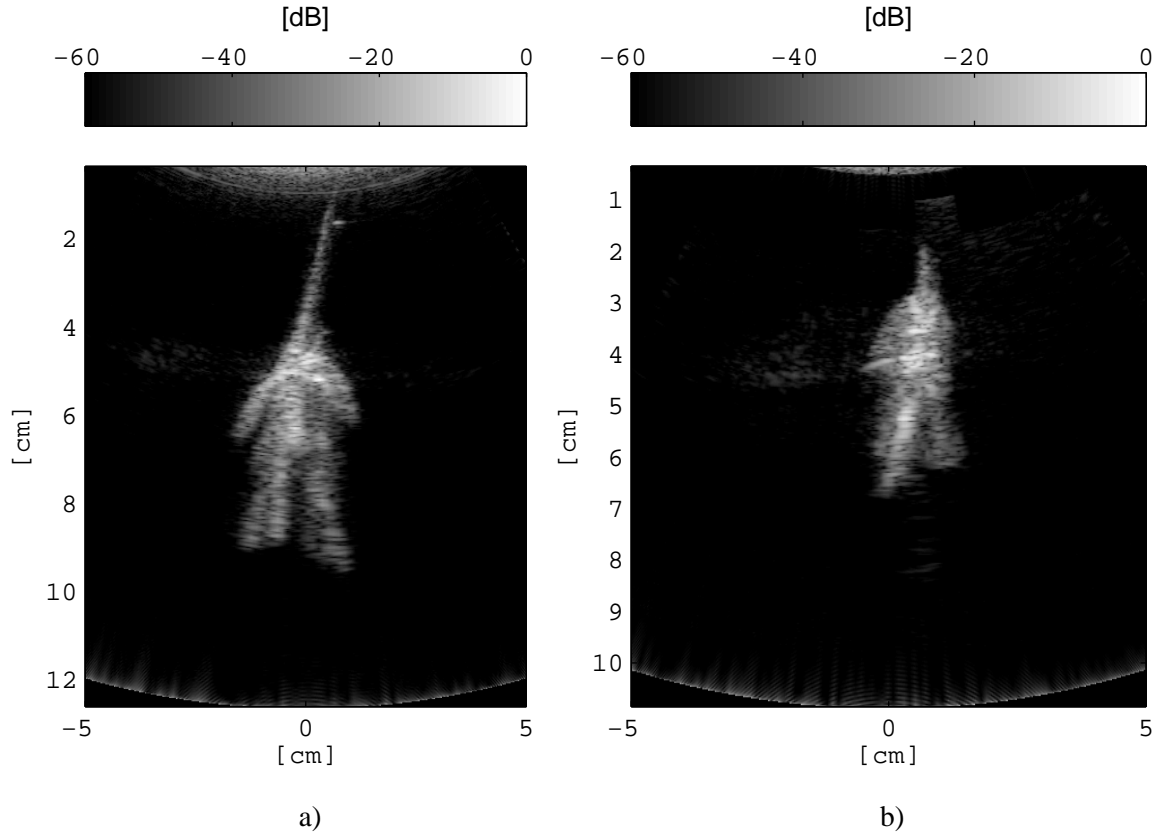


Figure 2.13: Average cross section images of the tail of the fish. The transducer center frequency is 2.5 MHz. The angle α is 0° . The saithe fish2 (a), and the cod fish3 (b).

are fewer and not as clear in the curves of the saithe. So, an energy distribution curve of the backscatter of a saithe can be distinguished from an energy distribution curve of a cod.

The statements above are true at all frequencies in the low MHz range, specifically at 6, 3.5, and 2.5 MHz as presented in Fig 2.8, 2.9, and 2.10. The use of the normalized log compressed energy shows that at different frequencies the shapes of the energy curves for particular species remain at about the same but the energy distribution curves of saithe and cod appear clearly different.

The backscatter energy from the head and the body of the fish is higher than the energy from the tail. The part that contributes most to the backscatter is the bone structure of the fish (Fig. 2.11). The brightest regions in the range profile maps are the regions of bone structure. The head of the fish is very bright because most of the tissue in the head is bone. The results agree with the statement from the work of Gorska et al. [36,37]. The shadowing mostly caused by the bone structure makes some of the lower parts of the fish disappear from the range profiles. The swimbladder is positioned just below the bone structure. It is not clearly visible in the range profiles probably because of the shadowing. It can therefore be assumed that in the low MHz (2.5 - 6 MHz) the swimbladder gives very little scatter energy (it is 20% to 80% at 220 kHz in the work of Sun et al. [13]). The skin regions also contribute significantly to the backscatter. Most of the body and the tail of the fish are visible in the average cross section images, but only about two thirds of the head is visible due to the complicated bony tissue structure (Fig. 2.12, and 2.13).

It can be assumed from the results that the backscatter energy depends on the hardness of the tissue inside the fish as well as the shape of the skin surface. The orientation of the fish (angle α) also causes variation to the backscatter. The results agree with the results from the work of Jech et al. [38] that orientation is very important at high frequencies.

The energy distribution curves are interesting. As shown above, they can be useful to develop methods for fish species discrimination. The measurements have so far produced empirical ultrasound range profiles for $\alpha = -30^\circ, -15^\circ, 0^\circ, 15^\circ$, and 30° , but this is not sufficient for efficient species discrimination. The measurement procedure developed in this study can be used to generate a complete library of empirical ultrasound range profiles for a species to improve the efficiency.

2.4 Conclusions

In this case study, *in-vitro* experiments were performed to observe the ultrasound backscatter from fish in the low MHz frequency range. The results show that even though there are variations, a scan of the ultrasound backscatter along a fish of a specific species contains patterns that are characteristic for that species. The characteristic backscatter patterns of one species are different from those of another species. This is true at all frequencies in the low MHz range. The part of a fish that contributes most is not necessarily the swimbladder, but the results indicate that in the low MHz frequency range bone structures, and skin surfaces are more important. As expected, the orientation of the fish causes variations to the backscatter. But the procedure of measurements developed in this study can be used to produce empirical ultrasound range profiles from many directions to address this problem in fish species discrimination.

Simulation of ultrasound images of fish from CT images

This chapter contains a summary of the article [40]

- **An Hoai Pham**, Bjarne Stage, Martin Christian Hemmsen, Bo Lundgren, Mads Møller Pedersen, Tina Bock Pedersen, and Jørgen Arendt Jensen, "Simulation of ultrasound backscatter images from fish", published in *Proceedings of SPIE*, 2011, 7961-796152(1-10).

and the articles [41] and [42]

- **An Hoai Pham**, Bo Lundgren, Bjarne Stage, Mads Møller Pedersen, Martin Christian Hemmsen, Michael Bachmann Nielsen, and Jørgen Arendt Jensen, "Shadow effects in simulated ultrasound images derived from computed tomography images using a focused beam tracing model", published in *Journal of the Acoustical Society of America*, vol. 132, no. 1, pp. 487-497, 2012.
- **An Hoai Pham**, Bjarne Stage, Bo Lundgren, Martin Christian Hemmsen, Mads Møller Pedersen, and Jørgen Arendt Jensen, "Simulation of shadowing effects in ultrasound imaging from computed tomography images", published in *Proceedings of IEEE International Ultrasonics Symposium*, 2011, pp. 1411 -1414.

which are found in full length in Appendix B.1 and A.1, B.2, respectively. The journal paper in Appendix A.1 is an extended and elaborated version of the conference paper in Appendix B.2, and thus primary focus will be on the content of the journal paper.

3.1 Objective of Study

Ultrasound (US) range profiles for fish can be acquired using the empirical method described in Section 2. With only the empirical method, it would take a lot of time and effort to build a complete library of ultrasound range profiles even for one species. In order to begin the process of trying to do species discrimination, it would be necessary to have complete libraries of the range profiles for many species. Simulations can be used in addition to the empirical method to support and speed up the creation of the libraries. Even though it is difficult to use the simulation method to produce results that are similar to measurement results, the method has

many advantages over the empirical method. The simulation procedure can be made automatic to save manual work and supervision. Also, the influence of shape changes similar to shape changes of a free-swimming fish can relatively easily be investigated, whereas it is difficult to do so in an experiment with a fixed fish. For example, what is the influence of a fish body that is bent because the fish is turning. Therefore, the second case study was focused on developing a simulation method.

Frequencies above 500 kHz are in a range, where there are many medical ultrasound applications, and a medical ultrasound scanner was also used in the previous case study described in Section 2. It therefore seems natural to use the modeling methods well known in the medical ultrasound field [43–56]. The range profiles in Section 2 were calculated based on data from ultrasound slice images along the length of the fish. So, naturally the approach for the simulations was to generate simulated ultrasound slice images of fish. In the study a method was developed to use CT images to generate simulated ultrasound images that matched real ultrasound images reasonably well, like reproducing diffuse shadows. The method uses a model named focused beam tracing model, which is based on an earlier conventional straight ray ultrasound ray-tracing model. The investigations were performed assuming a linear array transducer, and the results are compared to the results from conventional methods as well as measurements.

3.2 Summary of Papers

The same basic measurement data (ultrasound scan and CT scan) on fish are used for the work in [40], [41], and [42]. Measurement procedures, initial setups, and calibration processes for the measurements as well as simulations are described in detail in [40]. The simulation method presented in [40] was used to generate simulated ultrasound images with sharp-edged shadows similar to those in conventional methods, but it was the first time such a method was applied on fish. A method using a focused beam tracing model to generate simulated ultrasound images with diffuse shadows is presented in [41]. The novelties of the work lie in the focused beam tracing model and a new way to derive relationships between the x-ray absorption values expressed in Hounsfield units (HU) and the corresponding ultrasound backscattering strength values in a CT scan image of a fish. The papers [40] and [41] describe the details of the work. Summaries of the methods and the results are presented in the following sections.

3.2.1 Materials and methods

The block diagram of the experiment is presented in Fig. 3.1. The measurements were performed on a cod first with the BK medical Profocus 2202 ultrasound scanner, then with a Toshiba Aquilion ONE CT scanner (Toshiba Medical Systems, Corp., Tochigi, Japan). The cod was not alive and the time difference between the two measurements was about 3 hours. The ultrasound scan was performed as described in Section 2 but with a linear instead of a convex array transducer. The angle α was always 0° . The fish was suspended in air during the CT scan. The measured ultrasound images were used to assess the similarity between measured and simulated ultrasound images. The geometry parameters of the ultrasound transducer and the setup parameters of the ultrasound scanner such as focusing, number of RF lines in an image used in the ultrasound scan, and the parameters of the CT images are used for the focused beam tracing model to calculate positions of simulated scatterers and their scattering strengths. The scatterer parameters and the transducer model parameters are used as inputs to the Field II

program as described in [57, 58] which calculates the sound fields used to generate simulated ultrasound images.

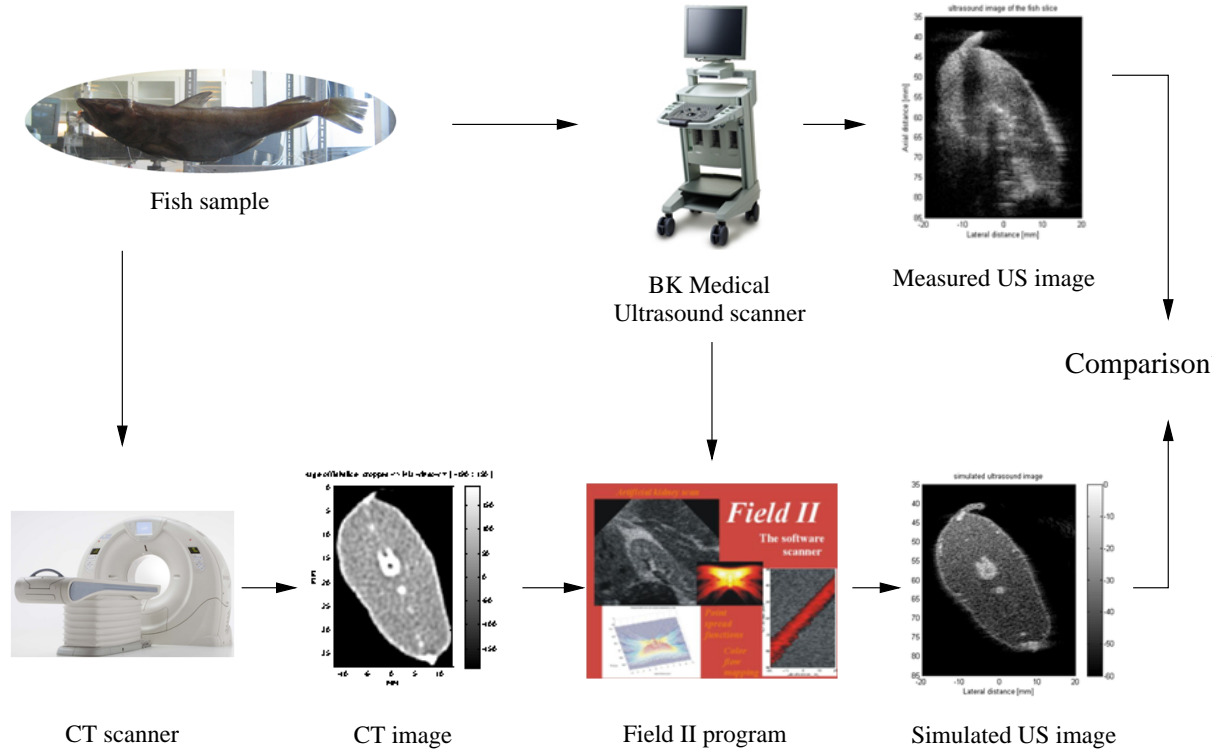


Figure 3.1: Block diagram of the procedure of the method. This is a replica of Fig. 1 in [41]

A block diagram of the simulation process is presented in Fig. 3.2. The steps in the procedure to calculate the positions of the scatterers are shown on the left-hand side of the dotted line and the steps in the procedure to calculate the amplitudes of the scatterers are shown on the right-hand side. One of the parameters needed to calculate the positions of the scatterers is the minimum total number of scatterers in the image area. To produce an ultrasound image with a fully developed speckle pattern, there should be at least 10 scatterers per resolution cell [59]. The minimum number used in the simulation should be [41]

$$n_{scatt} = 10 \frac{\text{imgvol}}{\text{rescell}} \quad (3.1)$$

where

$$\text{imgvol} = \text{CTimgarea} \times \text{eleheight} \quad (3.2)$$

$$\text{rescell} = N\lambda \text{FWHM}_l \text{FWHM}_{azi} \quad (3.3)$$

$$\text{FWHM}_i = F\#_i \cdot \lambda \quad (3.4)$$

where n_{scatt} is the number of scatterers, imgvol is the image volume in m^3 , CTimgarea is the area of the CT image which is converted from pixels to m^2 , and eleheight (in meters) is the height of the element (the size of the element perpendicular to the image plane) of the transducer. rescell is the volume of the resolution cell in m^3 , λ is the wavelength, and N is the number of cycles in the pulse. FWHM_l and FWHM_{azi} are the full width at half maximum

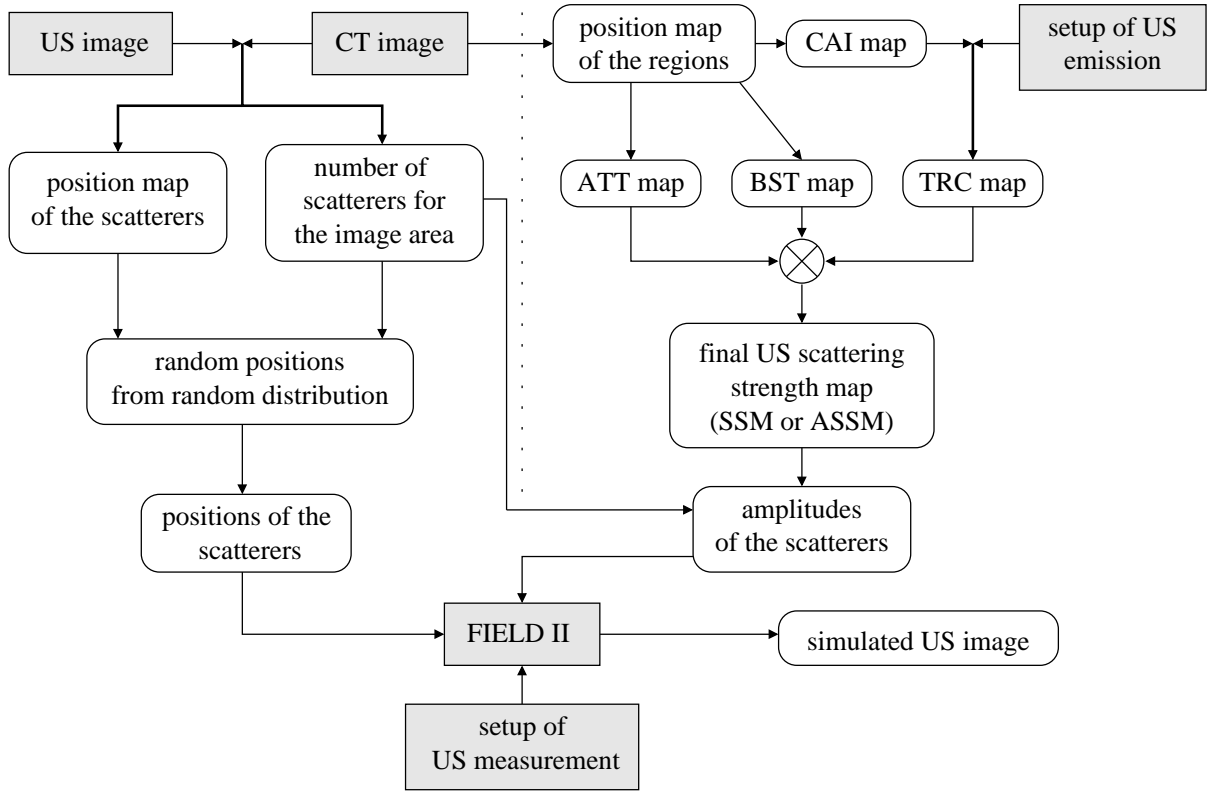


Figure 3.2: Block diagram of the simulation process. The square boxes with grey background are provided data and programs. The rounded boxes are intermediate results. This is a replica of Fig. 3 in [41]

laterally (in the image plane) and azimuthally (perpendicular to the image plane), respectively, of the point spread function at the focus point.

The amplitudes of the scatterers are calculated using the focused beam tracing model. The model is based on the ray-tracing model but takes into account the focusing of the ultrasound scanner. The transmit energy field in one emission is presented in Fig. 3.3a. In the case of the conventional ray-tracing model, the amplitudes of the scatterers are calculated by [41]

$$I_R(P) = K \frac{\text{BST}(P)}{\text{sum}L(P)} \text{ATT}(P) \text{TRC}(P) = K \cdot \text{SSM}(P) \quad (3.5)$$

where K is assumed to be 1. $\text{BST}(P)$ ($\text{cm}^{-1}\text{Sr}^{-1}$) is the backscattering coefficient of the medium at location P where a scatterer is located. ATT describes the two-way attenuation effect of the media. TRC is the two-way transmission coefficient due to the media borders. SSM is the scattering strength map, where $\text{SSM}(P)$ is the relative scattered energy returned to the transducer by the scatterer at P . $\text{sum}L(P)$ is the square of the total distance that the ray travels from the source of the sound beam to P .

In the case of the focused beam tracing method, for the em^{th} emission the ultrasound scattering strength map $\text{SSM}^{(em)}(P)$ is calculated by [41]

$$\text{SSM}^{(em)}(P) = \sum_{i=1}^m \text{SSM}_i^{(em)}(P) \quad (3.6)$$

where m is the number of active elements in one emission. $SSM_i^{(em)}(P) = 0$ if the i^{th} ray does not pass through P . Examples of active media used for calculation of ATT, BST, and TRC maps in one emission are presented in Fig. 3.3b. The final average ultrasound scattering strength map using the focused beam tracing model is calculated by [41]

$$ASSM(P) = \frac{1}{n} \sum_{em=1}^n SSM^{(em)}(P) \quad (3.7)$$

where n is the number of emissions or RF lines in an image. Examples of active media used for calculation of ATT, BST, and TRC maps in n emissions are presented in Fig. 3.4. The amplitudes of the scatterers in the focused beam tracing model are calculated by

$$I_R(P) = K \cdot ASSM(P) \quad (3.8)$$

Maps of the variables BST, ATT, CAI and TRC are calculated using a mapping table that converts HU to backscatter coefficients, attenuation coefficients, and characteristic acoustic impedance as presented in Table 3.1 [60–62].

Table 3.1: Mapping table from Hounsfield Unit to backscatter coefficients, attenuation coefficients, and characteristic acoustic impedance. This is a replica of Table I in [41].

Regions	Hounsfield unit	$\eta_b^{(M)}$ ($cm^{-1}sr^{-1}$)	$\alpha^{(m)}$ ($dB/(cm \cdot MHz)$)	Z_m ($kg/(m^2s)$)
Bone	[179, <i>maximum</i>]	[0.05, 0.1]	[100, 200]	$[6.5 \times 10^6, 7.38 \times 10^6]$
Soft tissue	[−41, 178]	[0.000125, 0.01]	[10, 32.5]	$[1.55 \times 10^6, 1.74 \times 10^6]$
Fat	[−741, −42]	[0.003, 0.019]	[1.25, 2]	1.33×10^6
Air-inside	[<i>minimum</i> , −742]	0	[400, 500]	0.4×10^3
Air-outside	not defined by HU	0	0.24	1.48×10^6

Paper [41] presents the details of the derivation of Eq. 3.1 to 3.7.

A BK Medical linear array transducer with 192 elements was used. The center frequency of the transmit pulse was 10 MHz. The transmit focus point was at a range of 45 mm. The scanner generated 384 image lines corresponding to 384 emissions in one ultrasound image. The CT images were obtained with a slice thickness of 0.5 mm and pixel sizes of $0.274 \text{ mm} \times 0.274 \text{ mm}$. Each simulated ultrasound image was generated using $n_{scatt} = 10^6$. The smallest point spread function is $0.54 \text{ mm} \times 0.3 \text{ mm}$.

3.2.2 Results

It took 10 minutes to generate one image line by Field II running as the only task on one machine or 1.83 hours for the whole simulated ultrasound image using 35 machines on the CFU cluster. Each of them was a Dell Power Edge 1750 server, Dual Intel Xeon 3.2 GHz (Dell, Inc., Texas) supporting Hyper-threading technology, and 2 gigabytes of random access memory. One sample slice of the fish was chosen to demonstrate the ray-tracing and focused beam tracing models. The results are presented in Fig. 3.5 to 3.7. Note that there are typos in Fig. 11 and 17 in paper [41]; the variable is relative energy that has no unit.

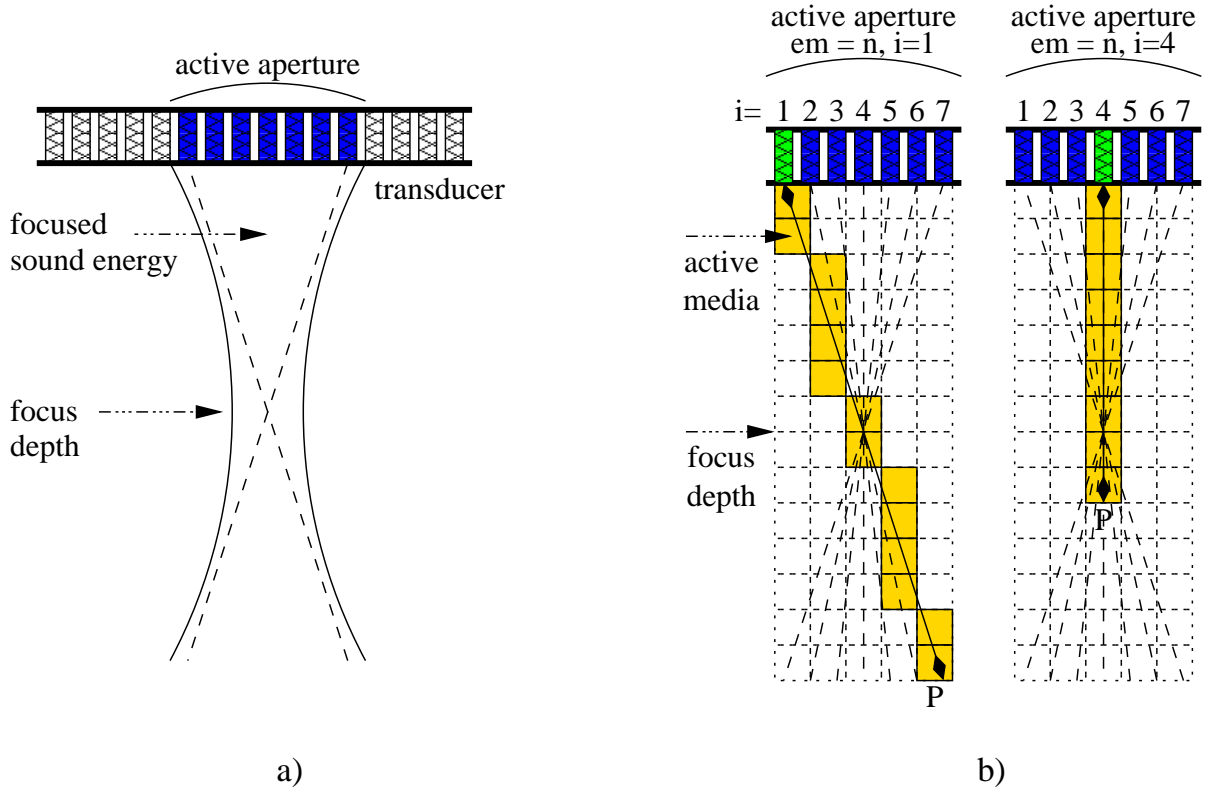


Figure 3.3: Energy transmission in one emission (a). Active media used for calculation of ATT, BST, and TRC maps in one emission in the focused beam tracing model (b). Two examples for different active media to calculate the acoustic properties of different media in the beams. The Fig. (b) is a replica of Fig. 4 in [41].

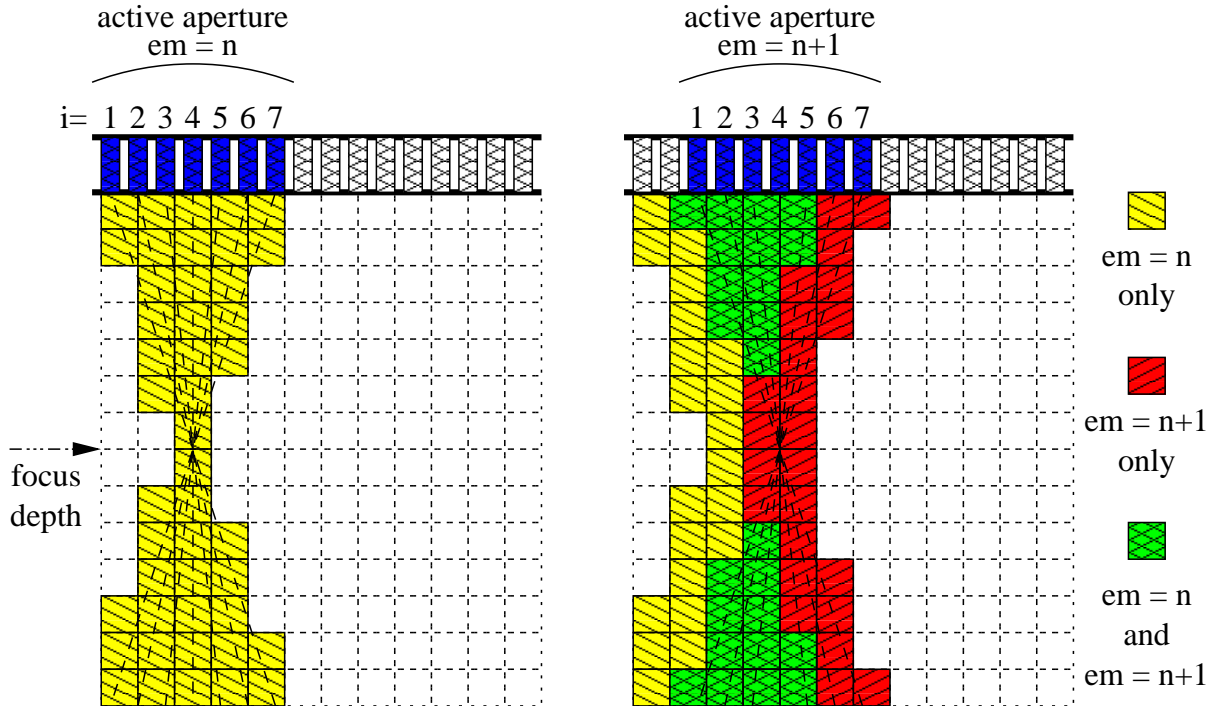


Figure 3.4: Active media used for calculation of ATT, BST, and TRC maps in n emissions in the focused beam tracing model. This is a replica of Fig. 5 in [41].

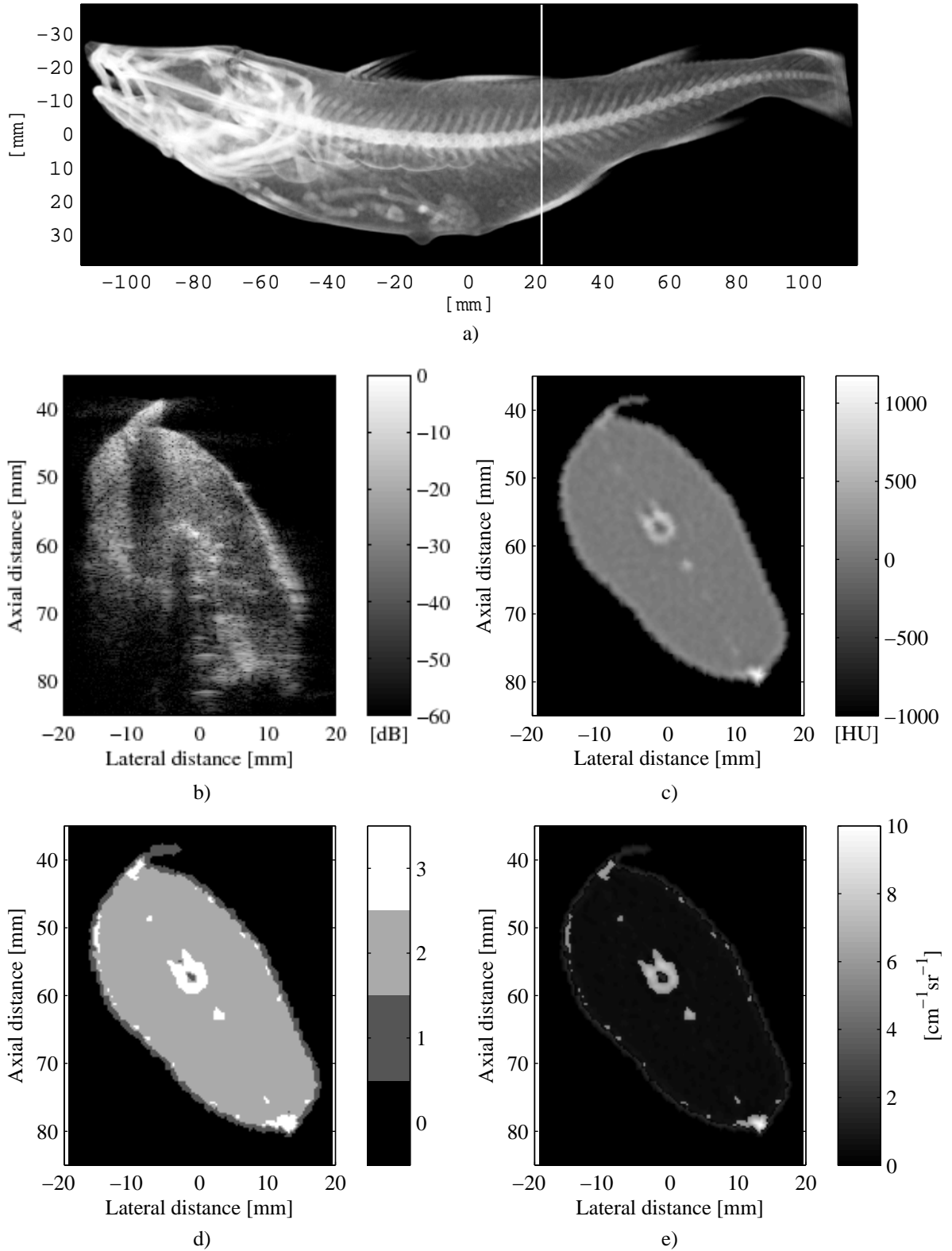


Figure 3.5: A snapshot of the three-dimensional CT of the fish (a). The vertical white line indicates the position of the slice used in the simulation. The measured ultrasound image of the slice of the fish (b). The CT image of the slice of the fish (c). The position map of the regions of the fish slice (d). Value 0: Air-outside, 1: Fat, 2: Soft tissue, 3: Bone. The BST map of the slice (e). Those are the replicas of Fig. 6 to 10 in [41], respectively.

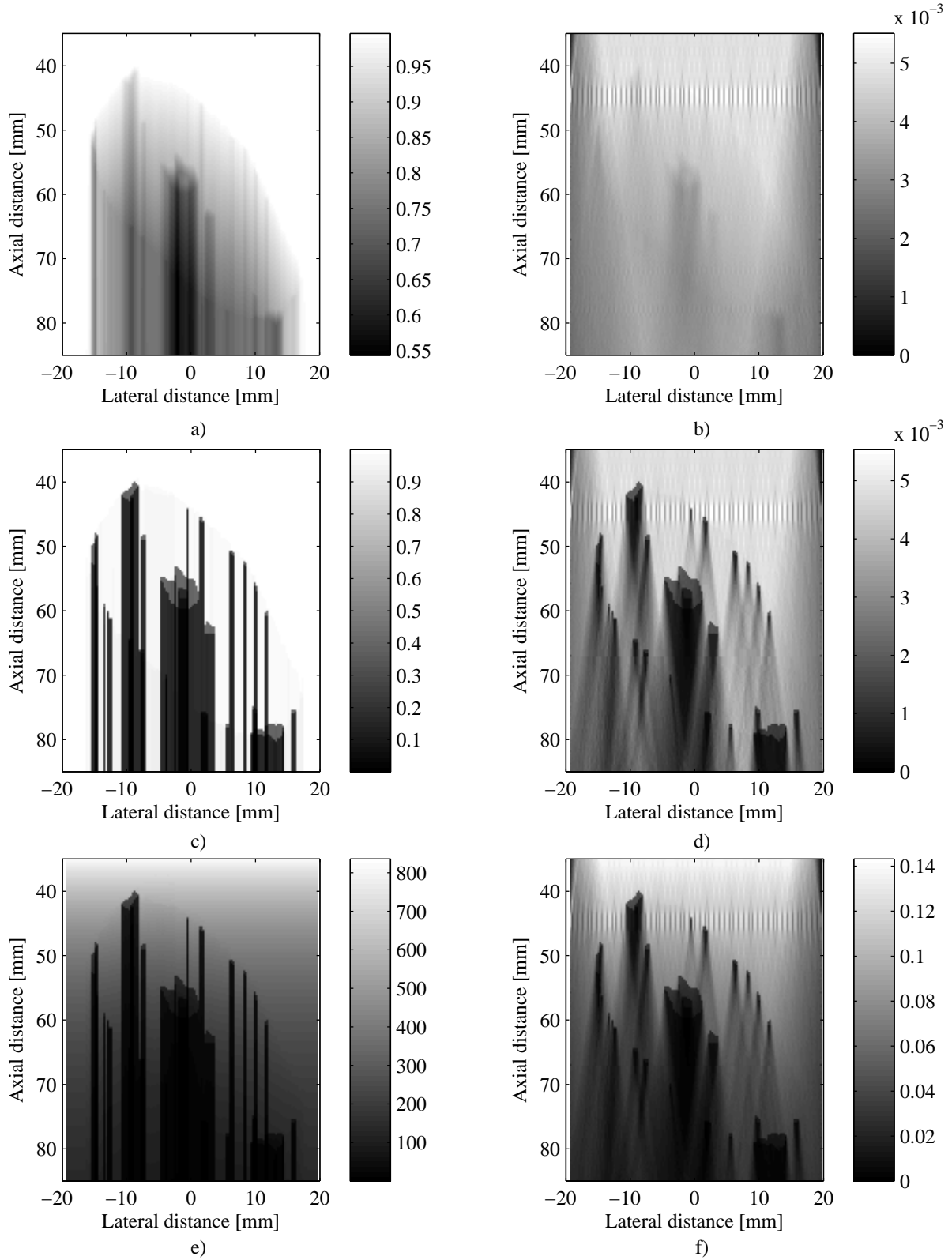


Figure 3.6: The ATT map of the slice for the ray-tracing model (a). The ATT map for the focused beam tracing model (b). The TRC map of the slice for the ray-tracing model (c). The TRC map for the focused beam tracing model (d). The SSM(P)/BST(P) map of the slice for the ray-tracing model (e). The ASSM(P)/BST(P) map of the slice for the focused beam tracing model (f). Those are the replicas of Fig. 11, 17, 14, 18, 15, 19 in [41], respectively.

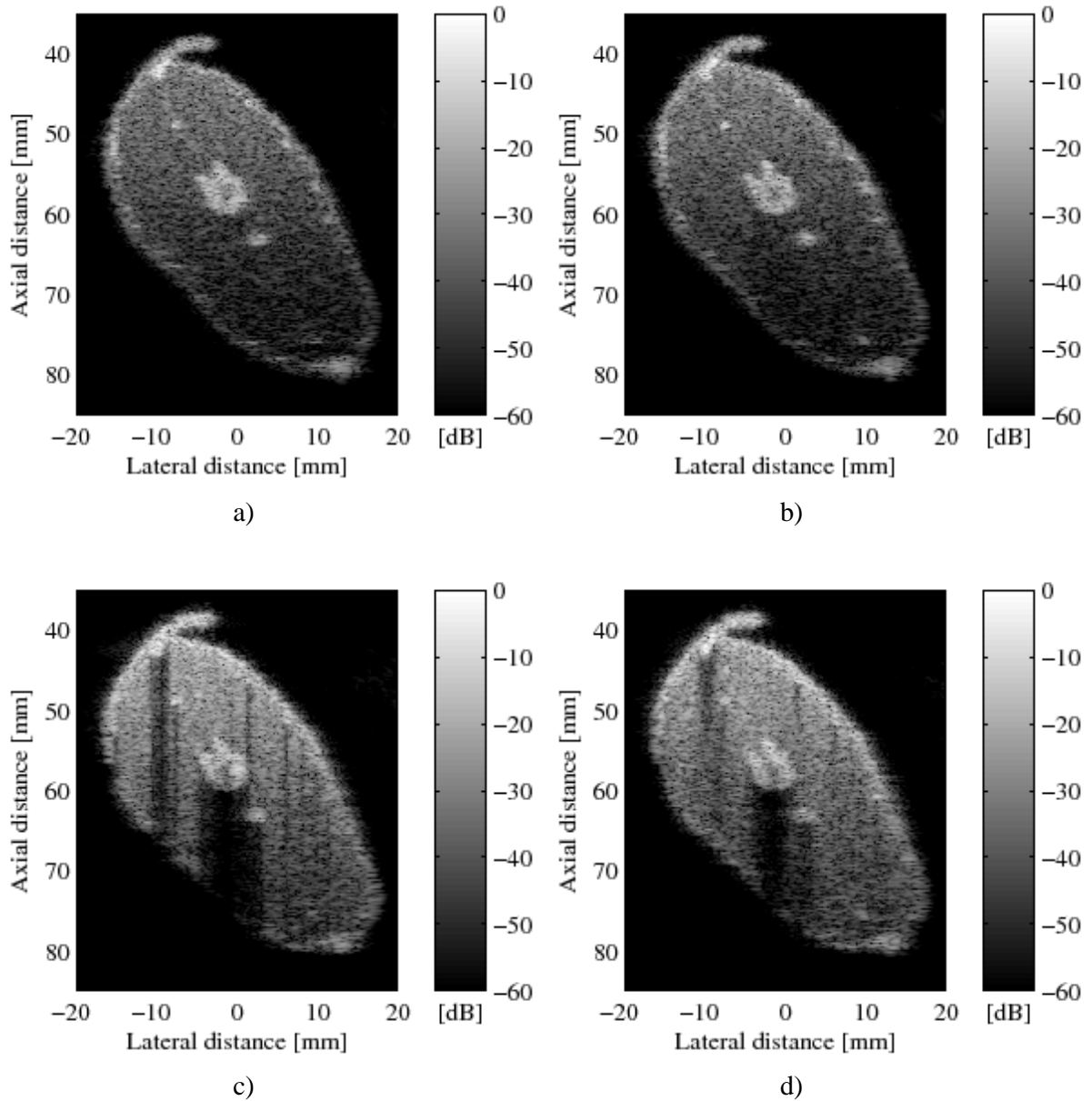


Figure 3.7: The simulated ultrasound image only from backscatter coefficients (a). The simulated ultrasound image using the ray-tracing model without TRC (b). The simulated ultrasound image with shadow effects using the ray-tracing model (c). The simulated ultrasound image with shadow effects using the focused beam tracing model (d). Those are the replicas in lower resolution of Fig. 12, 13, 16, 20 in [41], respectively.

3.2.3 Discussion

When shadowing is introduced, the simulated ultrasound images appear more realistic, especially with the focused beam tracing model. The real ultrasound beam in the measurements is not focused at a single point but concentrated in a small region, whereas the focus point is modeled as a very small point in the focused beam tracing method used in the simulation. This is the reason why there are artifacts in the maps at axial distance about 45 mm in Fig. 3.6b, d, and f, but not in the simulated ultrasound image in Fig. 3.7d. The sharpness of the shad-

ows in the measured ultrasound image is somewhere between what the ray-tracing model and the focused beam tracing model produce, which means that the focused beam tracing method needs further development. As shown by the ATT map the absorption inside the fish alone only reduces the energy by about 50%, which is not enough to introduce the shadow effects shown in the simulated ultrasound images. But the transmission losses caused by reflections at media borders seem to explain the shadow effects as shown by the TRC map.

Segmentation of the CT images was partly a user-dependent process. Different thresholding values influence especially the size and shape of skin and bone regions. It is difficult to distinguish between the fat and skin regions in the CT images when they are next to each other, because the x-ray absorption of skin and fat regions is very similar, making segmentation difficult. Segmentation was therefore made manually, which also gives an uncertainty with regard to the sound transmission through the skin. However, there is no well-established method available in the literature to validate it.

The FWHM_{azi} of the simulated point spread function of the BK transducer, calculated by Field II, is assumed to be the effective slice thickness of the ultrasound imaging modality. It varies as a function of depth. It is narrowest, about 0.6 mm, at the elevation focus at about 20 mm depth and about 8 mm at 80 mm depth, while the effective slice thickness of the CT imaging modality is a constant, about 0.5 mm. Hence, the simulation is more accurate at the elevation focus than at other depths. This also needs to be considered in future simulations.

The method is applied for a linear array transducer, but can be used for convex array and phase array transducers as well, because they also produce focused ultrasound beam in each emission. A similar mapping method could be used if the data are magnetic resonance images instead of CT images.

In conclusion, a new method with the focused beam tracing model was developed to simulate ultrasound images from CT images. The method uses the two-way transmission coefficients to capture the shadow effects. With this method the simulated ultrasound images display most of the characteristics of measured ultrasound images such as shadowing, attenuation, and edge-enhancement.

Fish species discrimination using range profiles in the MHz frequency range

This chapter contains a summary of the article [\[63\]](#)

- **An Hoai Pham**, Bo Lundgren, Bjarne Stage, and Jørgen Arendt Jensen, "Fish species discrimination using range profiles in the MHz frequency range", submitted to *IEEE Journal of Oceanic Engineering* in September 2012.

which is found in full length in Appendix [A.2](#). The additional data from this study are presented in Appendix [C.5](#).

4.1 Objective of Study

This case study was performed to investigate the possibility to do fish species discrimination by the range profile approach using a single-element transducer system in *ex-situ* experiments. The objective of this work is to develop a cost-effective, reliable, high-frequency, and wide-band ultrasound system with a single-element transducer as a continuation of the work from Lundgren and Nielsen [\[21, 22\]](#). The system should be portable so that it can be used directly for *in-situ* experiments.

4.2 Summary of Papers

The motivation for this case study is to try to measure range profiles as a possibility to identify fish. Therefore a system that consists of underwater cameras, a single-element transducer, and a dual-frequency multi-beam sonar to obtain range profiles of free-swimming fish, as well as video data and sonar data of the fish was built. The key device of the desired system is the single-element transducer to simplify the data acquisition as well as signal processing. Underwater cameras produce ground truth data, to know what is going on in a short range in front of the transducer, and to estimate the orientations, and positions of passing fish. The commercial dual-frequency multi-beam sonar is also used as a reliable device to record overview ultrasound data of the fish in front of the system. The workflow of the study is: choosing the transducer beam width and frequency range, selecting components like transceiver and data storage devices for the data acquisition setup based on the requirements of measurement range and frequency, designing a fixture and choosing the positions for the devices, calibrating the

system, and acquiring data from free-swimming fish. The paper [63] describes the details of the work. Short versions of materials and results sections of the paper are presented below.

4.2.1 Materials

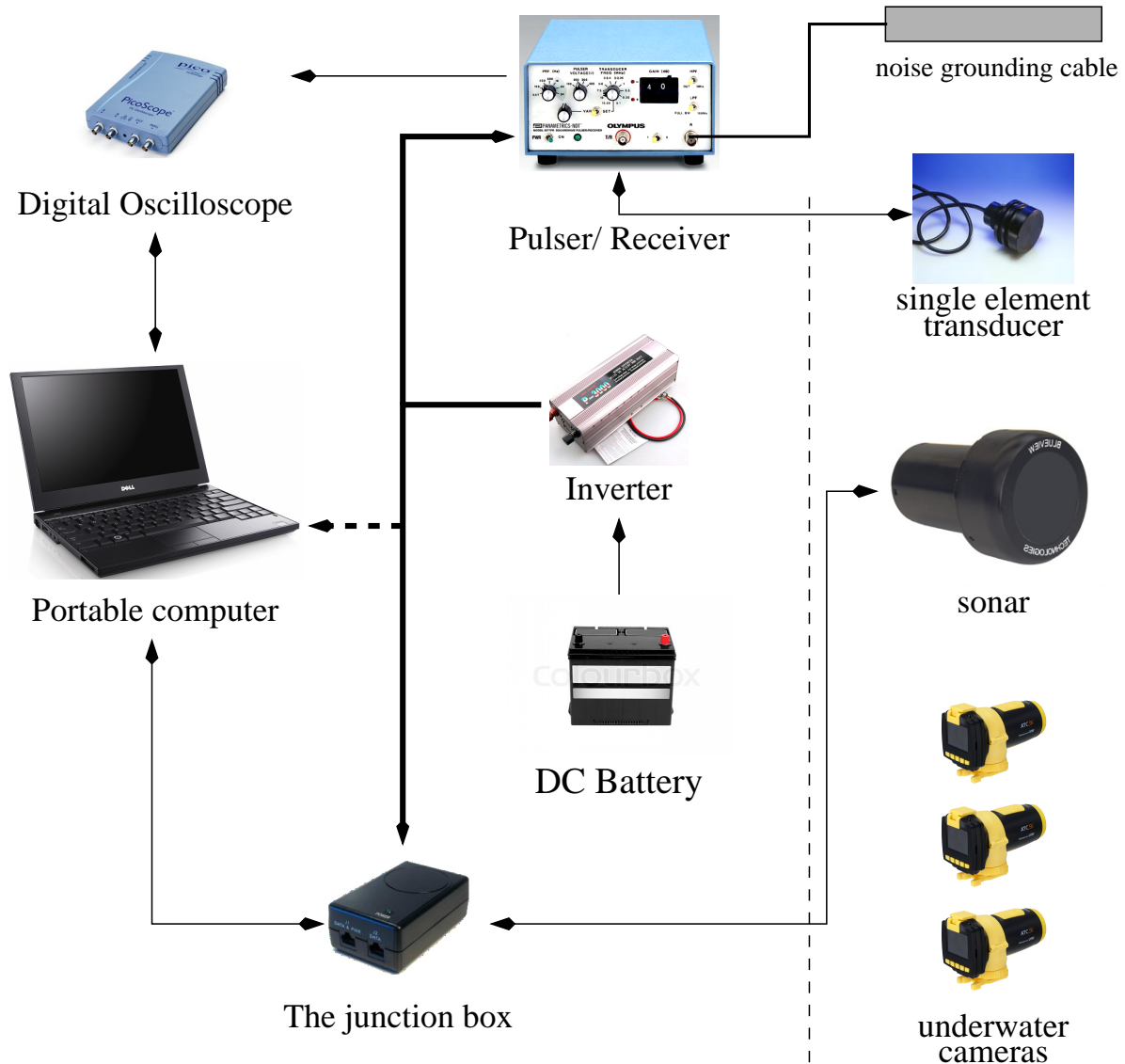


Figure 4.1: Block diagram of the system. The front-end of the system is on the left-hand side of the dotted line. This is a replica of Fig. 2 in [63].

The system was designed to be portable and can be used for *ex-situ* as well as *in-situ* experiments. The block diagram of the system is presented in Fig. 4.1. The front-end of the system consists of a Reson TC3210 1 MHz single-element transducer with a bandwidth of 300kHz, diameter of 2.54 cm, beam divergence angle of 4.5° , a Blueview P900-2250 dual-frequency multi-beam sonar, where only 900 kHz was used, and three Oregon ATC9K underwater cameras, where a resolution of 1280×720 pixels was used, all mounted on a fixture. The acoustic devices are connected by cables to the back-end, but the cameras operate independently. There are a battery and a secure digital (SD) card in each camera. The back-end consists of a Dell Latitude E4300 portable computer (PC), a Picoscope 4226 digital oscilloscope, where a sam-

pling frequency of 7.813 MHz was used, an Olympus pulser-receiver 5077PR, where a pulse repetition frequency of 100 Hz was used, a Provier junction box that delivers power over Ethernet (POE) to the sonar, a 12V battery, and a power inverter (12 VDC to 220 VAC) that supplies the pulser-receiver and the junction box. The pulser-receiver is used to ping (send the transmit pulse to the transducer), receive and amplify echo signals from the Reson transducer. The received signals are digitized and transferred to the PC using the Picoscope. The Olympus pulser-receiver is grounded to the water with a thick copper cable to reduce the ground loop noise in the received signals from the Reson transducer. The junction box transfers the control signals from the PC to the sonar as well as the sonar data back to the PC. The PC runs on its own battery but the dotted line from the inverter to the PC indicates that power can be provided to the PC if necessary.

The configuration of the front-end of the system is presented in Fig. 4.2. Fish positions are defined in a coordinate system with an x -axis parallel to the line between cameras C2 and C3, and with xz -plane parallel to the plane of the figure. The center of the aperture of the single-element transducer is used as the origin of the coordinate system. Positive z is away from the transducer and positive y is downwards. The multi-beam sonar is placed below the single-element transducer with its beam plane parallel to the xz -plane. The single-element transducer is directed so that the center line forms an angle $\alpha = 8.5^\circ$ with the center line of the multi-beam sonar, because the center part of the sonar image is not well-defined. An advantage is also that interfering signals from the sonar are reduced. The optical axis of camera C1 is directed as close as possible parallel to the transducer beam. The distances $C1C2 = 64.5$ cm, $C1C3 = 43.2$ cm, and $C2C3 = 99$ cm are measured between the centers of the camera lenses.

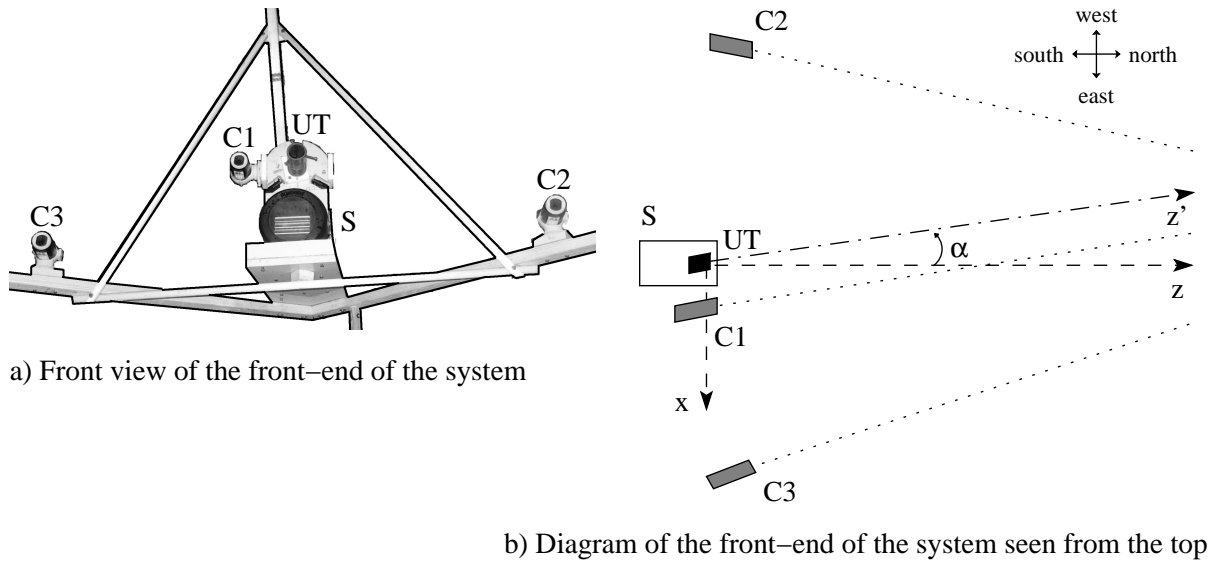


Figure 4.2: Setup of the front-end of the system. C1, C2, and C3 are three identical cameras. UT is the single-element transducer. S is the Blueview multi-beam sonar. The angle between the center line of the UT beam and the center line of the center beam of S is α . This is a replica of Fig. 3 in [63].

4.2.2 Results

The *ex-situ* experiments were performed in one of the large fish storage aquaria at the North Sea Oceanarium in Hirtshals, Denmark. A total of five hours of data have been recorded in the *ex-*

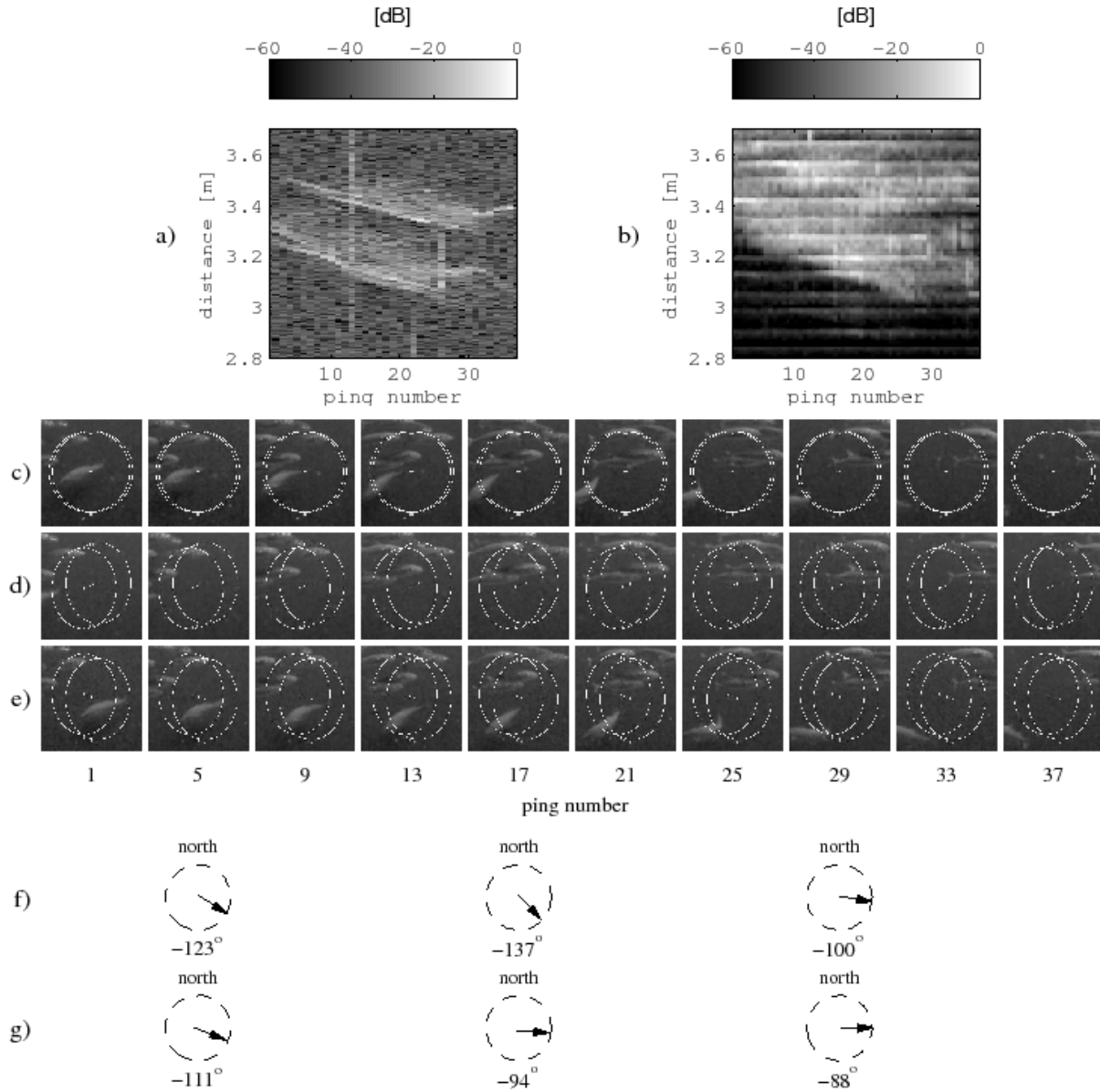


Figure 4.3: A measurement on two mackerels in a school. Range profiles of the mackerels (a), range profiles which are generated from sonar images (b), images from the center camera C1 (c), from the left-hand side camera C2 (d), and from the right-hand side camera C3 (e). Orientation of the mackerel positioned at about 3.2 m in range for ping numbers 5, 17, and 29 (f). Orientation of the mackerel positioned at about 3.5 m in range for ping numbers 5, 17, and 29 (g). This is a replica of Fig. 4 in [63].

situ experiments. Of these, three hours were processed and 131 measurements extracted comprising data from passes of 67 fish of five different species, both single fish and schools of fish. The fish species are cod, European sea bass (*Dicentrarchus labrax*), gilthead sea bream (*Sparus aurata*), Atlantic horse mackerel (*Trachurus trachurus*), and Atlantic mackerel (*Scomber scombrus*). The lengths of the fish are about 33 to 38 cm for the cods, 25 to 30 cm for the young sea basses, 50 cm for a mature sea bass, 34 to 39 cm for the sea breams, and 35 to 41 cm for the mackerel and horse mackerel. Of the 131 measurements, 82 were without sonar data and 49 with sonar data.

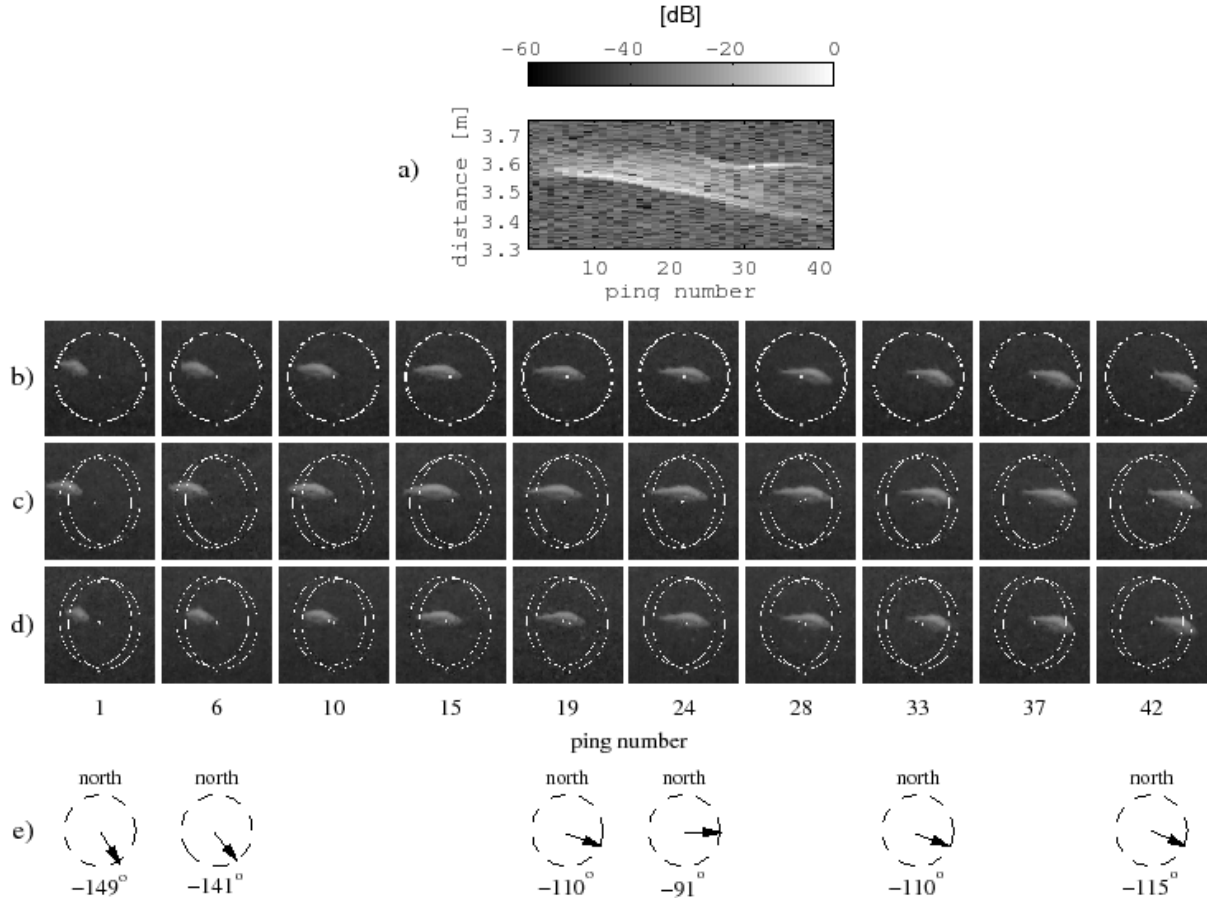


Figure 4.4: A cod turned and swam from left to right. Range profiles of the cod (a), images from the center camera C1 (b), from the left-hand side camera C2 (c), and from the right-hand side camera C3 (d). Orientation of the cod for ping numbers 1, 6, 19, 24, 33, and 42 (e). This is a replica of Fig. 5 in [63].

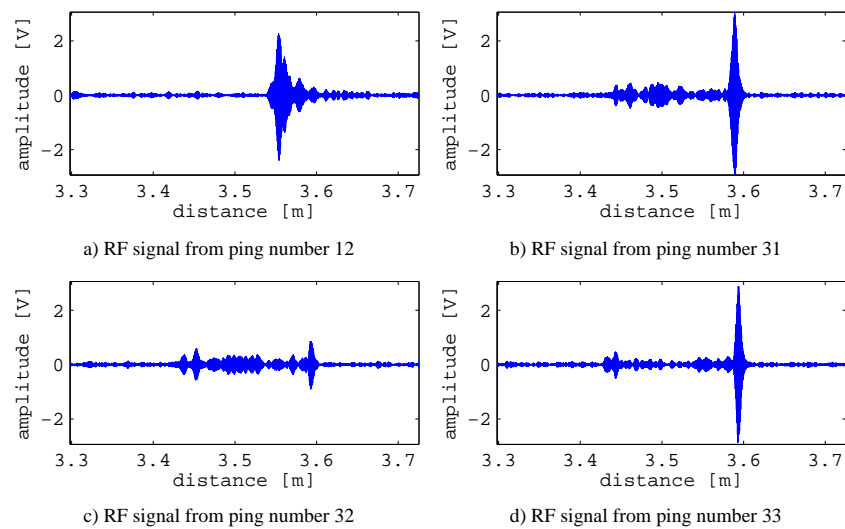


Figure 4.5: RF data of some specific pings in the measurement on a cod in Fig. 4.4a. This is a replica of Fig. 6 in [63].

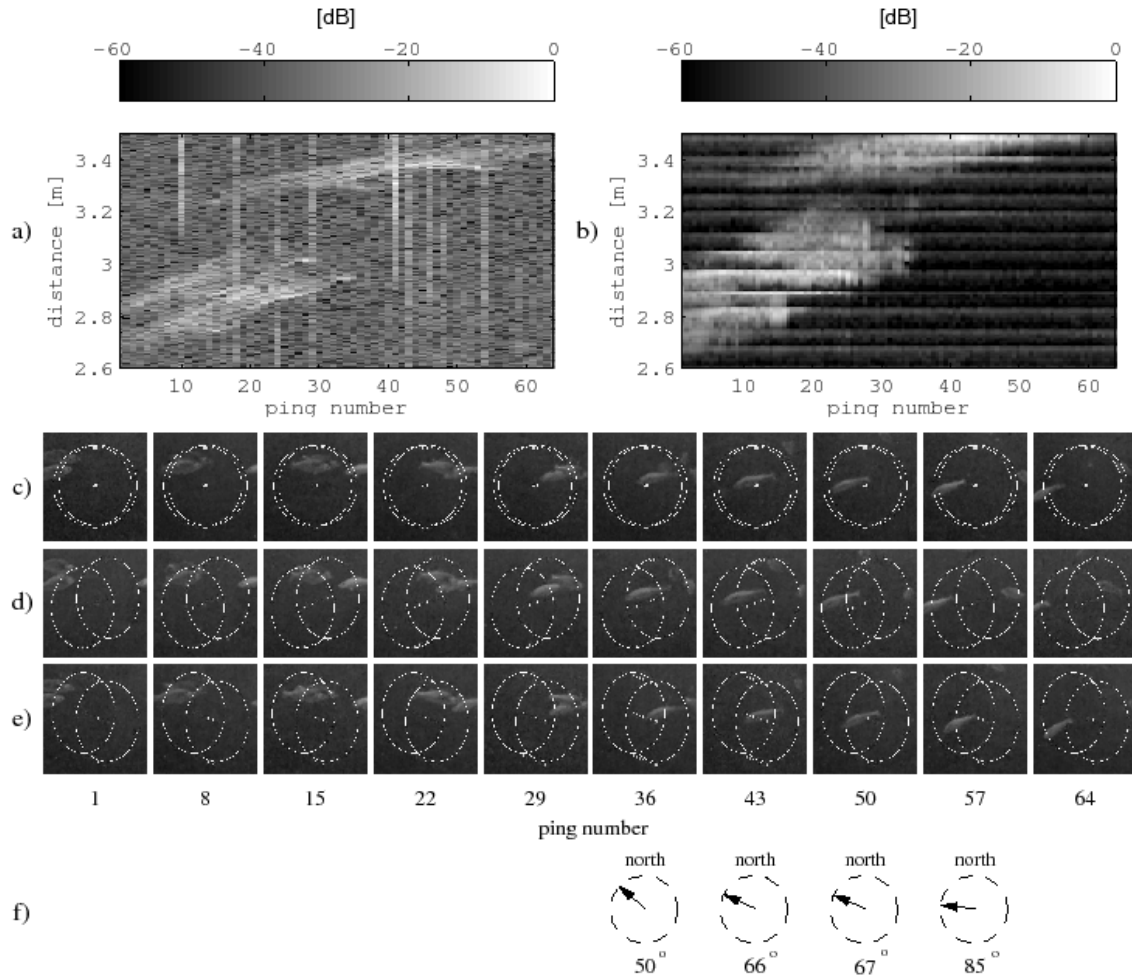


Figure 4.6: Two young sea basses swam from left to right, and then a cod swam from right to left. Range profiles of the sea basses and the cod (a), range profiles which are generated from sonar images (b), images from the center camera C1 (c), from the left-hand side camera C2 (d), and from the right-hand side camera C3 (e). Orientation of the cod for ping number 36, 43, 50, and 57 (f). This is a replica of Fig. 7 in [63].

To simplify descriptions below, north means that the fish swims away from the transducer and south that the fish swims towards the transducer. Similarly east means that the fish swims from the left-hand side to the right-hand side of the transducer beam; west means the opposite direction.

The results show range profiles and supporting data for various behavior of the fish. There are for example, data from two mackerels in a school which passed in front of the transducer in the southeast direction (Fig. 4.3). There is a cod which headed to the transducer from the left, turned towards the east, and then swam in the southeast direction (Fig. 4.4 and 4.5). There are data from two young sea basses and a cod (Fig. 4.6). The sea basses swam in the northeast direction. They met a cod that swam in the northwest direction. There is a school of 4 sea breams which passed in front of the transducer in the southeast direction (Fig. 4.7). In another case, they turned while they were passing the transducer beam, and then swam out in an opposite direction (Fig. 4.8). There are data of a school of mackerel and horse mackerel with a horse mackerel that swam in the southwest direction, turned, and then swam in the southeast direction (Fig. 4.9). There are also data of a school of mackerel and horse mackerel with many

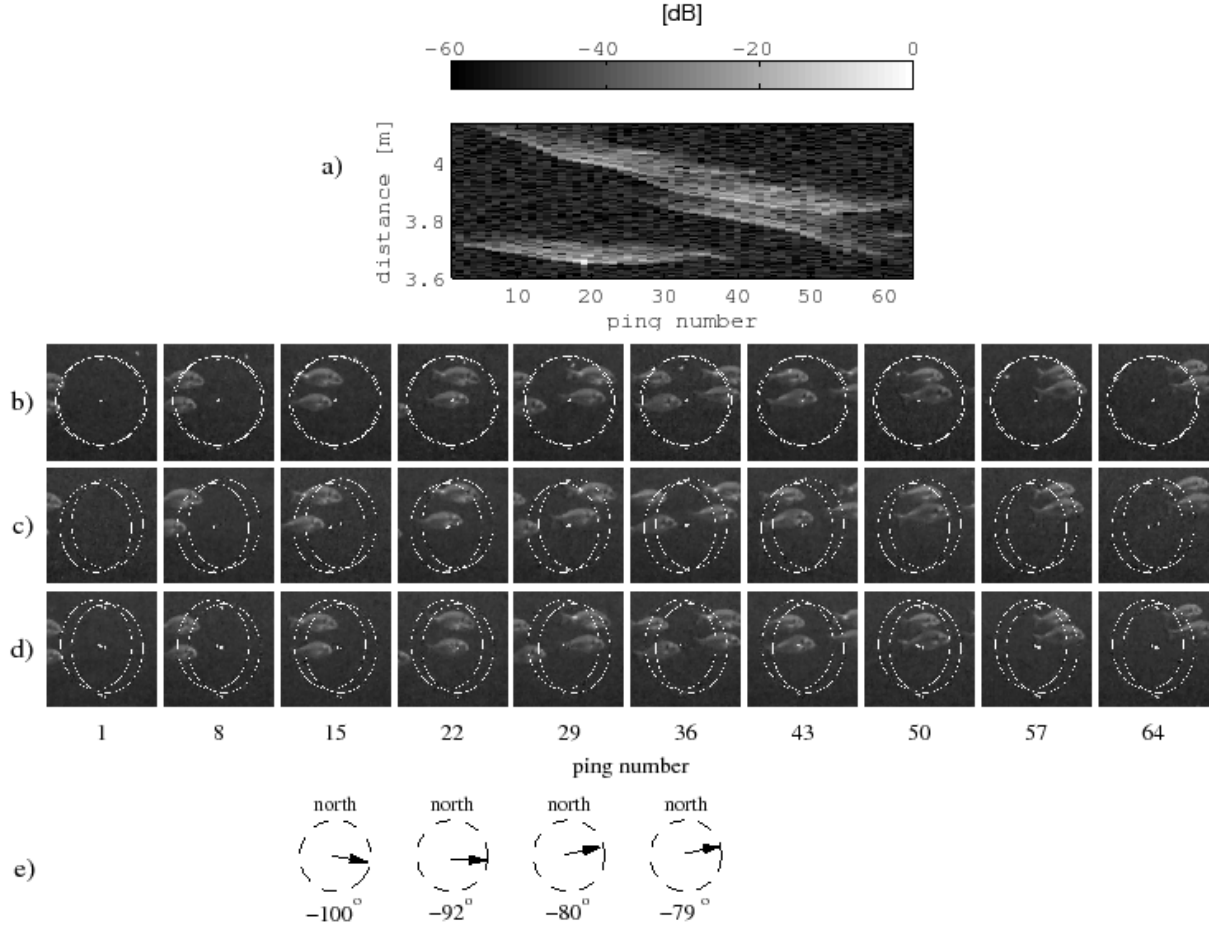


Figure 4.7: Four sea breams swam from left to right. Range profiles of the sea breams (a), images from the center camera C1 (b), from the left-hand side camera C2 (c), and from the right-hand side camera C3 (d). Orientation of the sea bream positioned at about 3.7 m in range for ping numbers 15, 22, 29, and 36 (e). This is a replica of Fig. 8 in [63].

complicated movement patterns (Fig. 4.10). Some other examples are presented in Appendix C.5. More details of the results are presented in the paper [63].

4.2.3 Discussion

In the 10 to 200 kHz frequency range the swimbladder is often considered the most important part of a fish for acoustic fish detection, because reflections from this part are often higher than from other parts. It is more difficult to detect fish of a species without swimbladder because the reflections are significantly weaker [64–66]. The work presented here indicates that in the low MHz frequency range surfaces areas of the fish are more important reflectors than the swimbladder, at least from the lateral side of the fish. An example is the measurement on mackerels. Although mackerel have no swimbladder the echoes from them are as strong as those from the other fish species.

When the fish moves, changes in the shape of the surface of the fish, changes in direction that the fish is heading, and the tail flicking generate variations in the range profiles. A simple case to interpret the variations is presented in Fig. 4.4. The echoes from the tail of the cod are as strong as or stronger than those from the other parts of the body. Fig. 4.5a shows that the energy

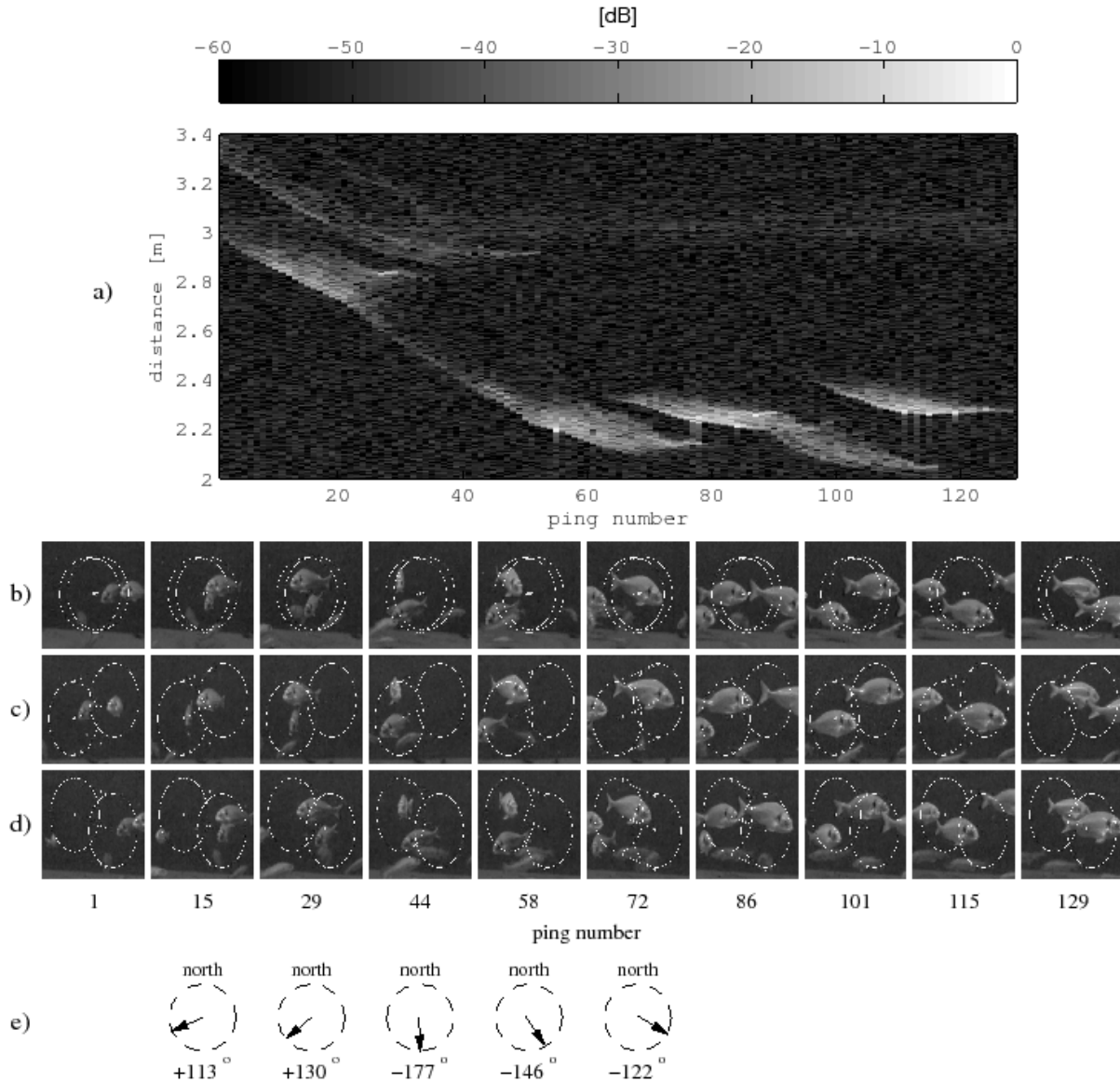


Figure 4.8: Four sea breams that swam from right to left, turned, and then swam left to right. Range profiles of the sea breams (a), images from the center camera C1 (b), from the left-hand side camera C2 (c), and from the right-hand side camera C3 (d). Orientation of the sea bream turned and positioned at about 2.7 m to 2.2 m for ping numbers 15, 29, 44, 58, and 72 (e). This is a replica of Fig. 9 in [63].

reflected from the body of the cod, including the swimbladder but not the tail, is high, because the body was more or less perpendicular to the transducer beam. The tail of the cod was still at an angle with the transducer beam, because the cod was turning to head eastwards. When the cod had finished turning and headed straight east, the reflections from the tail (ping 30 to 38 at about 3.6m in range) were very high and variable, at ping numbers 31 (Fig. 4.5b) and 33 (Fig. 4.5d) up to 3 times stronger than from other parts of the fish. At those pings, the tail was probably very close to perpendicular to the direction of the centerline of the transducer. When the cod flicked its tail, the maximum amplitude of the echo signals decreased to about one thirds of the previous value (ping number 32 (Fig. 4.5c)).

If the fish is directed along the centerline of the beam, it is expected that the length of the echo

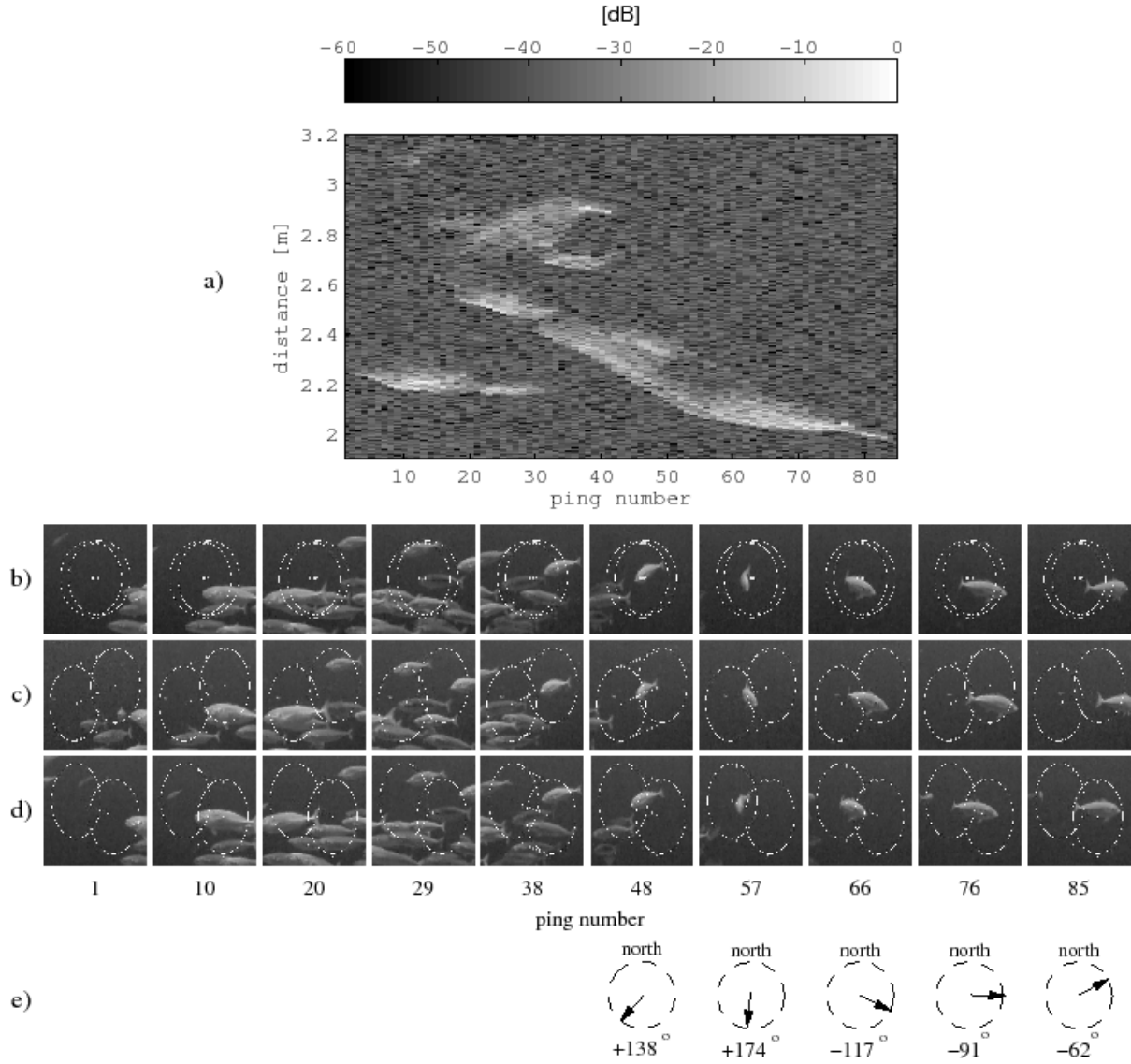


Figure 4.9: A school of mackerel and horse mackerel with a horse mackerel turning and swimming from left to right. Range profiles of the school of fish (a), images from the center camera C1 (b), from the left-hand side camera C2 (c), and from the right-hand side camera C3 (d). Orientation of the horse mackerel for ping numbers 48, 57, 66, 76, and 85 (e). This is a replica of Fig. 10 in [63].

would be approximately equal to the length of the fish. But the results from the measurements show that the length of the echo is not equal to the length of the fish. Because of the complex structure of the head part, only a small amount of sound energy is transmitted through to the other parts, and only a small part is scattered back into the direction of the transducer. When the fish direction becomes closer to being perpendicular to the transducer beam, the more ultrasound energy is backscattered, and the longer the echo signals become up to a maximum at a certain angle and then probably decrease again. The turning of the fish usually appears as a diffuse area in the range profile map as presented in Fig. 4.8a, and Fig. 4.9a. It is not possible to estimate the speed and orientation of the fish only from single-beam range profiles, but that could be done by using a split-beam transducer. In this work, the speed and orientation of the fish are estimated using the video data for a range up to 5 m.

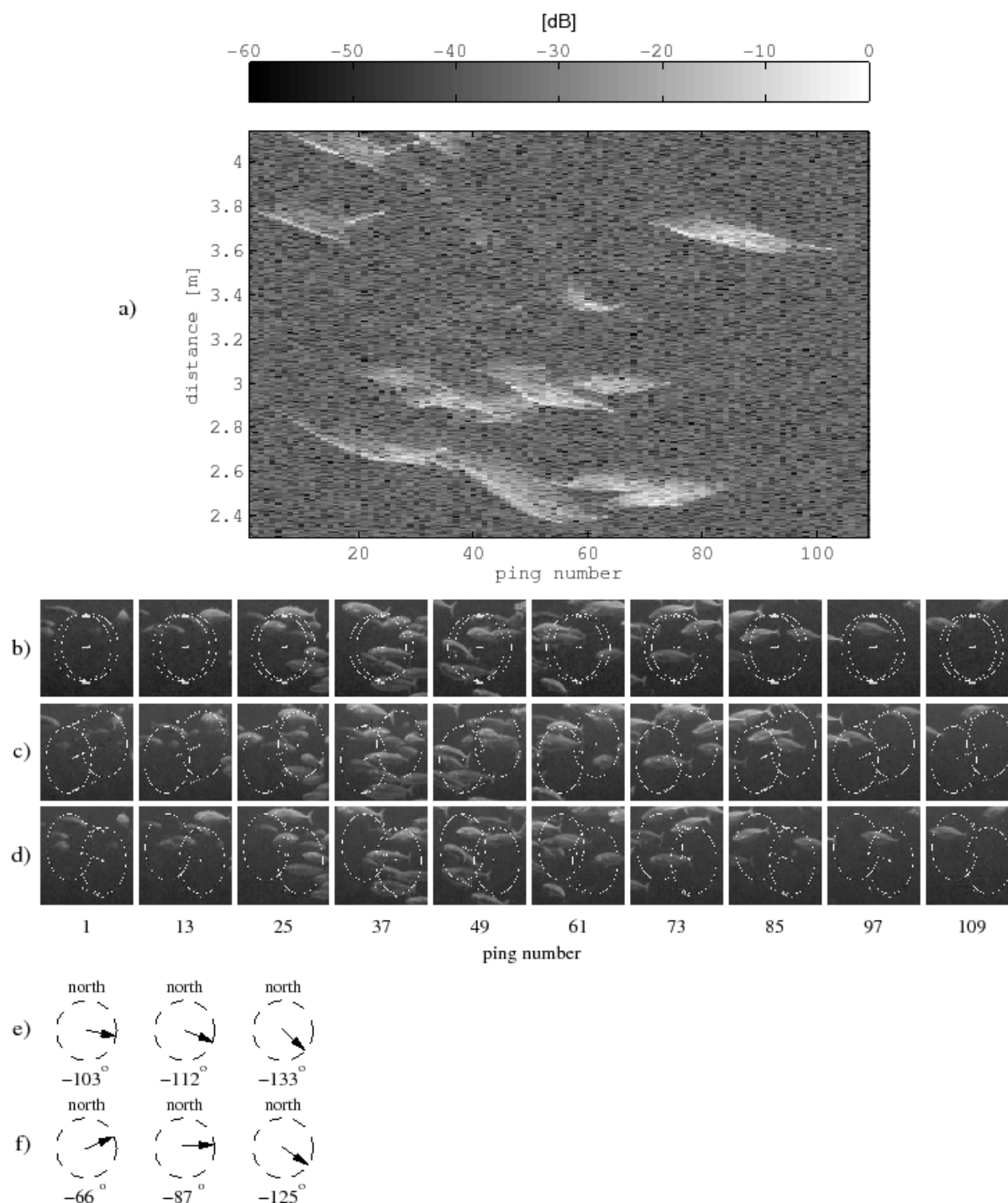


Figure 4.10: A school of mackerel and horse mackerel with many complicated movement patterns. Range profiles of the school of fish (a), images from the center camera C1 (b), from the left-hand side camera C2 (c), and from the right-hand side camera C3 (d). Orientation of the mackerel positioned at about 3.8 m in range for ping numbers 1, 13, and 25 (e). Orientation of the mackerel positioned at about 4 m in range for ping numbers 1, 13, and 25 (f). This is a replica of Fig. 11 in [63].

The results show that there are some features in the range profile maps that make it possible to discriminate between some fish species, if they pass by in front of the acoustic transducer in the same direction. For example, there is a clear difference between mackerel and sea bream headed in the southeast direction without turning in the beam as shown for mackerels in Fig. 4.3a, and in Fig. 4.10a ping numbers 1 to 34 at the range of 3.8 m and 4 m, and for sea breams in Fig. 4.7a.

In Fig. 4.7a ping number 19, and Fig. 4.8a ping number 56, 77-90, 110-120, the amplitudes of the echo signals are so high that saturation occurs, and they appear as bright spots in the range profile maps. In the experiments, this phenomenon did not appear for species other than sea breams. The saturation occurs even when the sea breams are at a relatively large distance of 3.6 m as presented in Fig. 4.7a. This probably happens because the body of the sea bream is flatter (high ratio between the height and the width of the body).

The experiments indicate that the range profiles for a particular species are typical for that species and in some cases sufficiently different from those of other species to make identification possible. Three main parts of the fish that cause the range profiles to be different from species to species are the head, the body, and the tail. The range profiles of the fish heading in different directions are different. For instance, in Fig. 4.4a at ping numbers 31 to 40, the tail of the cod heading southeast can be seen at the range of 3.6 m, which is at a greater distance than the other parts of the fish, while in Fig. 4.6a at ping numbers 41 to 55, the tail of a cod heading northwest can be seen at the range of 3.4 m, which is at a smaller distance than the other parts. The smoothly curved feature in Fig. 4.4a at ping numbers 1 to 40 in the range of 3.55 m to 3.4 m and a similar feature in Fig. 4.6a at ping numbers 18 to 55 in the range of 3.3 m to 3.45 m probably correspond to the heads of the cods.

The range profiles presented in Fig. 4.3b and Fig. 4.6b appear similar to those in Fig. 4.3a and Fig. 4.6a, but are more blurry probably because the range resolution of the sonar is less fine than that of the Reson transducer. The bright stripes occur in Fig. 4.3a and Fig. 4.6a because some of the reverberations originating from the sonar are received by the Reson transducer.

Conclusions

There are three case studies. Empirical ultrasound backscatter in the MHz frequency range from fish was investigated and presented in chapter 2. The results show that the part of fish that contributes most to the ultrasound backscatter in the MHz frequency range is not necessarily the swimbladder. They indicate that bone structures and skin surfaces are more important. The procedure of measurements developed in this study can be used to produce empirical ultrasound range profiles along the fish from many directions around the length axis of the fish.

Chapter 3 presented a novel method to generate simulated ultrasound images. The method takes into account some of the most pronounced characteristics of measured ultrasound images such as shadowing, and influence of attenuation. Those characteristics appeared in the results of the study in chapter 2. The simulation process can be used to produce simulated ultrasound range profiles as a complement to the empirical data presented in chapter 2.

A 1 MHz single-element transducer system was developed and presented in Chapter 4. It is useful for an initial *ex-situ* study of range profiles from free-swimming fish. Measurements were performed on fish that have swimbladder (cod, sea bass, gilthead sea bream, and horse mackerel) as well as on fish that do not have swimbladder (mackerel). There are indications that the variations in the range profiles seem to have some unique details to discriminate between species like mackerel and sea bream. In some cases the range profiles also indicate whether the head or the tail is closest to the transducer. It also has been shown that the surface areas of the fish are the most important elements that decide how much energy is backscattered in the low MHz frequency range. This conclusion is similar to one of the conclusions in the study in chapter 2. The disappearance of reflections from parts of a fish as shown by the range profiles, when the fish turned and headed towards the transducer as described in chapter 4 may be explained as the result of shadow effects similar to those mentioned in chapter 2 and 3.

The goal of this Ph.D. study has been to develop a method to investigate the possibility of *in-situ* identification of fish using high-frequency, wideband ultrasound. The results show that discrimination between fish species can be done in the *in-vitro* experiments presented in chapter 2. The results from the *ex-situ* experiments presented in chapter 4 indicate that the variation with time of the fish range profiles in the low MHz frequency range has recognizable features that are sufficiently distinct to identify them as fish echoes and to discriminate between species like mackerel and sea bream. The results from the *ex-situ* experiments in the aquarium tank presented in chapter 4 can be considered comparable to data obtained in *in-situ* experiments in a calm sea. There were even small waves and bubbles in the aquarium tank caused by the aquarium water pumps. The system used for the *ex-situ* experiments can therefore be considered ready for preliminary *in-situ* experiments. It can be concluded that the objectives of the Ph.D. study have been reached.

5.1 Future developments

To get closer to the goal of identifying fish directly by acoustic means, future experiments should be done with at least a split-beam transducer instead of a single-beam transducer. This would allow the possibility to determine, not only the speed of the fish along the beam, but also across the beam. It would probably also allow the use of more advanced processing of the acoustic signals to improve the angular resolution of the range profiles.

In this Ph.D. study the experience is that it is time consuming and a low possibility for fish passing through the transducer beam. It is therefore advisable to make more complete investigation of the backscatter from fish and develop a method that can be used for controlled environments before trying in *in-situ* fish identification experiments.

There are two types of experiments that are worth to investigate in the future. The first experiment type is experiments with immobilized fish that can be rotated using tethers. Empirical range profiles of the fish from many different directions can then be obtained using a 1 MHz split-beam transducer system similar to the system described in chapter 4. CT scan can be performed on the fish immediately after the ultrasound measurements to get the inputs for simulations as described in chapter 3. Very high resolution CT scan techniques are being developed at the moment. The parameters and the procedures of the simulations should be adjusted to take into account the 1 MHz split-beam transducer system. All of these measurements should be used to build libraries of range profiles at 1 MHz from fish. However the range profiles representing a tail flicking effect (see paper [63] in Appendix A.2) cannot be obtained from this type of experiment because the fish is immobilized.

Another possibility is experiments in which fish swim in a long closed transparent swim tunnel immersed in an aquarium tank. The tunnel should have one straight relatively narrow section where the fish orientation does not vary too much. The direction of the straight part can be changed to adjust the orientation of the swimming fish. The reflection signals from the tube can be reduced in the received signals using echo-canceling technique like those used in blood flow measurements in medical ultrasound imaging. In that way range profiles of the free-swimming fish can be obtained that include the tail flicking effect.

Energy distribution curves obtained by summing total energy of individual range profiles of a range profile maps could possibly be used to develop a method for fish identification. If the energy distributions can be used for the identification, it could supplement the use of libraries of range profiles.

Bibliography

- [1] J. E. Simmonds and D. MacLennan, *Fisheries Acoustics: Theory and Practice*, chapter 7.5.3, 3.5, and 3.7.2 (Blackwell, Oxford, UK) (2005).
- [2] M. V. Trevorrow and Y. Tanaka, “Acoustic and in situ measurements of freshwater amphipods (*jesogammarus annandalei*) in lake biwa, japan”, *Limnology and Oceanography* **42**(1), 121–132 (1997).
- [3] E. Belcher, W. Hanot, and J. Burch, “Dual-frequency identification sonar (DIDSON)”, in *Proceedings of the 2002 International Symposium on Underwater technology*, 187–192 (2002).
- [4] K. J. Benoit-Bird, W. W. L. Au, C. D. Kelly, and C. Taylor, “Acoustic backscattering by deepwater fish measured in situ from a manned submersible”, *Deep-Sea Research Part I-Oceanographic research papers* **50**(2), 221–229 (2003).
- [5] P. G. Fernandes, P. Stevenson, A. S. Brierley, F. Armstrong, and E. J. Simmonds, “Autonomous underwater vehicles: future platforms for fisheries acoustics”, *ICES Journal of Marine Science* **60**, 684–691 (2003).
- [6] R. A. Moursund, T. J. Carlson, and R. D. Peters, “A fisheries application of a dual-frequency identification sonar acoustic camera”, *ICES Journal of Marine Science* **60**, 678–683 (2003).
- [7] J. A. Holmes, G. M. W. Cronkite, H. J. Enzenhofer, and T. J. Mulligan, “Accuracy and precision of fish-count data from a dual -frequency identification sonar (DIDSON) imaging system”, *ICES Journal of Marine Science* **63**, 543–555 (2006).
- [8] R. P. Mueller, R. S. Brown, H. Hop, and L. Moulton, “Video and acoustic camera techniques for studying fish under ice: a review and comparison”, *Rev. Fish Biol. Fisheries* **16**, 213–226 (2006).
- [9] S. L. Maxwell and N. E. Gove, “Assessing a dual-frequency identification sonars’ fish-counting accuracy, precision, and turbid river range capability”, *J. Acoust. Soc. Am.* **122**(6), 3364–3377 (2007).
- [10] J. Han, N. Honda, A. Asada, and K. Shibata, “Automated acoustic method for counting and sizing farmed fish during transfer using DIDSON”, *Fish Sci.* **75**, 1359–1367 (2009).

- [11] T. K. Stanton, D. Chu, J. M. Jech, and J. D. Irish, “New broadband methods for resonance classification and high-resolution imagery of fish with swimbladders using a modified commercial broadband echosounder”, *ICES Journal of Marine Science* **67**, 365–378 (2010).
- [12] K. Huang and C. S. Clay, “Backscattering cross sections of live fish: Pdf and aspect”, *J. Acoust. Soc. Am.* **67(3)**, 795–802 (1980).
- [13] Y. Sun, R. Nash, and C. S. Clay, “Acoustic measurements of the anatomy of fish at 220 kHz”, *J. Acoust. Soc. Am.* **78(5)**, 1772–1776 (1985).
- [14] W. W. L. Au and K. J. Benoit-Bird, “Acoustic backscattering by hawaiian lutjanid snappers. II. Broadband temporal and spectral structure”, *J. Acoust. Soc. Am.* **114(5)**, 2767–2774 (2003).
- [15] D. B. Reeder, J. M. Jech, and T. K. Stanton, “Broadband acoustic backscatter and high-resolution morphology of fish: Measurement and modeling”, *J. Acoust. Soc. Am.* **116(2)**, 747–761 (2004).
- [16] W. W. L. Au, B. K. Branstetter, K. J. Benoit-Bird, and R. A. Kastelein, “Acoustic basis for fish prey discrimination by echolocating dolphins and porpoises”, *J. Acoust. Soc. Am.* **126(1)**, 460–467 (2009).
- [17] W. W. L. Au, J. K. Horne, and C. Jones, “Basis of acoustic discrimination of chinook salmon from other salmons by echolocating orcinus orca”, *J. Acoust. Soc. Am.* **128(4)**, 2225–2232 (2010).
- [18] J. S. Jaffe and P. L. D. Roberts, “Estimating fish orientation from broadband, limited-angle, multiview, acoustic reflections”, *J. Acoust. Soc. Am.* **129(2)**, 670–680 (2011).
- [19] P. L. D. Roberts, J. S. Jaffe, and M. M. Trivedi, “Multiview, broadband acoustic classification of marine fish: A machine learning framework and comparative analysis”, *IEEE Journal of Oceanic Engineering* **36**, 90–104 (2011).
- [20] O. Sand and A. D. Hawkins, “Acoustic properties of the cod swimbladder”, *Journal of experiment biology* **58(3)**, 797–820 (1972).
- [21] B. Lundgren and J. R. Nielsen, “Hydroacoustic ex situ target strength measurements on juvenile cod (*Gadus morhua* L.)”, *ICES Journal of Marine Science* **56**, 627–639 (1999).
- [22] B. Lundgren and R. N. Nielsen, “A method for the possible species discrimination of juvenile gadoids by broad-bandwidth backscattering spectra vs. angle of incidence”, *ICES Journal of Marine Science* **65(4)**, 581–593 (2008).
- [23] E. J. Simmonds, F. Armstrong, and P. J. Copland, “Species identification using wideband backscatter with neural network and discriminant analysis”, *ICES Journal of Marine Science* **53**, 189–195 (1996).
- [24] A. Bertrand, E. Josse, and J. Masse, “In situ acoustic target-strength measurement of bigeye (*thunnus obesus*) and yellowfin tuna (*thunnus albacares*) by coupling split-beam echosounder observations and sonic tracking”, *ICES Journal of Marine Science* **56**, 51–60 (1999).

- [25] R. Jorgensen and K. Olsen, "Acoustic target strength of capelin measured by single-target tracking in a controlled cage experiment", *ICES Journal of Marine Science* **59**, 1081–1085 (2002).
- [26] J. Lilja, T. J. Marjomaki, J. Jurvelius, T. Rossi, and E. Heikkola, "Simulation and experimental measurement of side-aspect target strength of atlantic salmon (*salmo salar*) at high frequency", *Can. J. Fish. Aquat. Sci.* **61**, 2227–2236 (2004).
- [27] K. Sawada, H. Takahashi, K. Abe, T. Ichii, K. Watanabe, and Y. Takao, "Target-strength, length, and tilt-angle measurements of pacific saury (*cololabis saira*) and japanese anchovy (*engraulis japonicus*) using an acoustic-optical system", *ICES Journal of Marine Science* **66**, 1212–1218 (2009).
- [28] R. J. Korneliussen, "The acoustic identification of atlantic mackerel", *ICES Journal of Marine Science* **67**, 1749–1758 (2010).
- [29] H.-J. Lu, M. Kang, H.-H. Huang, C.-C. Lai, and L.-J. Wu, "Ex situ and in situ measurements of juvenile yellowfin tuna *thunnus albacares* target strength", *Fish Sci.* **77**, 903–913 (2011).
- [30] F. Gerlotto, M. Soria, and P. Freon, "From two dimensions to three: the use of multibeam sonar for a new approach in fisheries acoustics", *Can. J. Fish. Aquat. Sci.* **56**, 6–12 (1999).
- [31] M. C. Langkau, H. Balk, M. B. Schmidt, and J. Borcharding, "Can acoustic shadows identify fish species? A novel application of imaging sonar data", *Fisheries Management and Ecology* 1–10 (2012).
- [32] S. P. Jacobs and J. A. O'Sullivan, "Automatic target recognition using sequences of high resolution radar range-profiles", *IEEE Transactions on Aerospace and Electronic Systems* **36**(2), 364–381 (2000).
- [33] J. K. Horne and C. S. Clay, "Sonar systems and aquatic organisms: matching equipment and model parameters", *Canadian Journal of Fisheries and Aquatic Sciences* **55**, 1296–1306 (1998).
- [34] W. W. L. Au and K. J. Benoit-Bird, "Broadband backscatter from individual hawaiian mesopelagic boundary community animals with implications for spinner dolphin foraging", *Journal of the Acoustical Society of America* **123**, 2884–2894 (2008).
- [35] R. Barr and R. F. Coombs, "Target phase: An extra dimension for fish and plankton target identification", *Journal of the Acoustical Society of America* **118**, 1358–1371 (2005).
- [36] N. Gorska, E. Ona, and R. Korneliussen, "Acoustic backscattering by atlantic mackerel as being representative of fish that lack a swimbladder. Backscattering by individual fish", *ICES Journal of Marine Science* **62**, 984–995 (2005).
- [37] N. Gorska, R. Korneliussen, and E. Ona, "Acoustic backscatter by schools of adult atlantic mackerel", *ICES Journal of Marine Science* **64**, 1145–1151 (2007).
- [38] J. M. Jech, D. M. Schael, and C. S. Clay, "Application of three sound scattering models to threadfin shad (*dorosoma petenense*)", *Journal of the Acoustical Society of America* **98**, 2262–2269 (1995).

- [39] M. C. Hemmsen, S. I. Nikolov, M. M. Pedersen, M. J. Pihl, M. S. Enevoldsen, J. M. Hansen, and J. A. Jensen, "Implementation of a versatile research data acquisition system using a commercially available medical ultrasound scanner", *IEEE Trans. Ultrason., Ferroelec., Freq. Contr.* **59**, 1487–1499 (2011).
- [40] A. H. Pham, B. Stage, M. C. Hemmsen, B. Lundgren, M. M. Pedersen, T. B. Pedersen, and J. A. Jensen, "Simulation of ultrasound backscatter images from fish", in *Proceedings of SPIE*, 7961, 796152(1–10) (2011).
- [41] A. H. Pham, B. Lundgren, B. Stage, M. M. Pedersen, M. C. Hemmsen, M. B. Nielsen, and J. A. Jensen, "Shadow effects in simulated ultrasound images derived from computed tomography images using a focused beam tracing model", *J. Acoust. Soc. Am.* **132**, 487–497 (2012).
- [42] A. H. Pham, B. Stage, B. Lundgren, M. C. Hemmsen, M. M. Pedersen, and J. A. Jensen, "Simulation of shadowing effects in ultrasound imaging from computed tomography images", in *Proceedings of IEEE International Ultrasonics Symposium*, 1411–1414 (2011).
- [43] J. Bamber and R. Dickinson, "Ultrasonic B-scanning - A computer-simulation", *Physics in Medicine and Biology* **25**, 463–479 (1980).
- [44] J. A. Jensen and P. Munk, "Computer phantoms for simulating ultrasound B-mode and CFM images", in *Acoustical Imaging*, edited by S. Lees and L. A. Ferrari, volume 23, 75–80 (1997).
- [45] J. A. Jensen and S. Nikolov, "Fast simulation of ultrasound images", in *Proc. IEEE Ultrason. Symp.*, volume 2, 1721–1724 (2000).
- [46] M. Song, R. Haralick, and F. Sheehan, "Ultrasound imaging simulation and echocardiographic image synthesis", in *Proceedings of the International Conference on Image Processing*, volume III, 420–423 (2000).
- [47] S. C. Groot, R. Hamers, F. H. Post, C. P. Botha, and N. Bruining, "IVUS simulation based on histopathology", *Computers in Cardiology*, 681–684 (2006).
- [48] W. Wein, A. Khamene, D. A. Clevert, O. Kutter, and N. Navab, "Simulation and fully automatic multimodal registration of medical ultrasound", in *Proceedings of the 10th international conference on Medical image computing and computer-assisted intervention*, 136–143 (2007).
- [49] J. L. Dillenseger, S. Laguitton, and E. Delabrousse, "Fast simulation of ultrasound images from a CT volume", *Comput. Biol. Med.* **39**, 180–186 (2009).
- [50] S. U. Gjerald, R. Brekken, and T. A. N. Hernes, "Real-time ultrasound simulation for low cost training simulators", in *Proceedings of SPIE*, 7629, 76290B(1–10) (2010).
- [51] A. Hostettler, C. Forest, A. Forgione, L. Soler, and J. Marescaux, "Real-time ultrasonography simulator based on 3D CT-scan images", in *Medicine meets virtual reality 13: The magical next becomes the medical now*, volume 111 of *Studies in Health Technology and Informatics (IOS, Amsterdam)*, 191–193 (2005).
- [52] R. Shams, R. Hartley, and N. Navab, "Real-time simulation of medical ultrasound from CT images", in *Lecture Notes in Computer Science*, volume 5242, 734–741 (2008).

- [53] A. Karamalis, W. Wein, and N. Navab, “Fast ultrasound image simulation using the westervelt equation”, volume 6361 of *Lecture Notes in Computer Science*, 243–250 (2010).
- [54] E.-J. Rijkhorst, D. Heanes, F. Odille, D. Hawkes, and D. Barratt, “Simulating dynamic ultrasound using MR-derived motion models to assess respiratory synchronisation for image-guided liver interventions”, volume 6135 of *Lecture Notes in Computer Science*, 113–123 (2010).
- [55] B. Buerger, C. Abkai, and J. Hesser, “Simulation of dynamic ultrasound based on CT models for medical education”, in *Medicine Meets Virtual Reality 16*, volume 132 of *Studies in Health Technology and Informatics*, 56–61 (2008).
- [56] M. I. Daoud and J. C. Lacefield, “Distributed three-dimensional simulation of B-mode ultrasound imaging using a first-order k-space method”, *Physics in Medicine and Biology* **54**, 5173–5192 (2009).
- [57] J. A. Jensen, “Field: A Program for Simulating Ultrasound Systems”, *Med. Biol. Eng. Comp.* **10th Nordic-Baltic Conference on Biomedical Imaging, Vol. 4, Supplement 1, Part 1**, 351–353 (1996).
- [58] J. A. Jensen and N. B. Svendsen, “Calculation of Pressure Fields from Arbitrarily Shaped, Apodized, and Excited Ultrasound Transducers”, *IEEE Trans. Ultrason., Ferroelec., Freq. Contr.* **39**, 262–267 (1992).
- [59] T. A. Tuthilla, R. H. Sperrya, and K. J. Parker, “Deviations from Rayleigh statistics in ultrasonic speckle”, *Ultrasonic Imaging* **10**, 81–89 (1988).
- [60] U. Schneider, E. Pedroni, and A. Lomax, “The calibration of CT Hounsfield units for radiotherapy treatment planning”, *Physics in Medicine and Biology* **41**, 111–124 (1996).
- [61] J. C. Bamber, *Acoustical Characteristics of Biological Media*, chapter 141, section 4 (John Wiley and Sons, Inc.) (2007).
- [62] J. A. Jensen, *Estimation of Blood Velocities Using Ultrasound: A Signal Processing Approach* (Cambridge University Press, New York) (1996).
- [63] A. H. Pham, B. Lundgren, B. Stage, and J. A. Jensen, “Fish species discrimination using range profiles in the MHz frequency range”, *IEEE Journal of Oceanic Engineering* submitted (2012).
- [64] C. S. Clay and J. K. Horne, “Acoustic models of fish: The atlantic cod (*gadus morhua*)”, *J. Acoust. Soc. Am.* **96(3)**, 1661–1668 (1994).
- [65] K. G. Foote, “Importance of the swimbladder in acoustic scattering by fish: A comparison of gadoid and mackerel target strengths”, *J. Acoust. Soc. Am.* **67(6)**, 2084–2089 (1980).
- [66] K. G. Foote, “Rather-high-frequency sound scattering by swimbladdered fish”, *J. Acoust. Soc. Am.* **78(2)**, 688–700 (1985).

List of Figures

1.1	Images from the sonar and front camera on the ROV captured at the same time	3
1.2	Photos of the fish	4
1.3	Ultrasound images of the fish scanning at 12 MHz using a BK Medical Viking ultrasound scanner	4
2.1	Setup of the measurements. <i>M</i> is a pad made of vibration absorbing material. <i>F</i> is a fish. <i>T</i> is a convex array transducer. <i>A</i> is an angle adjustment device. <i>C</i> is a controller for the mechanical scanner to move the transducer in the direction along the fish.	9
2.2	A photo of the setup for the measurements.	9
2.3	Adjustment of angle α between the fish and the transducer center beam. <i>M</i> is the pad made of vibration absorbing material. <i>F</i> is a fish. <i>T</i> is the convex array transducer. A cross section of the fish and different angle adjustments (a). The angle adjustment device (b).	10
2.4	Photos of four fishes used for the measurements.	13
2.5	Energy distributions of the three cods fish1, fish3, fish4. The length of the fish is normalized to the total length of the fish. The transducer center frequency is 6 MHz. The values of the angle α are 0° (a), 30° (b), and -30° (c).	14
2.6	Energy distributions of the cod fish1, and the saithe fish2. The length of the fish is normalized to the total length of the fish. The transducer center frequency is 6 MHz. The values of the angle α are 0° (a), 30° (b), and -30° (c).	15
2.7	Energy distributions of the cod fish1, and the saithe fish2. The length of the fish is normalized to the total length of the fish. The transducer center frequency is 6 MHz. The values of the angle α are 15° (a), and -15° (b).	16
2.8	Energy distributions of the saithe fish2. The length of the fish is normalized to the total length of the fish. The transducer center frequencies are 6, 3.5, and 2.5 MHz. The values of the angle α are 0° (a), 30° (b), and -30° (c).	17
2.9	Energy distributions of the cod fish3. The length of the fish is normalized to the total length of the fish. The transducer center frequencies are 6, 3.5, and 2.5 MHz. The values of the angle α are 0° (a), 30° (b), and -30° (c).	18

2.10	Energy distributions of the cod fish4. The length of the fish is normalized to the total length of the fish. The transducer center frequencies are 6, 3.5, and 2.5 MHz. The values of the angle α are 0° (a), 30° (b), and -30° (c).	19
2.11	Range profile maps in the yz plane of the saithe fish2 (a), and the cod fish3 (b). The transducer center frequency is 2.5 MHz. The angle α is 0° . The vertical white lines are to mark the limits between different parts of the fish.	20
2.12	Average cross section images of different parts of the fish. The transducer center frequency is 2.5 MHz. The angle α is 0° . The head of the saithe fish2 (a), the head of the cod fish3 (b), the body of the saithe (c), and the body of the cod (d).	21
2.13	Average cross section images of the tail of the fish. The transducer center frequency is 2.5 MHz. The angle α is 0° . The saithe fish2 (a), and the cod fish3 (b).	22
3.1	Block diagram of the procedure of the method. This is a replica of Fig. 1 in [41]	27
3.2	Block diagram of the simulation process. The square boxes with grey background are provided data and programs. The rounded boxes are intermediate results. This is a replica of Fig. 3 in [41]	28
3.3	Energy transmission in one emission (a). Active media used for calculation of ATT, BST, and TRC maps in one emission in the focused beam tracing model (b). Two examples for different active media to calculate the acoustic properties of different media in the beams. The Fig. (b) is a replica of Fig. 4 in [41]. . . .	30
3.4	Active media used for calculation of ATT, BST, and TRC maps in n emissions in the focused beam tracing model. This is a replica of Fig. 5 in [41].	30
3.5	A snapshot of the three-dimensional CT of the fish (a). The vertical white line indicates the position of the slice used in the simulation. The measured ultrasound image of the slice of the fish (b). The CT image of the slice of the fish (c). The position map of the regions of the fish slice (d). Value 0: Air-outside, 1: Fat, 2: Soft tissue, 3: Bone. The BST map of the slice (e). Those are the replicas of Fig. 6 to 10 in [41], respectively.	31
3.6	The ATT map of the slice for the ray-tracing model (a). The ATT map for the focused beam tracing model (b). The TRC map of the slice for the ray-tracing model (c). The TRC map for the focused beam tracing model (d). The $SSM(P)/BST(P)$ map of the slice for the ray-tracing model (e). The $ASSM(P)/BST(P)$ map of the slice for the focused beam tracing model (f). Those are the replicas of Fig. 11, 17, 14, 18, 15, 19 in [41], respectively.	32
3.7	The simulated ultrasound image only from backscatter coefficients (a). The simulated ultrasound image using the ray-tracing model without TRC (b). The simulated ultrasound image with shadow effects using the ray-tracing model (c). The simulated ultrasound image with shadow effects using the focused beam tracing model (d). Those are the replicas in lower resolution of Fig. 12, 13, 16, 20 in [41], respectively.	33

4.1	Block diagram of the system. The front-end of the system is on the left-hand side of the dotted line. This is a replica of Fig. 2 in [63].	36
4.2	Setup of the front-end of the system. C1, C2, and C3 are three identical cameras. UT is the single-element transducer. S is the Blueview multi-beam sonar. The angle between the center line of the UT beam and the center line of the center beam of S is α . This is a replica of Fig. 3 in [63].	37
4.3	A measurement on two mackerels in a school. Range profiles of the mackerels (a), range profiles which are generated from sonar images (b), images from the center camera C1 (c), from the left-hand side camera C2 (d), and from the right-hand side camera C3 (e). Orientation of the mackerel positioned at about 3.2 m in range for ping numbers 5, 17, and 29 (f). Orientation of the mackerel positioned at about 3.5 m in range for ping numbers 5, 17, and 29 (g). This is a replica of Fig. 4 in [63].	38
4.4	A cod turned and swam from left to right. Range profiles of the cod (a), images from the center camera C1 (b), from the left-hand side camera C2 (c), and from the right-hand side camera C3 (d). Orientation of the cod for ping numbers 1, 6, 19, 24, 33, and 42 (e). This is a replica of Fig. 5 in [63].	39
4.5	RF data of some specific pings in the measurement on a cod in Fig. 4.4a. This is a replica of Fig. 6 in [63].	39
4.6	Two young sea basses swam from left to right, and then a cod swam from right to left. Range profiles of the sea basses and the cod (a), range profiles which are generated from sonar images (b), images from the center camera C1 (c), from the left-hand side camera C2 (d), and from the right-hand side camera C3 (e). Orientation of the cod for ping number 36, 43, 50, and 57 (f). This is a replica of Fig. 7 in [63].	40
4.7	Four sea breams swam from left to right. Range profiles of the sea breams (a), images from the center camera C1 (b), from the left-hand side camera C2 (c), and from the right-hand side camera C3 (d). Orientation of the sea bream positioned at about 3.7 m in range for ping numbers 15, 22, 29, and 36 (e). This is a replica of Fig. 8 in [63].	41
4.8	Four sea breams that swam from right to left, turned, and then swam left to right. Range profiles of the sea breams (a), images from the center camera C1 (b), from the left-hand side camera C2 (c), and from the right-hand side camera C3 (d). Orientation of the sea bream turned and positioned at about 2.7 m to 2.2 m for ping numbers 15, 29, 44, 58, and 72 (e). This is a replica of Fig. 9 in [63].	42
4.9	A school of mackerel and horse mackerel with a horse mackerel turning and swimming from left to right. Range profiles of the school of fish (a), images from the center camera C1 (b), from the left-hand side camera C2 (c), and from the right-hand side camera C3 (d). Orientation of the horse mackerel for ping numbers 48, 57, 66, 76, and 85 (e). This is a replica of Fig. 10 in [63].	43

4.10	A school of mackerel and horse mackerel with many complicated movement patterns. Range profiles of the school of fish (a), images from the center camera C1 (b), from the left-hand side camera C2 (c), and from the right-hand side camera C3 (d). Orientation of the mackerel positioned at about 3.8 m in range for ping numbers 1, 13, and 25 (e). Orientation of the mackerel positioned at about 4 m in range for ping numbers 1, 13, and 25 (f). This is a replica of Fig. 11 in [63].	44
C.1	Range profile maps of the 3 cods. The transducer frequency is 6 MHz. The angel α is 0° . Fish1 (a). Fish3 (b). Fish4 (c).	128
C.2	Range profile maps of the 3 cods. The transducer frequency is 6 MHz. The angel α is 30° . Fish1 (a). Fish3 (b). Fish4 (c).	129
C.3	Range profile maps of the 3 cods. The transducer frequency is 6 MHz. The angel α is -30° . Fish1 (a). Fish3 (b). Fish4 (c).	130
C.4	Range profile maps of a cod and a saithe. The transducer frequency is 6 MHz. The angel α is 0° . Fish1 (a). Fish2 (b).	131
C.5	Range profile maps of a cod and a saithe. The transducer frequency is 6 MHz. The angel α is 30° . Fish1 (a). Fish2 (b).	132
C.6	Range profile maps of a cod and a saithe. The transducer frequency is 6 MHz. The angel α is -30° . Fish1 (a). Fish2 (b).	133
C.7	Range profile maps of a cod and a saithe. The transducer frequency is 6 MHz. The angel α is 15° . Fish1 (a). Fish2 (b).	134
C.8	Range profile maps of a cod and a saithe. The transducer frequency is 6 MHz. The angel α is -15° . Fish1 (a). Fish2 (b).	135
C.9	Range profile maps of the saithe fish2. The angel α is 0° . The transducer frequency is 6 MHz (a), 3.5 MHz (b), 2.5 MHz (c).	137
C.10	Range profile maps of the saithe fish2. The angel α is 30° . The transducer frequency is 6 MHz (a), 3.5 MHz (b), 2.5 MHz (c).	138
C.11	Range profile maps of the saithe fish2. The angel α is -30° . The transducer frequency is 6 MHz (a), 3.5 MHz (b), 2.5 MHz (c).	139
C.12	Range profile maps of the cod fish3. The angel α is 0° . The transducer frequency is 6 MHz (a), 3.5 MHz (b), 2.5 MHz (c).	140
C.13	Range profile maps of the cod fish3. The angel α is 30° . The transducer frequency is 6 MHz (a), 3.5 MHz (b), 2.5 MHz (c).	141
C.14	Range profile maps of the cod fish3. The angel α is -30° . The transducer frequency is 6 MHz (a), 3.5 MHz (b), 2.5 MHz (c).	142
C.15	Range profile maps of the cod fish4. The angel α is 0° . The transducer frequency is 6 MHz (a), 3.5 MHz (b), 2.5 MHz (c).	143
C.16	Range profile maps of the cod fish4. The angel α is 30° . The transducer frequency is 6 MHz (a), 3.5 MHz (b), 2.5 MHz (c).	144
C.17	Range profile maps of the cod fish4. The angel α is -30° . The transducer frequency is 6 MHz (a), 3.5 MHz (b), 2.5 MHz (c).	145

C.18	Average cross section images of the saithe fish2. The transducer frequency is 2.5 MHz. The head with $\alpha = 30^\circ$ (a), and $\alpha = -30^\circ$ (d). The body with $\alpha = 30^\circ$ (b), and $\alpha = -30^\circ$ (e). The tail with $\alpha = 30^\circ$ (c), and $\alpha = -30^\circ$ (f).	146
C.19	Average cross section images of the saithe fish2. The transducer frequency is 3.5 MHz. The head with $\alpha = 0^\circ$ (a), $\alpha = 30^\circ$ (d), and $\alpha = -30^\circ$ (g). The body with $\alpha = 0^\circ$ (b), $\alpha = 30^\circ$ (e), and $\alpha = -30^\circ$ (h). The tail with $\alpha = 0^\circ$ (c), $\alpha = 30^\circ$ (f), and $\alpha = -30^\circ$ (i).	147
C.20	Average cross section images of the saithe fish2. The transducer frequency is 6 MHz. The head with $\alpha = 0^\circ$ (a), $\alpha = 30^\circ$ (d), and $\alpha = -30^\circ$ (g). The body with $\alpha = 0^\circ$ (b), $\alpha = 30^\circ$ (e), and $\alpha = -30^\circ$ (h). The tail with $\alpha = 0^\circ$ (c), $\alpha = 30^\circ$ (f), and $\alpha = -30^\circ$ (i).	148
C.21	Average cross section images of the saithe fish2. The transducer frequency is 6 MHz. The head with $\alpha = 15^\circ$ (a), $\alpha = -15^\circ$ (d). The body with $\alpha = 15^\circ$ (b), $\alpha = -15^\circ$ (e). The tail with $\alpha = 15^\circ$ (c), $\alpha = -15^\circ$ (f).	149
C.22	Average cross section images of the cod fish3. The transducer frequency is 2.5 MHz. The head with $\alpha = 30^\circ$ (a), $\alpha = -30^\circ$ (d). The body with $\alpha = 30^\circ$ (b), $\alpha = -30^\circ$ (e). The tail with $\alpha = 30^\circ$ (c), $\alpha = -30^\circ$ (f).	150
C.23	Average cross section images of the cod fish3. The transducer frequency is 3.5 MHz. The head with $\alpha = 0^\circ$ (a), $\alpha = 30^\circ$ (d), and $\alpha = -30^\circ$ (g). The body with $\alpha = 0^\circ$ (b), $\alpha = 30^\circ$ (e), and $\alpha = -30^\circ$ (h). The tail with $\alpha = 0^\circ$ (c), $\alpha = 30^\circ$ (f), and $\alpha = -30^\circ$ (i).	151
C.24	Average cross section images of the cod fish3. The transducer frequency is 6 MHz. The head with $\alpha = 0^\circ$ (a), $\alpha = 30^\circ$ (d), and $\alpha = -30^\circ$ (g). The body with $\alpha = 0^\circ$ (b), $\alpha = 30^\circ$ (e), and $\alpha = -30^\circ$ (h). The tail with $\alpha = 0^\circ$ (c), $\alpha = 30^\circ$ (f), and $\alpha = -30^\circ$ (i).	152
C.25	Two small sea basses and a big sea bass swam from right to left. Range profiles of the sea basses (a), images from the center camera C1 (b), from the left-hand side camera C2 (c), from the right-hand side camera C3(d).	153
C.26	Two small sea basses swam from left to right and a big sea bass turned and swam from right to left. Range profiles of the sea basses (a), images from the center camera C1 (b), from the left-hand side camera C2 (c), from the right-hand side camera C3(d).	154
C.27	A measurement using an Olympus 1 MHz single-element Videoscan transducer. A horse mackerel swam from right to left. Range profiles of the fish (a), images from the center camera C1 (b), from the left-hand side camera C2 (c), from the right-hand side camera C3(d).	155

List of Tables

2.1	A list of figures for an overview of the results	12
3.1	Mapping table from Hounfield Unit to backscatter coefficients, attenuation coefficients, and characteristic acoustic impedance. This is a replica of Table I in [41].	29

Articles in Journals

**A.1 Shadow effects in simulated ultrasound images derived from
computed tomography images using a focused beam tracing
model**

This article was published in *Journal of the Acoustical Society of America*, vol. 132, no. 1, pp. 487-497, 2012.

Shadow effects in simulated ultrasound images derived from computed tomography images using a focused beam tracing model

An Hoai Pham,^{a)} Bo Lundgren, and Bjarne Stage

National Institute of Aquatic Resources, Technical University of Denmark, Jægersborg Alle 1, DK-2920 Charlottenlund, Denmark

Mads Møller Pedersen and Michael Bachmann Nielsen

Department of Radiology, Copenhagen University Hospital, Rigshospitalet, DK-2100 Copenhagen, Denmark

Martin Christian Hemmsen and Jørgen Arendt Jensen

Center for Fast Ultrasound Imaging, Department of Electrical Engineering, Building 349, Technical University of Denmark, DK-2800 Kgs. Lyngby, Denmark

(Received 17 November 2011; revised 11 May 2012; accepted 13 May 2012)

Simulation of ultrasound images based on computed tomography (CT) data has previously been performed with different approaches. Shadow effects are normally pronounced in ultrasound images, so they should be included in the simulation. In this study, a method to capture the shadow effects has been developed, which makes the simulated ultrasound images appear more realistic. The method using a focused beam tracing model gives diffuse shadows that are similar to the ones observed in measurements on real objects. Ultrasound images of a cod (*Gadus morhua*) were obtained with a BK Medical 2202 ProFocus ultrasound scanner (BK Medical, Herlev, Denmark) equipped with a dedicated research interface giving access to beamformed radio frequency data. CT images were obtained with an Aquilion ONE Toshiba CT scanner (Toshiba Medical Systems Corp., Tochigi, Japan). CT data were mapped from Hounsfield units to backscatter strength, attenuation coefficients, and characteristic acoustic impedance. The focused beam tracing model was used to create maps of the transmission coefficient and scattering strength maps. FIELD II was then used to simulate an ultrasound image of $38.9 \times 55.3 \times 4.5$ mm, using 10^6 point scatterers. As there is no quantitative method to assess quality of a simulated ultrasound image compared to a measured one, visual inspection was used for evaluation.

© 2012 Acoustical Society of America. [http://dx.doi.org/10.1121/1.4726031]

PACS number(s): 43.80.Jz, 43.20.El, 43.20.Px, 43.80.Vj [CCC]

Pages: 487–497

I. INTRODUCTION

In fisheries, knowledge about fish properties, such as species and size, is important both when doing resource management and commercial fishing. With the conventional methods, it is usually not possible to get good information about these properties before the fish has been caught, which may lead to misjudging the available fish stocks and wasteful use of the living resources. Therefore, better methods to identify the fish before they are caught are needed.

Acoustical fish identification methods are already in use, because they have better detection ranges than any known optical methods. The present methods use frequencies in the range of 10–500 kHz and give reasonable estimation of size distribution, if the species is known, but cannot significantly support the determination of the actual species, if it is not known.^{1–4} It is expected that using higher frequencies and broader bandwidths than used until now will give more information useful for fish species' identification. Since the objective is to identify fish at ranges up to 30 m with a single element transducer, the expected data would be ultrasound (US) range profiles of fish

from various unknown orientations of the fish. The US range profile is the amplitude and phase variation of the signal recorded during the echo from the fish. The preparation for the identification is to build a library of empirical range profiles for known orientations of each fish species and then use modeling to predict the range profiles from other orientations.

Frequencies above 500 kHz are in a range where there are many medical US applications. It, therefore, seems natural to use the modeling methods well known in the medical US field.^{5–18} An US range profile from a fish depends on the distribution of acoustic properties in the fish body, which cannot be directly measured on a live fish. One way to estimate this distribution is to use computed tomography (CT) scan images, because approximate relations between CT scan properties and acoustical properties are available in the literature.^{19–21} If the distribution based on the CT images is realistic, it would be possible to calculate a simulated US range profile for any orientation of the fish. In order to check if the distribution is a reasonable approximation, this paper presents an improved method to produce simulated US images based on the CT images and assess the quality of the results by comparing with the measured US images. Shadow effects are normally pronounced in US images, so they should be included in the simulation.

^{a)}Author to whom correspondence should be addressed. Electronic mail: haph@aquas.dtu.dk

There are many different methods to simulate US images. In 1979, Bamber and Dickinson⁵ developed a method that can predict the appearance and properties of B-scan images, but it was applied on plastic sponges and synthetic tissue structures. Jensen and Munk⁶ and Jensen and Nikolov⁷ used FIELD II to generate simulated US images based on backscattering maps derived from synthetic clinical images. The backscatter coefficients were proportional to the intensities of the pixels in the clinical images. The method can simulate blood flow, as well as US images of soft tissues. In the studies of Song *et al.*⁸ and Groot *et al.*⁹ an US ray-tracing model was used to simulate US images. The US beam was modeled as straight rays traveling through different media, backscattered from the scatterers and then traveling back to the receiver. The intensity was calculated taking into account the influences of the attenuation, the impedance of the media, and the backscatter coefficients of the scatterers. However, the work of Song *et al.*⁸ and Groot *et al.*⁹ focused only on capturing the main highlights of the structures in the US images, not the speckle patterns or the shadow effects. Another approach used the combination of reflection and transmission images as in the case of the Wein *et al.* study.¹⁰ Statistical similarity metrics like the mutual information and correlation ratio were used to assess the correspondence between the original CT and US intensities. In the study of Dillenseger *et al.*, the scatterers were distributed using the one-dimensional marked regularity model and a fast Hilbert filling curves algorithm.¹¹ Their CT images were segmented into air, fat, soft tissue, and bone. The size of the point spread function in simulated US images varied as a function of depth. Gjerald *et al.*¹² proposed to multiply a pre-simulated speckle pattern image by a CT image. They claimed that the US images can be simulated in real time. The simulated US images do not appear realistic but look like CT images with speckle patterns on. The above-mentioned methods could not capture the shadow effects, which normally appear in measured US images.

There are shadow effects in clinical US images and it is important to include those effects in the simulation. Hostettler *et al.*¹³ managed to capture the shadow effects. Based on CT images, three other kinds of images were created: Multiple echo images, absorption images, and texture images. They were merged to obtain the simulated images. The method of Hostettler *et al.* was not described in detail because it has been patented. They also claimed that reverberation and enhancement effects were captured. But neither of those effects was present or clearly visible in the result. They also used ray-tracing to model the US beams. In another similar method, Shams *et al.*,¹⁴ Karamalis *et al.*,¹⁵ and Rijkhorst *et al.*¹⁶ used the combination of scattering textures, reflection textures, and transmission textures to generate simulated US images. Those textures were created based on CT images in most of the cases, but magnetic resonance (MR) images in the study of Rijkhorst *et al.* The shadow effects were captured in the simulated US images. The CT images were post-processed using contrast and edge enhancement and the attenuation of the media was not taken into account. The CT images were segmented into different tissue regions. The regions were assigned fixed characteristic acoustic impedance. The characteristic acoustic impedances were used to create the transmission textures and the reflection textures. The scattering textures were created based on

the contrast and edge-enhanced CT images. The model was modified by Burger *et al.*¹⁷ by taking attenuation into account. They also took account of the width of the straight US beam that varies as a function of depth. There were shadow effects in the simulated US images, but there were no measured US images to assess the quality of the results. Daoud and Lacefield¹⁸ used a first-order *k*-space method and were able to simulate shadow effects in their US images. They also took into account the attenuation of the medium. They only used a tissue mimicking phantom in their simulation to illustrate the method. There were no examples of actual clinical images. Although they focused on improving the simulation speed, it was still a slow process.

In this study, a new method to introduce shadow effects has been developed, which makes the simulated US images appear realistic. The method not only takes into account the attenuation of the media, but also introduces shadow effects that appear in a measured US image. The method uses a CT image as a basic map to find the scatterer map for the simulation. The CT data give not only the structure data of the scanned object but also material properties, such as attenuation. Derived relationships between Hounsfield unit (HU) and US scattering strength were used. A focused beam tracing model is used in the new method that takes into account the transducer properties, as well as the sound emission sequence used to form a *B*-mode image. The method is described in the following sections.

II. MATERIALS AND METHODS

The development of the new method described in this work was initiated during processing of the data from an experiment²² set up to investigate the possibility to predict the US scattering properties of fish. A part of this work was to evaluate how well simulated US images could be generated from CT images. In the experiment, a cod (*Gadus morhua*) was supported by a special fixture and scanned with both a BK Medical Profocus 2202 ultrasound scanner (BK Medical, Herlev, Denmark) and a Toshiba Aquilion ONE CT scanner (Toshiba Medical Systems Corp., Tochigi, Japan). The cod was not alive and the time difference between the two measurements was 3 h. The measurement and simulation procedure of the method is presented in Fig. 1. It consists of the following steps: Preparation of the fish, acquisition of US data, acquisition of CT data, simulation of US images based on CT data, and assessment of the simulation results. Acoustic property data derived from CT data are input to a simulation program to generate simulated US images. The measured US images are used for the quality assessment of the simulation.

A. Basic theory

The program FIELD II is used for the simulation of US images.^{23,24} FIELD II uses linear acoustics to calculate the transmitted and backscattered US fields as well as the US pressure received at the transducer. To generate a *B*-mode image, a number of independent scatterers are specified, as well as their positions and amplitudes. The amplitude is the relative acoustic scattering strength of each scatterer. By

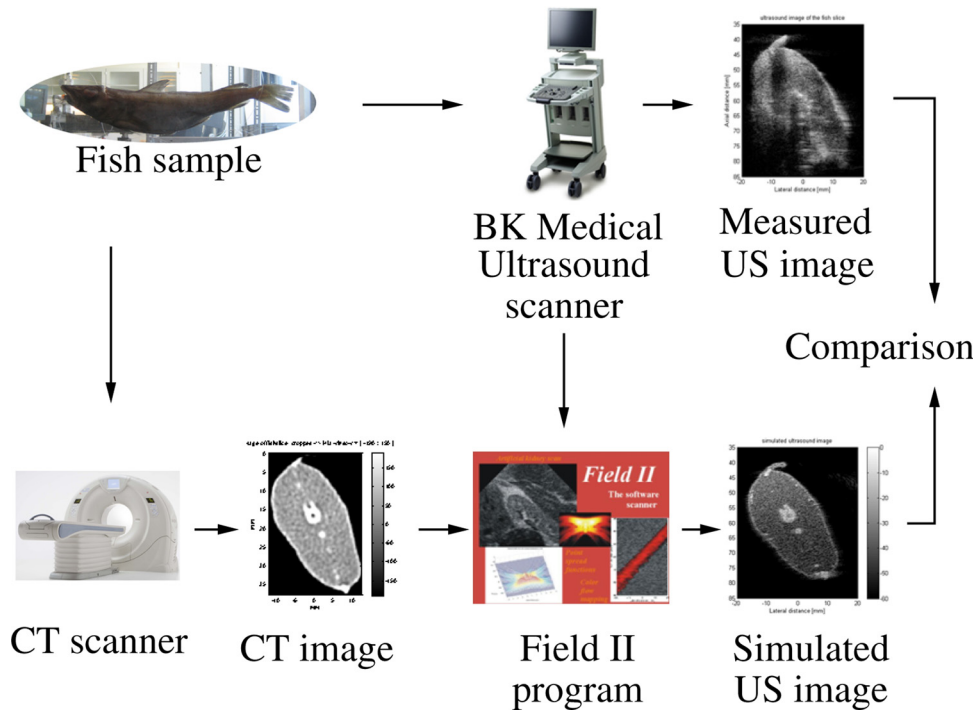


FIG. 1. (Color online) Block diagram of the procedure of the method.

adjusting the number of scatterers and their relative amplitudes, a proper US image is generated.⁶ In this work, the positions and amplitudes of the scatterers are derived from a CT image. There is still no well-established relationship between the HU of CT data and acoustic scattering strength to be found in the literature. However, an approximate relationship is suggested in Sec. II A 2.

1. Propagation of sound through media with the US ray-tracing model

At 10 MHz, the wavelength of sound in water is small (approximately 0.15 mm) compared to structural details in a fish. Therefore, in this case a reasonable approximation is to model US beams as straight US rays. Consider a sound ray traveling from P_0 to P passing through M media as in Fig. 2. A scatterer is positioned at the point P inside a medium and the source of sound is at P_0 . When the sound propagates through different media to the scatterer, part of the sound energy is backscattered. The backscattered wave is transmitted through the media along a similar path back to P_0 . With the assumption of no second- or higher-order scattering and very few scatterers on the boundaries between the media compared to the number of scatterers inside the media, the intensity received at P_0 is⁸

$$I_R(P) = I_s \frac{\eta_b^{(M)} V}{\left(\sum_{m=1}^M l_m \right)^2} \exp \left(-4 \sum_{m=1}^M \alpha^{(m)} l_m \right) \times \prod_{m=1}^{M-1} \alpha_t^{(m,m+1)}(\theta_i^{(m)}) \alpha_t^{(m+1,m)}(\theta_t^{(m)}), \quad (1)$$

where I_s (W/m²) is the initial intensity at P_0 , $\eta_b^{(M)}$ (cm⁻¹ sr⁻¹) is the backscattering coefficient of the medium at P , V (cm³) is the volume of the scatterer, $\alpha^{(m)}$ (Np cm⁻¹)

is the attenuation of the m th medium along the ray path, l_m is the distance the wave has propagated within the m th medium, α_t is the intensity transmission coefficients, and θ_i and θ_t are the incident and transmission angles between the surface normal to the interface of the media and the direction of the sound wave, respectively. Equation (1) describes the influences of the attenuation (the exponential factor) and the transmission (the product factor) properties of the media, as well as the backscatter property of the scatterer (the fraction factor) on the received intensity of the US beam at P_0 .

The intensity transmission coefficients are given by²¹

$$\alpha_t^{(m,m+1)}(\theta_i^{(m)}) = \frac{4Z_m Z_{m+1} \cos^2 \theta_i^{(m)}}{\left(Z_m \cos \theta_i^{(m)} + Z_{m+1} \cos \theta_t^{(m)} \right)^2} \quad (2)$$

where Z_m (kg/(m² s)) is the characteristic acoustic impedance of the m th medium.

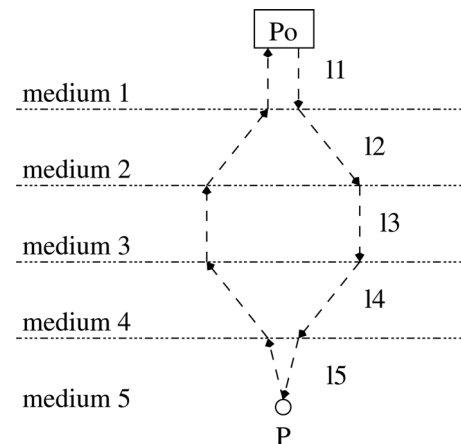


FIG. 2. Ray-tracing modeling for propagation of sound through a number of media ($M=5$).

2. Acoustic scattering strength derived from CT data

If a very small angle of incidence is assumed $\cos \theta_i = \cos \theta_t \approx 1$ at all media boundaries, then

$$\alpha_i^{(m,m+1)}(\theta_i^{(m)}) = \alpha_i^{(m+1,m)}(\theta_t^{(m)}) \approx \frac{4Z_m Z_{m+1}}{(Z_m + Z_{m+1})^2},$$

and Eq. (1) can be rewritten as

$$I_R(P) = K \frac{\text{BST}(P)}{\text{sum}L(P)} \text{ATT}(P) \text{TRC}(P) = K \cdot \text{SSM}(P) \quad (3)$$

where

$$K = I_s V, \quad (4)$$

$$\text{BST}(P) = \eta_b^{(M)}, \quad (5)$$

$$\text{sum}L(P) = \left(\sum_{m=1}^M l_m \right)^2, \quad (6)$$

$$\text{ATT}(P) = \exp \left(-4 \sum_{m=1}^M \alpha^{(m)} l_m \right), \quad (7)$$

$$\begin{aligned} \text{TRC}(P) &= \prod_{m=1}^{M-1} \alpha_i^{(m,m+1)}(\theta_i^{(m)}) \alpha_t^{(m+1,m)}(\theta_t^{(m)}) \\ &= \prod_{m=1}^{M-1} (\alpha_i^{(m,m+1)}(\theta_i^{(m)}))^2 \end{aligned} \quad (8)$$

$$\text{SSM}(P) = \frac{\text{BST}(P)}{\text{sum}L(P)} \text{ATT}(P) \text{TRC}(P). \quad (9)$$

$\text{BST}(P)$ [or $\eta_b^{(M)}$, see Eqs. (1) and (5)] is the backscatter properties of medium M in which point P is located. ATT describes the two-way attenuation effect of the media from 1 to M and back. TRC is the two-way transmission coefficient due to the media borders. SSM is the scattering strength map, where $\text{SSM}(P)$ is the relative scattered energy returned to the transducer by the scatterer at point P , and K is assumed to be 1.

For the simulation in this work, $\eta_b^{(M)}$, $\alpha^{(m)}$, and Z_m are calculated based on the CT image. If it is assumed that the HU ranges for the different tissue types of fish are similar to that of human tissue types, a table of HU ranges for various tissues can be produced from values in the literature. The CT image is segmented into four main categories: Bone, soft tis-

sue, fat, and air, which are listed in Table I.^{19–21} [Note that in this paper the definition of HU is $1000(\mu - \mu_{\text{water}})/\mu_{\text{water}}$, where μ is an x-ray absorption value.] The corresponding ranges of $\eta_b^{(M)}$, $\alpha^{(m)}$, and Z_m for those categories can also be found in the literature and they are listed in Table I as well. With the use of the relationships given in Table I the HU values of the pixels in the CT image are used to produce a back-scattering coefficient map, an attenuation coefficient map, and a characteristic acoustic impedance map. The mapping ranges in Table I have not been verified by experiments on fish. They are assumed to be correct for the purpose of demonstrating the simulation method.^{19–21}

B. Simulation

The basis for the simulated US images is the CT images. The pixel size of the CT images, the geometry, and the characteristics of the US transducer are known and used as input parameters to the simulation. The simulation process is presented in Fig. 3. In Fig. 3, the procedure to find the positions of the scatterers is on the left-hand side of the dotted line. The procedure to find the amplitudes of the scatterers is on the right-hand side of the dotted line.

1. Position map and number of scatterers

The image alignment achieved between the US imaging planes and the CT images is as follows: The sets of two-dimensional CT and US images are reconstructed to three-dimensional (3D) blocks and then rescaled so that the fish in the two blocks has the same length in meters. Then the CT image block was translated and rotated until the head, the tail, and the fins of the fish in the two blocks were aligned. As indicated in the upper left-hand side of the Fig. 3, one CT image and a corresponding US image of the same slice of the fish were selected. The CT image was cropped, rotated, and scaled so that the objects in the CT image had the same orientations and sizes as the ones in the US image. The boundaries of the image were selected to be close to the boundaries of the image of the fish slice to minimize the processing time. The coordinates of the CT image were translated to fit with the measured US image, but the resolution was kept equal to the one in the CT image. The result was a media map of the regions that contain the scatterers. A number of scatterers are placed randomly from a uniform distribution inside the image volume used for the simulation. The number of scatterers is proportional to the ratio of the image volume and the volume of the resolution cell as in Eq. (13). The volume of the resolution cell in m^3 is calculated by

TABLE I. Mapping table from Hounsfield unit to backscatter, attenuation coefficients, and characteristic acoustic impedance.

Regions	Hounsfield unit	$\eta_b^{(M)}$ ($\text{cm}^{-1} \text{sr}^{-1}$)	$\alpha^{(m)}$ (dB/(cm MHz))	Z_m ($\text{kg}/(\text{m}^2 \text{s})$)
Bone	[179, maximum]	[0.05, 0.1]	[100, 200]	$[6.5 \times 10^6, 7.38 \times 10^6]$
Soft tissue	[-41, 178]	[0.000125, 0.01]	[10, 32.5]	$[1.55 \times 10^6, 1.74 \times 10^6]$
Fat	[-741, -42]	[0.003, 0.019]	[1.25, 2]	1.33×10^6
Air-inside	[minimum, -742]	0	[400, 500]	0.4×10^3
Air-outside	not defined by HU	0	0.24	1.48×10^6

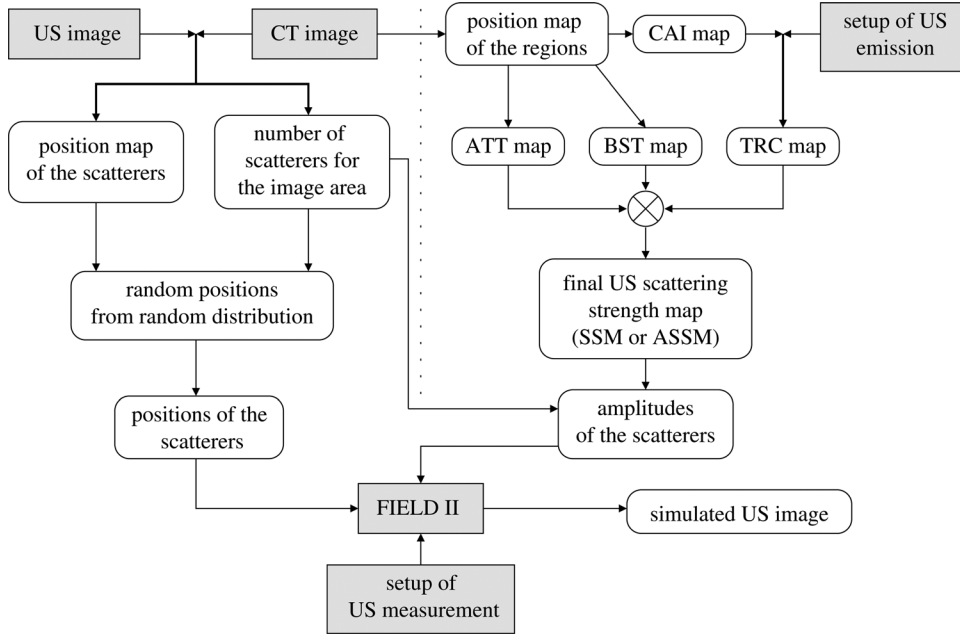


FIG. 3. Block diagram of the simulation process. The square boxes with grey background are provided data and programs. The rounded boxes are intermediate results.

$$\text{rescell} = N\lambda\text{FWHM}_l\text{FWHM}_{\text{azi}}, \quad (10)$$

$$\text{FWHM}_i = F\#_i \cdot \lambda \quad (11)$$

where λ is the wavelength and N is the number of cycle in the pulse, FWHM_l and FWHM_{azi} are the full width at half maximum laterally and azimuthally, respectively, of the point spread function at the focus point. The image volume in m^3 is calculated by

$$\text{imgvol} = \text{CTimgarea} \times \text{eleheight}, \quad (12)$$

where CTimgarea is the area of the CT image, which is converted from pixels to m^2 , and eleheight (in meters) is the height of the element of the transducer. This height is assumed to be the effective slice thickness of the US image. To produce an US image with a fully developed speckle pattern, there should be at least 10 scatterers per resolution cell.²⁵

Thus, the number of scatterers used in the simulation should be

$$n_{\text{scatt}} = 10 \times \frac{\text{imgvol}}{\text{rescell}}. \quad (13)$$

2. Segmentation and mapping tables

As indicated in the upper right-hand side of Fig. 3, the CT image was segmented into different regions using different thresholds corresponding to the HU range limits for bone, soft tissue, fat, and air regions. The thresholds are defined in Table I. The fish body is in the center of the CT image delimited by a region of fat along its outer edge. The air region outside the fish body was defined as the air-outside region. There is sometimes also an air region inside the fish body, which is defined as an air-inside region. This separation into two different types of air regions was necessary, because the fish was suspended in air during the CT scan and in water during the US scan. A position map of the

regions was then generated. In the maps of the different acoustic coefficients, the air-outside fish regions will be mapped with the acoustic properties of water. The backscatter coefficient map, the attenuation coefficient map, and the characteristic acoustic impedance map were generated using Table I. The information of the US emission provided by the US scanner and the characteristic acoustic impedance map were used to calculate the energy transmission coefficient map as described in the following sections.

3. US scattering strength map and the simulated US image

The final US scattering strength map is calculated using Eq. (3) with the assumption that each pixel is a different medium and all scatterers within the medium have the same l_m . There were n_{scatt} values for random positions generated from a uniform distribution within the limits of the position map of the scatterers and the FWHM_{azi} . The amplitudes of the scatterers were first assigned values based on the final US scattering strength map using the position values. Scatterers within a particular medium were all assigned to have the same scattering strength values based on the HU values of the corresponding pixel in the CT image. Then they were multiplied with random values drawn from a normal distribution within $[-1, 1]$ to introduce the constructive and destructive interference of US wave. The US scanner setup parameters, the 3D positions, and amplitudes of the scatterers were input to FIELD II and the simulated US image was generated.

4. Shadow effects using the ray-tracing model

In US images, shadow effects are normally pronounced. The shadow effects appear when the sound travels through a boundary between two media where there is a large change in characteristic acoustic impedance. This phenomenon is included in the simulation through the

modification of the US scattering strength map by the two-way transmission coefficient TRC in Eq. (9). The others terms in Eq. (9) only contribute to form the structure in the simulated US image.

Simple but unrealistic shadow effects are introduced in the simulation when using the US ray-tracing modeling.⁸ With this model, the sound transmitted by each emission is modeled as a straight ray that has the origin at the center of the active aperture. The sound is then transmitted into the media as a ray perpendicular to the active aperture. The number of rays is equal to the number of image lines in the measured US image. For each ray, it is assumed that there is no loss of energy from the active aperture to the first medium corresponding to the top of the image. According to Eqs. (3)–(8) the maps of BST, sumL, ATT, and TRC can be calculated independently. The final US scattering strength map SSM is calculated using Eq. (9).

5. Shadow effects using the focused beam tracing model

In most US imaging systems, only some of the transducer elements are excited for each emission to produce an electronically focused US beam. Unlike in the previous method where the sound was modeled as a ray with constant width, in reality the US energy becomes concentrated in the area around the focus point, and then diverges again in the media. A new method to take this fact into account was developed to create shadow effects that appear more realistic. The method, thus, uses a focused beam tracing model.

a. The US scattering strength map for one emission. In the focused beam tracing model, the sound produced in each emission is modeled as group of rays that intersect at a focus point. The focus point is located at the center of the active aperture in the lateral direction and at the focus depth in the axial direction. The number of rays is equal to the number of active elements. The positions of the active media that each ray passes through are derived from the positions of the corresponding active element and the focus point (see Fig. 4). Then for each active medium on a ray the BST, sumL, ATT, and TRC are calculated using Eqs. (5)–(8).

For the em^{th} emission, the US scattering strength map $SSM^{(em)}(P)$ is calculated by

$$SSM^{(em)}(P) = \sum_{i=1}^m SSM_i^{(em)}(P), \quad (14)$$

where m is the number of active elements in one emission. $SSM_i^{(em)}(P)$ is calculated by Eq. (9) if the i^{th} ray passes through P . Otherwise, $SSM_i^{(em)}(P) = 0$.

b. The US scattering strength map for n emissions. For each of the n emissions, the position of the center of the active aperture is placed at the same position as the corresponding image line. The positions of the active elements are then derived relative to this position. The same procedure as described in Sec. II B 5 a is repeated n times (Fig. 5). The results are n US SSMs.

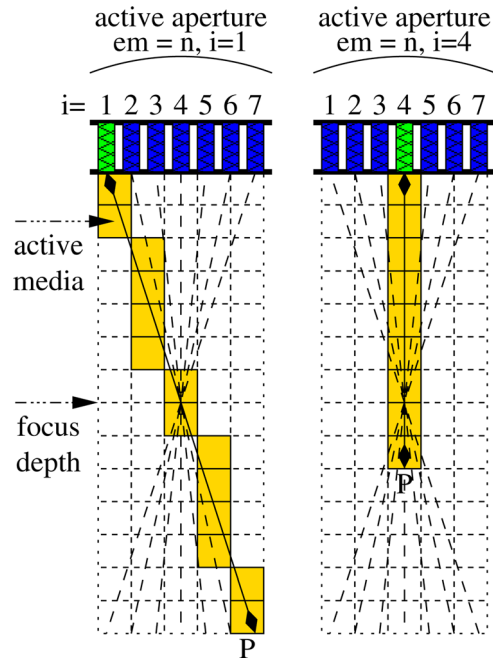


FIG. 4. (Color online) Active media used for calculation of ATT, BST, and TRC maps in one emission in the focused beam tracing model. Two examples are given for different active media to calculate the acoustic properties of different media on the beams.

The average of the n US SSMs gives a final US SSM,

$$ASSM(P) = \frac{1}{n} \sum_{em=1}^n SSM^{(em)}(P). \quad (15)$$

C. Measurement and simulation setup parameters

The acoustic scanning of the fish was performed at the Center for Fast Ultrasound Imaging (CFU) using a ProFocus 2202 scanner (BK Medical), equipped with a dedicated research interface connected to a personal computer through an X64-CL Express camera link interface (Dalsa, Waterloo, ON, Canada). The system allows acquisition of digitally beamformed radio frequency (RF) echo data.²⁶

A BK Medical linear array transducer with 192 elements was used. The center frequency of the transmit pulse was 10 MHz. The transducer was attached to an electromechanical linear scanner on top of an aquarium with the fish already suspended in a fixture at the center of the water volume. The transmit focus point of the transducer was at a range of 45 mm and the transmit f -number was 3.6. Dynamic focusing was used with the receive f -number equal to 0.5. The gain of the US scanner was adjusted, so that the speckle pattern appeared with a roughly uniform intensity in the soft tissue areas in the US images. Digitally beamformed RF data and a parameter setup file of the scanner were retrieved using the program CFU GRABBER.²⁶ The parameter files were saved to be used afterwards for the simulation. The scanner generated 384 image lines corresponding to 384 emissions in one US image.

The CT scanning of the fish was performed at Rigshospitalet in Copenhagen, Denmark. The fixture with the fish was placed in a sealed box and transported to the hospital. The

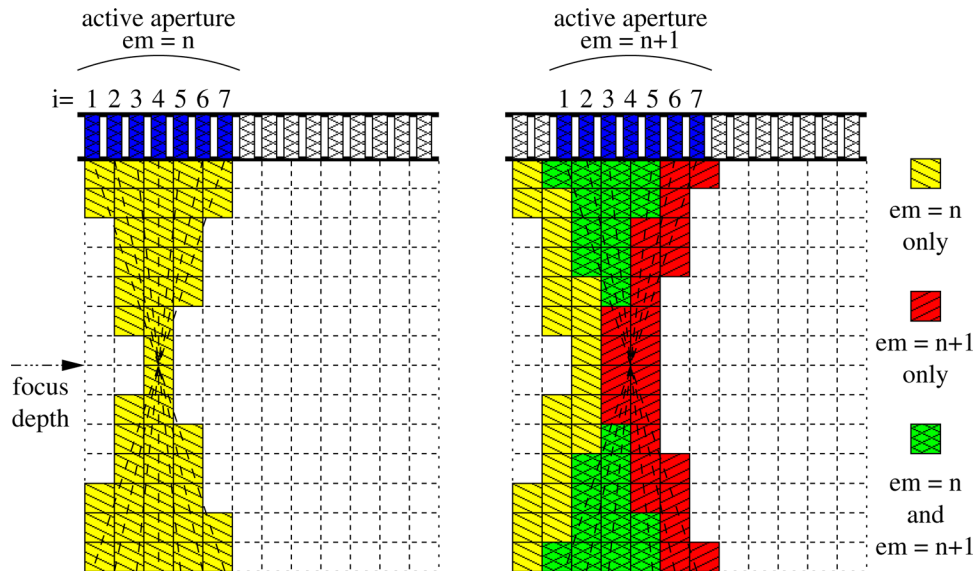


FIG. 5. (Color online) Active media used for calculation of ATT, BST, and TRC maps in n emissions in the focused beam tracing model.

box with the fish was scanned with a Toshiba Aquilion ONE CT scanner. The CT images were obtained with a slice thickness of 0.5 mm and pixel sizes of $0.274 \text{ mm} \times 0.274 \text{ mm}$.

The simulation parameters are given in Table II, with the resolution cell rescell and the image volume imgvol. The number of scatterers n_{scatt} was calculated by using Eq. (13). Each simulated US image was generated using $n_{\text{scatt}} = 10^6$.

The smallest simulated point spread function is $0.54 \text{ mm} \times 0.3 \text{ mm}$. It took 10 min to generate one image line by FIELD II running as the only task on one machine or 1.83 h for the whole simulated US image using 35 machines on the CFU cluster. The CFU cluster consists of 50 machines, each of them a Dell Power Edge 1750 server, Dual Intel Xeon 3.2 GHz (Dell, Inc., Texas) supporting Hyper-threading technology, and 2 Gbytes of random access memory.

III. RESULTS

One sample slice of the fish was chosen to demonstrate the methods of simulation. A snapshot of a 3D CT image of the fish is shown in Fig. 6. The vertical white line indicates

the position of the slice used in the simulation. The measured US image and the CT image of the slice of the fish are shown in Figs. 7 and 8, respectively.

A. The simulated US image without shadow effects

A position map of the regions of the fish slice is presented in Fig. 9. The BST and ATT maps of the slice are shown in Figs. 10 and 11, respectively. It seems that the ATT map might introduce the shadow effects to the simulated US image. Two simulated US images of the slice of the fish are presented in Figs. 12 and 13. The US SSM for Fig. 12 was calculated using Eq. (9) with $\text{ATT}(P) = \text{TRC}(P) = 1$, whereas for Fig. 13 only $\text{TRC}(P) = 1$. The simulated US images appear very similar to the CT image, and with a more fine grain speckle pattern than in the measured US image. The images capture the effect of the increasing width of the point spread functions of the scatterers when the distance between the focus point and the scatterers increases. The BST map decides the structure of the simulated US images. No shadow effects appeared in the images and the ATT map could not introduce shadow effects to the simulated US image in Fig. 13.

B. Shadow effects in the simulated US image using the ray-tracing model

In the measured US image (Fig. 7), there are shadows below the regions appearing behind bone regions (high HU

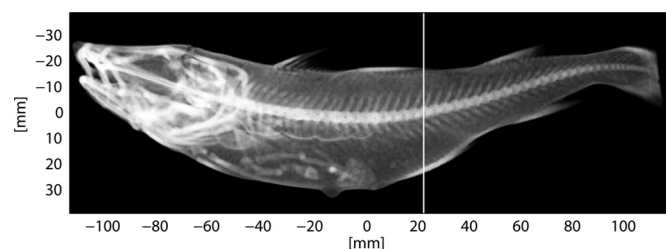


FIG. 6. A snapshot of the three-dimensional CT of the fish. (The vertical white line indicates the position of the slice used in the simulation.)

TABLE II. Measurement parameters for the simulation.

Parameters	Values
f_0 (MHz)	10
Number of elements	192
Number of lines in an ultrasound image	384
Maximum number of active elements	64
Element kerf (μm)	35
Element width (μm)	173
Element height (μm)	4500
Element pitch (μm)	208
Element elevation focus (mm)	20
Focus depth (mm)	45
Transmit F#	3.65
Receive F#	0.5
rescell (mm^3)	0.1053
imgvol (mm^3)	9680
n_{scatt}	10^6

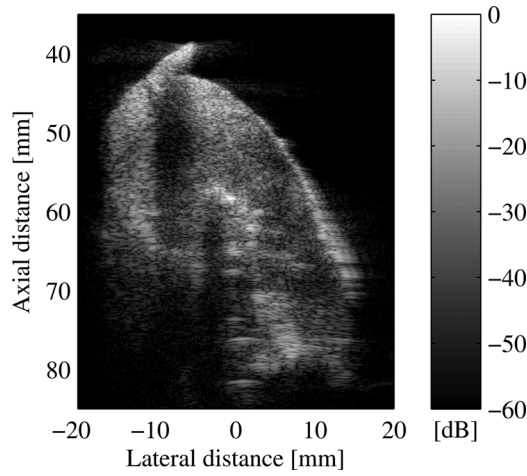


FIG. 7. The measured US image of the slice of the fish.

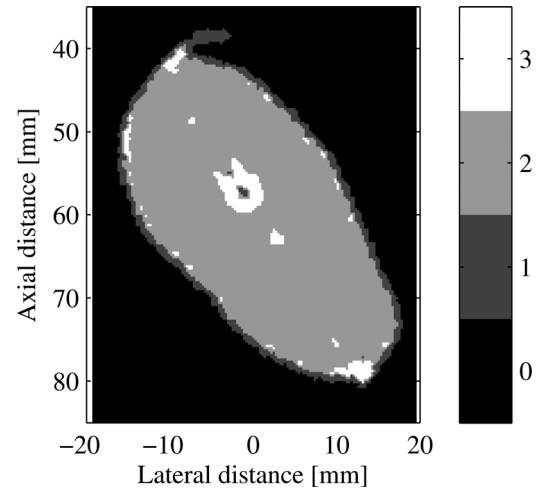


FIG. 9. The position map of the regions of the fish slice. (0: Air-outside, 1: Fat, 2: Soft tissue, 3: Bone.)

values in Fig. 8) and a shadow below the transition region, where sound passes from the fish fin to water and from water to the fish body. Similarly, the skin regions in the upper part of the fish in the measured US image appear enhanced, probably because the sound intensity decreases quickly in those regions. To introduce those effects in the simulation, the ray-tracing model was used to simulate the US image shown in Fig. 16 using Eq. (9). The assumption of this model is that plane waves were used to create the ATT map and TRC map. The ATT and TRC maps are shown in Figs. 11 and 14, respectively. A low value in the TRC map means that the beam has passed through borders between media with high differences in characteristic acoustic impedance. Because of the plane wave assumption neither the ATT nor the TRC map calculations includes the effects caused by the focusing of the US beams. The $SSM(P)/BST(P)$ map is presented in Fig. 15 to show the effects of the combination of $sumL$, ATT, and TRC. The background of Fig. 15 is a transitional area of values, high values at the top and lower values to the bottom, whereas it is constant values in Fig. 14. The simulated US image captured the shadow effects. The enhancement effect is only visible in the skin region on the upper part of the fish slice close to the transducer, where the energy from the transducer is high.

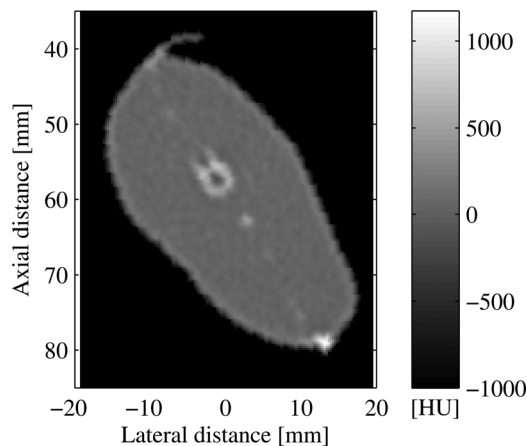


FIG. 8. The CT image of the slice of the fish.

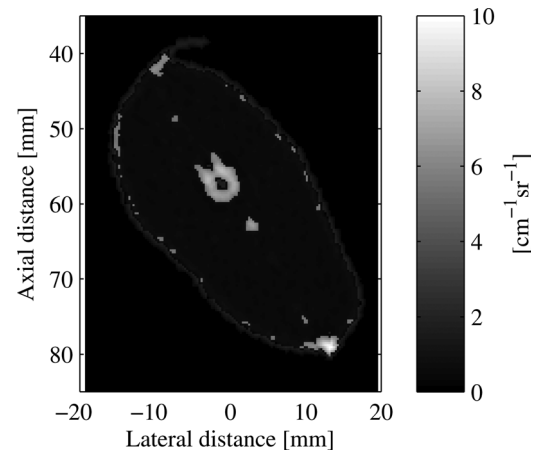


FIG. 10. The BST map of the slice.

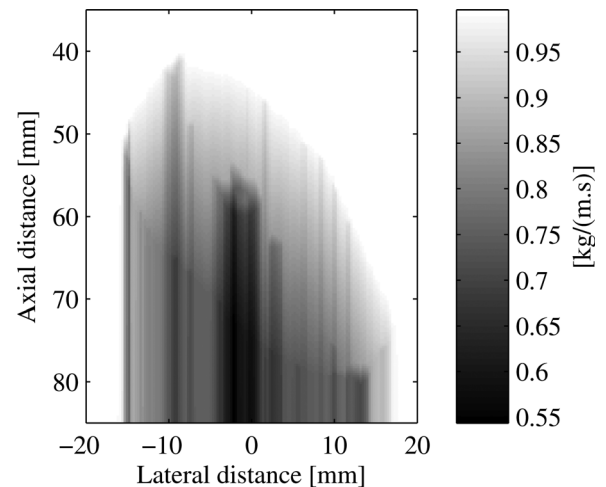


FIG. 11. The ATT map of the slice for the ray-tracing model.

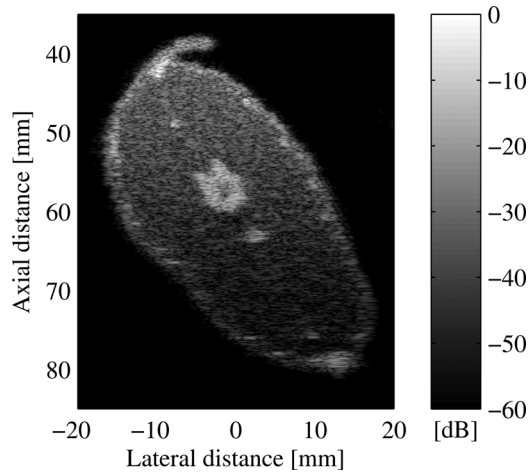


FIG. 12. The simulated US image only from backscatter coefficients.

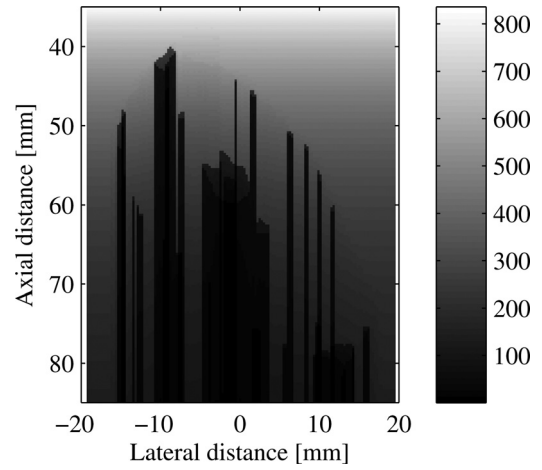


FIG. 15. The $SSM(P)/BST(P)$ map of the slice for the ray-tracing model.

C. Shadow effects in the simulated US image using the focused beam tracing model

In Fig. 7, the shadows are influenced by the fact that the sound waves produced by the transducer are not sharp, straight beams. The focused beam tracing model takes this phenomenon into account. The simulated US image produced using this method is presented in Fig. 20. The transmission coefficients at the same position will be different if the transmit focus is different. The ATT and TRC maps of this model are presented in Figs. 17 and 18, respectively. In both figures, the maximum values are at the focus depth. The method gives diffuse shadows with decreasing width below the shadow regions similar to the feature in the measured image. The average scattering strength map was calculated using Eq. (15) and the $ASSM(P)/BST(P)$ map is shown in Fig. 19. In this map, the maximum values are no longer at the focus depth.

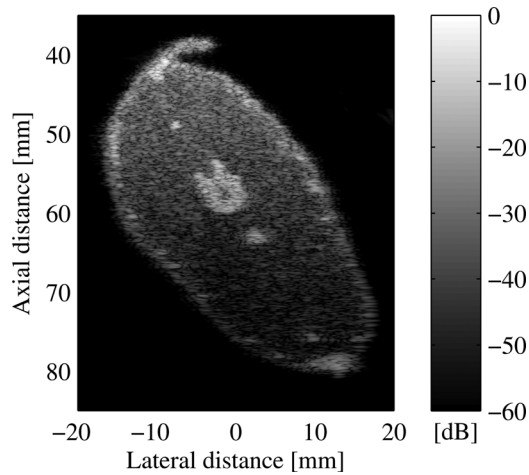


FIG. 13. The simulated US image using the ray-tracing model without TRC.

IV. DISCUSSION

Since no qualitative method to assess quality of a simulated US image compared to a measured one exists, visual inspection was used. The simulated US images in Figs. 12

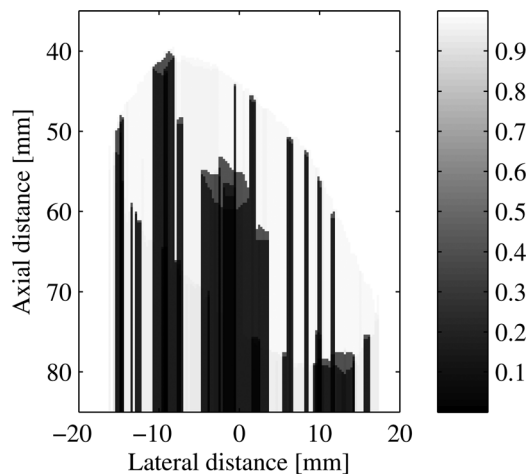


FIG. 14. The TRC map of the slice for the ray-tracing model.

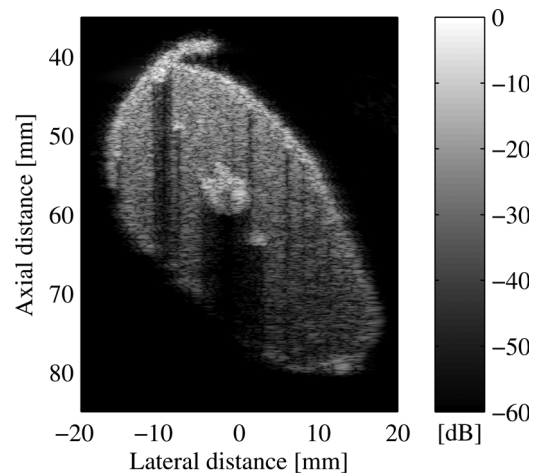


FIG. 16. The simulated US image with shadow effects using the ray-tracing model.

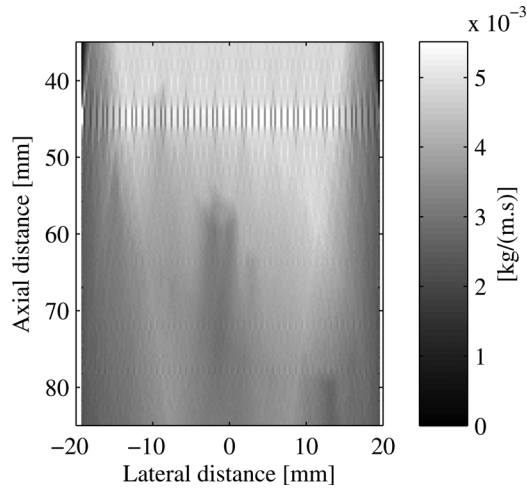


FIG. 17. The ATT map for the focused beam tracing model.

and 13 are not realistic and very different to the measured one in Fig. 7. The shadow effects are normally pronounced in US images, so they should be included in the simulation. When shadowing is introduced, the simulated US image in Fig. 16 appears more realistic than in Figs. 12 and 13.

The ray-tracing model described in Sec. II B 4 does not take into account the influence of the type of the US transducer on the simulated image. The focused beam tracing model in Sec. II B 5 produces more realistic shadowing in the simulated image. The method is applied for a linear array transducer, but can be used for convex array and phase array transducers as well, because they also produce focused US beam in each emission. A similar mapping method could be used if the data are MR images instead of CT images. The fat and skin regions cannot be distinguished in the CT images, which give an uncertainty with regard to the sound transmission through the skin. The segmentation of the CT images is normally a user-dependent process. Different thresholding values influence, especially the size and shape of skin and bone regions. It is difficult to distinguish between them when they are next to each other, as the x-ray absorption of skin and fat regions is very similar, mak-

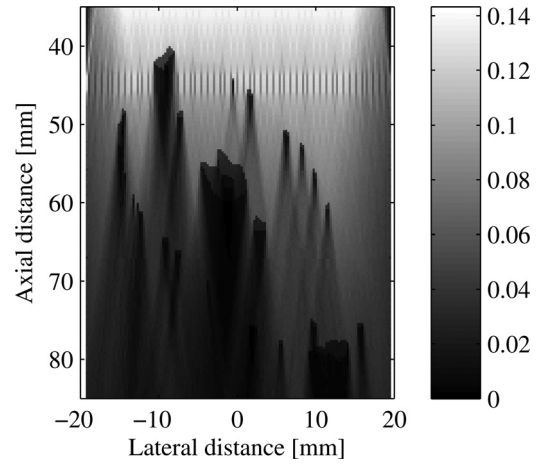


FIG. 19. The ASSM(P)/BST(P) map of the slice for the focused beam tracing model.

ing segmentation difficult. Segmentation is therefore made manually, and there is no well-established method available in the literature to validate it. In the measurement, the US beam is not focused at a single point but a region. The shadows in the measured US image are a compromise between the ray-tracing model and the focused beam tracing model. The amplitude weight of ATT map on the final scattering strength map is not enough to introduce the shadow effects. However, it makes the upper part of the fish brighter than the lower part. The focus point is modeled as a very small point. This is the reason why there are artifacts in the ATT and TRC maps at axial distance about 45 mm in Figs. 17–19, but the artifacts do not appear in 20. The FWHM perpendicular to the image plane of the simulated point spread function of the BK transducer, calculated by FIELD II, is assumed to be the effective slice thickness of the US imaging modality. It varies as a function of depth. It is narrowest, about 0.6 mm, at the elevation focus at about 20 mm depth and about 8 mm at 80 mm depth, while the effective slice thickness of the CT imaging modality is a constant, about 0.5 mm. Hence, the simulation is more accurate at the elevation focus than at the other depths. This also needs to be considered in future simulations.

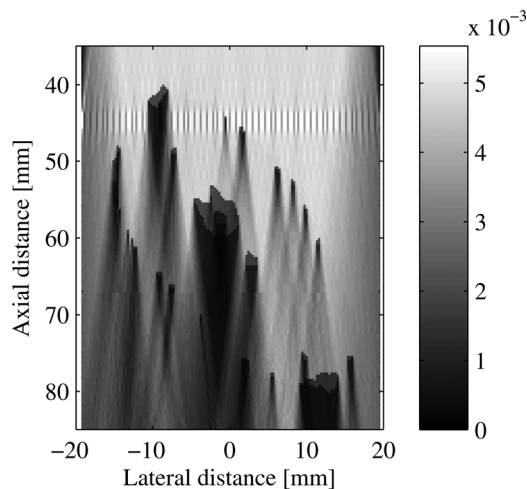


FIG. 18. The TRC map for the focused beam tracing model.

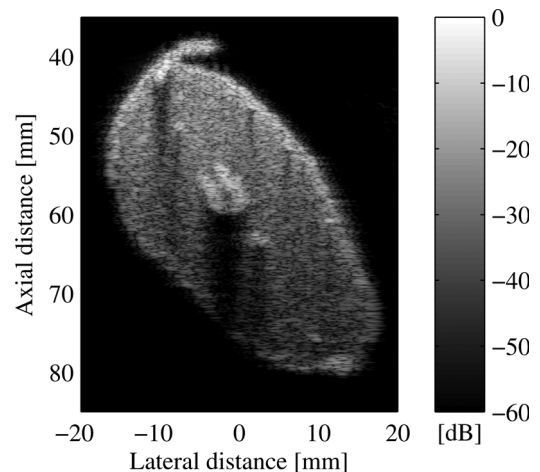


FIG. 20. The simulated US image with shadow effects using the focused beam tracing model.

V. CONCLUSION

In this work, a new method to introduce shadow effects has been tested that makes the simulated US image from the CT image appear more realistic. The experiment provides the US data for assessment of the simulation results, as well as instrument parameters and CT data for the simulation process. The method emphasizes the necessity of mapping the HU to the backscattering, attenuation coefficients, and characteristic acoustic impedance in the simulation of US images from CT images. There are three different ways to construct the final simulated US image with the same setup: Without shadow effects, with shadow effects using the ray-tracing model, and with shadow effects using the focused beam tracing model. The simulation that only used the backscatter coefficients cannot introduce shadow effects into the simulated US image. The image appears similar to the CT image and is much more uniform than the measured US image. The ray-tracing model produces shadow effects in the simulated US image. But the shadow effects are still not similar to the ones in the measured US image. The last approach, the focused beam tracing model, generates the simulated US image with shadow effects that are similar to the ones in the measured US image.

In conclusion, a new method with the focused beam tracing model was developed to simulate US images from CT images. The method uses the two-way transmission coefficients to capture the shadow effects. With this method the simulated US images display most of the characteristics of measured US images such as shadowing, attenuation, and edge-enhancement.

ACKNOWLEDGMENTS

This work is sponsored by a grant from the Globalization project of the Technical University of Denmark (DTU). Special thanks to Stina Bjørk Stenersen Hansen at the National Institute of Aquatic Resources (DTU Aqua) for supplying the fish specimens, Karl-Johan Stæhr at DTU Aqua for advice on experimental details in connection with the US scan, and Tina Bock Pedersen at the Copenhagen University Hospital, Rigshospitalet for the CT scanning of the fish.

- ¹J. E. Simmonds and D. MacLennan, *Fisheries Acoustics: Theory and Practice* (Blackwell, Oxford, UK, 2005), Chaps. 3.5, 3.7.2, and 7.5.3.
- ²R. J. Korneliusen, Y. Heggelund, I. K. Eliassen, and G. O. Johansen, "Acoustic species identification of schooling fish," *ICES J. Mar. Sci.* **66**, 1111–1118 (2009).
- ³B. Lundgren and R. N. Nielsen, "A method for the possible species discrimination of juvenile gadoids by broad-bandwidth backscattering spectra vs. angle of incidence," *ICES J. Mar. Sci.* **65**(4), 581–593 (2008).
- ⁴J. M. Burgos and J. K. Horne, "Acoustic characterization and classification of pelagic organism distributions," *ICES J. Mar. Sci.* **65**, 1235–1247 (2008).
- ⁵J. Bamber and R. Dickinson, "Ultrasonic B-scanning—A computer-simulation," *Phys. Med. Biol.* **25**, 463–479 (1980).

- ⁶J. A. Jensen and P. Munk, "Computer phantoms for simulating ultrasound B-mode and CFM images," *Acoust. Imaging* **23**, 75–80 (1997).
- ⁷J. A. Jensen and S. Nikolov, "Fast simulation of ultrasound images," *Proc.-IEEE Ultrason. Symp.* **2**, 1721–1724 (2000).
- ⁸M. Song, R. Haralick, and F. Sheehan, "Ultrasound imaging simulation and echocardiographic image synthesis," in *Proceedings of the International Conference on Image Processing* (2000), Vol. III, pp. 420–423.
- ⁹S. C. Groot, R. Hamers, F. H. Post, C. P. Botha, and N. Bruining, "IVUS simulation based on histopathology," *Comput. Cardiol.*, 681–684 (2006).
- ¹⁰W. Wein, A. Khamene, D. A. Clevert, O. Kutter, and N. Navab, "Simulation and fully automatic multimodal registration of medical ultrasound," in *Proceedings of the 10th International Conference on Medical Image Computing and Computer-Assisted Intervention* (2007), pp. 136–143.
- ¹¹J. L. Dillenseger, S. Laguiton, and E. Delabrousse, "Fast simulation of ultrasound images from a CT volume," *Comput. Biol. Med.* **39**, 180–186 (2009).
- ¹²S. U. Gjerald, R. Brekken, and T. A. N. Hernes, "Real-time ultrasound simulation for low cost training simulators," *Proc. SPIE* **7629**, 76290B (1–10) (2010).
- ¹³A. Hostettler, C. Forest, A. Forgione, L. Soler, and J. Marescaux, "Real-time ultrasonography simulator based on 3D CT-scan images," in *Medicine Meets Virtual Reality 13: The Magical Next Becomes the Medical Now*, Studies in Health Technology and Informatics (IOS, Amsterdam, 2005), Vol. 111, pp. 191–193.
- ¹⁴R. Shams, R. Hartley, and N. Navab, "Real-time simulation of medical ultrasound from CT images," *Lect. Notes Comput. Sci.* **5242**, 734–741 (2008).
- ¹⁵A. Karamalis, W. Wein, and N. Navab, "Fast ultrasound image simulation using the Westervelt equation," *Lect. Notes Comput. Sci.* **6361**, 243–250 (2010).
- ¹⁶E.-J. Rijkhorst, D. Heanes, F. Odille, D. Hawkes, and D. Barratt, "Simulating dynamic ultrasound using MR-derived motion models to assess respiratory synchronisation for image-guided liver interventions," *Lect. Notes Comput. Sci.* **6135**, 113–123 (2010).
- ¹⁷B. Buerger, C. Abkai, and J. Hesser, "Simulation of dynamic ultrasound based on CT models for medical education," in *Medicine Meets Virtual Reality 16: parallel, combinatorial, convergent: NextMed by Design*, Studies in Health Technology and Informatics (IOS, Amsterdam, 2008), Vol. 132, pp. 56–61.
- ¹⁸M. I. Daoud and J. C. Lacefield, "Distributed three-dimensional simulation of B-mode ultrasound imaging using a first-order k-space method," *Phys. Med. Biol.* **54**, 5173–5192 (2009).
- ¹⁹U. Schneider, E. Pedroni, and A. Lomax, "The calibration of CT Hounsfield units for radiotherapy treatment planning," *Phys. Med. Biol.* **41**, 111–124 (1996).
- ²⁰J. C. Bamber, *Acoustical Characteristics of Biological Media* (Wiley, Hoboken, NJ, 2007), Chap. 141, Sec. 4.
- ²¹J. A. Jensen, *Estimation of Blood Velocities Using Ultrasound: A Signal Processing Approach* (Cambridge University Press, New York, 1996), Chap. 2.
- ²²A. H. Pham, B. Stage, M. C. Hemmsen, B. Lundgren, M. M. Pedersen, T. B. Pedersen, and J. A. Jensen, "Simulation of ultrasound backscatter images from fish," *Proc. SPIE* **7961**, 796152 (1–10) (2011).
- ²³J. A. Jensen, "Field: A program for simulating ultrasound systems," *Med. Biol. Eng. Comput.* **34**, 351–353 (1996).
- ²⁴J. A. Jensen and N. B. Svendsen, "Calculation of pressure fields from arbitrarily shaped, apodized, and excited ultrasound transducers," *IEEE Trans. Ultrason. Ferroelectr. Freq. Control* **39**, 262–267 (1992).
- ²⁵T. A. Tuthilla, R. H. Sperry, and K. J. Parker, "Deviations from Rayleigh statistics in ultrasonic speckle," *Ultrason. Imaging* **10**, 81–89 (1988).
- ²⁶M. C. Hemmsen, S. I. Nikolov, M. M. Pedersen, M. J. Pihl, M. S. Enevoldsen, J. M. Hansen, and J. A. Jensen, "Implementation of a versatile research data acquisition system using a commercially available medical ultrasound scanner," *IEEE Trans. Ultrason. Ferroelectr. Freq. Control*, in press (2012).

A.2 Fish species discrimination using range profiles in the MHz frequency range

This article was submitted to *IEEE Journal of Oceanic Engineering* in September 2012.

Fish species discrimination using range profiles in the MHz frequency range

An Hoai Pham, Bo Lundgren, Bjarne Stage,
and Jørgen Arendt Jensen, *Life Fellow, IEEE*

Abstract

Range profiles from free-swimming fish in the low MHz frequency range have been measured. The results indicate that the surface areas (also fins and tail) of the fish can give echoes that are stronger than the swimbladder can give (up to 3 times), and therefore important for identification. This is different from the case in the frequency range well below 1 MHz where the swimbladder is often considered the most important part for acoustic fish detection. A portable system consisting of a Reson TC3210 1 MHz single-element transducer, a BlueView P900-2250 Dual Frequency sonar, and three Oregon ATC9K cameras on a fixture was developed to both detect and try to identify fish. The transducer is connected to an Olympus pulser-receiver monitored by a portable computer through a Picoscope 4226 PC oscilloscope. *Ex situ* experiments to measure the ultrasound backscatter from several fish species were performed at the North Sea Oceanarium in Hirtshals, Denmark. The positions, orientations, and lengths of the fish were estimated by three-dimensional image analysis, while species were identified manually from the video sequences.

Index Terms

underwater acoustics, small animal experiment, *ex situ* experiment.

A. H. Pham is with the National Institute of Aquatic Resources, Technical University of Denmark, Jægersborg Alle 1, DK-2920 Charlottenlund, Denmark, and the Center for Fast Ultrasound Imaging, Dept. of Elec.Eng. Build. 349, Technical University of Denmark, DK-2820 Kgs. Lyngby, Denmark. e-mail: haph@aqua.dtu.dk

B. Lundgren, and B. Stage are with the National Institute of Aquatic Resources, Technical University of Denmark, Jægersborg Alle 1, DK-2920 Charlottenlund, Denmark.

J. A. Jensen is with the Center for Fast Ultrasound Imaging, Dept. of Elec.Eng. Build. 349, Technical University of Denmark, DK-2820 Kgs. Lyngby, Denmark.

Manuscript received September, 2012; revised .

Fish species discrimination using range profiles in the MHz frequency range

I. INTRODUCTION

The purpose of this work is to develop a cost effective, reliable method for species discrimination as a continuation of the work from [1], [2]. For this purpose, a system was built to study the ultrasound backscatter in the 1 MHz frequency range from fish. This would be useful in resource management as well as in commercial fishing. Many groups have researched on similar topics with different approaches. In some experiments, the fish were immobilized, anesthetized and tied to a fixture as in [3]–[10]. The fixture could be rotated and the information about the orientation of the fish could be derived from the fixture orientation. Single element transducers were used to get the target strength from the fish for different orientations of the fish. In other experiments, a net was used to limit an area where fish swam free such as in [1], [2], [11]. In addition to the single element transducers, cameras were used in stereo configuration to estimate the orientation of the fish. Then the target strengths of the fish as a function of frequency were obtained for many different orientations of the fish. Drawbacks of these previous approaches were that the fixture or net interfered with the backscatter signals from the fish and that the net limited the mobility of the fish. Other groups have performed experiments on free swimming fish without a net to avoid this drawback as in [12]–[21]. All of those experiments followed the target strength approach and were performed in the frequency range well below 1 MHz except the work of [7]. Recently new approaches to use transducers in the MHz frequency range and wider bandwidths have been applied. Many groups have used multi-beam sonars, such as a dual frequency identification sonar (DIDSON) to identify fish species ([22]–[26]). The device gives a two dimensional ultrasound image for each ping and the orientation and the position of the fish can be derived from the images. The drawback of this approach is that the sonar only provides information on the amplitude, and not the phase of the backscattered signals from fish.

One possible approach to identify fish species is to build libraries of reference range profiles of fish as it is done in some radar systems used to identify aircraft as in [27]. A range profile is the amplitude and phase variation of the echo signal from fish. In order to get sufficient

resolution, the wavelength should be shorter than the dimensions of various parts of the fish. But short wavelength means high frequency and high absorption in water, which results in short measurement range. Therefore it has been found that a frequency about 1 MHz is a suitable compromise giving a wavelength of about 1.5 mm, and a useful range of about 10 m for fish of 20-100 cm length. In order to make a simple system it was decided to start with a single element transducer. The system was developed using the basic ideas from the work of [1], [2] but the experiments were performed on free-swimming fish in two aquaria. The content of this paper presents the setup of the system, the calibration of the system, and the acquisition and processing of the data.

II. MATERIALS AND METHODS

The objective of this work is to investigate if range profiles obtained with an ultrasound system with a 1 MHz single element transducer contain sufficient information to be used to identify fish. Three cameras are used in a stereo configuration to find the angle between a fish and the ultrasound beam as well as the spatial position in the beam to help interpretation of the ultrasound data. As a supplement a multi-beam sonar is used to also find the angle of the fish in the horizontal plane and the distance between the fish and the transducer to compare the pros and cons of the data from the single element transducer and the multi-beam sonar.

A. Basic theory

1) *Setup of the ultrasound system:* The range profile method assumes that a short sound pulse is transmitted from the single element transducer. The sound pulse propagates through the water, hits and insonifies a fish causing scattered sound in all directions. Some of the backscattered sound travels back and hits the transducer which converts it to a backscatter signal from the fish. The backscatter signal displayed as a function of time or distance and is called a range profile of the fish. To get a good range profile the whole fish should be insonified by the ultrasound beam. Resolution of the range profile depends on the target resolution of the ultrasound system. The target resolution is usually divided into two categories: range resolution and angular (bearing) resolution and is the ability to distinguish between two points that are very close in either range or bearing. The bearing is the direction of a target relative to the direction of the transducer beam.

In this work, the water volume insonified by the main lobe of the single element transducer is called the acoustic transducer beam. First, assume that the fish is swimming in the beam towards the transducer, i.e., the angle between the beam and the fish is zero degrees. Then the range resolution of the transducer determines whether the various parts of the fish, e.g., the head and the fin, can be distinguished in the range profile or not. It is thus an advantage if the range resolution is as small as possible. The range resolution S_r (m) is calculated according to [28]

$$S_r \approx \frac{v}{2B_{tx}} \quad (1)$$

where v is the speed of sound in the medium ($\text{m}\cdot\text{s}^{-1}$), and B_{tx} is the bandwidth of the transmitted pulse (Hz). The range resolution of the system using a frequency modulated transmitted pulse depends on the bandwidths of the transmitted pulse and the receiver. It is desirable to have a receiver bandwidth equal to B_{tx} to obtain the best range resolution. However, the center frequency f_c (Hz) should also be considered. Transducers are resonant systems and their bandwidths are proportional to their center frequencies. The bandwidth is typically somewhere between 0.2 to $0.5f_c$. A transducer with higher center frequency f_c can have wider bandwidth or better range resolution.

If the fish swims perpendicular to the acoustic transducer beam, the beam width determines whether the whole fish is insonified or not. The beam divergence angle θ is the angle measured from the center of the acoustic axis to the point where the sound pressure has decreased to half maximum (-6dB) to the side of the acoustic axis in the far field. For a circular transducer $\sin \theta$ is approximated as [29]

$$\sin \theta \approx 1.2 \frac{\lambda}{D} = 1.2 \frac{v}{Df_c} \approx \theta \quad (2)$$

where λ is the wave length (m), D is the diameter of the circular transducer (m), and θ is in radians. The angular resolution is the minimum angular separation at which two equal objects at the same range can be separated. The angular resolution as a distance between two target points S_a (m) at a certain distance from the transducer is calculated by [28]

$$S_a \approx 2R\theta \quad (3)$$

where R is the distance (m) from the center of the transducer to a target. Using Eq. 2, Eq. 3 can be rewritten

$$S_a \approx 2.4 \frac{R}{D} \frac{v}{f_c} \quad (4)$$

For a specific center frequency and medium, the angular resolution varies as a function of distance to the target as well as the diameter of the transducer. The minimum distance R_{min} , at which the whole fish is insonified by the acoustic transducer beam, is where the angular resolution equals the length of the fish. Thus, if the center frequency of the transducer is chosen, the diameter of the transducer is determined by the minimum distance, at which fish of a certain maximum length are to be investigated.

After the transducer has sent a pulse into the water, the ultrasound system waits for a period T (s) before sending out another pulse. During this period, echoes from objects in the ultrasound beam are received by the transducer. The maximum useable range R_{max} (m) of the system is then defined by [30]

$$R_{max} = \frac{vT}{2} = \frac{v}{2f_{PRF}} \quad (5)$$

where f_{PRF} is the pulse repetition frequency (Hz) of the ultrasound system. R_{max} depends almost only on the pulse repetition frequency f_{PRF} , because the velocity of sound v changes little in water.

2) *Setup of the cameras:* In addition to the single element transducer system, two or more of the cameras are used to estimate the distances between points on a fish and the transducer. These data are used to calculate the angles between parts of the fish and the acoustic transducer beam. The distances between the cameras should be chosen so that the overlap of the imaging volumes of the cameras contains the whole fish, when the largest fish is at the minimum expected distance from the transducer. Then the error level of the distance estimation is evaluated to make sure that the setup of the cameras is adequate for the experiments. Fig.1 is used as a common figure for different cases.

Assume that two cameras are used in a stereo configuration so that the center lines of the cameras and the single element transducer are parallel to each other as presented in Fig.1.

Distance HM to a fish at the position M is calculated by

$$HM = \frac{C1C2}{\frac{K1M1}{C1K1} + \frac{K2M2}{C2K2}} \quad (6)$$

where H is the center of the chosen single element transducer. The two cameras at $C1$ and $C2$ are identical, so $C1K1 = C2K2$, and Eq. 6 thus becomes

$$HM = C1C2 \frac{C1K1}{K1M1 + K2M2} = C1C2 \frac{C1K1}{KxMx} \quad (7)$$

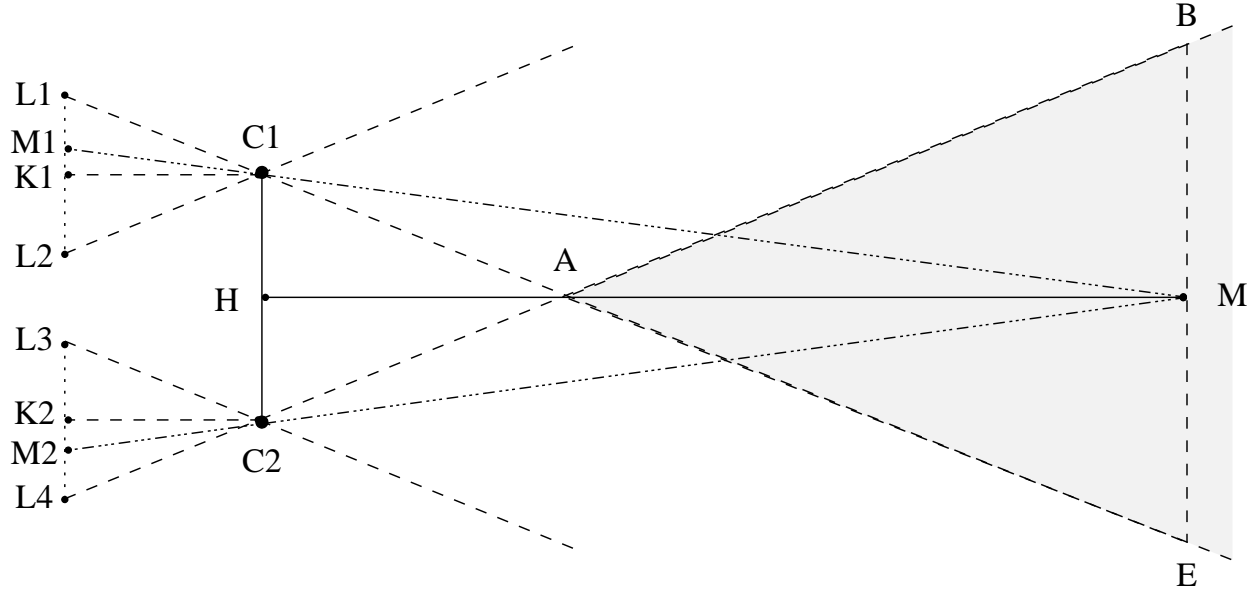


Fig. 1. Two cameras are used in a stereo configuration. $C1$ and $C2$ are the positions of the lenses of the cameras. $L1L2$ and $L3L4$ are the image planes of camera $C1$ and $C2$ respectively. A and M are object points in front of the cameras. H is the projection of M on $C1C2$, $K1$ and $K2$ are the projections of $C1$ and $C2$ on the image planes of the cameras. $M1$ and $M2$ are the image points of M on $L1L2$ and $L3L4$, respectively. The shaded area is the overlap of the two cameras. HM is the distance from the fish to $C1C2$. BE is the length of the fish in a specific experiment.

where

$$KxMx = K1M1 + K2M2 \quad (8)$$

If the fish has moved from one distance HM to another distance $HM + \partial HM$, the relation between ∂HM and the corresponding change in $KxMx$ in the image planes is calculated by

$$\partial HM = -C1C2 \frac{C1K1}{KxMx^2} \partial KxMx \quad (9)$$

Combining Eqs. (7) and (9) gives:

$$\partial HM = -HM^2 \frac{\partial KxMx}{C1C2 \times C1K1} \quad (10)$$

The distance error due to a 1 pixel combined image position error is thus

$$\delta_{e_{C1C2}} = \left| \frac{\partial HM}{\partial KxMx} \right| = \frac{HM^2}{C1C2 \times C1K1} \quad (11)$$

A large distance $C1C2$ and a small distance HM gives the best estimation of the distance. However, the requirement is $HM \geq R_{min}$ so that the whole fish is insonified by the acoustic transducer beam. R_{min} is calculated using Eqs. (3) or (4) where $S_a = BE$.

B. The setup of the system

The system was designed to be portable and can be used for *ex situ* as well as *in situ* experiments. The block diagram of the system is presented in Fig. 2. There are two main parts, the front-end and the back-end of the system. The front-end consists of a Reson TC3210 1 MHz single element transducer, a Blueview P900-2250 dual frequency sonar, and three Oregon ATC9K underwater cameras, all mounted on a fixture. The acoustic parts are connected by cables to the back-end, but the cameras operate independently. There is a battery and a secure digital (SD) card in each camera. The back-end consists of a Dell Latitude E4300 portable computer (PC), a Picoscope 4226 digital oscilloscope, an Olympus pulser-receiver 5077PR, a Proviever junction box that delivers power over Ethernet (POE) to the sonar, a 12V battery, and a power inverter (12 VDC to 220 VAC) to supply the pulser-receiver and junction box. The pulser-receiver is used to ping (send the transmit pulse to the transducer), receive and amplify echo signals from the Reson transducer. The received signals are digitized and transferred to the PC using the Picoscope. The Olympus pulser-receiver is grounded to the water with a thick copper cable to reduce the ground loop noise in the received signals from the Reson transducer. The junction box transfers the control signals from the PC to the sonar as well as the sonar data back to the PC. The PC runs on its own battery but the dotted line from the inverter to the PC indicates that power can be provided to the PC if necessary.

The configuration of the front-end of the system is presented in Fig. 3. Fish positions are defined in a coordinate system with an x -axis parallel to the line between cameras $C2$ and $C3$ and the xz -plane parallel to the figure plane. The center of the aperture of the single element transducer is used as the origin of the coordinate system. Positive z is away from the transducer and positive y is downwards. The multi-beam sonar is placed below the single element transducer with its beam plane parallel to the zx -plane. The single element transducer is directed so that the center line forms an angle α with the center line of the multi-beam sonar, because the center part of the sonar image is not well-defined. An advantage is that interfering signals from the sonar are reduced. The optical axis of camera $C1$ is directed as close as possible parallel to the transducer beam.

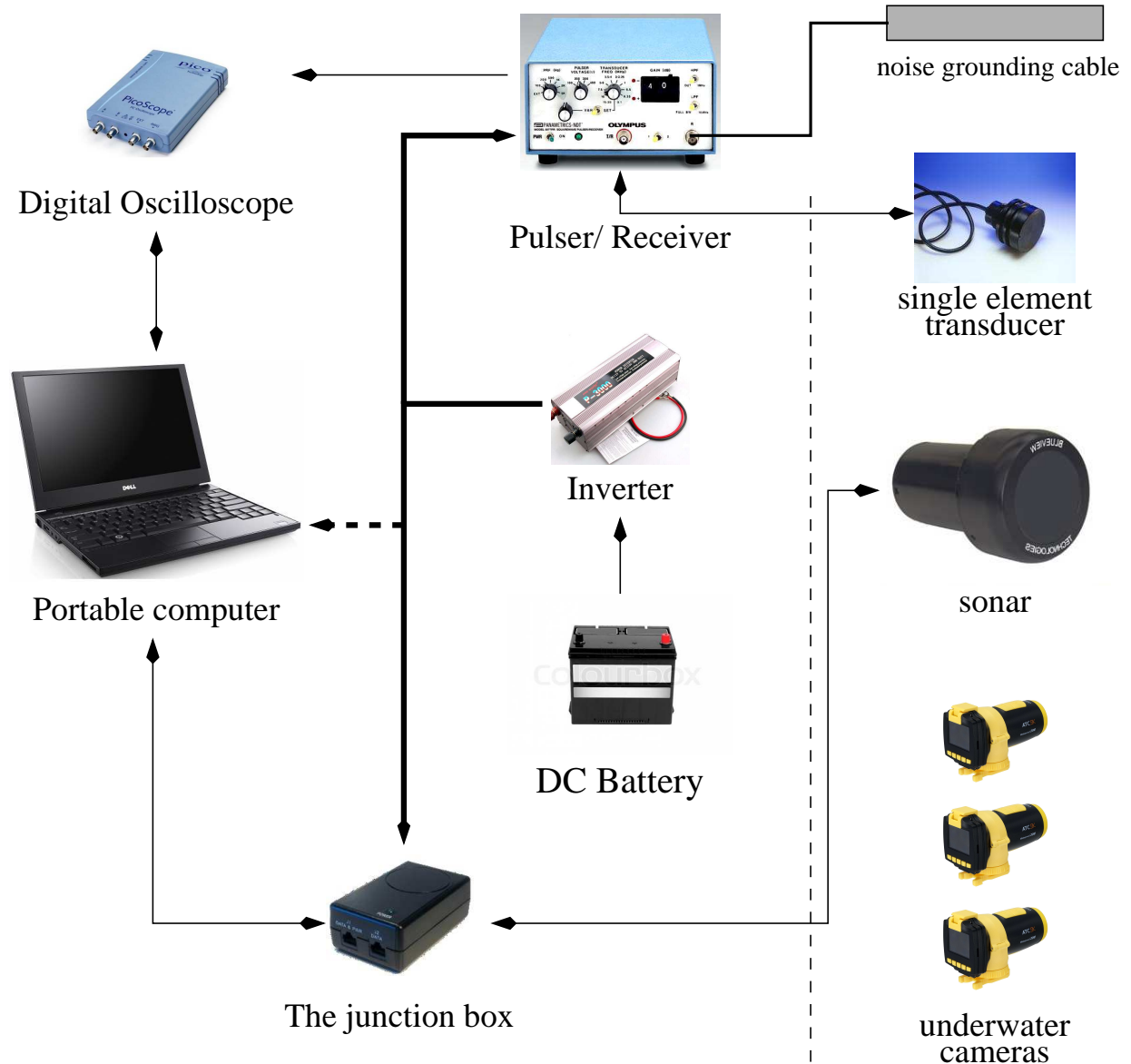


Fig. 2. (Color online) Block diagram of the system. The front-end of the system is on the left-hand side of the dotted line.

C. The parameters and procedure of the measurements

The parameters of the measurements are presented in Table I. The distances $C1C2$, $C1C3$, and $C2C3$ are measured between the centers of the cameras lenses.

The *ex situ* experiments were performed in one of the large fish storage aquaria at the North Sea Oceanarium in Hirtshals, Denmark. The procedures of each measurement are: time synchronization of the data, calibration of the cameras, establishing markers of the acoustic

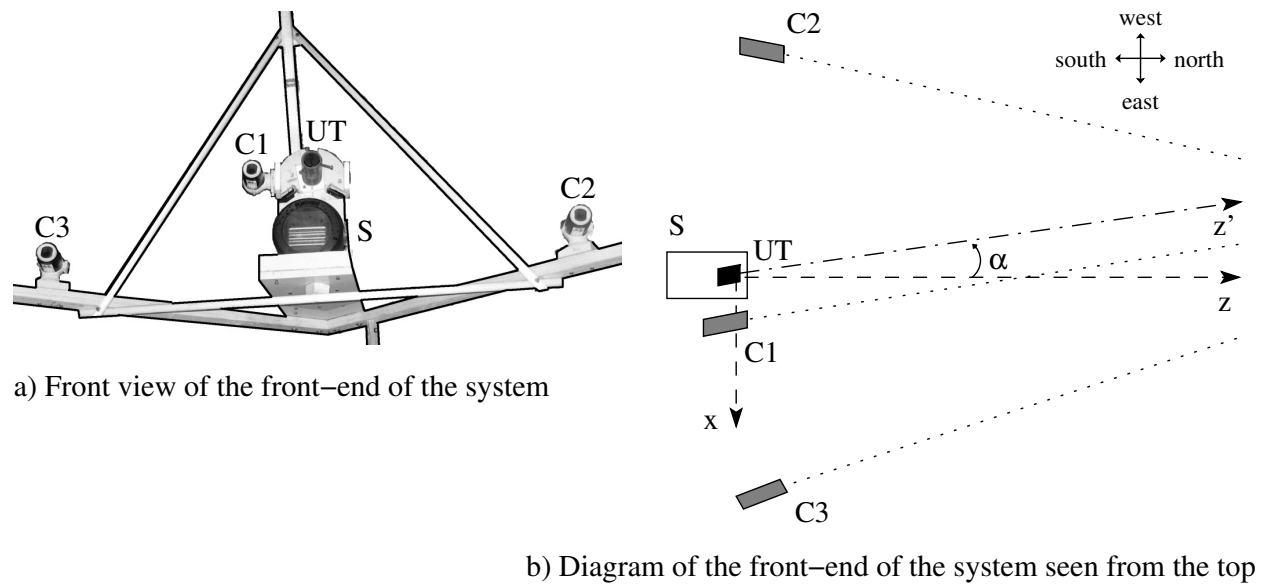


Fig. 3. Setup of the front-end of the system. $C1$, $C2$, and $C3$ are three identical cameras. UT is the single element transducer. S is the multibeam sonar. The angle between UT beam and the center beam of S is α .

transducer beam in the video data, and acquisition of ultrasound backscatter data from fish.

Time synchronization between the cameras and the instruments controlled by the PC was performed by displaying the PC system time on the screen with millisecond precision and recording videos of the screen after the cameras were started before each experiment, while the front-end of the system was still out of the water. If any of the cameras were turned off during the measurements, time synchronization was performed again. The front-end was moved into the water and the recording of the ultrasound data from the Reson transducer and the Blueview sonar was started.

Data for the calibration of the cameras was then obtained by moving a calibration plate with a matrix of dots in front of the cameras at a couple of different distances. The plate was rotated to get images from different angles at each distance. Data for the establishment of markers of the acoustic transducer beam in the video data was obtained using a 1 cm in diameter steel ball. It was positioned at different distances away from the Reson transducer in front of the cameras and moved until an echo signal of the steel ball appeared in the signal display of the Picoscope program. As an aid the position of the steel ball was monitored by the sonar. At each distance, the steel ball was then moved to find positions of maximum and minimum visible echo signals

TABLE I
PARAMETERS FOR THE MEASUREMENTS

Parameters	values
UT	
f_c (kHz)	1000
Bandwidth B_{tx}	$0.3 f_c$
Diameter D (cm)	2.54
f_{PRF} (Hz)	100
θ (degree)	4.5
R_{min} (m) ($BE = 0.30m, 0.35m, 0.5m$)	(1.91, 2.23, 3.18)
Range resolution S_r (mm) ($v = 1500ms^{-1}$)	2.5
f_s (MHz)	7.813
α (degree)	8.5
cameras	
Resolution (pixel \times pixel)	1280 \times 720
$C1K1$	1140
Factory Field of view (FOV) in air (degree)	120
Calibrated vertical FOV (degree)	35
Calibrated horizontal FOV (degree)	58
$C1C2$ (cm)	64.5
$C1C3$ (cm)	43.2
$C2C3$ (cm)	99
$\delta_{e_{C2C3}}$ (m \cdot pixel $^{-1}$) for ($HM = 1.91m, 5m$)	(0.003, 0.022)
$\delta_{e_{C1C2}}$ (m \cdot pixel $^{-1}$) for ($HM = 1.91m, 5m$)	(0.005, 0.034)
$\delta_{e_{C1C3}}$ (m \cdot pixel $^{-1}$) for ($HM = 1.91m, 5m$)	(0.007, 0.050)
Sonar	
Center frequency (kHz)	900
Number of beams	256
Beam width (degree)	1×20
Beam spacing (degree)	0.18
FOV (degree)	45×20
Range resolution (mm)	25.4

corresponding to the center and the limits of the acoustic transducer beam. Then the plate and the steel ball were removed.

To start the acquisition of the ultrasound backscatter from fish, the system was positioned one meter above the bottom to wait for the fish to pass by inside the acoustic transducer beam.

When that happened echo signals appeared on the Picoscope display. If the echo quality looked reasonable signal data was saved by manual activation.

D. Data processing

The video films from the three cameras were processed and displayed side by side, using a program called Video-reader, which was developed using the C++ programming language and the OpenCV library ([31]). The films could be stepped frame by frame either all together or separately. Synchronization of the camera data was performed using the PC timestamp images, by stepping individual films until the same PC-time was shown on all images. The clocks of the cameras could keep synchronization through a measurement of up to at least three hours. There is an option in the program to input parameters of a virtual calibration grid with known 3D shape, position and angular orientation in the previously defined fixture coordinate system and then calculate its position and shape on all the displayed images. The positions and shapes of the virtual grid images depend on the intrinsic and extrinsic camera parameters entered into the program. The video data of the calibration plate are then displayed. The intrinsic and extrinsic camera parameters, as well as the position and angular orientation of the calibration grid are then adjusted until all the virtual grid images match all the plate and dot matrix images for several plate positions and orientations. The process is iterative and when a reasonable match has been obtained the intrinsic and extrinsic parameters of the cameras have been found. Another option in the program is to display either a small virtual round object or virtual fish model at a given distance and direction (and orientation of the fish model). Circles marking the limits of the acoustic transducer beam at given distances are also displayed on images. The positions of those circles were obtained by processing the steel ball calibration data.

A measurement of ultrasound backscatter from fish is a set of ultrasound data from the Reson transducer and the sonar as well as video data from the cameras. The procedure to extract data from one measurement is: examine the ultrasound data from the Reson transducer to find echoes of objects, note the corresponding PC timestamp, use the Video-reader program to identify and display the corresponding video images to check that the echoes are from fish and that a whole fish is insonified by the acoustic transducer beam. The procedure to process a data set is: raw RF data were processed using an optimal bandpass filter to improve the signal to noise ratio, the analytic signals were calculated using the *hilbert()* function on the processed RF data (Signal

Processing Toolbox, Matlab), the envelopes of the RF signals were calculated by taking the absolute values of the analytic signals, the envelopes were normalized, log-compressed. The range profile map of the data set is the envelopes displayed as functions of distance and ping number. To study the variation of the acoustic backscatter from the fish as a function of time (and position in the transducer beam) the acoustic and video data are displayed ping by ping and image by image.

III. RESULTS

A total of five hours of data have been recorded in the *ex situ* experiments. Of these, three hours were processed and 131 measurements extracted comprising data from passes of 67 fish of five different species, both single fish and schools of fish. The fish species are cod (*Gadus morhua*), European sea bass (*Dicentrarchus labrax*), gilthead sea bream (*Sparus aurata*), Atlantic horse mackerel (*Trachurus trachurus*), and Atlantic mackerel (*Scomber scombrus*). The lengths of the fish are about 33 to 38 cm for the cods, 25 to 30 cm for the young sea basses, 50 cm for a mature sea bass, 34 to 39 cm for the sea breams, and 35 to 41 cm for the mackerel and horse mackerel. There were 82 measurements without sonar data and 49 measurements with sonar data. There are data from fish entering the acoustic transducer beam from the left as well as from the right. A few fish swam into the beam, then turned to swim along the beam direction, then again turned and swam out of the beam in the opposite direction. There are data from passes of single fish such as cod and mature sea bass, a pair of young sea basses, a school of four sea breams, and a school of mackerel and horse mackerel. Some examples of the measurements are discussed in the following paragraphs. To simplify descriptions in the following section, north means that the fish swims away from the transducer and south that the fish swims towards the transducer. Similarly east means that the fish swims from the left hand side to the right hand side of the transducer beam; west means the opposite direction.

Data from a measurement on two mackerels are presented in Fig. 4. They swam in a school that passed in front of the Reson transducer in the south east direction. The range profiles of the fish are presented in Fig. 4a. The range profiles present combined echoes from first heads of the fishes, then heads and bodies, whole fishes, bodies and tails and finally only tails. For example, the range profiles at ping numbers 25 to 34 contain echoes of the tail of the nearest of the two mackerels, and profiles at ping numbers 32 to 37 contain echoes of the tail of the

second mackerel. The longest profile is about 20 cm and appears when the whole fish is in the beam. This length is likely to be the distance between the head and tail of the fish along the transducer beam. The swimming direction of the fish was south-east as obtained from the video images. Fig. 4b presents range profiles of the two fish generated from the corresponding sonar images. Each range profile was generated by adding the intensity data from about 51 sonar beams in an angle range corresponding to the main lobe of the Reson transducer weighted by the angular sensitivity pattern of the beam. Fig. 4c, d and e present images from the cameras corresponding to a number of specific pings of the Reson transducer. The position of the acoustic transducer beam in the images is shown by circle marks at the minimum and maximum distances axis presented in Fig. 4a. The rectangular marks indicate distances in the center, at the top and bottom of the beam with an interval of 10 cm. Due to the position of the cameras the rectangle and the circle marks in Fig. 4c and e represent larger distances, when positioned more to the right hand side, while it is opposite in Fig. 4d. An echo from a fish appears only if the fish is within the marks of the acoustic transducer beam for all three cameras. An example is the images corresponding to ping number 1 in Fig. 4.

A measurement on a cod is presented in Fig. 5. From the video images presented in Fig. 5b, c, and d, it can be seen that at first the cod swam southwards along the center line of the Reson transducer, then turned eastwards, and finally swam out of the beam in the south-east direction. The range profiles corresponding to 42 continuous pings are presented in Fig. 5a. The lengths of the echo signals from the cod vary as the cod passes by. The maximum length of the echo signals is about 20 cm. From ping number 8 to 25, the echo signals from the body of the cod are higher than the other parts and with maximum amplitude at ping number 12 as shown in Fig. 6a. However, from ping number 31 to 35, the echo signals from the tail are much higher than from the other parts (up to 3 times in amplitude) as shown in Fig. 6b, c, and d for ping numbers 31, 32 and 33, respectively. It will be called the tail echo effect in this work. The direction of the body of the cod was the same in all three pings, only the direction of the tail was changed because the cod flicked its tail to swim.

Data from a measurement on 2 small sea basses and a cod are presented in Fig. 7. The sea basses swam in the north-east direction. A cod entered from the time corresponding to ping number 13, and swam in the north-west direction. The swimming direction of the cod in this data set is different from the one presented in Fig. 5. The differences will be discussed in the

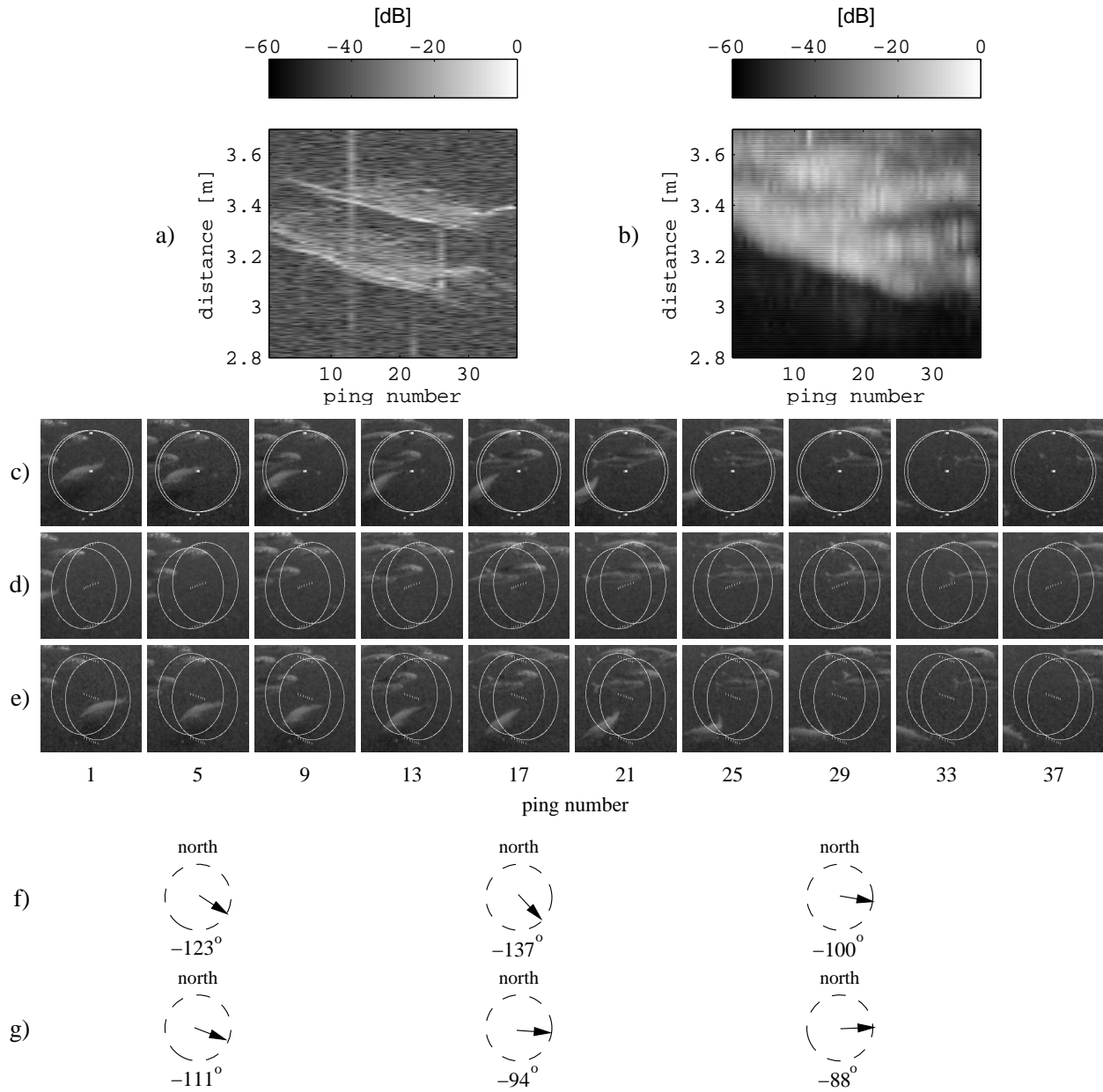


Fig. 4. (The best image quality is in the electronic version) A measurement on two mackerels in a school. Range profiles of the mackerels (a), range profiles generated from sonar images (b), images from the center camera $C1$ (c), from the left hand side camera $C2$ (d), and from the right hand side camera $C3$ (e). Orientation of the mackerel positioned at about 3.2 m in range for ping numbers 5, 17, and 29 (f). Orientation of the mackerel positioned at about 3.5 m in range for ping numbers 5, 17, and 29 (g).

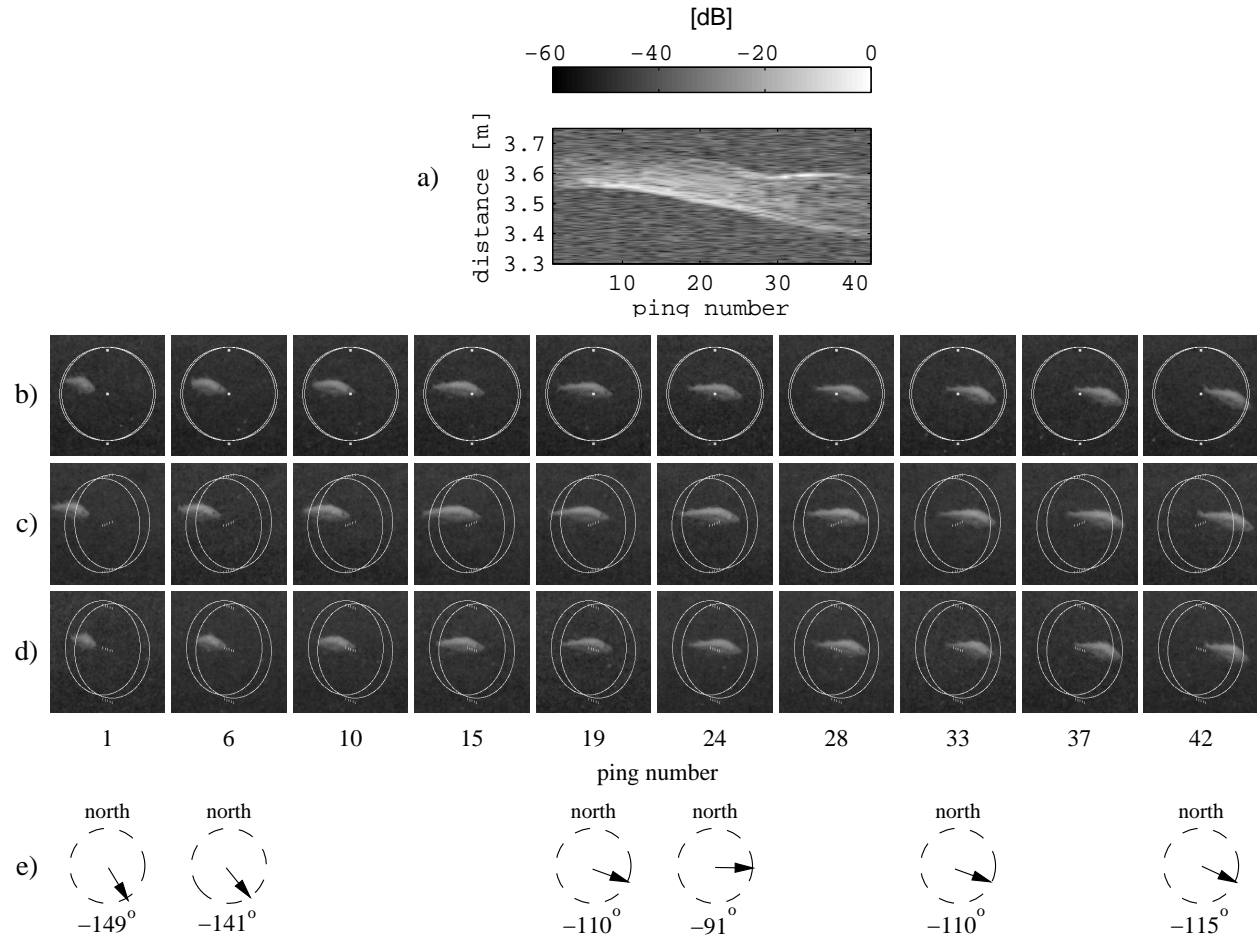


Fig. 5. A cod turned and swam from left to right. Range profiles of the cod (a), images from the center camera $C1$ (b), from the left hand side camera $C2$ (c), and from the right hand side camera $C3$ (d). Orientation of the cod for ping number 1, 6, 19, 24, 33, and 42 (e).

next section. The range profiles in Fig. 7b were generated from corresponding sonar images in the same way as those in Fig. 4b.

Data from two measurements on four sea breams are presented in Fig. 8 and Fig. 9. The fish swam in the south-east direction as shown in Fig. 8, whereas the movement patterns are more complicated in Fig. 9. At ping numbers 1 to 32 in Fig. 9a, the strong echo signals at the range from 3 m down to 2.7 m are echo signals from fish number 1, heading westwards. Echo signals at the range from 3.4 m down to 2.9 m are echo signals from fish number 2, heading southward, while slowly moving westward. From ping number 33 to number 51, fish number 1 was turning southwards, while moving westward; fish number 2 was also started turning westwards. From

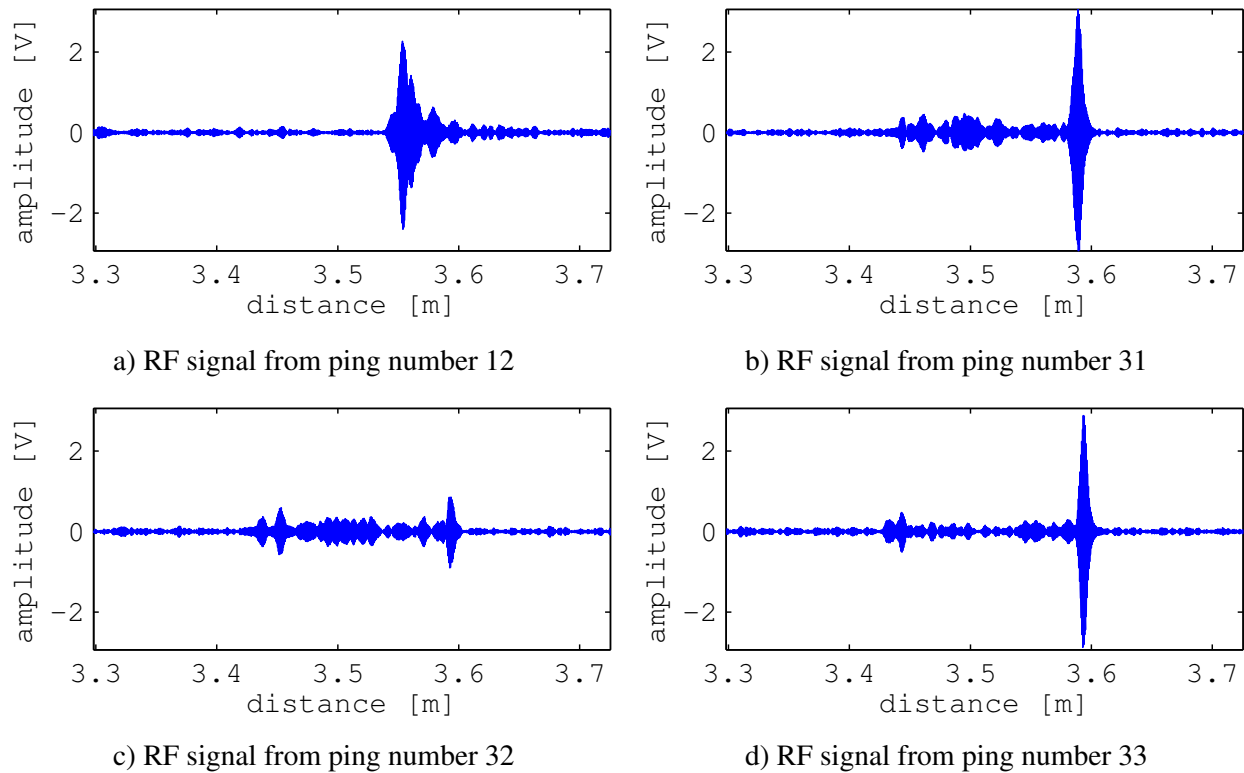


Fig. 6. RF data of some specific pings in the measurement on a cod in Fig. 5.

ping number 52 to 59, fish number 2 continued to turn and head westward, and then the echo signals from this fish disappeared, while fish number 1 turned to head in the south-east direction until echoes disappeared at ping 80. From ping number 65 to 90, fish number 3, at about 2.3 m in range headed in the south-east direction. From ping number 91, fish number 2, at about 2.1 m in range, turned back and headed in the south-east direction until ping number 120. From ping 100 until the last ping, fish number 4, at about 2.4 m in range, appeared and also turned to head in the south-east direction.

A measurement on a school of both mackerel and horse mackerel is presented in Fig. 10. From ping 30 at 2.4 m distance to the last ping 85 at 2 m distance, a horse mackerel headed in the south-west direction, first made a turn southwards, and then continued until it headed in the south-east direction and disappeared. From ping number 1 to 30, at 2.2 m in range, a horse mackerel heads westward. From ping number 20 to 33, at 2.4 to 2.6 m in range, a mackerel is headed in the south-west direction. At 2.6 m up to 3 m in range from ping number 20 to 48,

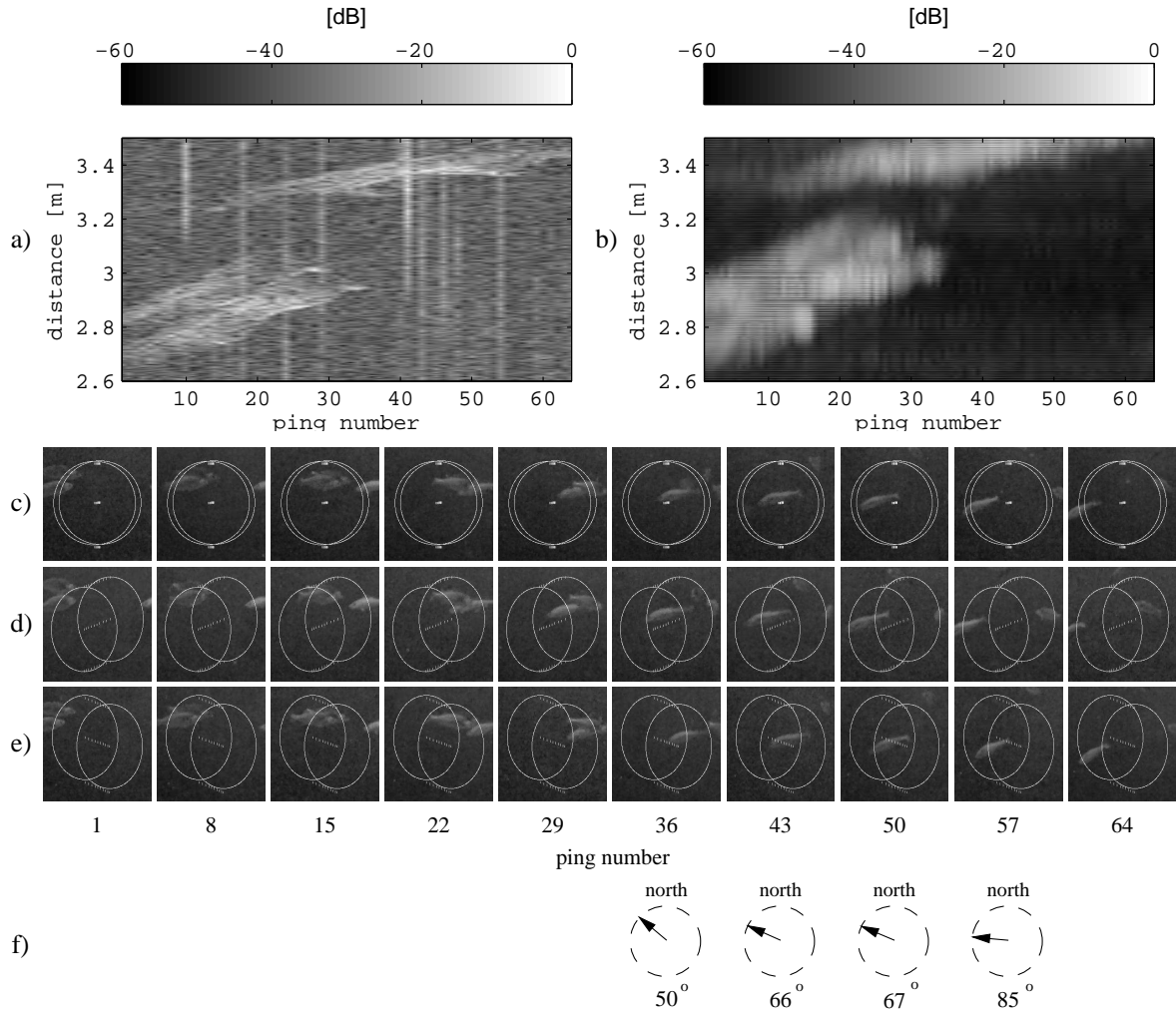


Fig. 7. Two young sea basses swam from left to right, then a cod swam from right to left. Range profiles of the fish (a), range profiles which are generated from sonar images (b), images from the center camera *C1* (c), from the left hand side camera *C2* (d), and from the right hand side camera *C3* (e). Orientation of the cod for ping number 36, 43, 50, and 57 (f).

there are a horse mackerel and a mackerel both heading westwards. The horse mackerel was closer to the Reson transducer than the mackerel at the time of ping 20. Then, from ping 33, when the signals from the mackerel disappeared, signals from another mackerel appeared. This can be interpreted with the support from the video data, not with only the range profiles. The new mackerel headed towards the Reson transducer, then turned to head westwards.

Another measurement on the school of mackerel and horse mackerel is presented in Fig. 11. The movements of the fish in this measurement are more complicated than in the previous

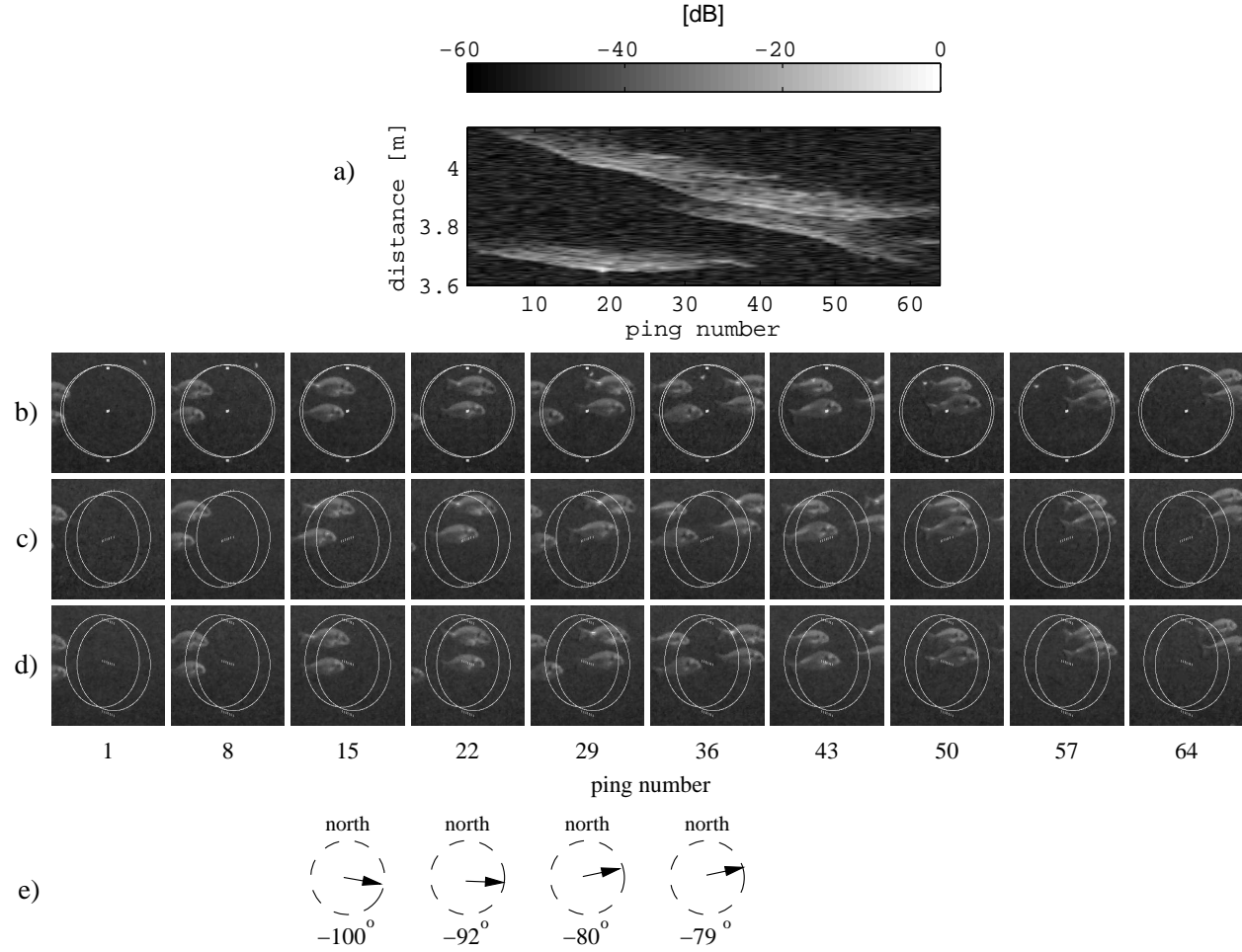


Fig. 8. Four sea breams swim from left to right. Range profiles of the fishes (a), images from the center camera $C1$ (b), from the left hand side camera $C2$ (c), and from the right hand side camera $C3$ (d). Orientation of the sea bream positioned at about 3.7 m in range for ping number 15, 22, 29, and 36 (e).

measurement. The fish swam close to each other and changed direction rapidly. Echoes from two mackerels at 3.8 m and 4 m in range from ping number 1 to 34 headed in the south-east direction begins the measurement.

IV. DISCUSSION

In the 10 to 200 kHz frequency range the swimbladder is often considered the most important part of a fish for acoustic fish detection, because reflections from this part is often higher than from other parts. It is more difficult to detect fish of a species without swimbladder because the reflections are significantly weaker ([32]–[34]). The work presented here indicates that

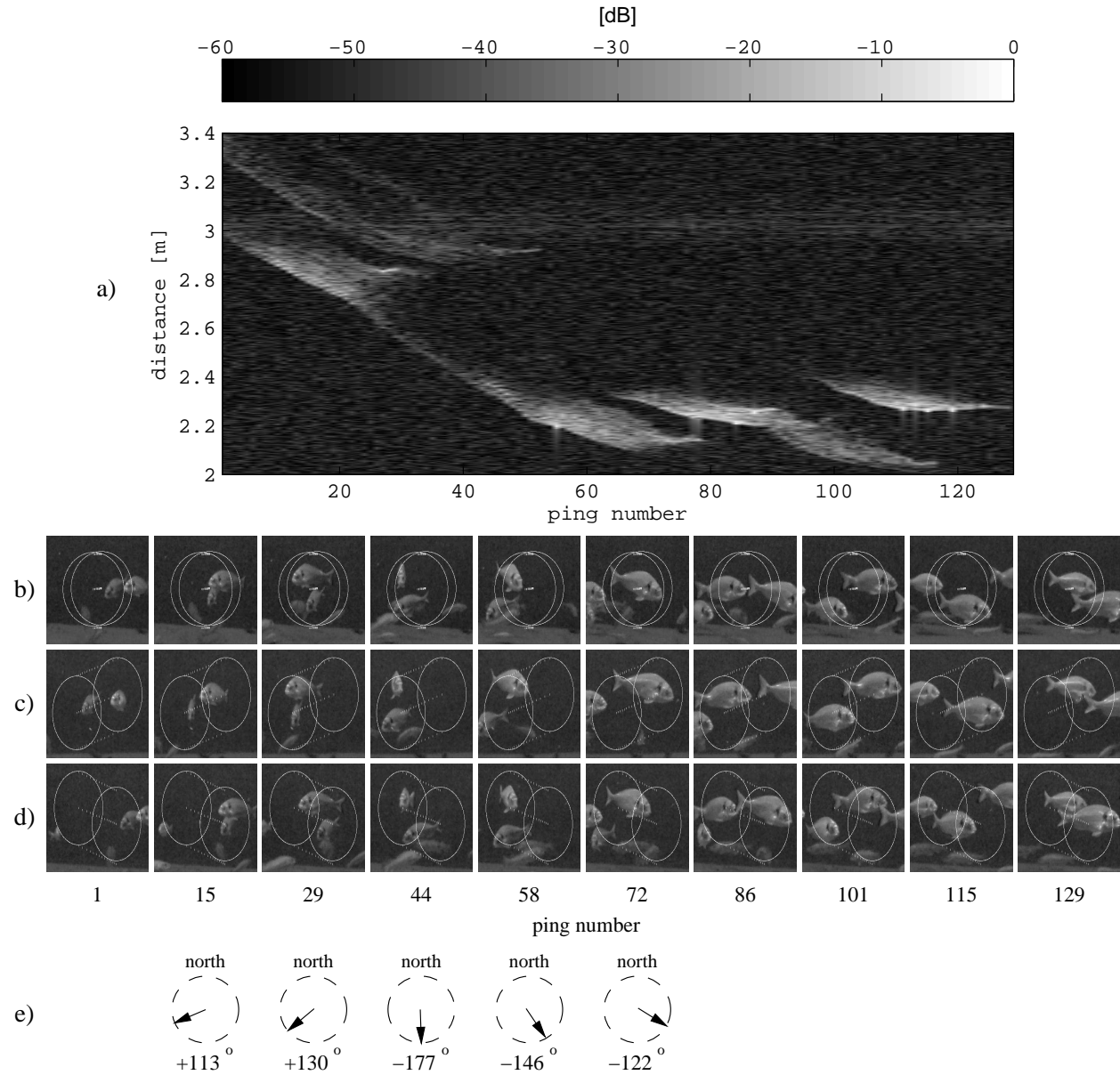


Fig. 9. Four sea breams that swam from right to left, turned, then swam left to right. Range profiles of the fishes (a), images from the center camera $C1$ (b), from the left hand side camera $C2$ (c), and from the right hand side camera $C3$ (d). Orientation of the sea bream turned and positioned at about 2.7 m to 2.2 m for ping number 15, 29, 44, 58, and 72 (e).

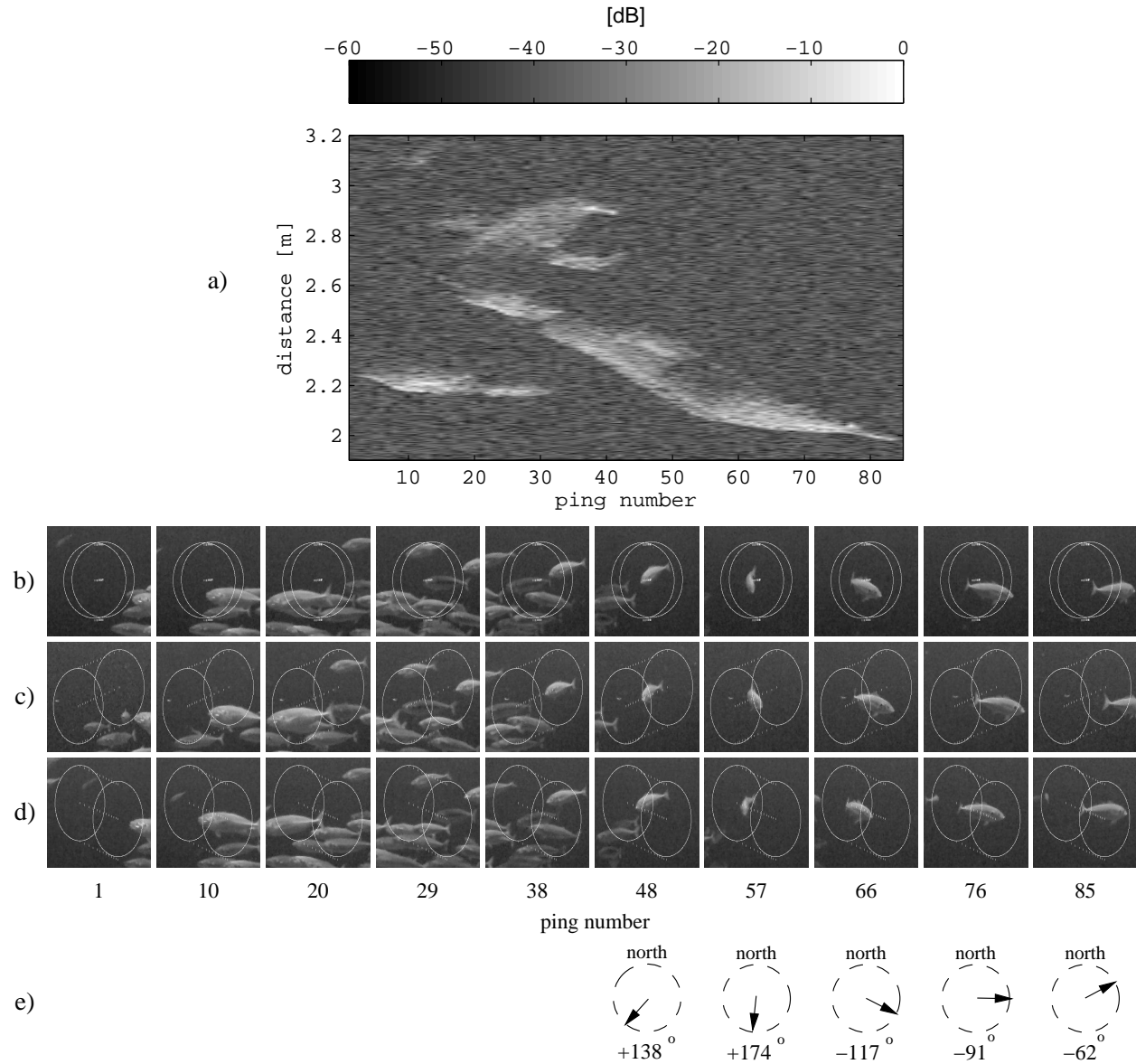


Fig. 10. A school of mackerel and horse mackerel with a horse mackerel turning and swimming from left to right. Range profiles of the fishes (a), images from the center camera $C1$ (b), from the left hand side camera $C2$ (c), and from the right hand side camera $C3$ (d). Orientation of the horse mackerel for ping number 48, 57, 66, 76, and 85 (e).

in the low MHz frequency range surfaces areas of the fish are more important reflectors than the swimbladder, at least from the side. An example is the measurement on the two mackerels presented in Fig. 4. Although mackerel have no swimbladder the echoes from them are as strong as those from the other fish species.

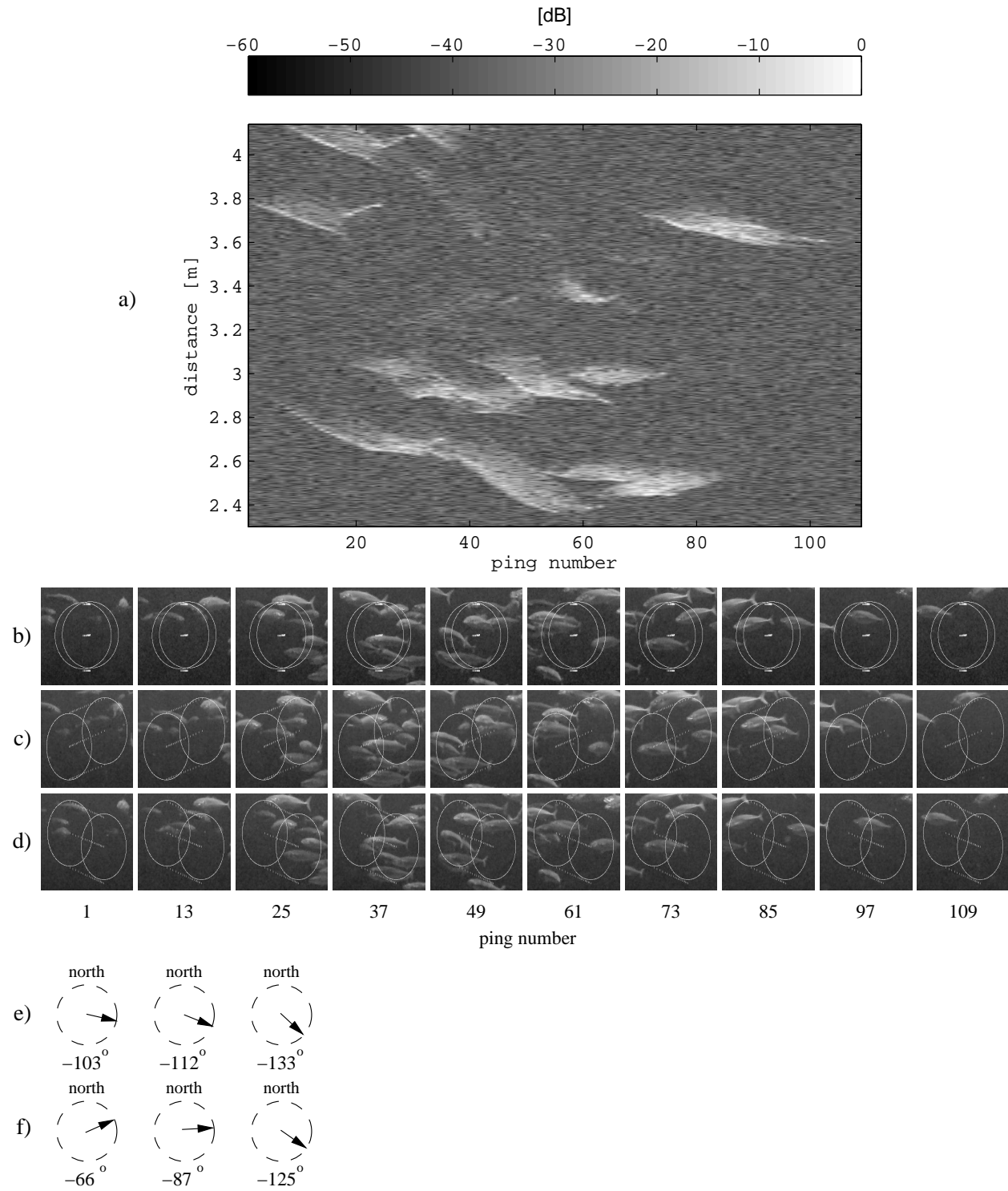


Fig. 11. A school of mackerel and horse mackerel with many complicated movement patterns. Range profiles of the fishes (a), images from the center camera $C1$ (b), from the left hand side camera $C2$ (c), and from the right hand side camera $C3$ (d). Orientation of the mackerel positioned at about 3.8 m in range for ping numbers 1, 13, and 25 (e). Orientation of the mackerel positioned at about 4 m in range for ping numbers 1, 13, and 25 (f).

When the fish moves changes in the shape of the surface of the fish, changes in direction the fish is heading and the tail flicking generate variations in the range profiles. A simple case to interpret the variations is presented in Fig. 5. The echoes from the tail of the cod can be as strong or stronger than those from the other parts of the body. Fig. 6a shows that the energy reflected from the body of the cod, including the swimbladder but not the tail, is high, because the body was more or less perpendicular to the transducer beam. The tail of the cod was still at an angle with the transducer beam, because the cod was turning to head eastward. When the cod had finished turning and headed straight east, the reflections from the tail were at some pings much stronger (up to 3 times) than from other parts of the fish. At ping numbers 31 to 38 the amplitudes of the echoes at about 3.6 m in range are very high and variable. At ping numbers 31 (Fig. 6b) and 33 (Fig. 6d), the tail was probably very close to perpendicular to the direction of the centerline of the transducer. When the cod flicked its tail the maximum amplitude of the echo signals decreased to one third of the previous value (compare ping number 32 (Fig. 6c) to ping numbers 31 and 33). The larger the proportion of the surface area that is close to perpendicular to the transducer beam, the more acoustic energy is backscattered.

If the fish is directed along the centerline of the beam, it is expected that the length of the echo would approximately be equal to the length of the fish. Because of the complex structure of the head part, only a small amount of sound energy is transmitted through to the other parts and only a small part is backscattered into the direction of the transducer. When the fish direction becomes closer to being perpendicular to the transducer beam, the more ultrasound energy is backscattered, and the longer the echo signals become up to a maximum at a certain angle and then probably decreasing again. The turning of the fish usually appears as a diffuse area in range profile map as in Fig. 9a, and Fig. 10a. It is not possible to estimate the speed and orientation of the fish only from single beam range profiles, but that could be done by using a split beam transducer. In this work, the speed and orientation of the fish is estimated using the video data for a range up to 5 m.

The results show that there are some features in the range profile maps that make it possible to discriminate between some fish species, if they pass by in front of the acoustic transducer beam in the same direction. For example, there is a clear difference between mackerel and sea bream headed in the south-east direction without turning in the beam as shown in Fig. 4a for mackerels, in Fig. 11a ping numbers 1 to 34 at the range of 3.8 m and 4 m for mackerels, and

in Fig. 8a for sea breams.

In Fig. 8a ping number 19, and Fig. 9a ping number 56, 77-90, 110-120, the amplitudes of the echo signals are so high that saturation occurs and they appear as bright spots in the range profile map. In the experiments, this phenomenon did not appear for species other than sea breams. The saturation occurs even when the sea breams are at a relatively large distance of 3.6 m as in Fig. 8a. This probably happens because the body of the sea bream is flatter (high ratio between the height and the width of the body).

The experiments indicate that the range profiles for a particular species are typical for that species and in some cases sufficiently different from those of other species to make identification possible. Three main parts of the fish that cause the range profiles to be different from species to species are the head, the body, and the tail. The range profiles of the fish heading in different directions are different. For instance, in Fig. 5a at ping numbers 31 to 40, the tail of the cod heading south-east can be seen at the range of 3.6 m, which is at a greater distance than the other parts of the fish, while in Fig. 7a at ping numbers 41 to 55, the tail of a cod heading north-west can be seen at the range of 3.4 m, which is at a smaller distance than the other parts. The smoothly curved feature in Fig. 5a at ping numbers 1 to 40 in the range of 3.55 m to 3.4 m and a similar feature in Fig. 7a at ping numbers 18 to 55 in the range of 3.3 m to 3.45 m probably correspond to the heads of the cods.

The range profiles presented in Fig. 4b and Fig. 7b appear similar to those in Fig. 4a and Fig. 7a, but are more blurry probably because the range resolution of the sonar is less fine than that of the Reson transducer. The bright stripes occur in Fig. 4a and Fig. 7a because some of the reverberations originating from the sonar are received by the Reson transducer.

V. CONCLUSIONS

In this work, it has been shown that a system consisting of cameras in stereo configuration, a single element transducer and a multibeam sonar is useful for an initial *ex situ* study of range profiles from free-swimming fish. The range profiles produced by the single element transducer consist of RF data with a high range resolution compared to the sonar data. Measurements performed on fish that have a swimbladder (cod, sea bass, gilthead sea bream, and horse mackerel) as well as on fish that do not have a swimbladder (mackerel) show that the variation with time of the fish range profiles in the low MHz frequency has recognizable features that is sufficiently

distinct to identify them as fish echoes. There are also indications that the variations in the range profiles seem to have some unique details to discriminate between different species like mackerel and sea bream. In some cases the range profiles also indicate whether the head or the tail is closest to the transducer. It has also been shown that the surface areas of the fish are the most important elements that decide how much energy is backscattered from the fish, while the swimbladder is less important.

To get closer to the goal of identifying fish directly by acoustic means, future experiments should be done with at least a split-beam transducer instead of a single-beam transducer. This would allow the possibility to determine, not only the speed of the fish along the beam, but also across the beam. It would probably also allow the use of more advanced processing of the acoustic signals to improve the angular resolution of the range profiles.

ACKNOWLEDGMENT

This work is sponsored by a grant from the Globalization project of the Technical University of Denmark. Special thanks to the North Sea Oceanarium in Hirtshals, Denmark for providing the work place and fish samples for the experiments.

REFERENCES

- [1] B. Lundgren and J. R. Nielsen, "A method for the possible species discrimination of juvenile gadoids by broad-bandwidth backscattering spectra vs. angle of incidence," *ICES Journal of Marine Science*, vol. 65(4), pp. 581–593, 2008.
- [2] —, "Hydroacoustic ex situ target strength measurements on juvenile cod (*gadus morhua* L.)," *ICES Journal of Marine Science*, vol. 56, pp. 627–639, 1999.
- [3] W. W. L. Au, J. K. Horne, and C. Jones, "Basis of acoustic discrimination of chinook salmon from other salmons by echolocating orcinus orca," *J. Acoust. Soc. Am.*, vol. 128(4), pp. 2225–2232, 2010.
- [4] W. W. L. Au and K. J. Benoit-Bird, "Acoustic backscattering by hawaiian lutjanid snappers. ii. broadband temporal and spectral structure," *J. Acoust. Soc. Am.*, vol. 114(5), pp. 2767–2774, 2003.
- [5] W. W. L. Au, B. K. Branstetter, K. J. Benoit-Bird, and R. A. Kastelein, "Acoustic basis for fish prey discrimination by echolocating dolphins and porpoises," *J. Acoust. Soc. Am.*, vol. 126(1), pp. 460–467, 2009.
- [6] K. Huang and C. S. Clay, "Backscattering cross sections of live fish: Pdf and aspect," *J. Acoust. Soc. Am.*, vol. 67(3), pp. 795–802, 1980.
- [7] J. S. Jaffe and P. L. D. Roberts, "Estimating fish orientation from broadband, limited-angle, multiview, acoustic reflections," *J. Acoust. Soc. Am.*, vol. 129(2), pp. 670–680, 2011.
- [8] D. B. Reeder, J. M. Jech, and T. K. Stanton, "Broadband acoustic backscatter and high-resolution morphology of fish: Measurement and modeling," *J. Acoust. Soc. Am.*, vol. 116(2), pp. 747–761, 2004.

- [9] P. L. D. Roberts, J. S. Jaffe, and M. M. Trivedi, "Multiview, broadband acoustic classification of marine fish: A machine learning framework and comparative analysis," *IEEE Journal of Oceanic Engineering*, vol. 36, no. 1, pp. 90–104, 2011.
- [10] Y. Sun, R. Nash, and C. S. Clay, "Acoustic measurements of the anatomy of fish at 220 khz," *J. Acoust. Soc. Am.*, vol. 78(5), pp. 1772–1776, 1985.
- [11] O. Sand and A. D. Hawkins, "Acoustic properties of the cod swimbladder," *Journal of experiment biology*, vol. 58(3), pp. 797–820, 1972.
- [12] K. J. Benoit-Bird, W. W. L. Au, C. D. Kelly, and C. Taylor, "Acoustic backscattering by deepwater fish measured in situ from a manned submersible," *Deep-Sea Research Part I-Oceanographic research papers*, vol. 50(2), pp. 221–229, 2003.
- [13] A. Bertrand, E. Josse, and J. Masse, "In situ acoustic target-strength measurement of bigeye (thunnus obesus) and yellowfin tuna (thunnus albacares) by coupling split-beam echosounder observations and sonic tracking," *ICES Journal of Marine Science*, vol. 56, pp. 51–60, 1999.
- [14] R. Jorgensen and K. Olsen, "Acoustic target strength of capelin measured by single-target tracking in a controlled cage experiment," *ICES Journal of Marine Science*, vol. 59, pp. 1081–1085, 2002.
- [15] R. J. Korneliussen, "The acoustic identification of atlantic mackerel," *ICES Journal of Marine Science*, vol. 67, pp. 1749–1758, 2010.
- [16] J. Lilja, T. J. Marjomaki, J. Jurvelius, T. Rossi, and E. Heikkola, "Simulation and experimental measurement of side-aspect target strength of atlantic salmon (salmo salar) at high frequency," *Can. J. Fish. Aquat. Sci.*, vol. 61, pp. 2227–2236, 2004.
- [17] H.-J. Lu, M. Kang, H.-H. Huang, C.-C. Lai, and L.-J. Wu, "Ex situ and in situ measurements of juvenile yellowfin tuna thunnus albacares target strength," *Fish Sci.*, vol. 77, pp. 903–913, 2011.
- [18] K. Sawada, H. Takahashi, K. Abe, T. Ichii, K. Watanabe, and Y. Takao, "Target-strength, length, and tilt-angle measurements of pacific saury (cololabis saira) and japanese anchovy (engraulis japonicus) using an acoustic-optical system," *ICES Journal of Marine Science*, vol. 66, pp. 1212–1218, 2009.
- [19] E. J. Simmonds, F. Armstrong, and P. J. Copland, "Species identification using wideband backscatter with neural network and discriminant analysis," *ICES Journal of Marine Science*, vol. 53, pp. 189–195, 1996.
- [20] T. K. Stanton, D. Chu, J. M. Jech, and J. D. Irish, "New broadband methods for resonance classification and high-resolution imagery of fish with swimbladders using a modified commercial broadband echosounder," *ICES Journal of Marine Science*, vol. 67, pp. 365–378, 2010.
- [21] M. V. Trevorrow and Y. Tanaka, "Acoustic and in situ measurements of freshwater amphipods (jesogammarus annandalei) in lake biwa, japan," *Limnology and Oceanography*, vol. 42(1), pp. 121–132, 1997.
- [22] E. Belcher, W. Hanot, and J. Burch, "Dual-frequency identification sonar (didson)," in *Proceedings of the 2002 International Symposium on Underwater technology*, 2002, pp. 187–192.
- [23] F. Gerlotto, M. Soria, and P. Freon, "From two dimensions to three: the use of multibeam sonar for a new approach in fisheries acoustics," *Can. J. Fish. Aquat. Sci.*, vol. 56, pp. 6–12, 1999.
- [24] M. C. Langkau, H. Balk, M. B. Schmidt, and J. Borcharding, "Can acoustic shadows identify fish species? a novel application of imaging sonar data," *Fisheries Management and Ecology*, pp. 1–10, 2012.
- [25] S. L. Maxwell and N. E. Gove, "Assessing a dual-frequency identification sonars' fish-counting accuracy, precision, and turbid river range capability," *J. Acoust. Soc. Am.*, vol. 122(6), pp. 3364–3377, 2007.
- [26] R. A. Moursund, T. J. Carlson, and R. D. Peters, "A fisheries application of a dual-frequency identification sonar acoustic camera," *ICES Journal of Marine Science*, vol. 60, pp. 678–683, 2003.

- [27] S. P. Jacobs and J. A. O'Sullivan, "Automatic target recognition using sequences of high resolution radar range-profiles," *IEEE Transactions on Aerospace and Electronic Systems*, vol. 36(2), pp. 364–381, 2000.
- [28] M. A. Richards, *Fundamentals of Radar Signal Processing*. McGraw-Hill, New York, 2005.
- [29] W. R. Hendee and E. R. Ritenour, *Medical imaging physics*. Wiley-Liss, Inc., New York, 2002.
- [30] P. Lacomme, J.-P. Hardange, J.-C. Marchais, and E. Normant, *Air and spaceborne radar systems: An introduction*. William Andrew Publishing, Norwich, United States of America, 2001.
- [31] G. Bradski and A. Kaehler, *Learning OpenCV*. O'Reilly Media Inc., 2008.
- [32] C. S. Clay and J. K. Horne, "Acoustic models of fish: The atlantic cod (*gadus morhua*)," *J. Acoust. Soc. Am.*, vol. 96(3), pp. 1661–1668, 1994.
- [33] K. G. Foote, "Importance of the swimbladder in acoustic scattering by fish: A comparison of gadoid and mackerel target strengths," *J. Acoust. Soc. Am.*, vol. 67(6), pp. 2084–2089, 1980.
- [34] —, "Rather-high-frequency sound scattering by swimbladdered fish," *J. Acoust. Soc. Am.*, vol. 78(2), pp. 688–700, 1985.

LIST OF TABLES

I	Parameters for the measurements	9
---	---	---

LIST OF FIGURES

1	Two cameras are used in a stereo configuration. $C1$ and $C2$ are the positions of the lenses of the cameras. $L1L2$ and $L3L4$ are the image planes of camera $C1$ and $C2$ respectively. A and M are object points in front of the cameras. H is the projection of M on $C1C2$, $K1$ and $K2$ are the projections of $C1$ and $C2$ on the image planes of the cameras. $M1$ and $M2$ are the image points of M on $L1L2$ and $L3L4$, respectively. The shaded area is the overlap of the two cameras. HM is the distance from the fish to $C1C2$. BE is the length of the fish in a specific experiment.	5
2	(Color online) Block diagram of the system. The front-end of the system is on the left-hand side of the dotted line.	7
3	Setup of the front-end of the system. $C1$, $C2$, and $C3$ are three identical cameras. UT is the single element transducer. S is the multibeam sonar. The angle between UT beam and the center beam of S is α	8

4	(The best image quality is in the electronic version) A measurement on two mackerels in a school. Range profiles of the mackerels (a), range profiles generated from sonar images (b), images from the center camera <i>C1</i> (c), from the left hand side camera <i>C2</i> (d), and from the right hand side camera <i>C3</i> (e). Orientation of the mackerel positioned at about 3.2 m in range for ping numbers 5, 17, and 29 (f). Orientation of the mackerel positioned at about 3.5 m in range for ping numbers 5, 17, and 29 (g).	13
5	A cod turned and swam from left to right. Range profiles of the cod (a), images from the center camera <i>C1</i> (b), from the left hand side camera <i>C2</i> (c), and from the right hand side camera <i>C3</i> (d). Orientation of the cod for ping number 1, 6, 19, 24, 33, and 42 (e).	14
6	RF data of some specific pings in the measurement on a cod in Fig. 5.	15
7	Two young sea basses swam from left to right, then a cod swam from right to left. Range profiles of the fish (a), range profiles which are generated from sonar images (b), images from the center camera <i>C1</i> (c), from the left hand side camera <i>C2</i> (d), and from the right hand side camera <i>C3</i> (e). Orientation of the cod for ping number 36, 43, 50, and 57 (f).	16
8	Four sea breams swam from left to right. Range profiles of the fishes (a), images from the center camera <i>C1</i> (b), from the left hand side camera <i>C2</i> (c), and from the right hand side camera <i>C3</i> (d). Orientation of the sea bream positioned at about 3.7 m in range for ping number 15, 22, 29, and 36 (e).	17
9	Four sea breams that swam from right to left, turned, then swam left to right. Range profiles of the fishes (a), images from the center camera <i>C1</i> (b), from the left hand side camera <i>C2</i> (c), and from the right hand side camera <i>C3</i> (d). Orientation of the sea bream turned and positioned at about 2.7 m to 2.2 m for ping number 15, 29, 44, 58, and 72 (e).	18
10	A school of mackerel and horse mackerel with a horse mackerel turning and swimming from left to right. Range profiles of the fishes (a), images from the center camera <i>C1</i> (b), from the left hand side camera <i>C2</i> (c), and from the right hand side camera <i>C3</i> (d). Orientation of the horse mackerel for ping number 48, 57, 66, 76, and 85 (e).	19

- 11 A school of mackerel and horse mackerel with many complicated movement patterns. Range profiles of the fishes (a), images from the center camera $C1$ (b), from the left hand side camera $C2$ (c), and from the right hand side camera $C3$ (d). Orientation of the mackerel positioned at about 3.8 m in range for ping numbers 1, 13, and 25 (e). Orientation of the mackerel positioned at about 4 m in range for ping numbers 1, 13, and 25 (f). 20

Articles in Conference Proceedings

B.1 Simulation of ultrasound backscatter images from fish

This paper was presented at the conference *SPIE - Medical imaging* in america and published in *Proceedings of SPIE*, 2011, 7961-796152(1-10).

Simulation of ultrasound backscatter images from fish

An Hoai Pham ^{a,b}, Bjarne Stage ^a, Martin Christian Hemmsen ^{b,d}, Bo Lundgren ^a, Mads Møller Pedersen ^{b,c}, Tina Bock Pedersen ^c and Jørgen Arendt Jensen ^b.

^a National Institute of Aquatic Resources, Technical University of Denmark,
Jægersborg Allé 1, 2920 Charlottenlund, Denmark;

^b Center for Fast Ultrasound Imaging, Dept. of Elec. Eng. Build. 349, Technical University of
Denmark, DK-2800 Kgs. Lyngby, Denmark;

^c Department of Radiology, Section of Ultrasound, Rigshospitalet, Copenhagen, Denmark;

^d BK Medical, Mileparken 34, DK-2730 Herlev, Denmark

ABSTRACT

The objective of this work is to investigate ultrasound (US) backscatter in the MHz range from fish to develop a realistic and reliable simulation model. The long term objective of the work is to develop the needed signal processing for fish species differentiation using US. In *in-vitro* experiments, a cod (*Gadus morhua*) was scanned with both a BK Medical ProFocus 2202 ultrasound scanner and a Toshiba Aquilion ONE computed tomography (CT) scanner. The US images of the fish were compared with US images created using the ultrasound simulation program Field II. The center frequency of the transducer is 10 MHz and the Full Width at Half Maximum (FWHM) at the focus point is 0.54 mm in the lateral direction. The transducer model in Field II was calibrated using a wire phantom to validate the simulated point spread function. The inputs to the simulation were the CT image data of the fish converted to simulated scatter maps. The positions of the point scatterers were assumed to be uniformly distributed. The scatter amplitudes were generated with a new method based on the segmented CT data in Hounsfield Units and backscatter data for the different types of tissues from the literature. The simulated US images reproduce most of the important characteristics of the measured US image.

Keywords: ultrasound, simulation, acoustical properties, small animal experiment, CT

1. INTRODUCTION

The management of fisheries of commercially important pelagic fish stocks relies on abundance estimates provided by data from scientific surveys.¹ Abundance estimates of pelagic fish species are commonly obtained by acoustic survey techniques.² During an acoustic survey of a sea area the acoustic energy scattered from layers in the pelagic volume is measured accurately along transects. A mean target strength for the fish population is obtained for each of a number of subareas by using knowledge about the size and species distribution and expected target strengths of the fish present. The total energy scattered from fish in the subarea is estimated from the measurements divided by the mean target strength then gives the fish population size in the subarea. Each species is then allocated a portion again based on the species and size distributions. Knowledge about the species present and their size distributions is obtained by physically sampling the pelagic volume using methods such as trawling. Trawling is a costly, time-consuming, and under certain circumstances imprecise method for acquiring knowledge about local species and size composition. An alternative could be an acoustic method for in-situ identification of fish species and estimation of size distribution.

Acoustic surveys are traditionally conducted with hull mounted transducers. As the acoustic attenuation increases with frequency, the highest usable frequency is determined by the water depth. Typical frequencies used for acoustic surveys are in the range 18-200 kHz. Some success has been achieved in identification of fish species using a multiple frequency approach in the kHz range,³ and the method is currently utilized as a supplement to physical sampling. Further improvement in identification accuracy is expected when using high frequency, wide band acoustics. Due to the limited range of high frequency acoustics, such transducers must be mounted on remotely operated vehicles or towed bodies in order to bring the transducer in the vicinity of the fish for measurement. Experimental determination of the target strength of fish is an elaborate procedure,⁴ as the target strength must be measured for each species, with individuals of different size, with multiple frequencies and many different angles of incidence. The experimental procedure can be supplemented by modeling of the acoustic scattering from fish. Not only can modeling confirm and extend the experimental results, but it can also provide valuable insight into which parts of the fish dominate the scattering process. In the kHz range, the acoustic

wavelength is typically much larger than the fish, and traditional low frequency scattering models have been employed.⁵ In the MHz region of frequencies the wavelength becomes much smaller than the fish and other modeling approaches must be taken. Medical ultrasound utilizes acoustics in the MHz range, so it seems natural to utilize the modeling methods employed in this field.^{6,7}

The subject of this paper is modeling of acoustic backscattering from fish in the MHz region. The modeling is verified by comparison with experimentally measured backscattering from fish samples.

2. OVERVIEW OF THE METHOD

The experiments in this work were performed *in-vitro* using a cod (*Gadus morhua*), which was scanned with both an ultrasound scanner and a CT scanner. The cod was not alive in this experiment, and the time difference between the two measurements was 3 hours. The block diagram of the experiment is presented in Fig.1. The degree of resemblance between measured and simulated US images was determined by visual inspection. The procedure of the experiment is illustrated in the figure. It consists of the following steps: preparation of fish sample and adjustment of instrument parameters; acquisition of ultrasound (US) and CT data; and finally simulation of US images based on the CT data. The following sections will describe the procedure in detail.

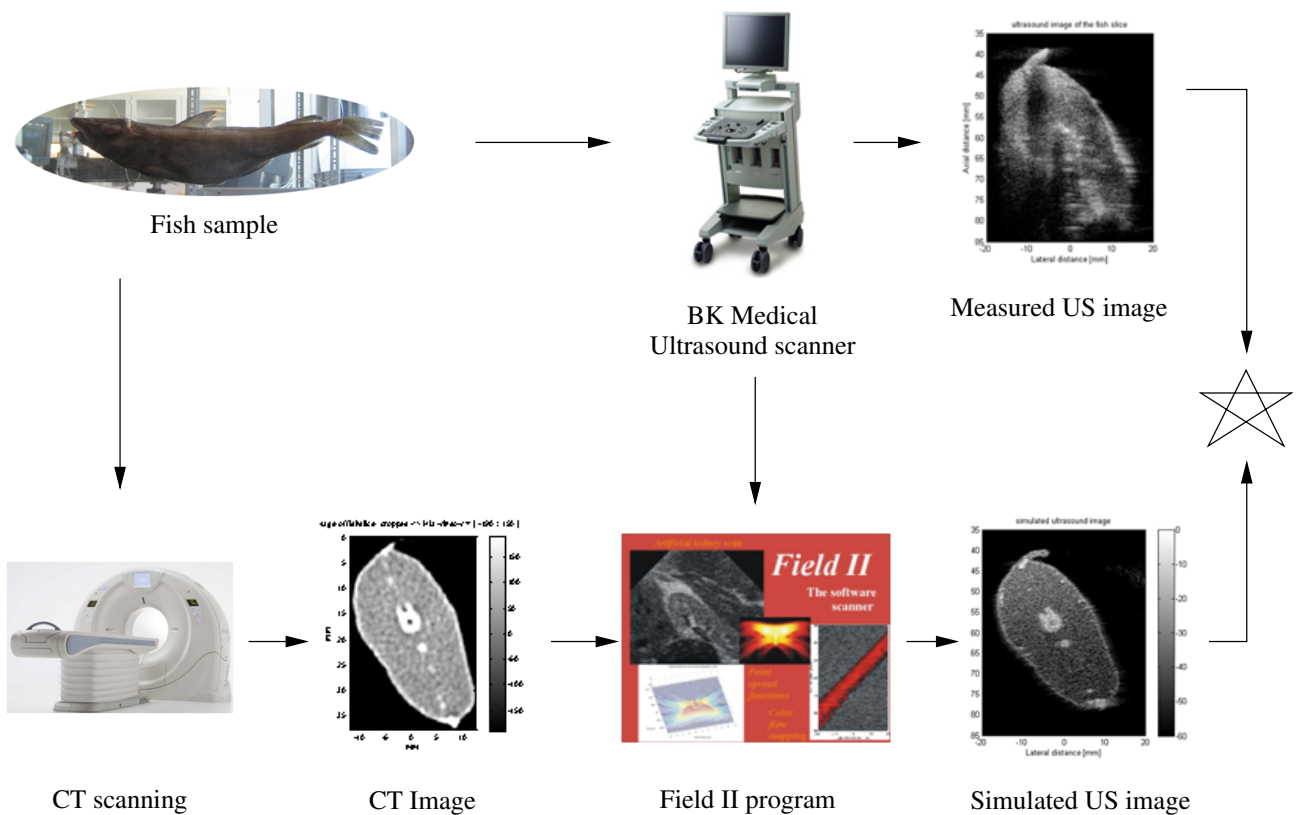


Figure 1. Block diagram of the *in-vitro* experiment.

3. EXPERIMENT

The cod was suspended in a fixture by fishing lines during the US scan as well as the CT scan. In addition, the fish and the fixture were encased in a box during the CT scan to avoid contamination of the hospital environment where the CT scanner used was localized. One of the challenges of this experiment was to choose the material for the fixture and the box to avoid noise and artifacts in the CT images of the fish. Based on the literature, Polyvinyl chloride (PVC) was chosen as a suitable material for fixtures as well as boxes. A pilot CT experiment using a banana instead of a fish was performed

before the actual experiment to test fixture and box and to adjust the parameters of the CT scanner. The banana was chosen as test specimen as its x-ray properties resemble the soft tissue parts of fish. The result shown in Fig. 2 indicated that the influence of the PVC fixture and box on the CT images of the banana was negligible. An additional CT scan was made using the same setup but with the addition of one liter of water in the box. The addition of water reduced the contrast and added noise to the images. Based on this result it was decided to perform the CT scan of the cod without water in the box.

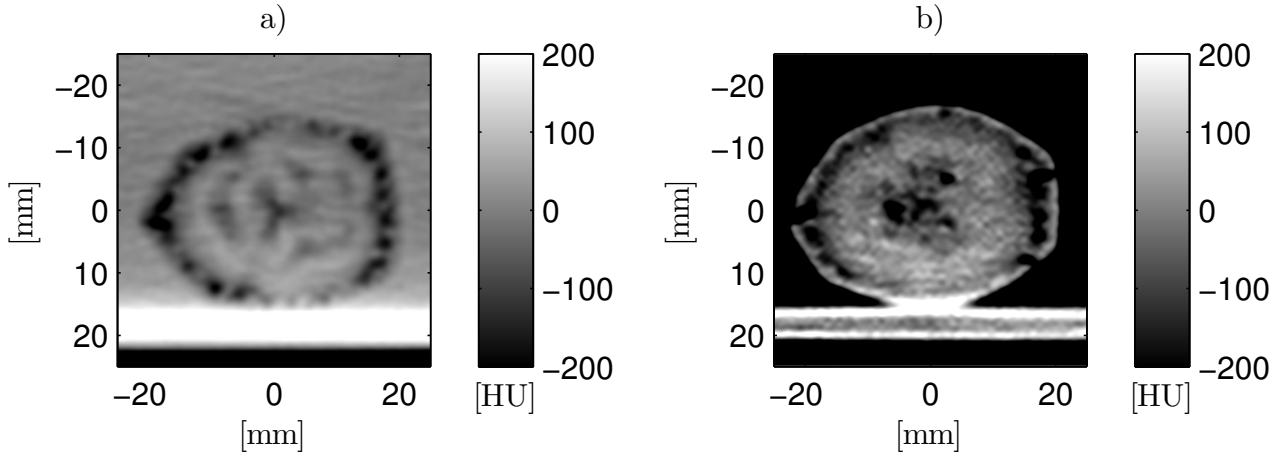


Figure 2. CT images of banana, with water (a), without water (b). The two CT images are not comparable. They are reconstructed with different pixel sizes.

3.1 Acoustic scanning

The acoustic scanning was done at the Center for Fast Ultrasound Imaging (CFU). The fish used was a cod with a length of approximately 210 mm. It was suspended using 0.1 mm fishing lines in a PVC fixture and placed in a small aquarium container filled with degassed water. The scanning was performed using a BK Medical Profocus 2202 scanner, equipped with a dedicated research interface connected to a PC through a X64-CL Express camera_link interface (Dalsa, Waterloo, Ontario, Canada). The system allows the acquisition of digitally beamformed RF echo data.⁸ A BK Medical 8804 10 MHz linear array transducer was attached to an electro-mechanical linear scanner on top of the aquarium. The transducer head was approximately 30 mm below the water surface. The transmit focus point of the transducer was at a range of 45 mm, and dynamic focusing was used in receive mode with the F# equal to 0.5. The overall gain and the time gain compensation (TGC) were adjusted, so that the full speckle pattern could be seen clearly in the soft tissue areas in the US images. Digitally beam-formed RF echo data and a parameter setup file of the scanner were retrieved using the program CFU Grabber.⁸ The measured US images of the fish were generated from the RF data using MATLAB. The parameter files were saved to be used afterwards for the simulations. The typical scan-time to cover the 200 mm fish from nose to tail was about 1 minute.

The same US scanner setup was used to obtain US images of a wire phantom with 8 metal wires. This data is necessary to verify the settings of the simulation program in the simulation stage.

3.2 CT scanning

The CT scanning of the fish was done at Rigshospitalet in Copenhagen. Immediately after the US scanning of the wire phantom, the fish and the fixture were put into the PVC box without water, and the sealed box was transported to the hospital. The box with the fish was scanned with a Toshiba Aquilion ONE CT scanner. It can produce CT images with a slice thickness of 0.5 mm and pixel sizes of 0.274 mm x 0.274 mm. The CT data, given in Hounsfield Units, were stored onto a harddrive, and the CT images of the fish were generated using MATLAB. In addition the CT data were used to generate “3D images” of the fish. By selecting suitable threshold levels, a 3D overview of anatomical details such as the bone structure of the fish can be created.

4. SIMULATION

The Field II^{6,7} software was used to generate the simulated US images. This program uses linear acoustics to simulate the transmitted, backscattered, and received US fields. The simulation of the final US images of the fish was prepared in two stages: First the wire phantom was simulated and compared to the output of the US-scan image to verify the parameter setting (calibration) of the transducer model for the Field II; then US scatterer maps were generated from the CT images of the fish.

4.1 Simulation of the wire phantom

The inputs used for the simulation of the wire phantom with Field II were the transducer model and the positions of the point scatterers representing a model of the wire phantom. The transducer model and the medium parameters were set according to the information in the parameter files that were saved during the acoustic scanning. The positions of the scatterers were found by locating the scattering maximum points in the US images of the wire phantom. An example of a measured US image and the corresponding simulated US image of the wire phantom are presented in Fig. 3

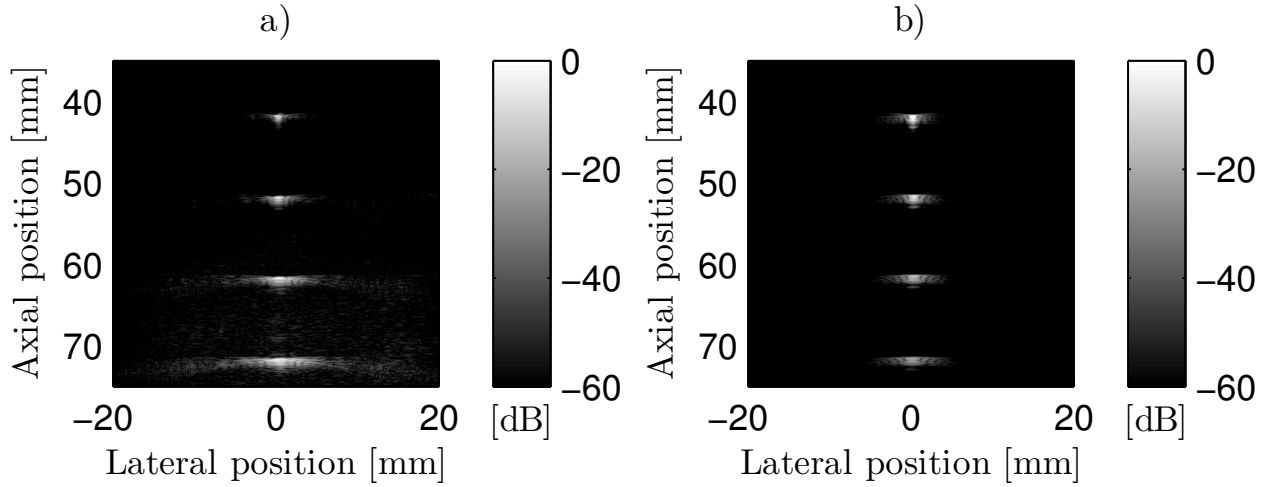


Figure 3. Measured US image of the wire phantom (a), Simulated US image of the wire phantom (b). The scales show the lateral distance from the acoustic centerline and the vertical distance from the transducer surface. Gray level indicates the relative signal strength in dB.

The simulated Full Width at Half Maximum (FWHM) values at the transmit focus point of the US imaging system used in this work were 0.54 mm and 0.3 mm in the lateral and axial directions, respectively. The positions of the point scatterers were 41.8 mm, 51.7 mm, 61.6 mm, and 71.6 mm away from the transducer in the axial direction. With the chosen parameters the discrepancy between the FWHM of the measured and simulated resolution were 6.7%, 0.6%, 0.1% and 10.4% in the lateral direction and 17%, 15%, 16.7%, and 21% in the axial direction, respectively. Pulse echo waves from a plane parallel to the surface of the US transducer was measured and used as the excitation wave for the simulation.

4.2 Simulation of the fish

The procedure for simulation of the fish was similar to the simulation of the wire phantom. The same transducer model and the same medium parameter were used. But the scatterers had to be modeled using a more elaborate method.

Different methods have been used to convert CT data into a US scatterer distribution. In the study of Dillenseger et al.,⁹ the scatterers were distributed using the 1D marked regularity model and a fast Hilbert filling curves algorithm. Their CT images were segmented into air, fat, soft tissue and bone. The regions were assigned the fixed tissue acoustical impedances that have been found in the literature. The resulting simulated images could not capture the shadowing effect of the real US images. Another approach used the combination of reflection and transmission images as in the case of Wein et al. study.¹⁰ The statistical similarity metrics like Mutual Information and Correlation Ratio were used to assess the correspondence between the original CT and US intensities. The method could not introduce the shadowing effect into the simulated images either. Daoud and Lacefield¹¹ used a first-order k -space method and were able to simulate shadowing effects in their US

images, but they had no real US images to compare with. Shams et al.¹² and Kutter et al.¹³ also used the combination of reflection and transmission images and managed to capture the shadowing effect in the images by introducing use of contrast and edge enhanced images obtained from the CT images. But the drawback of their method was that it had no close relation to the physical processes of ultrasound backscattering.

In this work, a similar method using a combination of transmission and reflection properties to calculate the propagation of ultrasound was used. However, the mapping of the strength of the scatterers was different. The block diagram of this method is presented in Fig.4

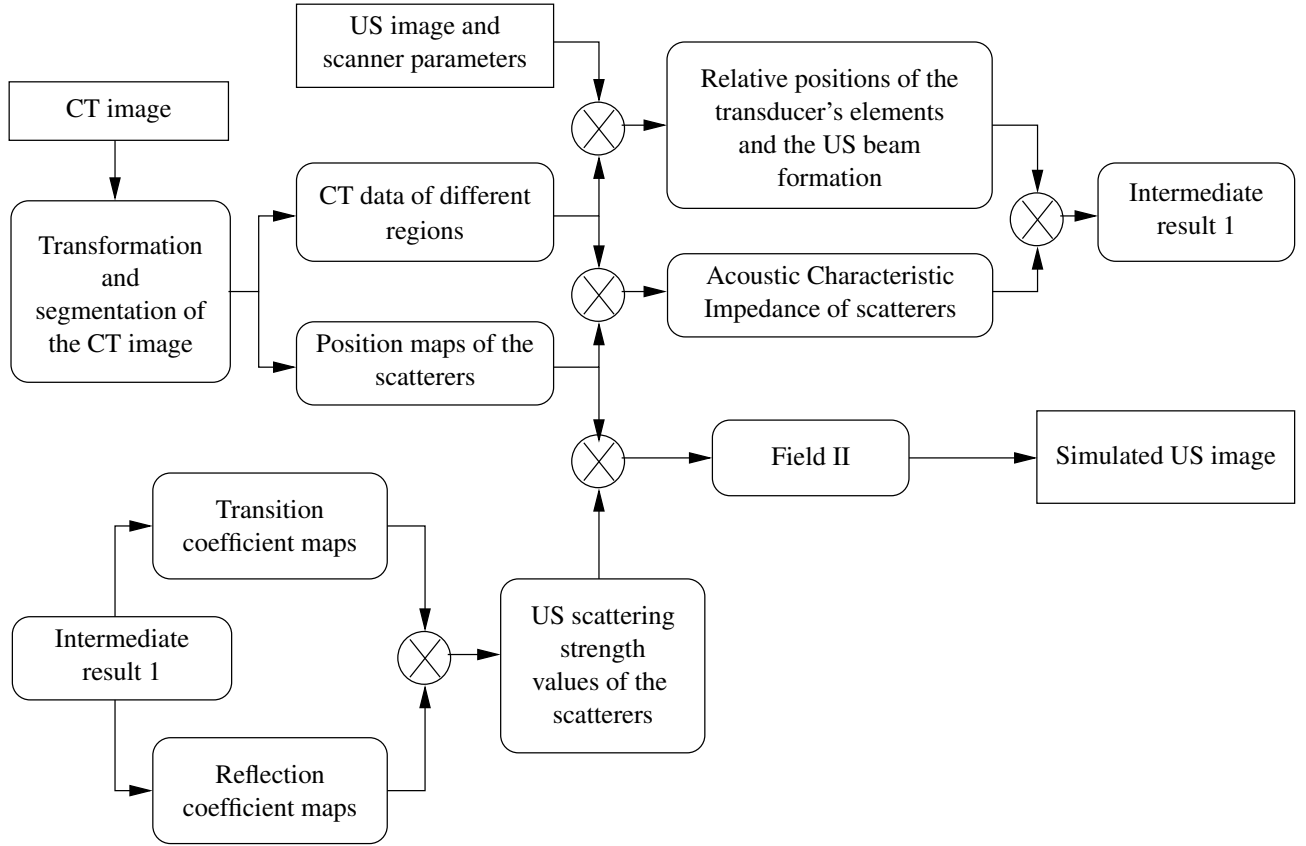


Figure 4. Block diagram of the US scattering strength distribution process

The CT images were cropped to get the same region of interest as in the US images. They were then segmented into regions containing fat, skin, soft tissue, and bone. Special regions were air-inside and air-outside the fish because the fish was CT scanned without surrounding water. In the CT image, the area outside the fish have Hounsfield Unit (HU) values of air, not water. But for the US scan, this region contains water. So for the simulation, the HU values of this region were then replaced by the HU values for water and a Gauss distributed scatterer strength and a uniform density distribution. The HU values of air-inside region remained the same, because this region also contained air in the US scan. The outputs at this stage were, thus, original CT data and position maps of the scatterers for the different regions. The combination of those outputs gave the Acoustic Characteristic Impedance (ACI) of the scatterers. Each region was assigned the values from local minimum to local maximum values, not a fixed value since the HU values of the points in that region were not the same. For instance, the minimum HU value in the bone region was 191, since the bone of a fish is softer than human bone; and the maximum HU value was 1200. They were scaled to the ACI from $(3.6 \times 10^6)^2 [MRayl^2]$ to $(7.38 \times 10^6)^2 [MRayl^2]$, since they were intensity coefficients as in Table 1.

The ACI of the scatterers were used to generate transition and reflection coefficient maps. The transition and reflection coefficient maps were created based on the fact that the energy of a US wave will change when it travels through a medium or from one medium to another. The transition coefficient maps the fraction of the energy remaining at each point in the

image, when the acoustic wave travels through it. The shadow effect is quantified by the transition coefficient maps. The reflection coefficient maps the fraction of the energy being reflected at each point. It quantifies the edge effect or boundary effect seen in US images, where boundaries between different media are often enhanced by high brightness.

Table 1. HU to ACI conversion table

Regions	HU range	ACI range [$MRayl^2$]
Fat.skin	$[-800, -190)$	$[1.5 \times 10^6, 1.5 \times 10^6)^2$
Soft tissue	$[-190, 190)$	$[1.55 \times 10^6, 1.74 \times 10^6)^2$
Bone	$[190, maximumvalue]$	$[3.6 \times 10^6, 7.38 \times 10^6)^2$
Water (replace air-outside)	X	$(1.48 \times 10^6)^2$

The transmission and reflection coefficient¹⁴ maps were given by

$$T_n = \prod_{k=1}^m T_k \quad (1)$$

$$T_1 = 1 \quad (2)$$

$$T_k = \frac{4Z_k Z_{k-1} \cos^2 \theta_{i_k}}{(Z_k \cos \theta_{i_k} + Z_{k-1} \cos \theta_{t_k})^2} \quad (3)$$

$$R_n = \left(\frac{Z_n \cos \theta_{i_n} - Z_{n-1} \cos \theta_{t_n}}{Z_n \cos \theta_{i_n} + Z_{n-1} \cos \theta_{t_n}} \right)^2, \quad (4)$$

where θ_i, θ_t are angle of incidence and transmission. Assume that there were only normal incidence and transmission $\cos \theta_{i_k} = \cos \theta_{i_n} = \cos \theta_{t_k} = \cos \theta_{t_n} = 1$. n is a point in the depth direction, T is the transmission mask points, R is the reflection mask points, m is the number of points in depth direction from the transmit element, and Z is the ACI of a point.

The US scattering strength maps of the scatterers are given by

$$IMG_{HUUUS}(x, y) = \alpha \cdot T(x, y) \cdot B(x, y) \cdot (1 + e^{\beta * R(x, y)}) \quad (5)$$

where $T(x, y)$ is the transmission coefficient maps; $B(x, y)$ is the ACI map; $R(x, y)$ is the reflection coefficient map; α, β are the shadowing effect coefficient and edge-enhancing coefficient, respectively. They are used to adjust the contrast of the simulated US images.

The relative position of the transducer elements and information on beam-forming algorithm of the scanner were obtained from the measured US images and the parameter files of the scanner. In this work, a 192 element transducer was used; the maximum number of active elements was 64 to beamform one line in the US image. The acoustic waves were beamformed with a fixed focus in transmit mode and dynamic focus in receive mode.

Finally, the Field II program was used to calculate the scattered sound field from a collection of sources defined by the scatterers in $IMG_{HUUUS}(x, y)$. To achieve fully developed speckle pattern US image from many random scatterers, there should be 10 scatterers in a resolution cell.¹⁵ The resolution cell was calculated by

$$rescell = N \times \lambda \times FWHM_l \times FWHM_{azi} \quad (6)$$

$$FWHM_i = F\#_i \times \lambda \quad (7)$$

where $rescell$ is the resolution cell, $N \times \lambda$ is the pulse length, i is denote of l and azi which stand for lateral and azimuth direction, respectively, and λ is the wave length. The number of scatterers should be used in this simulation was calculated by

$$nscatt = 10 \times \frac{imgdim}{rescell} \quad (8)$$

where $nscatt$ is the number of scatterers, $imgdim$ is the dimension of the US image. In this simulation, the resolution cell were $rescell = 0.1053mm^3$, the image dimension were $imgdim = 9680mm^3$, and the number of scatterers was about

10^6 . Hence, each simulated US image was generated using 10^6 point scatterers. The positions of the scatterers were within the position maps and were uniformly distributed. The amplitude values of the scatterers were the values of those scatterers in (5) and were random amplitude from a Gaussian distribution to model the difference in the density and speed of sound perturbations in the tissue. It took 5 to 6 hours to generate a ($38.9mm \times 55.3mm$) simulated US image of the fish with 10^6 scatterers using 35 machines in the cluster at CFU.

5. RESULTS

The segmentation of the CT images of the fish is presented in Fig. 5. The 3D reconstruction from CT images of the fish is in Fig. 5a. A sample CT image of the fish was used for the simulation and is in Fig. 5b. The position of the CT image relative to the fish is at the white vertical line at $20mm$ in the lateral direction in Fig. 5a. The position map of the different regions of the slice is Fig. 5c, where value 0 is for the air-outside region, value 1 is the fat-skin region, value 2 is the soft tissue region, value 3 is the bone region. Value 4 was assigned for air-inside region. But there was no air-inside region in this image, so there was only 3 types of values. The transmission coefficient map of the CT image is presented in Fig. 5d. It shows the shadow in the simulated image appeared. The reflection coefficient map is in Fig. 5e, and all the boundary area between different regions was captured.

The simulated US images for this section of the fish are presented in Fig. 6. In Fig. 6b, the pronounced shadowing effect of the US image was captured. The strongest shadows were due to the bones (most clearly seen in the center of the image) and the transition zones fish fin to water and water to fish body (upper left of the image). The edge-enhancing effect made the outline of the upper part of the fish which is close to the transducer, brighter than the one in the shadow in the lower part. The same phenomenon appears in the measured US image of the fish in Fig. 6a. The horizontally enhanced shadows in the concave zone at the lower part in the right side of the fish in Fig. 6a also appeared in Fig. 6b. The speckle pattern in the simulated US image appears much more uniform than in the measured image. One of the reasons is that the FWHM of the US imaging system is greater than the one simulated with Field II. The change in size as a function of depth of the point spread function appeared both in Fig. 6a&b. The FWHM in lateral direction of the point spread function is proportional to the depth. It becomes larger for the scatterers faraway from the transducer.

Future improvements should focus on developing a method that can generate a type of coefficient maps that can capture both the shadowing and edge enhancement effects. It could be done by using different values assigned to the ACI of the different regions.

6. CONCLUSION AND FUTURE PLANS

This work is the first time that an experiment on fish is performed using a combination of US and CT to generate simulated US images. A new method to make the US backscattering map from CT data has been developed that can capture many of the properties of real US image. This shows the advantages of simulation of US images of the same fish from CT data with other transducers and setups without performing the real experiments with US imaging system. The simulated US images of the fish not only capture the shadowing effects, but also take into account the noise of the medium.

This work is one step in an ongoing work to investigate the structure of the acoustical properties of marine organisms with the goal of improving the possibilities for direct acoustic in-situ identification. The next step will be to model the scattering from a whole fish first at high frequencies, but then also for lower frequencies suitable for more long-range underwater use.

7. ACKNOWLEDGMENT

This work is sponsored by grant from the Globalization project of the Technical University of Denmark (DTU). Special thanks to Stina Bjørk Stenersen Hansen, fisheries technician at the DTU-Aqua in Charlottenlund for supplying the fish specimens.

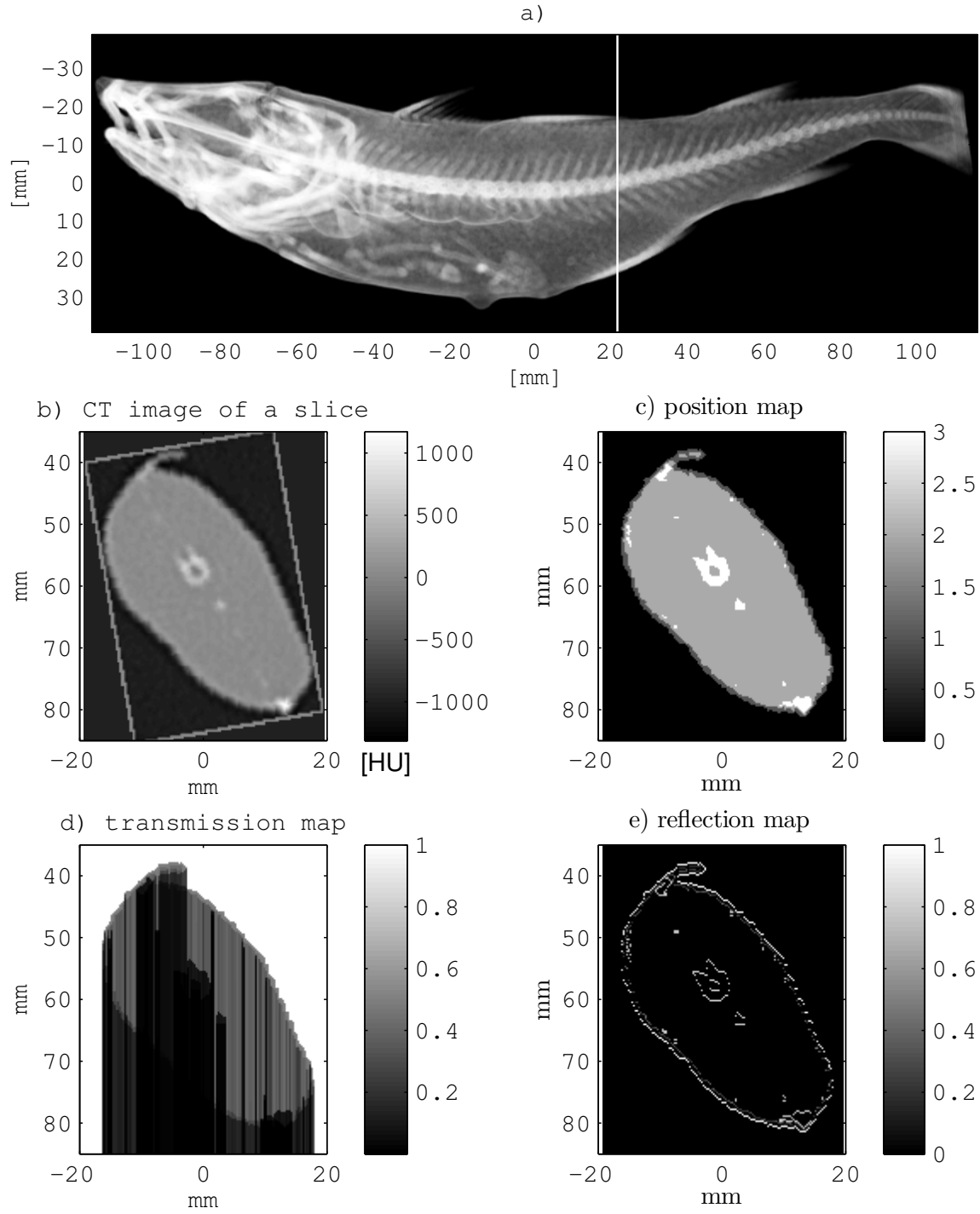


Figure 5. CT images segmentation and transformation; 3D CT image of the fish (a), CT image of a slice of the fish (b), position map of the different regions (c), transmission map (d), reflection map (e).

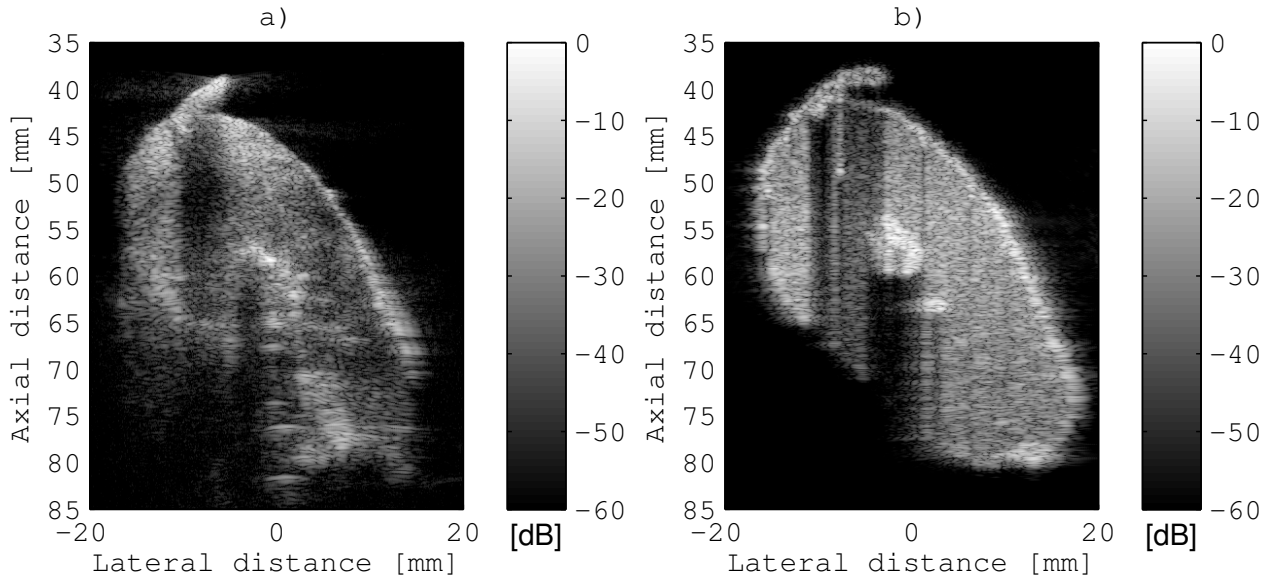


Figure 6. Measured US fish image (a), simulated US image of fish (b).

REFERENCES

- [1] Anonymous. Report of the working group for international, pelagic surveys (wgips). Technical report, <http://www.ices.dk/reports/SSGESST/2010/wgips10.pdf>, 19-22 January 2010, Galway, Ireland.
- [2] J. E. Simmonds and D. MacLennan. *Fisheries Acoustics: Theory and Practice*. Blackwell Science, 2005.
- [3] R. J. Korneliussen, Y. Heggelund, I. K. Eliassen, and G. O. Johansen. Acoustic species identification of schooling fish. *ICES Journal of Marine Science*, 66:1111–1118, 2009.
- [4] B. Lundgren and R. N. Nielsen. A method for the possible species discrimination of juvenile gadoids by broadband backscattering spectra vs. angle of incidence. *ICES Journal of Marine Science*, 65(4):581–593, 2008.
- [5] J. M. Burgos and J. K. Horne. Acoustic characterization and classification of pelagic organism distributions. *ICES Journal of Marine Science*, 65:1235–1247, 2008.
- [6] J. A. Jensen and N. B. Svendsen. Calculation of Pressure Fields from Arbitrarily Shaped, Apodized, and Excited Ultrasound Transducers. *IEEE Trans. Ultrason., Ferroelec., Freq. Contr.*, 39:262–267, 1992.
- [7] J. A. Jensen. Field: A Program for Simulating Ultrasound Systems. *Med. Biol. Eng. Comp.*, 10th Nordic-Baltic Conference on Biomedical Imaging, Vol. 4, Supplement 1, Part 1:351–353, 1996.
- [8] M. C. Hemmsen, M. M. Petersen, S. I. Nikolov, M. B., Nielsen, and J. A. Jensen. Ultrasound image quality assessment: A framework for evaluation of clinical image quality. In *Proceedings of SPIE—the international society for optical engineering*, volume 76291, pages 76290C–12. Medical Imaging 2010: Ultrasonic Imaging, Tomography, and Therapy, 2010.
- [9] J. L. Dillenseger, S. Laguitton, and E. Delabrousse. Fast simulation of ultrasound images from a ct volume. *Comput. Biol. Med.*, 39:180–186, 2009.
- [10] W. Wein, A. Khamene, D. A. Clevert, O. Kutter, and N. Navab. Simulation and fully automatic multimodal registration of medical ultrasound. In *Proceedings of the 10th international conference on Medical image computing and computer-assisted intervention*, pages 136–143, 2007.
- [11] M. I. Daoud and J. C. Lacefield. Distributed three-dimensional simulation of b-mode ultrasound imaging using a first-order k-space method. *Physics in Medicine and Biology*, 54:5173–5192, 2009.
- [12] R. Shams, R. Hartley, and N. Navab. Real-time simulation of medical ultrasound from ct images. In *Medical Image Computing and Computer-Assisted Intervention*, 2008.
- [13] O. Kutter, R. Shams, and N. Navab. Visualization and gpu-accelerated simulation of medical ultrasound from ct images. *Computer Methods and Programs in Biomedicine*, 94:250–266, 2009.

- [14] J. A. Jensen. *Estimation of Blood Velocities Using Ultrasound: A Signal Processing Approach*. Cambridge University Press, New York, 1996.
- [15] T. A. Tuthilla, R. H. Sperrya, and K. J. Parker. Deviations from rayleigh statistics in ultrasonic speckle. *Ultrasonic Imaging*, 10(2):81–89, 1988.

B.2 Simulation of shadowing effects in ultrasound imaging from computed tomography images

This paper was presented at the *IEEE International Ultrasonics Symposium* in 2011, and published in *Proceedings of IEEE International Ultrasonics Symposium*, 2011, pp. 1411 -1414.

Simulation of shadowing effects in ultrasound imaging from computed tomography images

An Hoai Pham^{1,2}, Bjarne Stage¹, Martin Christian Hemmsen^{2,4}, Bo Lundgren¹, Mads Møller Pedersen^{2,3}, and Jørgen Arendt Jensen²

¹National Institute of Aquatic Resources, Technical University of Denmark, Jægersborg Allé 1, 2920 Charlottenlund, Denmark;

²Center for Fast Ultrasound Imaging, Dept. of Elec. Eng. Build. 349, Technical University of Denmark, DK-2800 Kgs. Lyngby, Denmark;

³Dept. of Radiology, Copenhagen University Hospital, Rigshospitalet, DK-2100 Copenhagen, Denmark;

⁴R&D Applications & Technologies BK Medical, DK-2730 Herlev, Denmark

Abstract—Simulation of ultrasound (US) images based on computed tomography (CT) data has previously been performed with different approaches. Shadowing effects are normally pronounced in US images, so they should be included in the simulation. In this study, a new method to introduce shadowing effects has been developed which makes the simulated US images appear more realistic. US images of a cod (*Gadus morhua*) were obtained with a BK Medical 2202 ProFocus US scanner with a dedicated research interface giving access to beamformed RF data. The center frequency of the transmit pulse was 10 MHz. In transmit mode, the focus point was at 45 mm. 384 US focused beams were emitted to create the image. CT images with a slice thickness of 0.5 mm, and a pixel size of 0.2 x 0.2 mm, were obtained with an Aquilion ONE Toshiba CT scanner. CT data were mapped from Hounsfield Units (HU) to backscatter (BST), attenuation (ATT) coefficients, and characteristic acoustic impedance (CAI) with a new mapping method. The new approach uses focused beam tracing to create maps of the transmission coefficient (TRC) and then the scattering strength map (SSM). There were 384 maps of SSM corresponding to 384 emissions. Finally an average SSM map was calculated. Field II was used to simulate an US image with dimensions of 38.9 mm x 55.3 mm x 4.5 mm, using 10^6 point scatterers. Since no quantitative method to assess quality of a simulated US image compared to a measured one exists, visual inspection was used. The method gives diffuse shadows that are similar to the ones observed in measurements on real objects.

I. INTRODUCTION

Simulation of US images based on CT data has previously been performed with different methods. Shadowing effects are normally pronounced in US images, so they should be included in the simulation. Jensen et al [1], [2] using Field II [3], [4] generated simulated US images from backscatter maps of scatterers of clinical images. The method can simulate blood flow as well as US images of soft tissues. In a study of Song et al [5], an US ray-tracing model was used to simulate US images. The intensities of the ultrasound rays were calculated including the influences of attenuation, impedance and backscattered coefficients. However, their work focused only on capturing the main highlights of the structures in the US images, not the speckle pattern nor the shadowing effects. In the study of Dillenseger et al [6] the scatterers were distributed using the 1D marked regularity model and a fast Hilbert filling curves algorithm. The CT images were segmented into air, fat, soft tissue, and bone regions. The regions were assigned a

fixed tissue acoustical impedances that have been found in the literature. The size of the point spread function in simulated US images varies as a function of depth. Hostettler et al [7] managed to capture the shadowing effects in their simulation. The method was not described in detail because it has been patented. Shams et al, Kutter et al, and Rijkhorst et al [8], [9], [10] used the combination of scattering, reflection, and transmission textures to generate simulated US images. The textures were created based on CT images in most of the cases and MR images in Rijkhorst et al's study. Although shadowing effects were captured in the simulated US images, the CT images were post-processed by modification of contrast and edge enhancement. The attenuation of the media was not taken into account. Daoud and Lacefield [11] used a first-order k -space method and were able to simulate shadowing effects in their US images, but they used a tissue mimicking phantom in their simulation.

In this study, a new method to introduce shadowing effects has been developed to make simulated US images appear more realistic. The method not only takes into account the attenuation of the media but also introduces shadowing effects that appear in measured US image. The method used CT images as basic maps to find the scatterer maps for the simulation. The CT data give not only the structure data of the scanned object, but also material properties such as X-ray attenuation expressed in HU. Relationships between HU and US scattering strengths derived from data in the literature have been used. A focused beam tracing model is used that takes into account the transducer properties and the propagation paths of the emitted sound that form a B-mode image. The method is described in the next section.

II. METHODS

The procedure of the method is presented in Fig. 1. The acoustic scanning of a cod (*Gadus morhua*), which was not alive, was performed at the Center for Fast Ultrasound Imaging (CFU) using a ProFocus 2202 scanner (BK Medical, Herlev, Denmark), equipped with a dedicated research interface connected to a personal computer through a X64-CL Express camera link interface (Dalsa, Waterloo, Ontario, Canada). The system allows acquisition of digitally beamformed radio frequency (RF) echo data [12]. A BK Medical

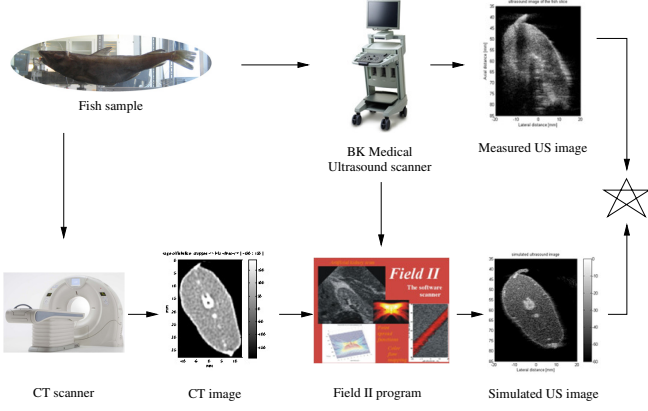


Fig. 1. Block diagram of the procedure of the method

8804 linear array transducer was used. The center frequency of the transmit pulse was 10 MHz. The transmit focus point of the transducer was at a range of 45 mm. Digitally beam-formed RF data and a parameter setup file of the scanner were retrieved using the program CFU Grabber [12]. The scanner generated 384 image lines corresponding to 384 emissions in one US image. The CT-scanning of the fish was performed at Rigshospitalet in Copenhagen, Denmark. The time difference between the two measurements was 3 hours. The fixture with the fish was placed in a sealed box and transported to the hospital. The box with the fish was scanned with a Toshiba Aquilion ONE CT scanner. The CT images were obtained with a slice thickness of 0.5 mm and pixel sizes of 0.274 mm x 0.274 mm.

The program Field II was used for the simulation process. In the US ray-tracing method, the US beams are modeled as straight US rays. Consider a sound ray traveling from P_0 to P through M media. With the assumption that there is no secondary or higher order backscatter and very few scatterers on the boundaries between the media compared to the number of scatterers inside the media, the intensity received at P_0 is [5]

$$I_R(P) = I_s \frac{\eta_b^{(M)} V}{\left(\sum_{m=1}^M l_m\right)^2} \exp\left(-4 \sum_{m=1}^M \alpha^{(m)} l_m\right) \times \prod_{m=1}^{M-1} \alpha_t^{(m,m+1)}(\theta_i^{(m)}) \alpha_t^{(m+1,m)}(\theta_t^{(m)}) \quad (1)$$

where I_s [W/m^2] is the initial intensity at P_0 , $\eta_b^{(M)}$ [$cm^{-1}Sr^{-1}$] is the backscattering coefficient of the medium at P , V [cm^3] is the volume of the scatterer, $\alpha^{(m)}$ [$Np.cm^{-1}$] is the attenuation of the m^{th} medium along the ray path, l_m is the distance the wave has propagated within the m^{th} medium, α_t is the intensity transmission coefficients, θ_i and θ_t are the incident and transmission angles between the surface normal to the interface of the media and the direction of the sound wave, respectively. The intensity transmission coefficients are given by [13]

$$\alpha_t^{(m,m+1)}(\theta_i^{(m)}) = \frac{4Z_m Z_{m+1} \cos^2 \theta_i^{(m)}}{(Z_m \cos \theta_i^{(m)} + Z_{m+1} \cos \theta_t^{(m)})^2} \quad (2)$$

where Z_m [$kg/(m^2.s)$] is the CAI of the m^{th} medium. If it is assumed very small angle of incidence $\cos \theta_i = \cos \theta_t \approx 1$ for all the scatterers, then

$$\alpha_t^{(m,m+1)}(\theta_i^{(m)}) = \alpha_t^{(m+1,m)}(\theta_t^{(m)}) \approx \frac{4Z_m Z_{m+1}}{(Z_m + Z_{m+1})^2} \quad (3)$$

and (1) can be rewritten

$$I_R(P) = I_s V \cdot \frac{\eta_b^{(M)}}{\left(\sum_{m=1}^M l_m\right)^2} \cdot \exp\left(-4 \sum_{m=1}^M \alpha^{(m)} l_m\right) \cdot TRC(P) = K \cdot SSM(P) \quad (4)$$

where $K = I_s V$ and is assumed to be 1. The transmission coefficient map is defined as:

$$TRC(P) = \prod_{m=1}^{M-1} (\alpha_t^{(m,m+1)}(\theta_i^{(m)}))^2 \quad (5)$$

The BST , $ATT = \alpha^{(m)}$ and CAI are mapped from the HU of the CT data using Table I.

In reality the US energy becomes concentrated in the area around the focus point, and then diverges again in the media. A new method to take this fact into account was developed to create shadowing effects that appear more realistic. The method presents an US focused beam tracing model. The sound produced in each emission is modeled as a group of rays that intersect at a focus point. The focus point is located at the center of the active aperture in the lateral direction and at the focus depth in the axial direction. The number of rays is equal to the number of active elements. The positions of the pixels that each ray passes through are derived from the positions of the corresponding active element and the focus point. For the em^{th} emission, the US scattering strength map is calculated by

$$SSM^{(em)}(P) = \sum_{i=1}^m SSM_i^{(em)}(P) \quad (6)$$

where m is the number of active elements in one emission. $SSM_i^{(em)}(P)$ is calculated by (4) if the i^{th} ray passes through P . Otherwise $SSM_i^{(em)}(P) = 0$. The average of the n US scattering strength maps gives a final US scattering strength map

$$ASSM(P) = \frac{1}{n} \sum_{em=1}^n SSM^{(em)}(P) \quad (7)$$

Each simulated US image was generated using 10^6 scatterers in the image area. The requirements and how to calculate the number of scatterers are described in [16]. The smallest simulated point spread function is 0.54 mm x 0.3 mm. It took 10 minutes to generate one image line by Field II running as the only task on one machine or 1.83 hours for the whole simulated US image using 35 machines on the CFU cluster. The CFU cluster consists of 50 machines, each of them a Dell Power Edge 1750 server, Dual Intel Xeon 3.2 GHz supporting Hyper-threading technology, and 2GB of RAM.

TABLE I

MAPPING TABLE FROM HOUNSFIELD UNIT TO BACKSCATTER, ATTENUATION COEFFICIENTS AND CHARACTERISTIC ACOUSTIC IMPEDANCE [14], [15]

Regions	Hounsfield Unit	$\eta_b^{(M)}$ [$cm^{-1}sr^{-1}$]	$\alpha^{(m)}$ [$dBcm^{-1}$]	Z_m [$kg/(m^2s)$]
Bone	[179, <i>maximum</i>]	[0.005, 0.1]	[100, 200]	[6.5×10^6 , 7.38×10^6]
Soft tissue	[-41, 178]	[0.000125, 0.01]	[10, 32.5]	[1.55×10^6 , 1.74×10^6]
Fat	[-741, -42]	[0.003, 0.019]	[1.25, 2]	1.33×10^6
Air-inside	[<i>minimum</i> , -742]	0	[400, 500]	0.4×10^3
Air-outside	not defined by HU	0	0.24	1.48×10^6

III. RESULTS

One sample slice of the fish was chosen to demonstrate the methods of simulation. The measured ultrasound image and the CT image of the slice of the fish are shown in Fig. 2 and Fig. 3, respectively. A simulated US image of the slice of the fish is presented in Fig. 4. The US scattering strength map for Fig. 4 was calculated using (4) with $\alpha_t^{(m,m+1)}(\theta_i^{(m)}) = 1$ to take into account the *BST* and *ATT*, and neglect the transmission properties of the media. The simulated US image appears very similar to the CT image, and with a more fine grain speckle pattern than in the measured US image. The image captures the effect of the increasing width of the point spread functions of the scatterers when the distance between the focus point and the scatterers increases. The *BST* coefficients decide the structure of the simulated US image but the *ATT* coefficients do not introduce visible shadowing effects.

In Fig. 2, the shadows are influenced by the fact that the transducer does not produced sharp, straight beams. The focused beam tracing method takes this phenomenon into account. The *TRC* map of this model for the slice of the fish is presented in Fig. 5. Note that the shape of the shadows is influenced by the transmit focus depth and that the maximum values are at the focus depth. The simulated ultrasound image produced using this method is presented in Fig. 6. The method gives diffuse shadows with decreasing width below the shadowing regions similar to the feature in the measured image.

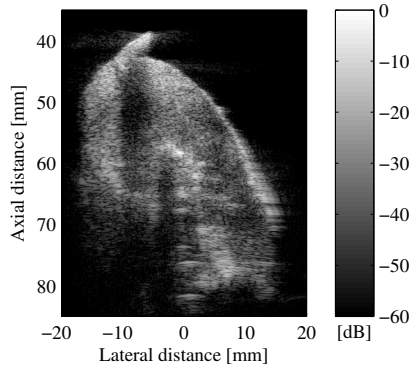


Fig. 2. The measured US image of the slice of the fish

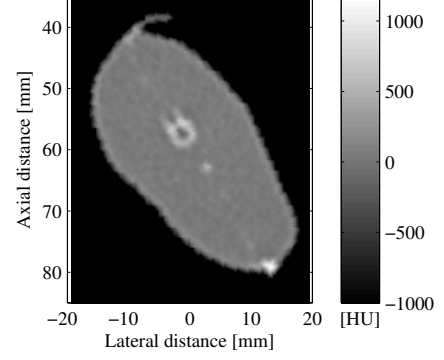


Fig. 3. The CT image of the slice of the fish

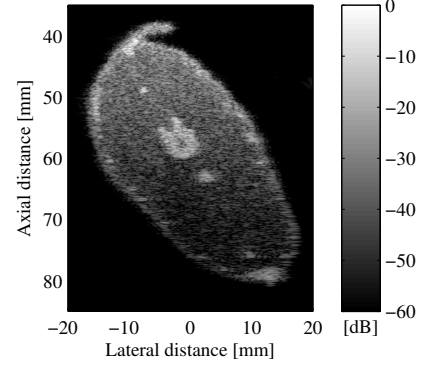


Fig. 4. The simulated US image using US ray-tracing model without TRC

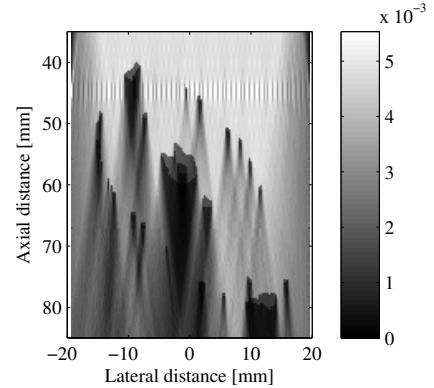


Fig. 5. The TRC map for US focused beam tracing model

Since no qualitative method to assess quality of a simulated ultrasound image compared to a measured one exists, visual

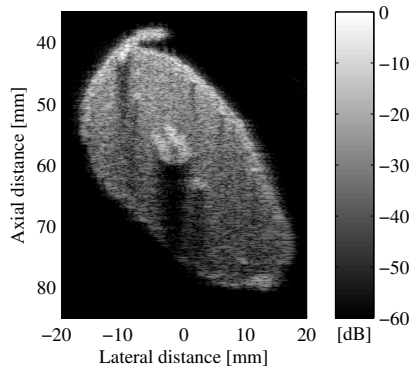


Fig. 6. The simulated US image with shadowing effects using US focused beam tracing model

inspection was used. The focus point was modeled as a very small point and there were artifacts in the TRC map at the focused depth in Fig. 5. But the artifacts do not appear in the simulated US image in Fig. 6 because of the smoothing effects of the random distribution of the scatterers. The method was applied for a linear array transducer, but can be used for convex and phase array transducers as well. Similar mapping method to find *BST*, *ATT* coefficients and *CAI* could be used if the data are MRI images instead of CT images.

IV. CONCLUSION

In this work, a new method to introduce shadowing effects has been tested that makes the simulated US image from the CT image appear more realistic. The experiment provides the US data for assessment of the simulation results as well as instrument parameters and CT data for the simulation process. The method emphasizes the necessity of mapping the Hounsfield Unit to the backscattering, attenuation coefficients and characteristic acoustic impedance in the simulation of US images from CT images. The focused beam tracing model generates the simulated US image with shadowing effects that are similar to the ones in the measured US image. The method uses the two-way transmission coefficients to capture the shadowing effects. In the appearance of the simulated US images, most of the characteristics of the measured US images such as shadowing effects, attenuation, edge-enhancement are presented.

ACKNOWLEDGMENT

This work is sponsored by grant from the Globalization project of the Technical University of Denmark (DTU). Special thanks to Stina Bjørk Stenersen Hansen, fisheries technician at the DTU-Aqua in Charlottenlund for supplying the fish specimens, and Tina Bock Pedersen at the Copenhagen University Hospital, Rigshospitalet for the CT scanning of the fish.

REFERENCES

- [1] J. A. Jensen and P. Munk, "Computer phantoms for simulating ultrasound B-mode and CFM images," in *Acoustical Imaging*, S. Lees and L. A. Ferrari, Eds., vol. 23, 1997, pp. 75–80.
- [2] J. A. Jensen and S. Nikolov, "Fast simulation of ultrasound images," in *Proc. IEEE Ultrason. Symp.*, vol. 2, 2000, pp. 1721–1724.
- [3] J. A. Jensen, "Field: A Program for Simulating Ultrasound Systems," *Med. Biol. Eng. Comp.*, vol. 10th Nordic-Baltic Conference on Biomedical Imaging, Vol. 4, Supplement 1, Part 1, pp. 351–353, 1996.
- [4] J. A. Jensen and N. B. Svendsen, "Calculation of Pressure Fields from Arbitrarily Shaped, Apodized, and Excited Ultrasound Transducers," *IEEE Trans. Ultrason., Ferroelec., Freq. Contr.*, vol. 39, pp. 262–267, 1992.
- [5] M. Song, R. Haralick, and F. Sheehan, "Ultrasound imaging simulation and echocardiographic image synthesis," in *2000 International Conference on Image Processing, vol III, Proceedings*, IEEE, Signal Processing Soc. IEEE, 2000, Proceedings Paper, pp. 420–423, IEEE International Conference on Image Processing (ICIP 2000), Vancouver, Canada, Sep. 10–13, 2000.
- [6] J. L. Dillenseger, S. Laguitton, and E. Delabrousse, "Fast simulation of ultrasound images from a ct volume," *Comput. Biol. Med.*, vol. 39, pp. 180–186, 2009.
- [7] A. Hostettler, C. Forest, A. Forgione, L. Soler, and J. Marescaux, "Real-Time Ultrasonography Simulator Based on 3D CT-Scan Images," in *Medicine meets virtual reality 13: The magical next becomes the medical now*, vol. 111. I O S PRESS, 2005, Article, pp. 191–193, 13th Conference on Medicine Meets Virtual Reality, Long Beach, CA, JAN 26–29, 2005.
- [8] R. Shams, R. Hartley, and N. Navab, "Real-time simulation of medical ultrasound from ct images," in *Medical Image Computing and Computer-Assisted Intervention*, 2008.
- [9] O. Kutter, R. Shams, and N. Navab, "Visualization and gpu-accelerated simulation of medical ultrasound from ct images," *Computer Methods and Programs in Biomedicine*, vol. 94, pp. 250–266, 2009.
- [10] E.-J. Rijkhorst, D. Heanes, F. Odille, D. Hawkes, and D. Barratt, "Simulating Dynamic Ultrasound Using MR-derived Motion Models to Assess Respiratory Synchronisation for Image-Guided Liver Interventions," in *Information processing in computer-assisted interventions*, Navab, N and Jannin, P, Ed., vol. 6135. Springer - Verlag Berlin, 2010, Article, pp. 113–123, 1st International Conference on Information Processing in Computer-Assisted Interventions (IPCAI 2010), Geneva, Switzerland, Jun. 23, 2010.
- [11] M. I. Daoud and J. C. Lacefield, "Distributed three-dimensional simulation of b-mode ultrasound imaging using a first-order k-space method," *Physics in Medicine and Biology*, vol. 54, pp. 5173–5192, 2009.
- [12] M. C. Hemmsen, S. I. Nikolov, M. M. Pedersen, M. J. Pihl, M. S. Enevoldsen, J. M. Hansen, and J. A. Jensen, "Implementation of a versatile research data acquisition system using a commercially available medical ultrasound scanner," *IEEE Trans. Ultrason., Ferroelec., Freq. Contr.*, p. Submitted, 2011.
- [13] J. A. Jensen, *Estimation of Blood Velocities Using Ultrasound: A Signal Processing Approach*. New York: Cambridge University Press, 1996.
- [14] J. C. Bamber, *Acoustical Characteristics of Biological Media*. John Wiley and Sons, Inc., 2007.
- [15] U. Schneider, E. Pedroni, and A. Lomax, "The calibration of ct hounsfield units for radiotherapy treatment planning," *Physics in Medicine and Biology*, vol. 41, no. 1, p. 111, 1996.
- [16] A. H. Pham, B. Stage, M. C. Hemmsen, B. Lundgren, M. M. Pedersen, T. B. Pedersen, and J. A. Jensen, "Simulation of ultrasound backscatter images from fish," in *Proceedings of SPIE—the international society for optical engineering. Medical Imaging 2011*, 2011, pp. 7961–184.

B.3 Ultrasound backscatter from free-swimming fish at 1 MHz for fish identification

This extended abstract was accepted as poster presentation and will be published in conference Proceedings, *IEEE International Ultrasonics Symposium* in October 2012.

An H. Pham^{1,2}, Bo Lundgren¹, Bjarne Stage¹, Jørgen Adrent Jensen²

¹National Institute of Aquatic Resources, Technical University of Denmark, Charlottenlund, Copenhagen, Denmark, ²Center for Fast Ultrasound Imaging, Dept. of Elec. Eng., Bldg. 349, Technical University of Denmark, DK-2800 Lyngby, Denmark

Submission ID: 94

Subject Classification: NSP Signal Processing

Presentation Preference: Poster

Student Paper: Yes **Participate in the Student Paper Competition:** Yes

Invited Speaker: No

Keywords: ultrasound, sonar, underwater camera, small animal experiment

Ultrasound backscatter from free-swimming fish at 1 MHz for fish identification

An H. Pham^{1,2}, Bo Lundgren¹, Bjarne Stage¹, Jørgen Adrent Jensen²

¹National Institute of Aquatic Resources, Technical University of Denmark, Charlottenlund, Copenhagen, Denmark, ²Center for Fast Ultrasound Imaging, Dept. of Elec. Eng., Bldg. 349, Technical University of Denmark, DK-2800 Lyngby, Denmark

Background, Motivation and Objective

Below MHz frequencies the swimbladder is often considered the most important part for acoustic fish detection. A portable system was developed to not only detect but also try to identify free-swimming fish. It has been used to measure the ultrasound backscatter from fish in the low MHz frequency range. The measurements show that the reflected energy from the surface of the fish is significantly stronger than from the swimbladder, therefore important for identification.

Statement of Contribution/Methods

The system consists of a RESON TC3210 1MHz single-element transducer (SET), a BlueView P900-2250 Dual Frequency sonar, and three Oregon ATC9K cameras on a fixture. The RESON transducer is connected to an Olympus pulser-receiver monitored by a portable computer through a Picoscope 4226 PC oscilloscope. Ex-situ experiments were performed at the NorthSea Oceanarium in Hirtshals, Denmark. The positions, orientations, and lengths of fish were estimated by 3D image analysis, taking the measured acoustic distance into account, while species were identified manually.

Results/Discussion

There are 57 recordings (about 2 hours out of 9) that have sufficient data quality where the whole fish is insonified by the acoustic beam of the SET. Each recording consists of data from the 3 cameras, the SET, and the sonar, comprising passes of 67 fish of 5 different species, both single and schooling. Fish swam not only across but also along the acoustic beam. Compared to the sonar, the SET gives higher distance resolution and preserves the phase data. Therefore it is expected that they contain information more useful for identification. The amplitudes of the backscatter signals from the fish depend strongly on the angle of incidence between the acoustic beam and the surface of the fish. The figure presents an example of the rf signals from a fish slowly flicking its tail to swim first along then across the acoustic beam. Figure a) is the envelope data for 42 pings (circa 2.8s). The signal at a distance of about 3.22m is much higher in figure c) than in figure b) because the tail is then closer to perpendicular to the acoustic beam. These experiments indicate that at 1 MHz the surface areas (also fins and tail) of the fish can give echoes that are much stronger (up to 3 times) than the swimbladder can.

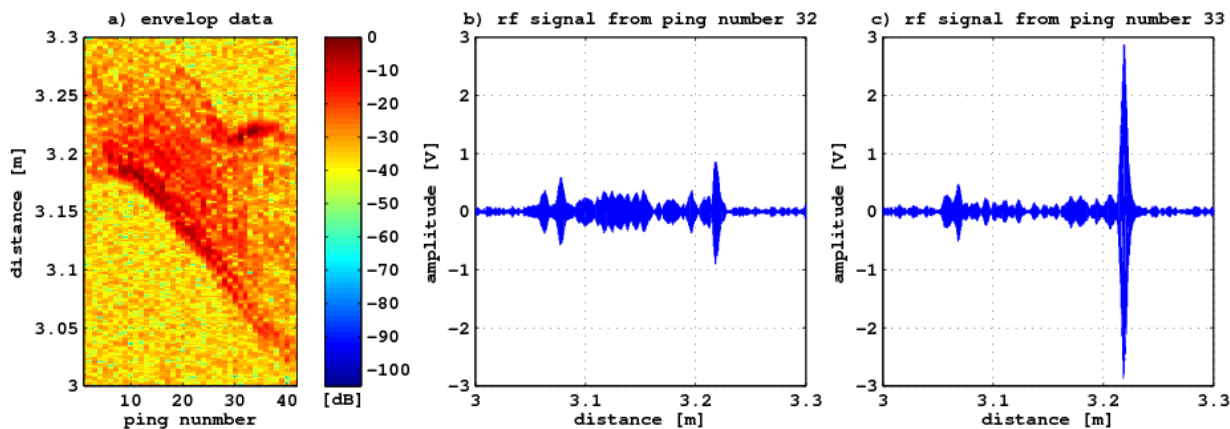


Figure. An example of acoustic signals from a fish that swam first along then across the acoustic beam of the SET

Other Results

C.1 Range profiles of three cods for the study presented in chapter [2](#)

This section presents range profile maps of the three cods corresponding to the energy distribution curves presented in Fig. [2.5](#).

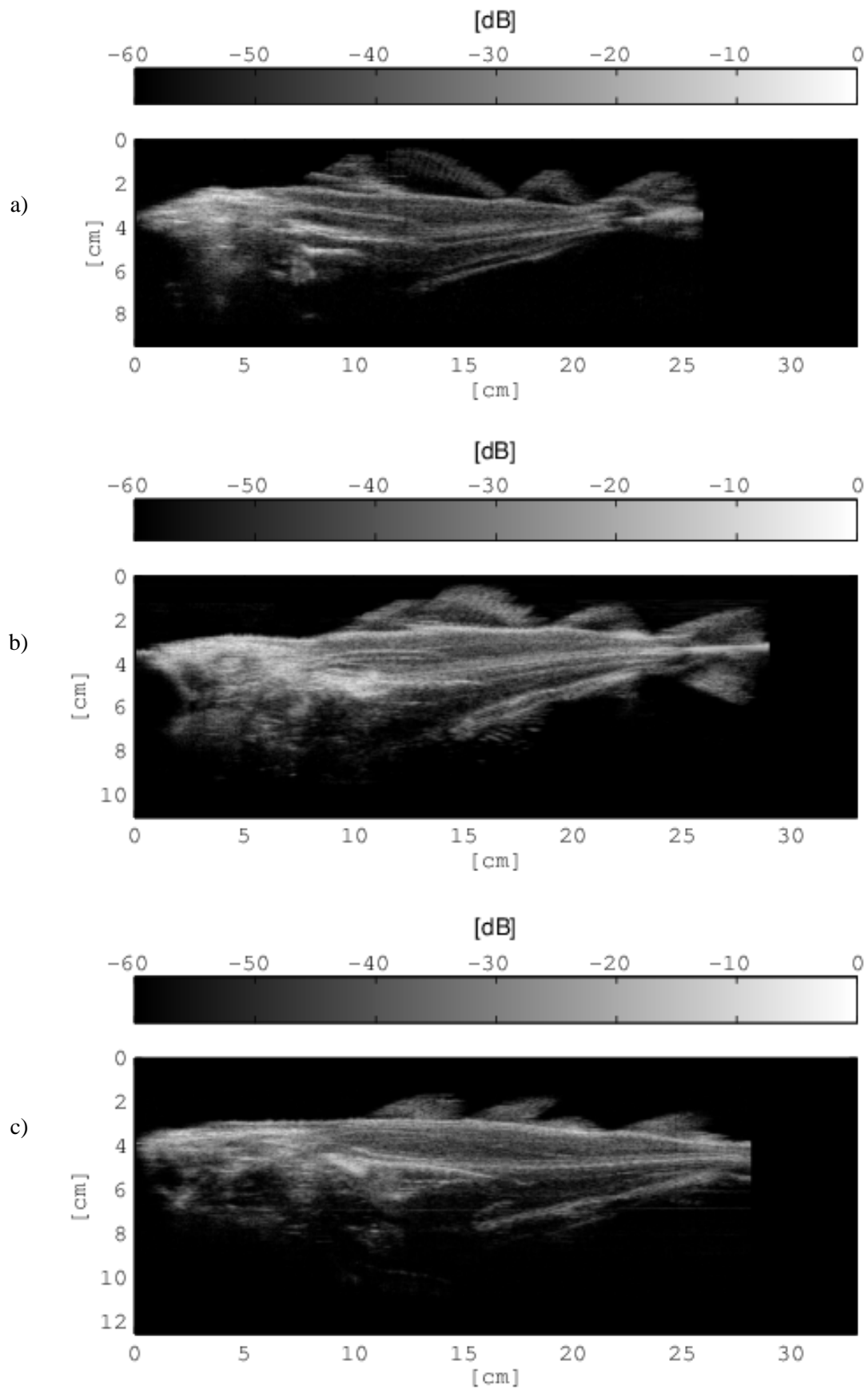


Figure C.1: Range profile maps of the 3 cods. The transducer frequency is 6 MHz. The angle α is 0° . Fish1 (a). Fish3 (b). Fish4 (c).

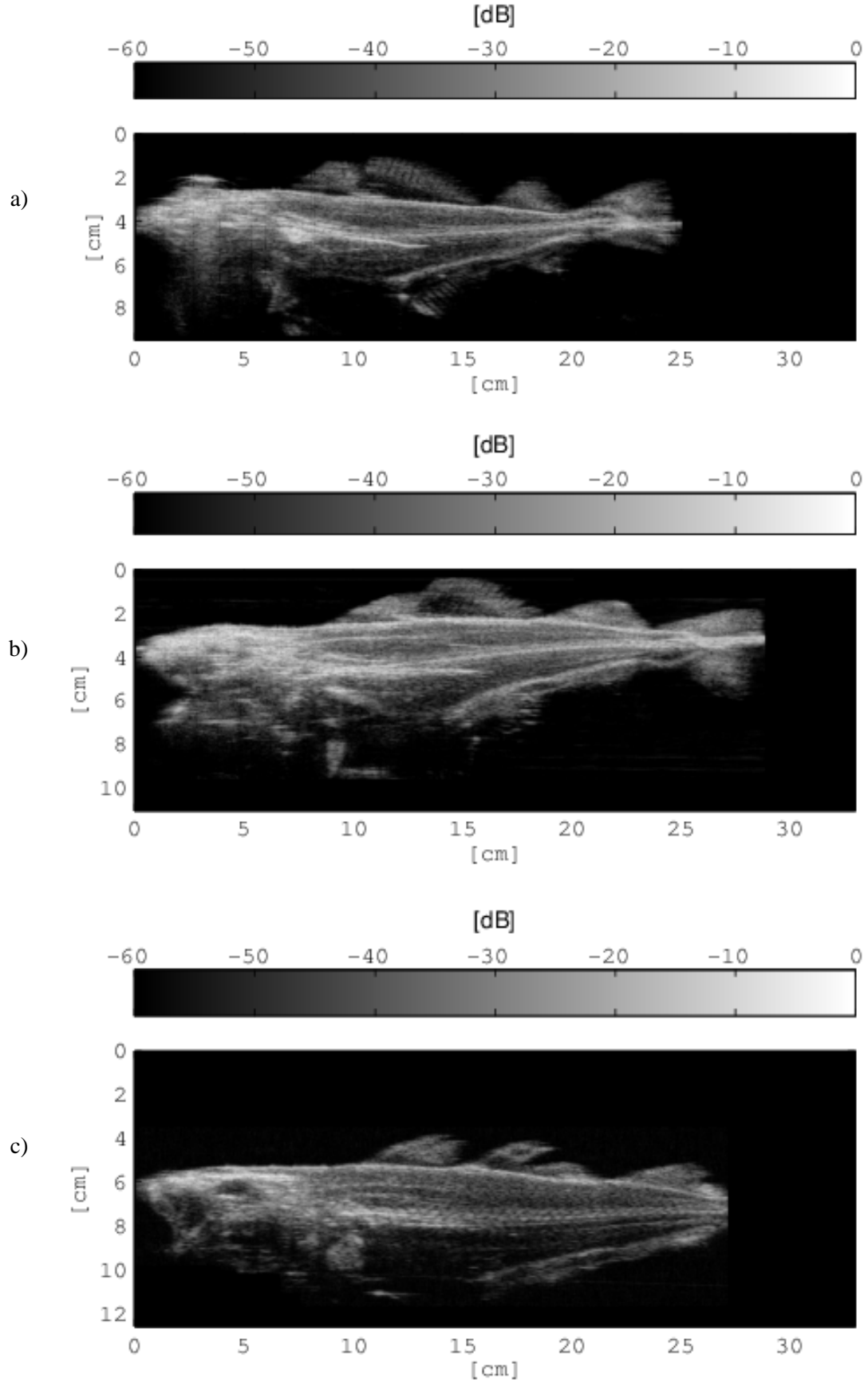


Figure C.2: Range profile maps of the 3 cods. The transducer frequency is 6 MHz. The angle α is 30° . Fish1 (a). Fish3 (b). Fish4 (c).

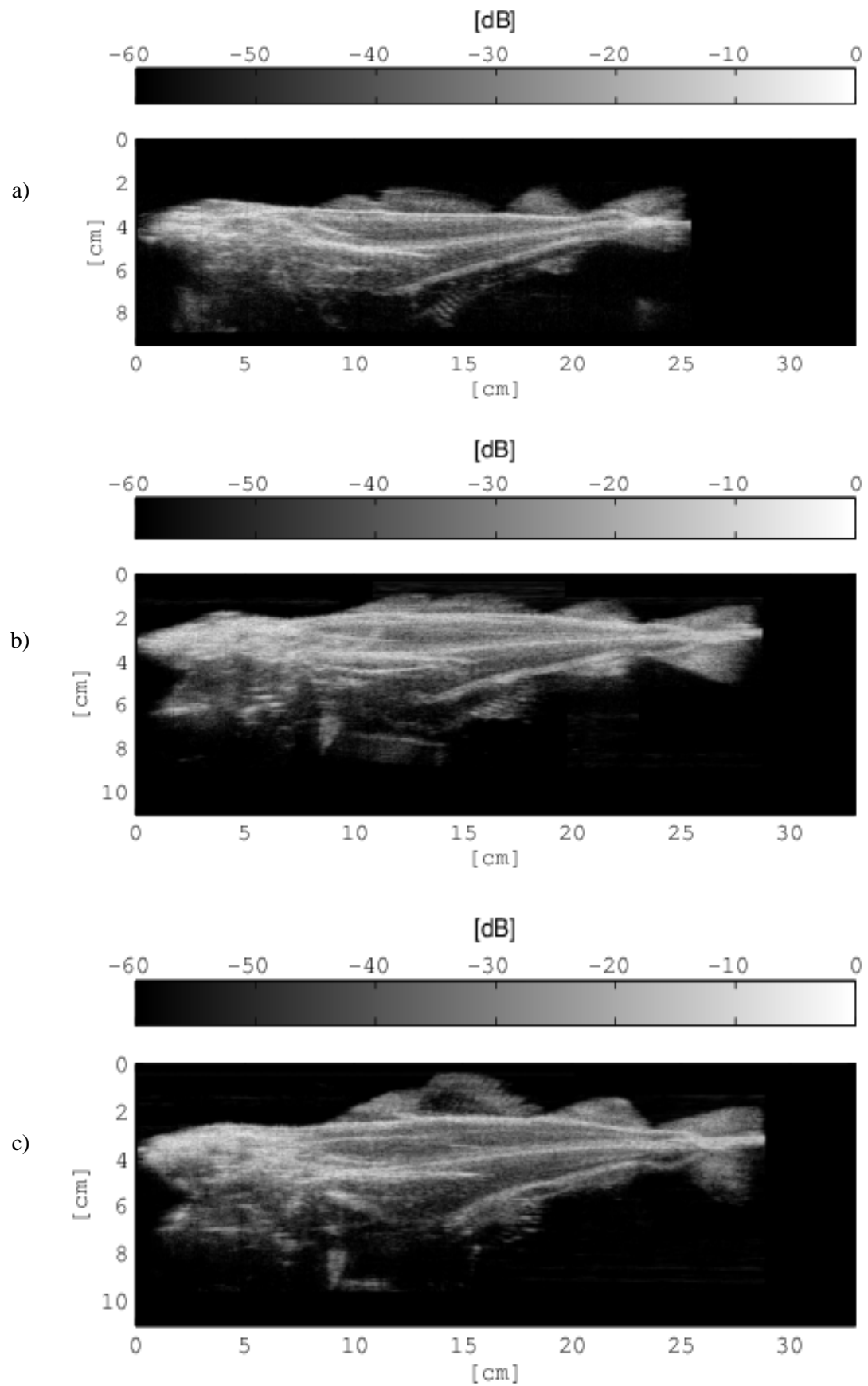


Figure C.3: Range profile maps of the 3 cods. The transducer frequency is 6 MHz. The angle α is -30° . Fish1 (a). Fish3 (b). Fish4 (c).

C.2 Range profiles of a cod and a saithe for the study presented in chapter 2

This section presents range profile maps of the cod fish1 and the saithe fish2 corresponding to the energy distribution curves presented in Fig. 2.6, and 2.7.

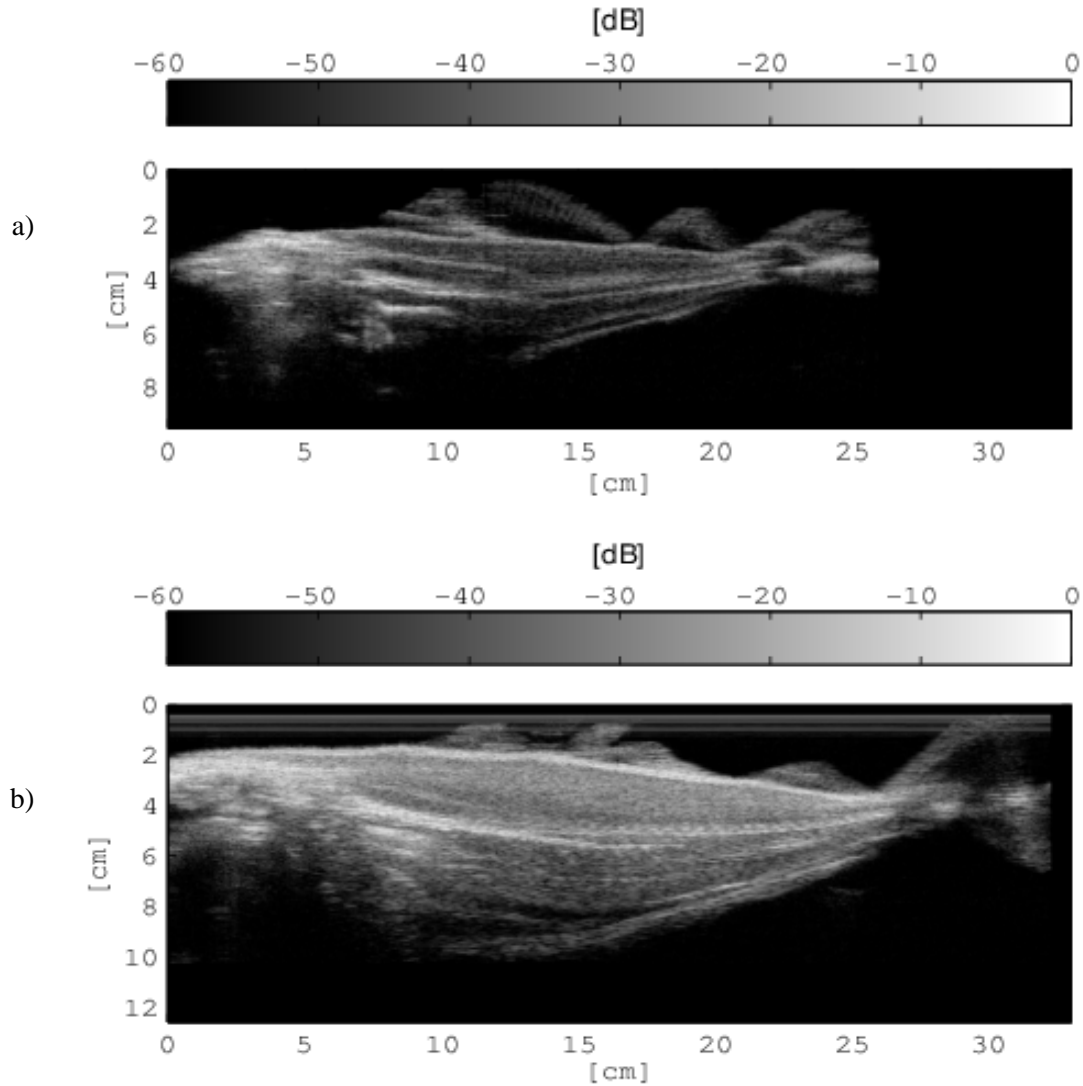


Figure C.4: Range profile maps of a cod and a saithe. The transducer frequency is 6 MHz. The angle α is 0° . Fish1 (a). Fish2 (b).

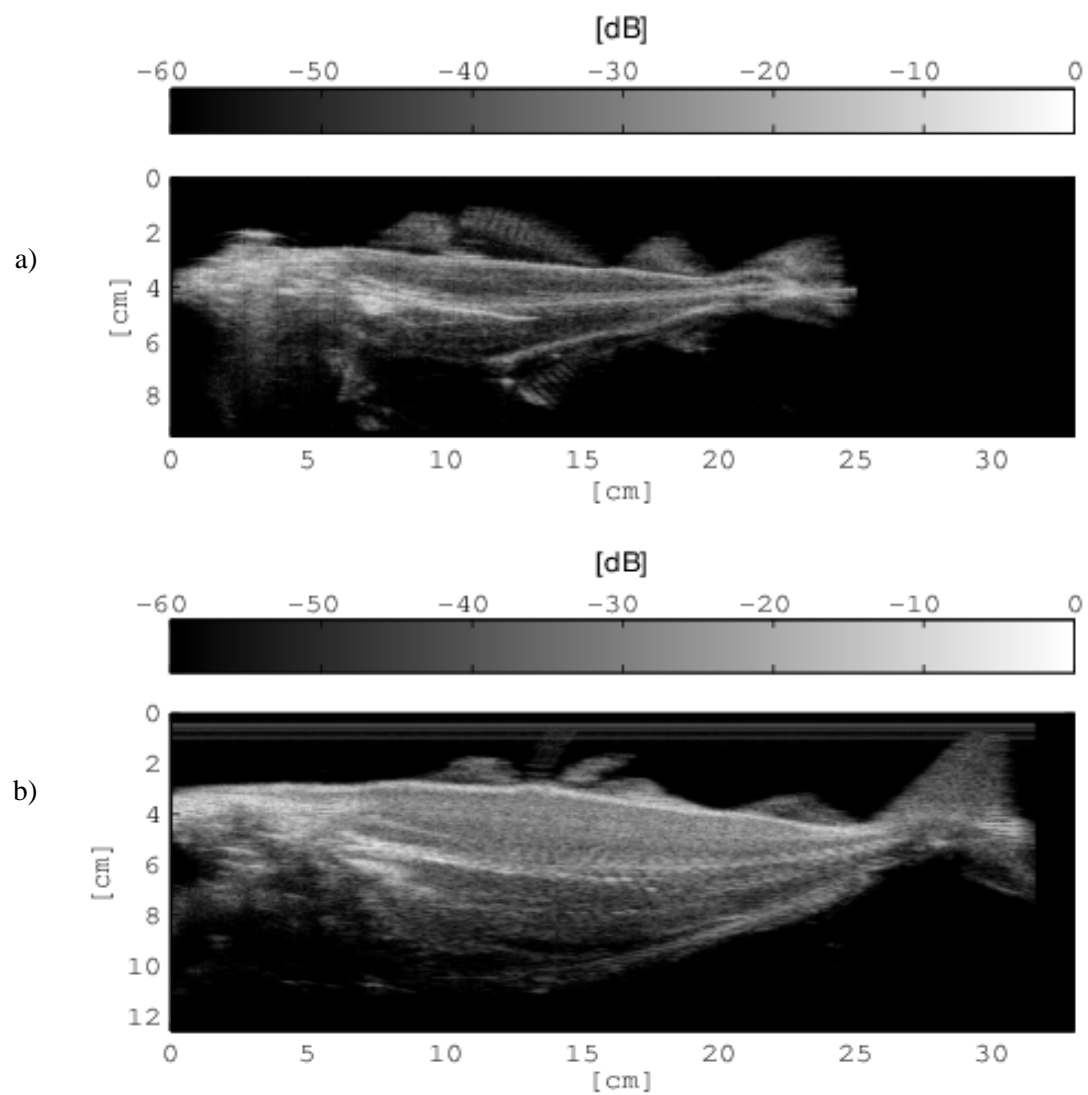


Figure C.5: Range profile maps of a cod and a saithe. The transducer frequency is 6 MHz. The angle α is 30° . Fish1 (a). Fish2 (b).

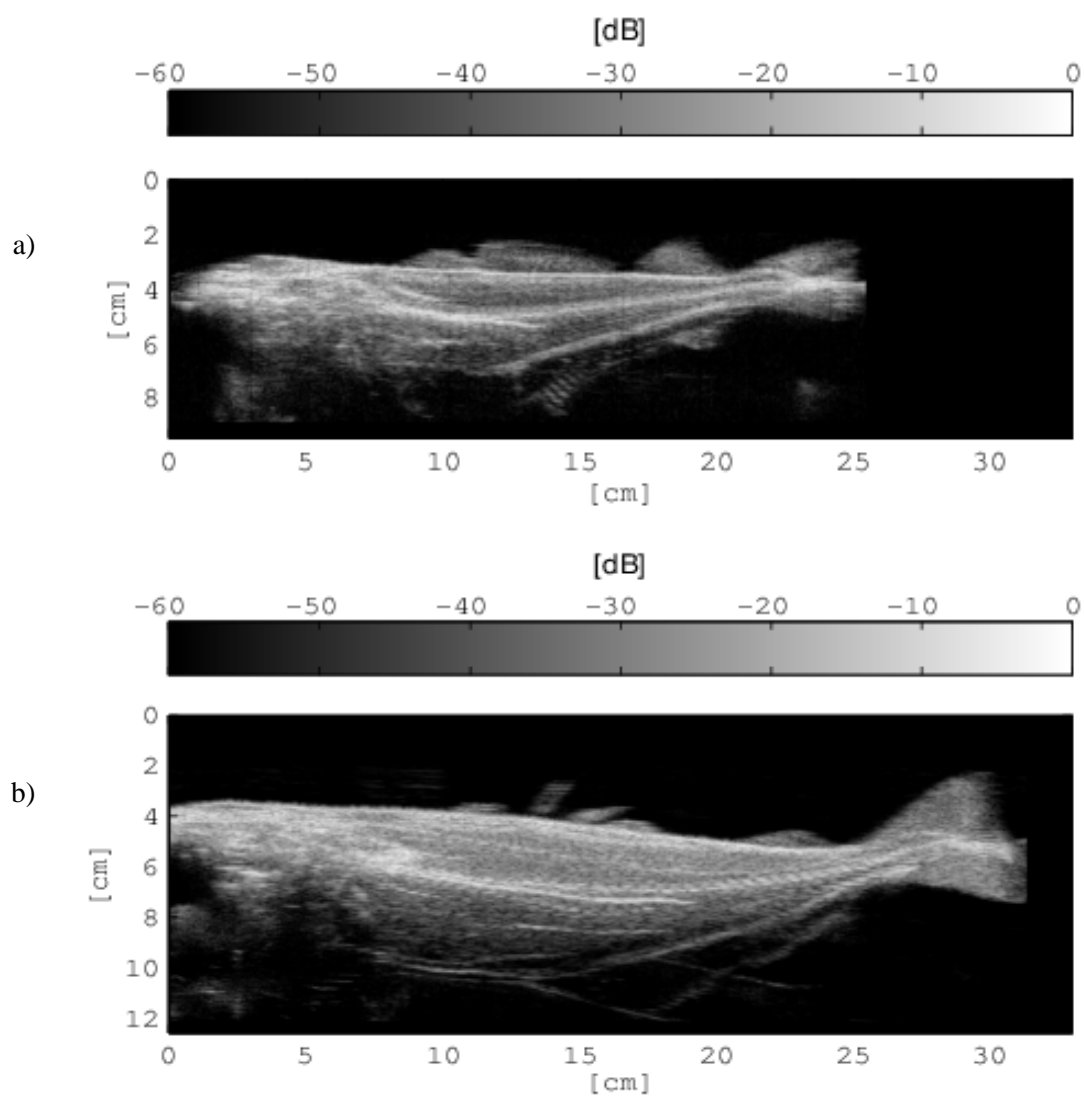


Figure C.6: Range profile maps of a cod and a saithe. The transducer frequency is 6 MHz. The angle α is -30° . Fish1 (a). Fish2 (b).

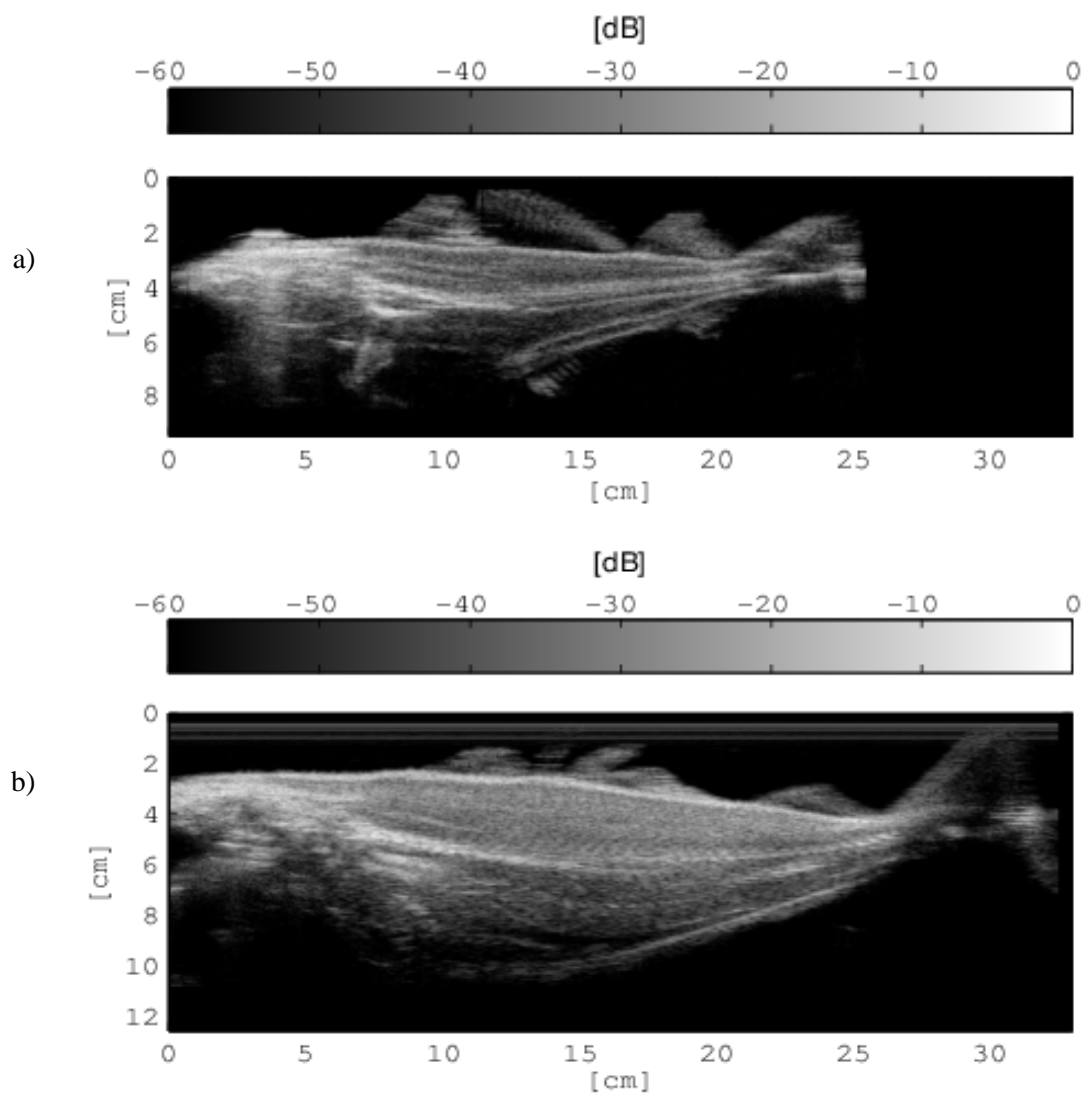


Figure C.7: Range profile maps of a cod and a saithe. The transducer frequency is 6 MHz. The angle α is 15° . Fish1 (a). Fish2 (b).

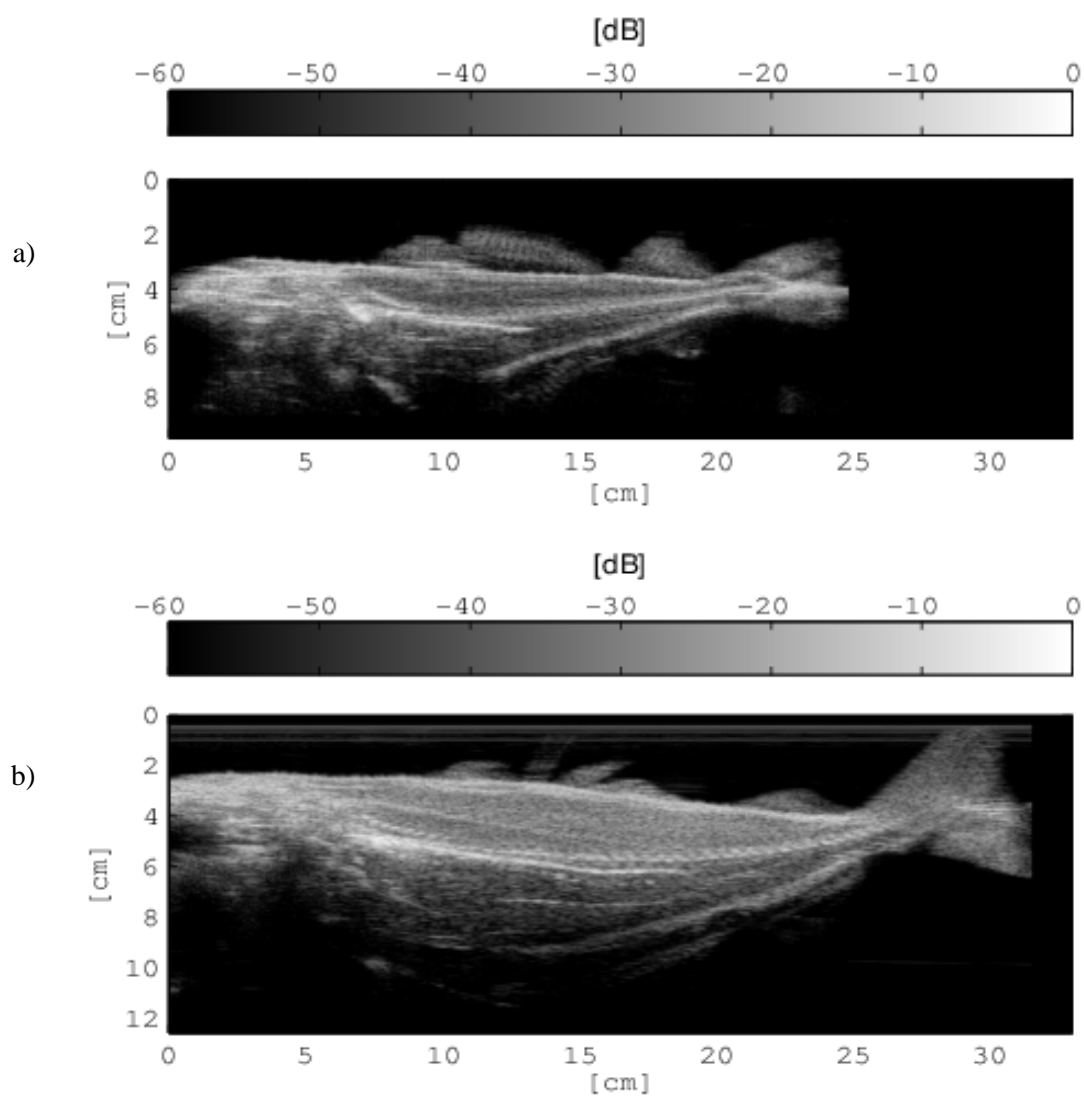


Figure C.8: Range profile maps of a cod and a saithe. The transducer frequency is 6 MHz. The angle α is -15° . Fish1 (a). Fish2 (b).

C.3 Range profiles of a saithe and two cods for the study presented in [chapter 2](#)

This section presents range profile maps of the saithe fish2 and the two cods fish3 and fish4 corresponding to the energy distribution curves presented in Fig. [2.8](#), [2.9](#), and [2.10](#).

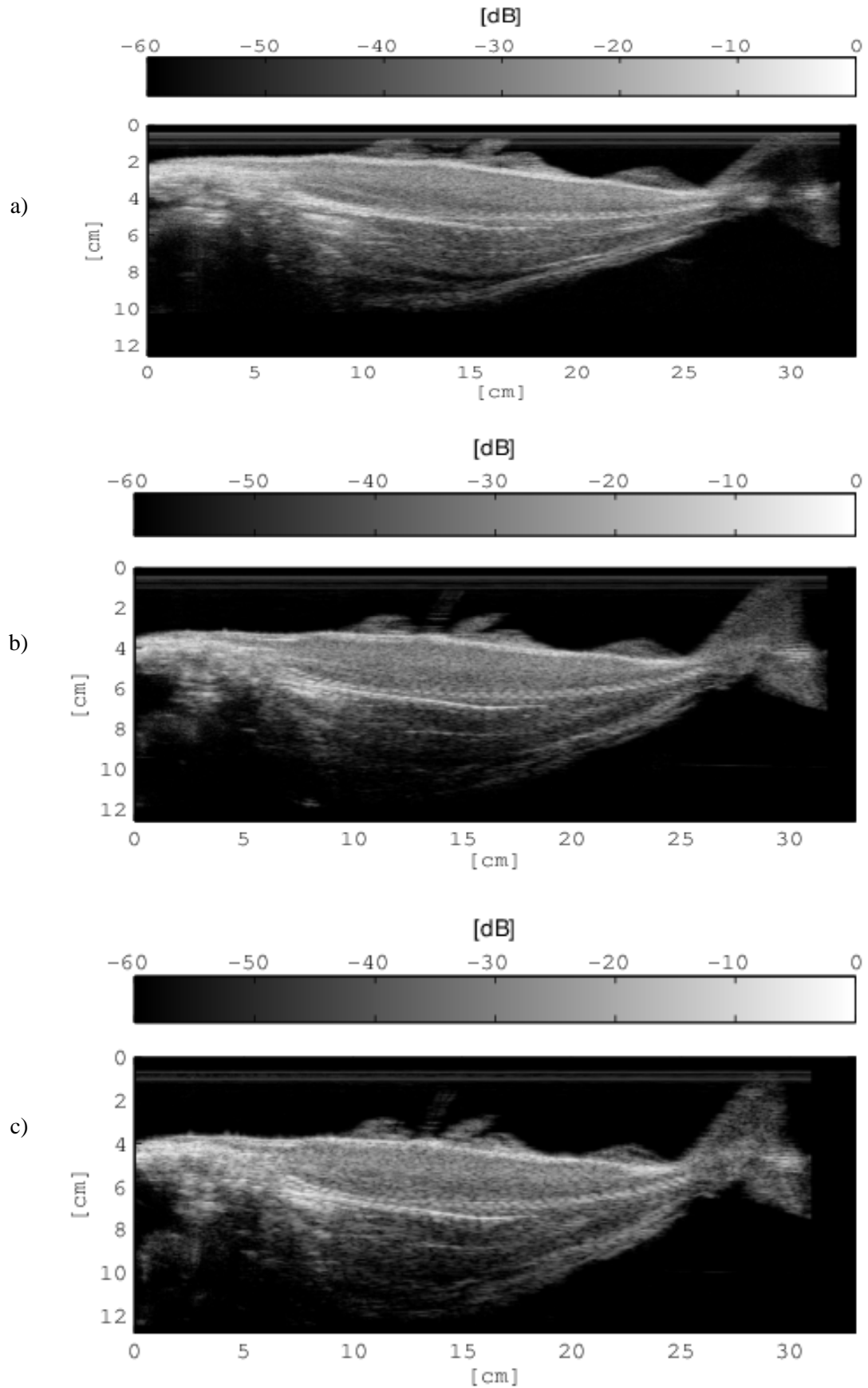


Figure C.9: Range profile maps of the saithe fish2. The angel α is 0° . The transducer frequency is 6 MHz (a), 3.5 MHz (b), 2.5 MHz (c).

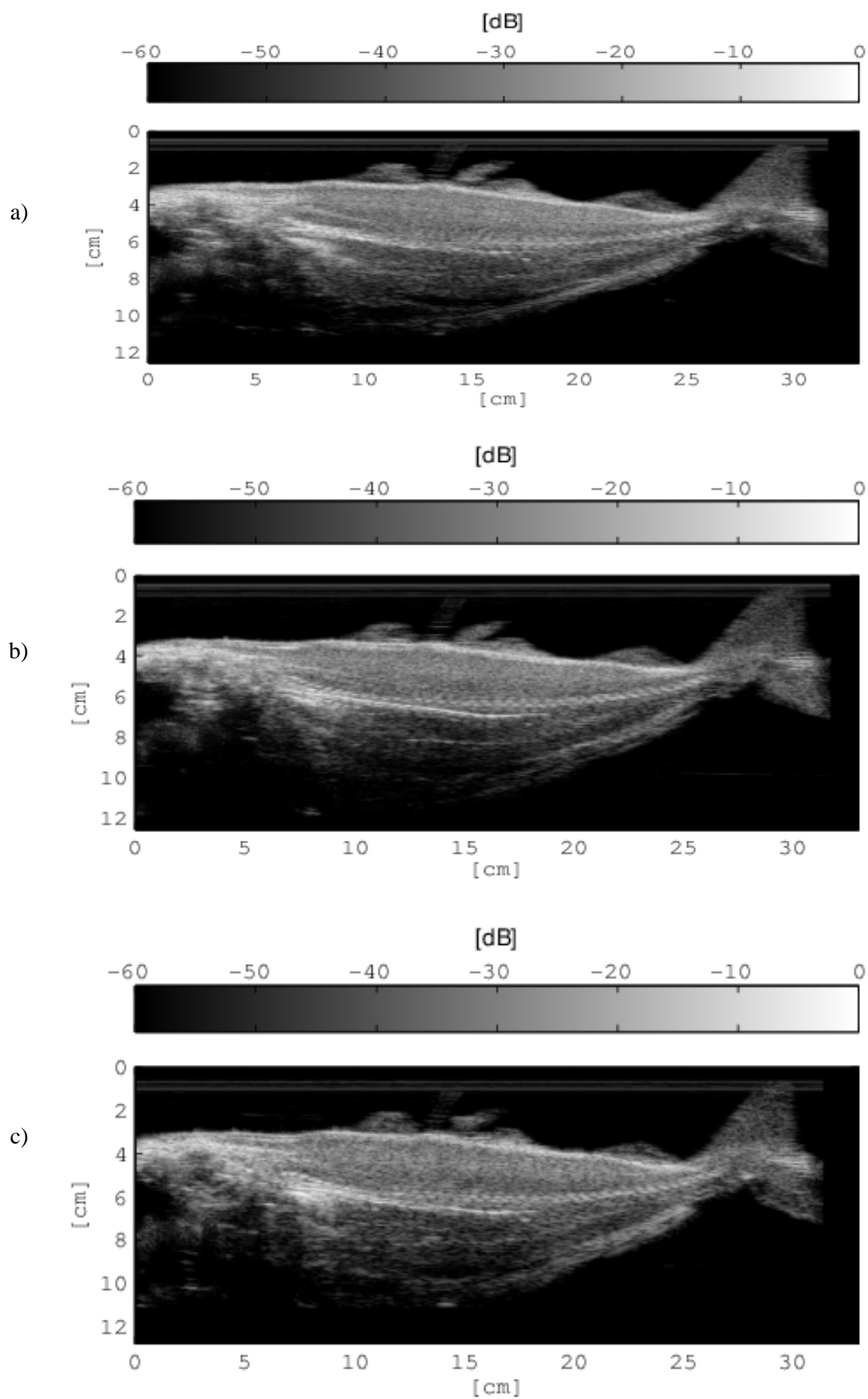


Figure C.10: Range profile maps of the saithe fish2. The angel α is 30° . The transducer frequency is 6 MHz (a), 3.5 MHz (b), 2.5 MHz (c).

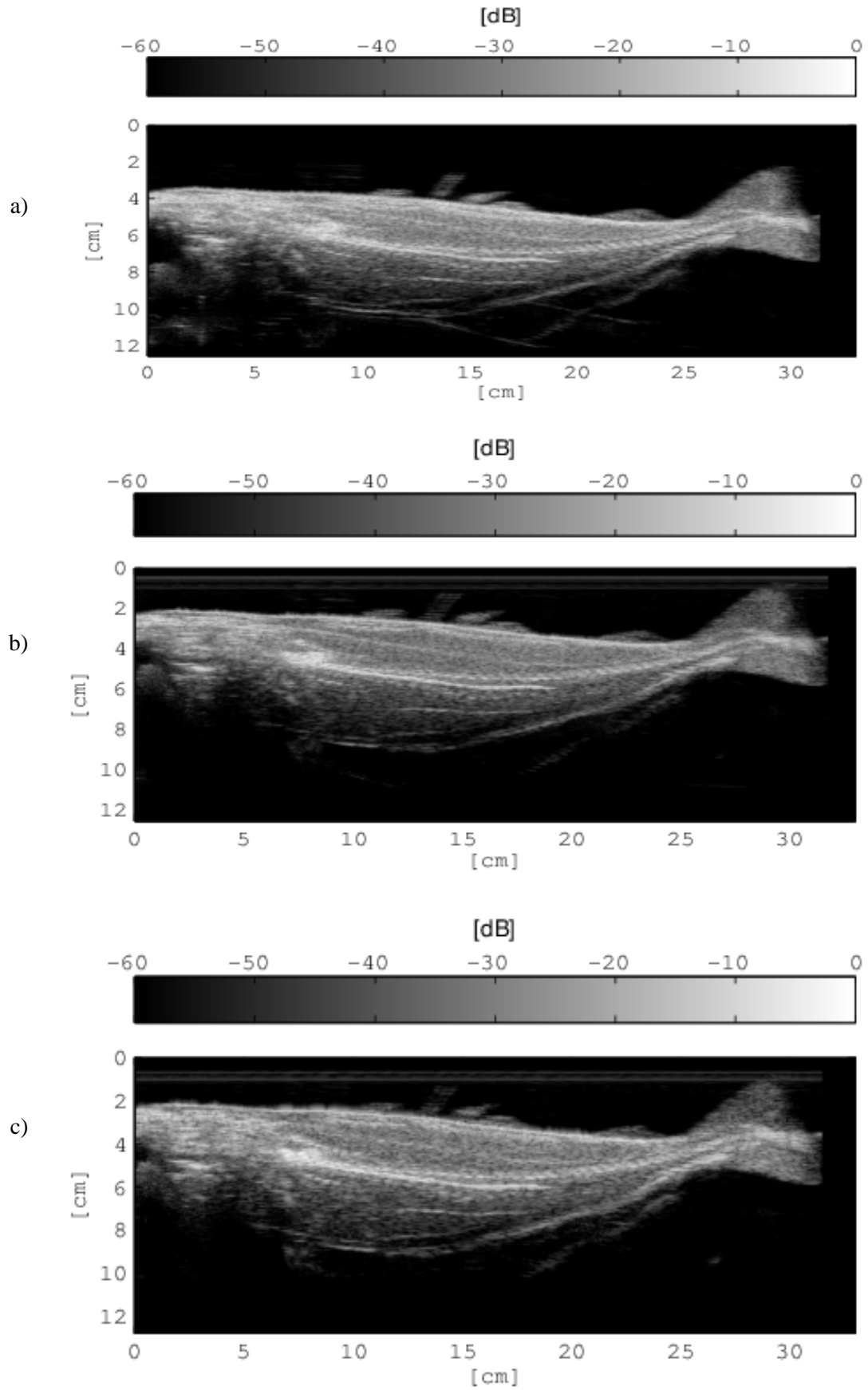


Figure C.11: Range profile maps of the saithe fish2. The angle α is -30° . The transducer frequency is 6 MHz (a), 3.5 MHz (b), 2.5 MHz (c).

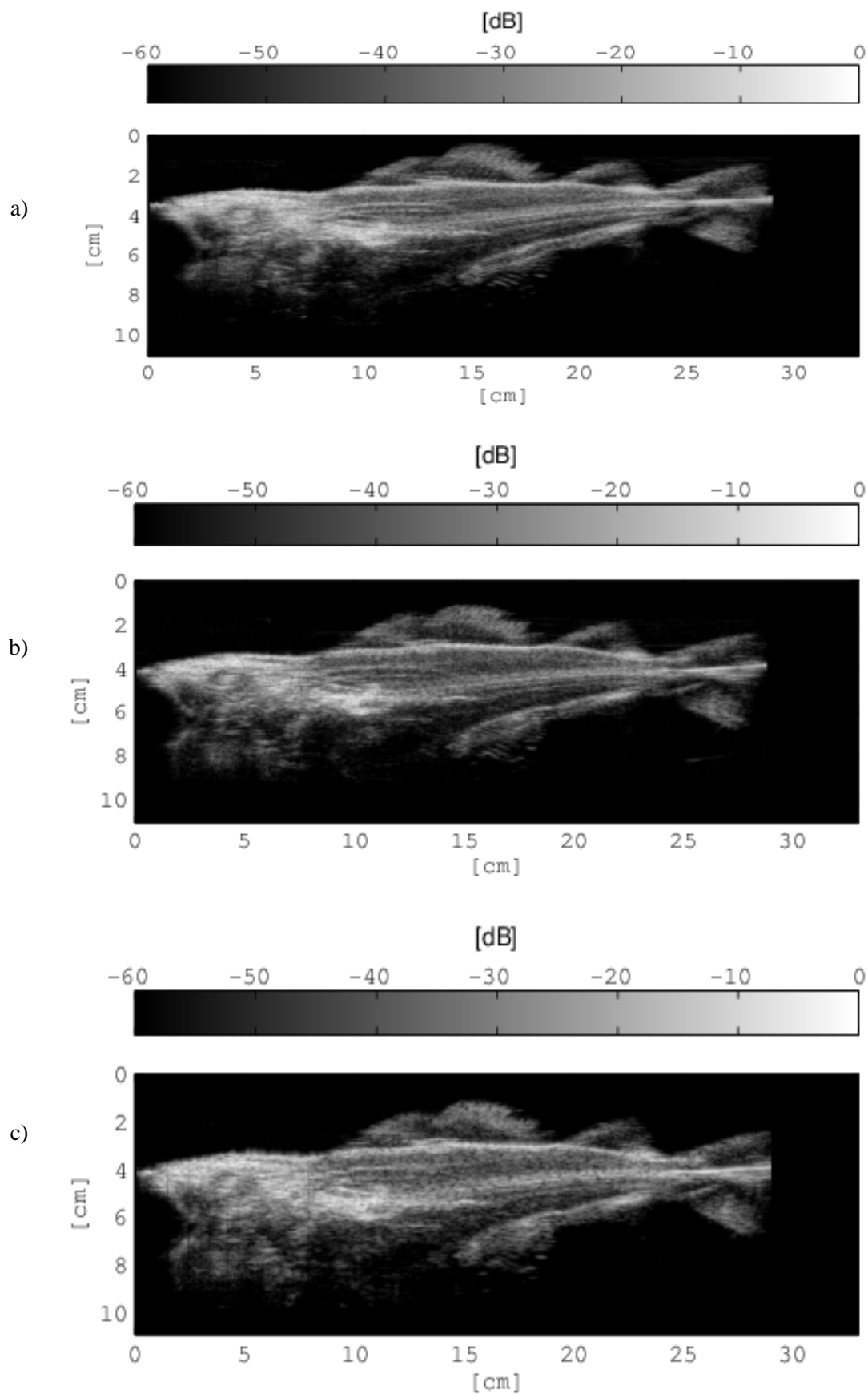


Figure C.12: Range profile maps of the cod fish3. The angel α is 0° . The transducer frequency is 6 MHz (a), 3.5 MHz (b), 2.5 MHz (c).

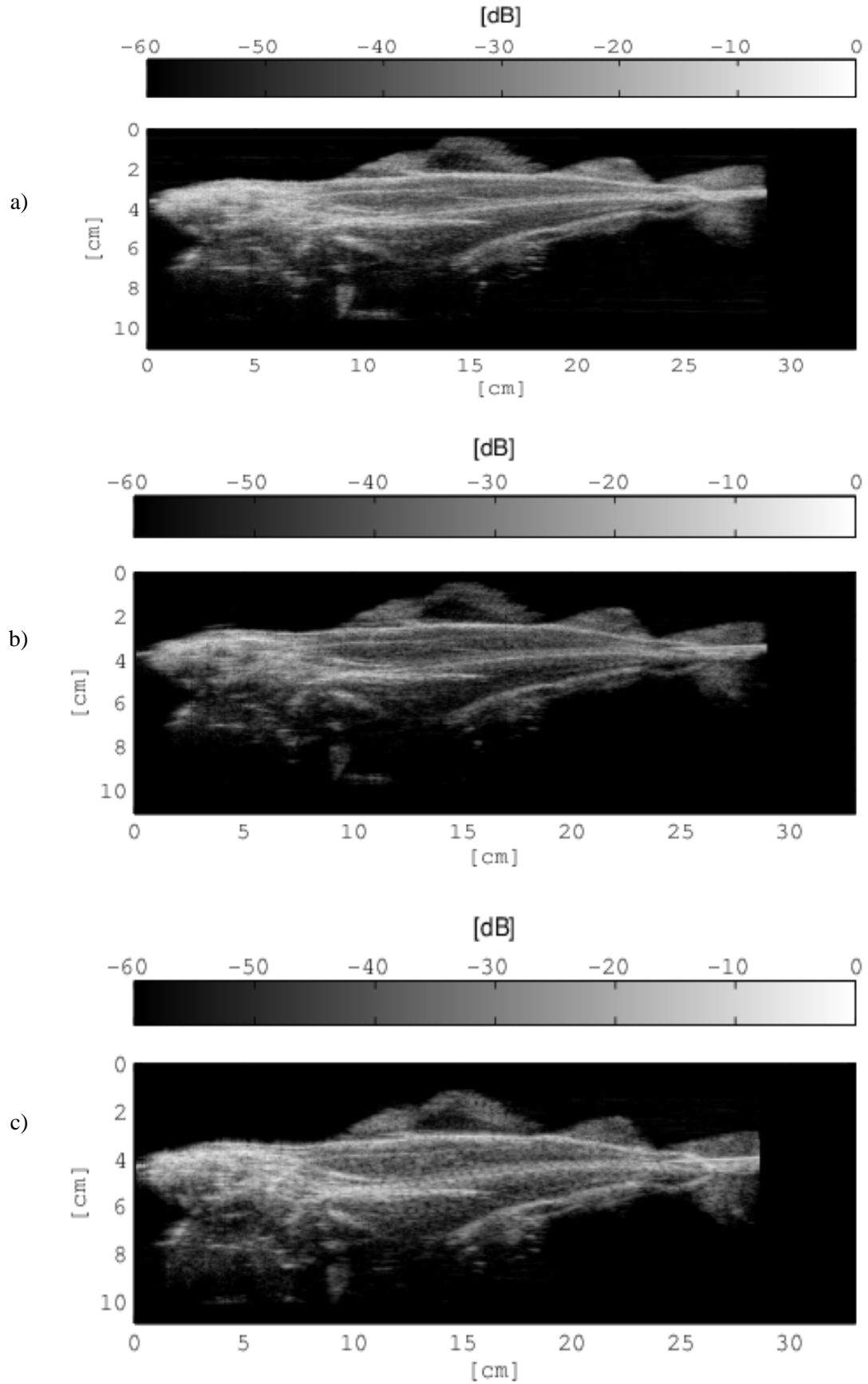


Figure C.13: Range profile maps of the cod fish3. The angel α is 30° . The transducer frequency is 6 MHz (a), 3.5 MHz (b), 2.5 MHz (c).

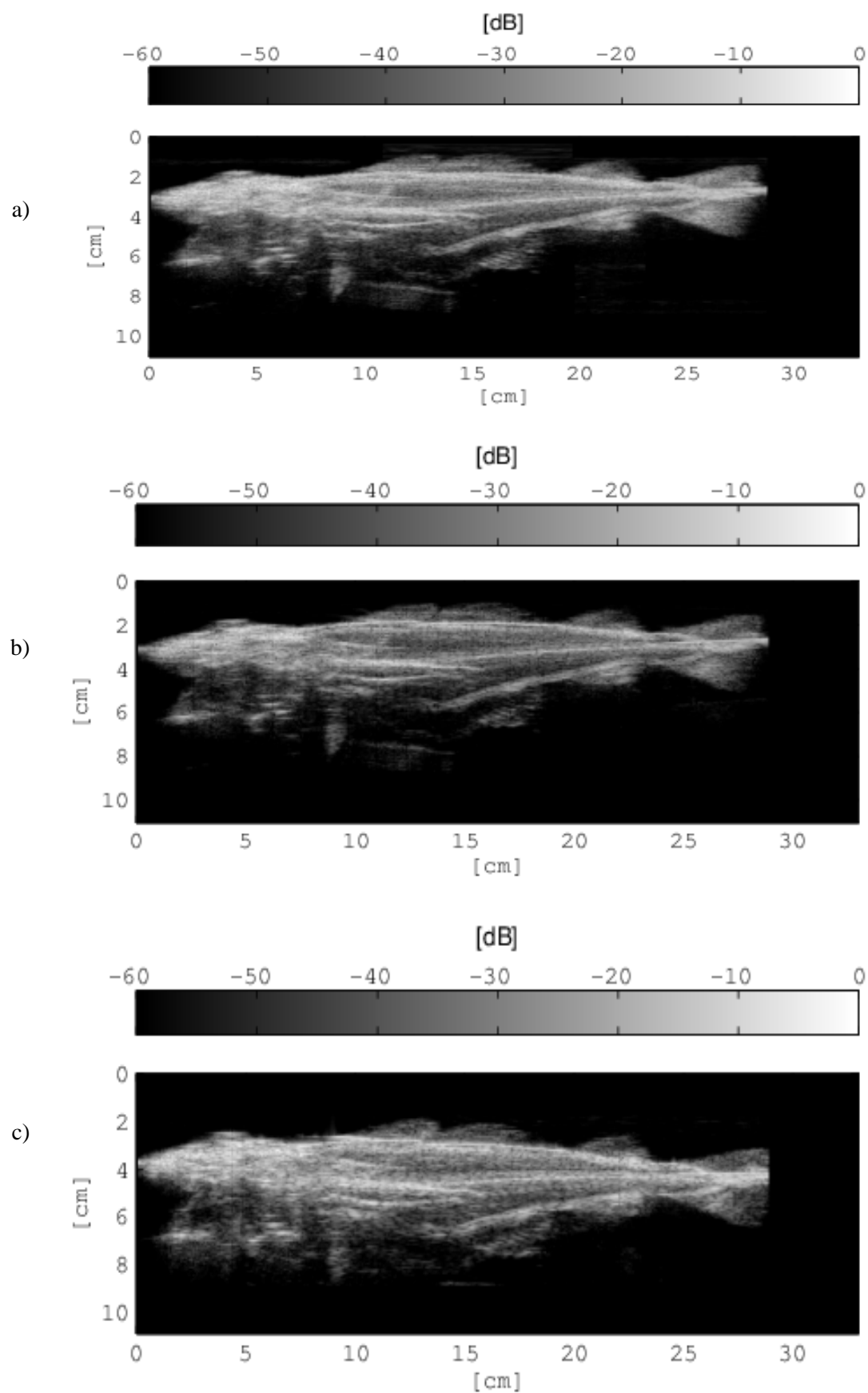


Figure C.14: Range profile maps of the cod fish3. The angel α is -30° . The transducer frequency is 6 MHz (a), 3.5 MHz (b), 2.5 MHz (c).

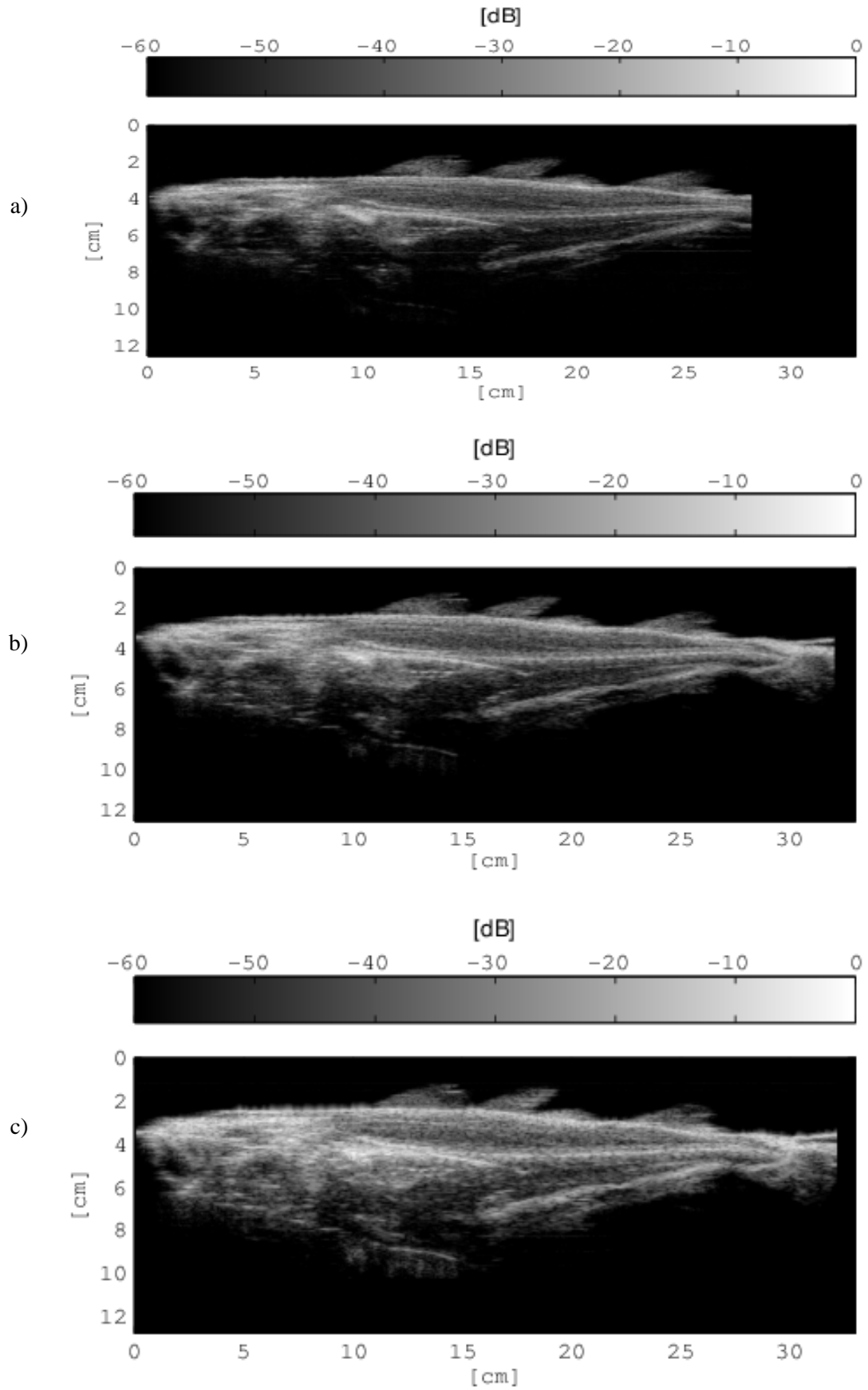


Figure C.15: Range profile maps of the cod fish4. The angel α is 0° . The transducer frequency is 6 MHz (a), 3.5 MHz (b), 2.5 MHz (c).

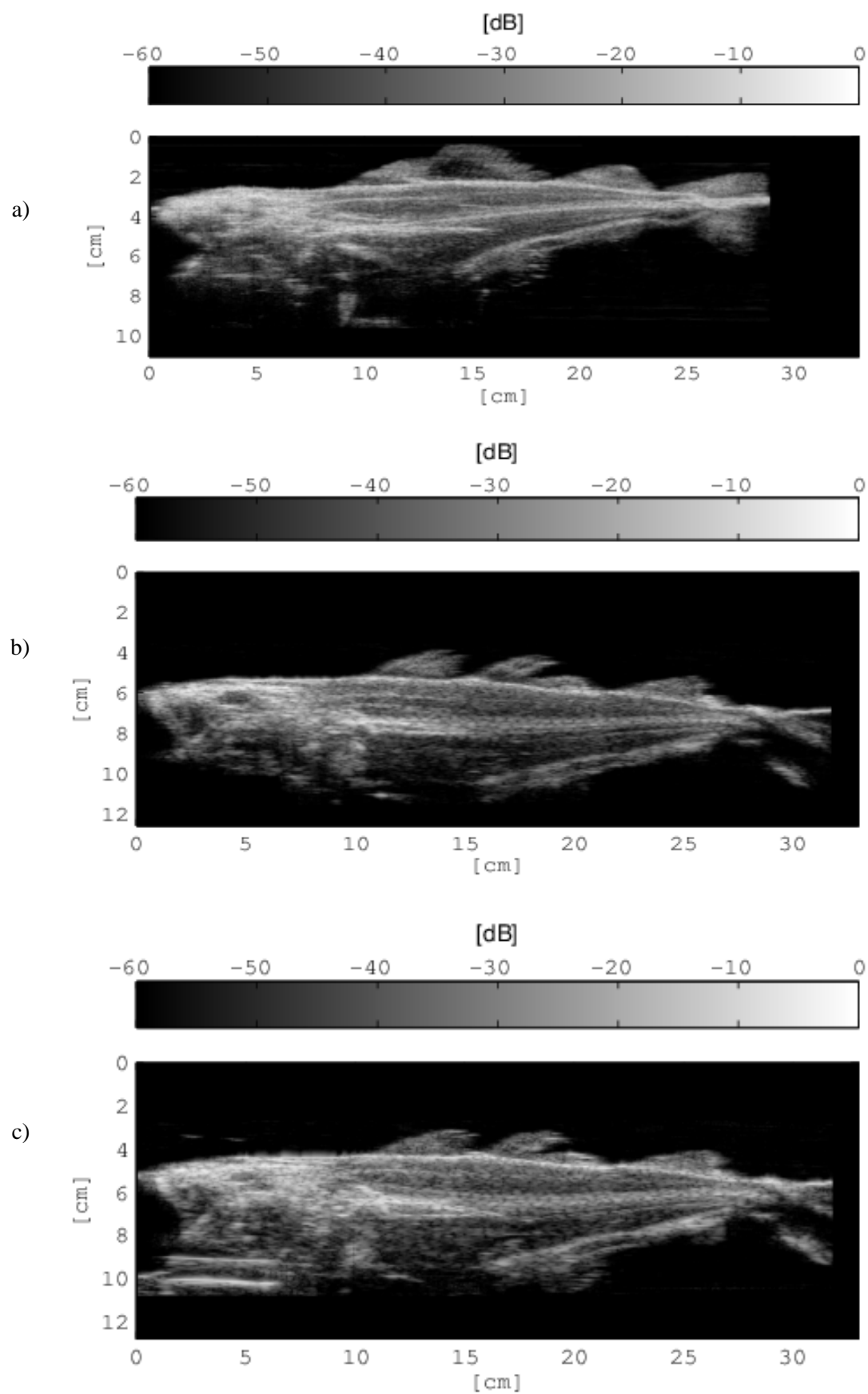


Figure C.16: Range profile maps of the cod fish4. The angel α is 30° . The transducer frequency is 6 MHz (a), 3.5 MHz (b), 2.5 MHz (c).

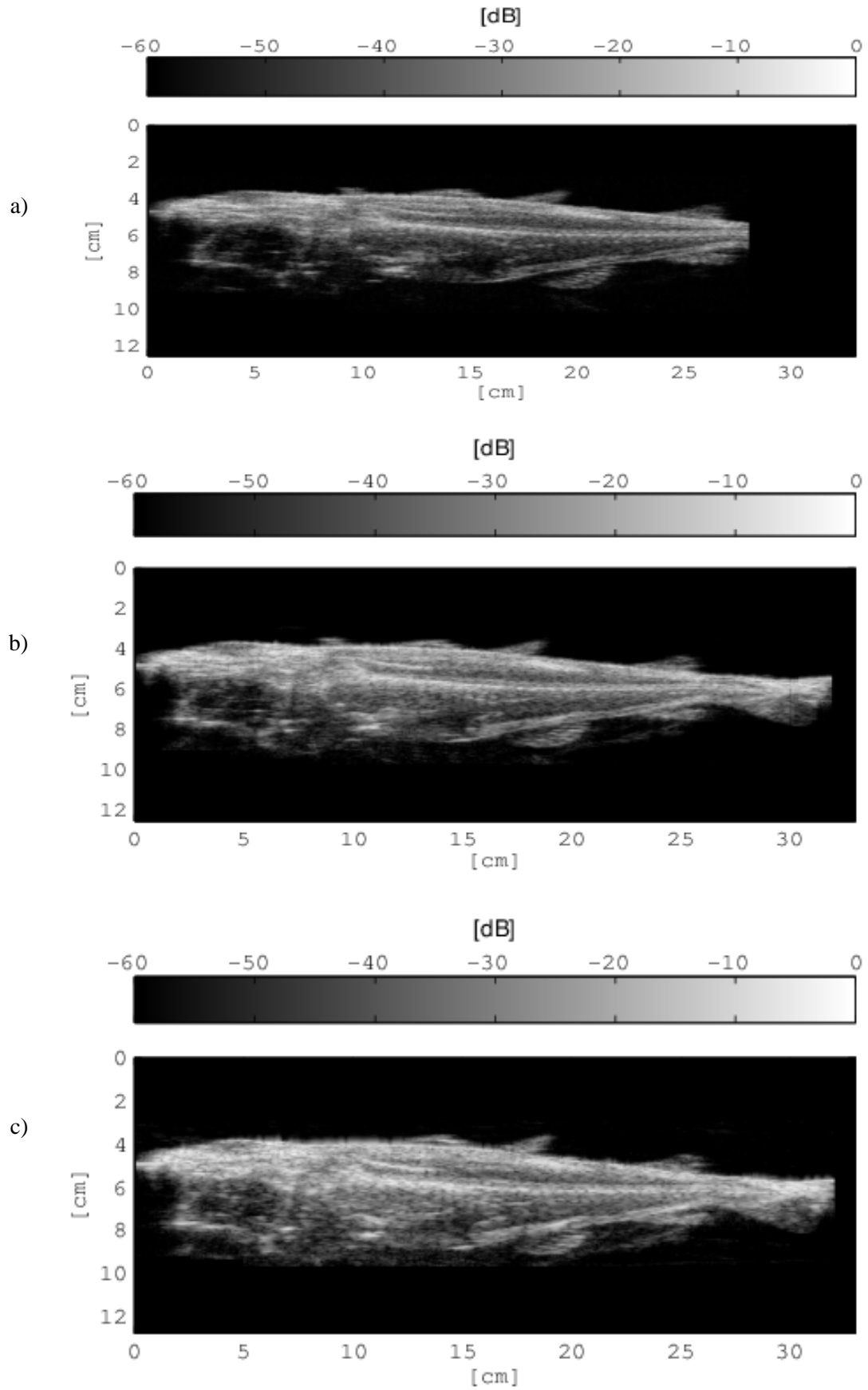


Figure C.17: Range profile maps of the cod fish4. The angel α is -30° . The transducer frequency is 6 MHz (a), 3.5 MHz (b), 2.5 MHz (c).

C.4 Average cross section images of a saithe and a cod for the study presented in chapter 2

This section presents average cross section images of the saithe fish2 and the cod fish3 corresponding to the energy distribution curves presented in Fig. 2.8, 2.9, and 2.10.

C.4.1 Average cross section images of the saithe fish2

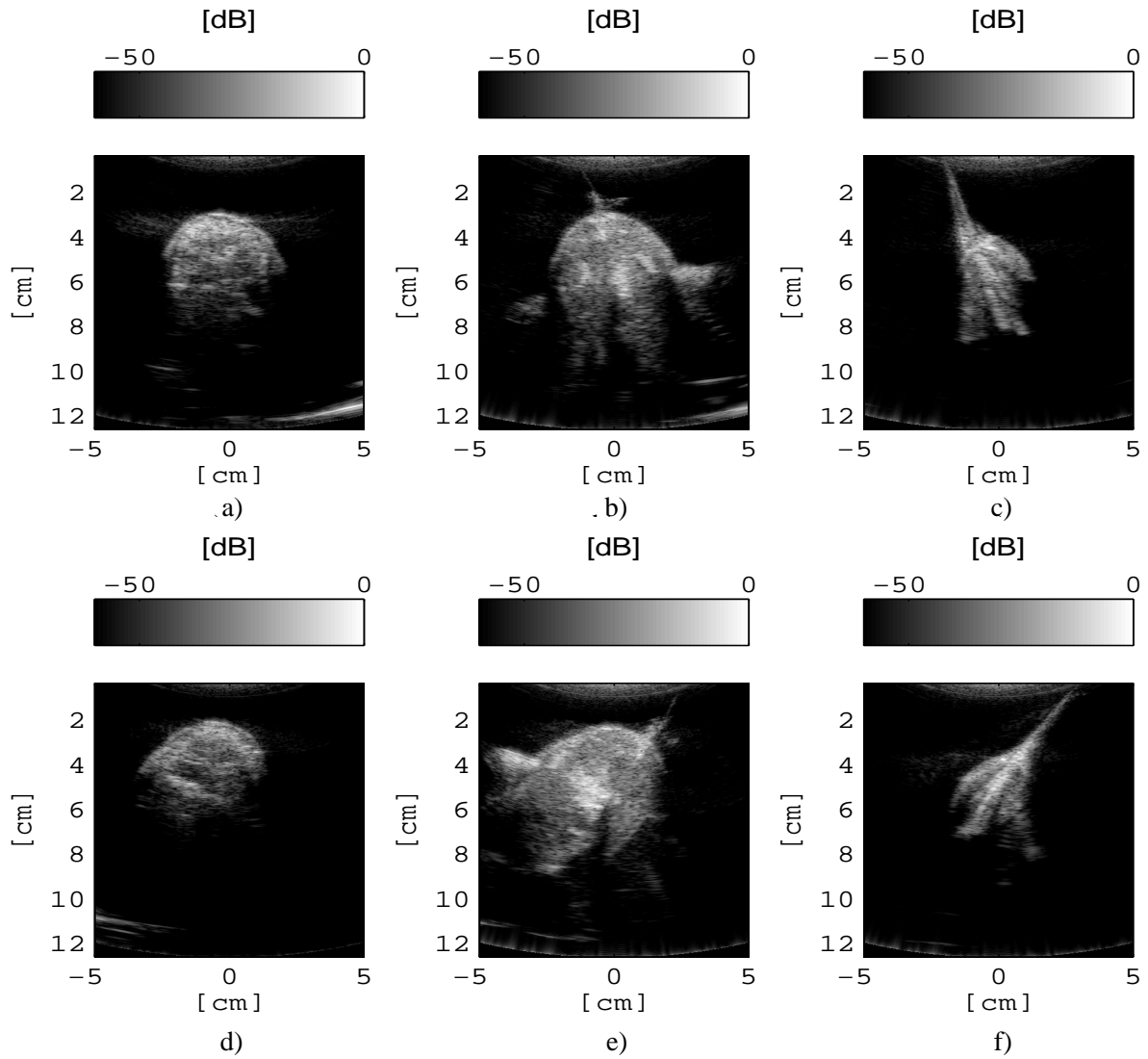


Figure C.18: Average cross section images of the saithe fish2. The transducer frequency is 2.5 MHz. The head with $\alpha = 30^\circ$ (a), and $\alpha = -30^\circ$ (d). The body with $\alpha = 30^\circ$ (b), and $\alpha = -30^\circ$ (e). The tail with $\alpha = 30^\circ$ (c), and $\alpha = -30^\circ$ (f).

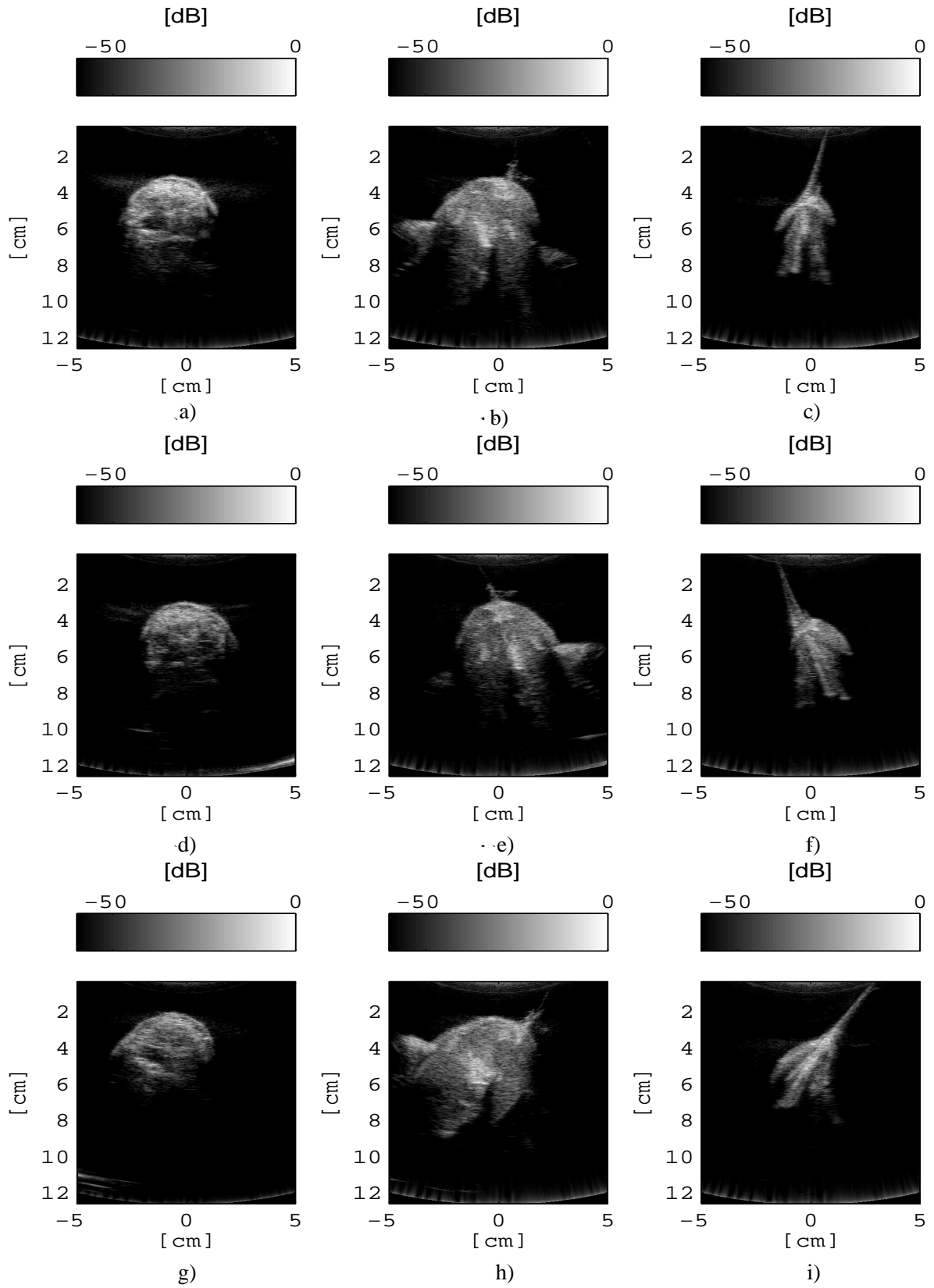


Figure C.19: Average cross section images of the saithe fish2. The transducer frequency is 3.5 MHz. The head with $\alpha = 0^\circ$ (a), $\alpha = 30^\circ$ (d), and $\alpha = -30^\circ$ (g). The body with $\alpha = 0^\circ$ (b), $\alpha = 30^\circ$ (e), and $\alpha = -30^\circ$ (h). The tail with $\alpha = 0^\circ$ (c), $\alpha = 30^\circ$ (f), and $\alpha = -30^\circ$ (i).

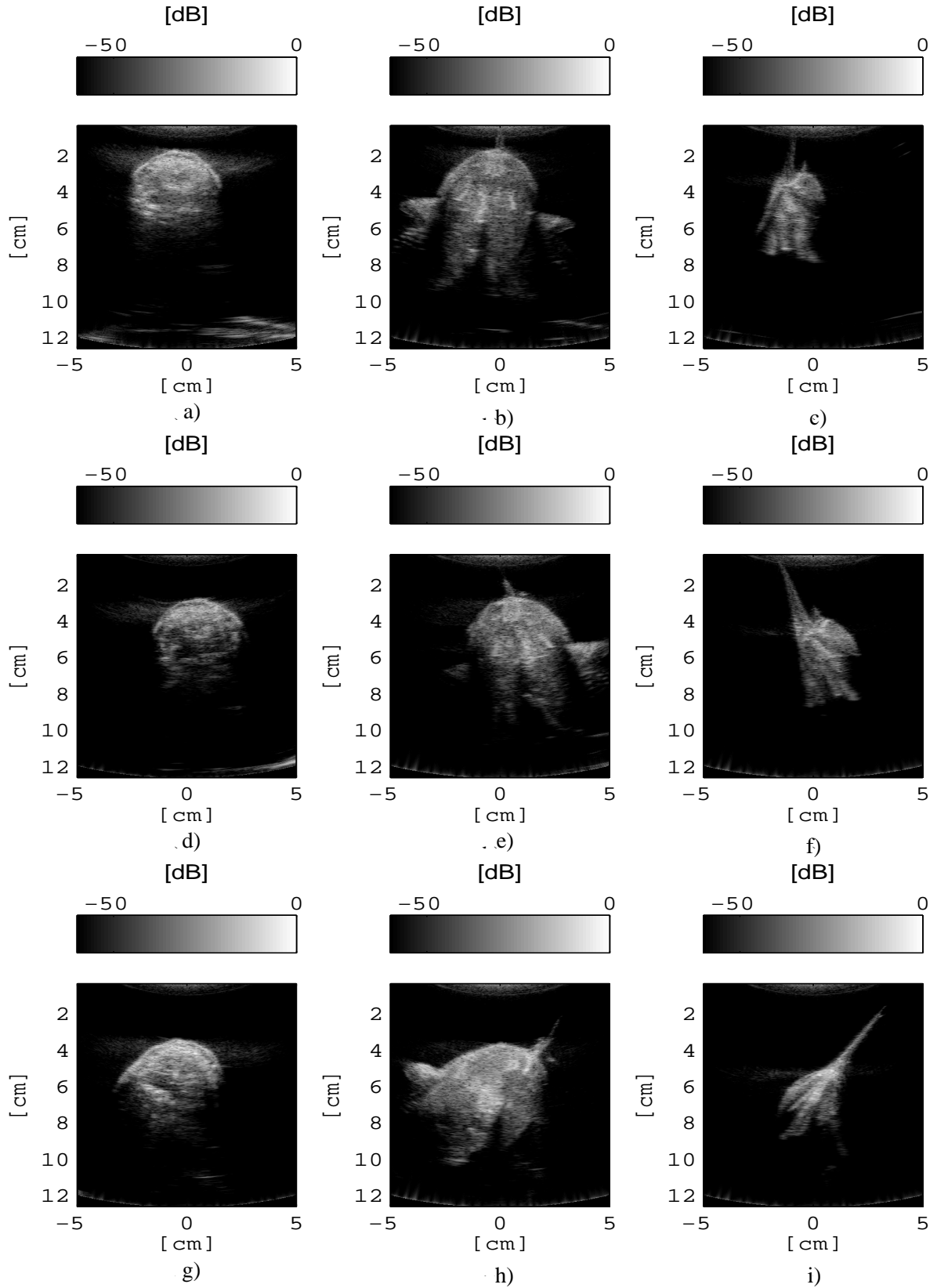


Figure C.20: Average cross section images of the saithe fish2. The transducer frequency is 6 MHz. The head with $\alpha = 0^\circ$ (a), $\alpha = 30^\circ$ (d), and $\alpha = -30^\circ$ (g). The body with $\alpha = 0^\circ$ (b), $\alpha = 30^\circ$ (e), and $\alpha = -30^\circ$ (h). The tail with $\alpha = 0^\circ$ (c), $\alpha = 30^\circ$ (f), and $\alpha = -30^\circ$ (i).

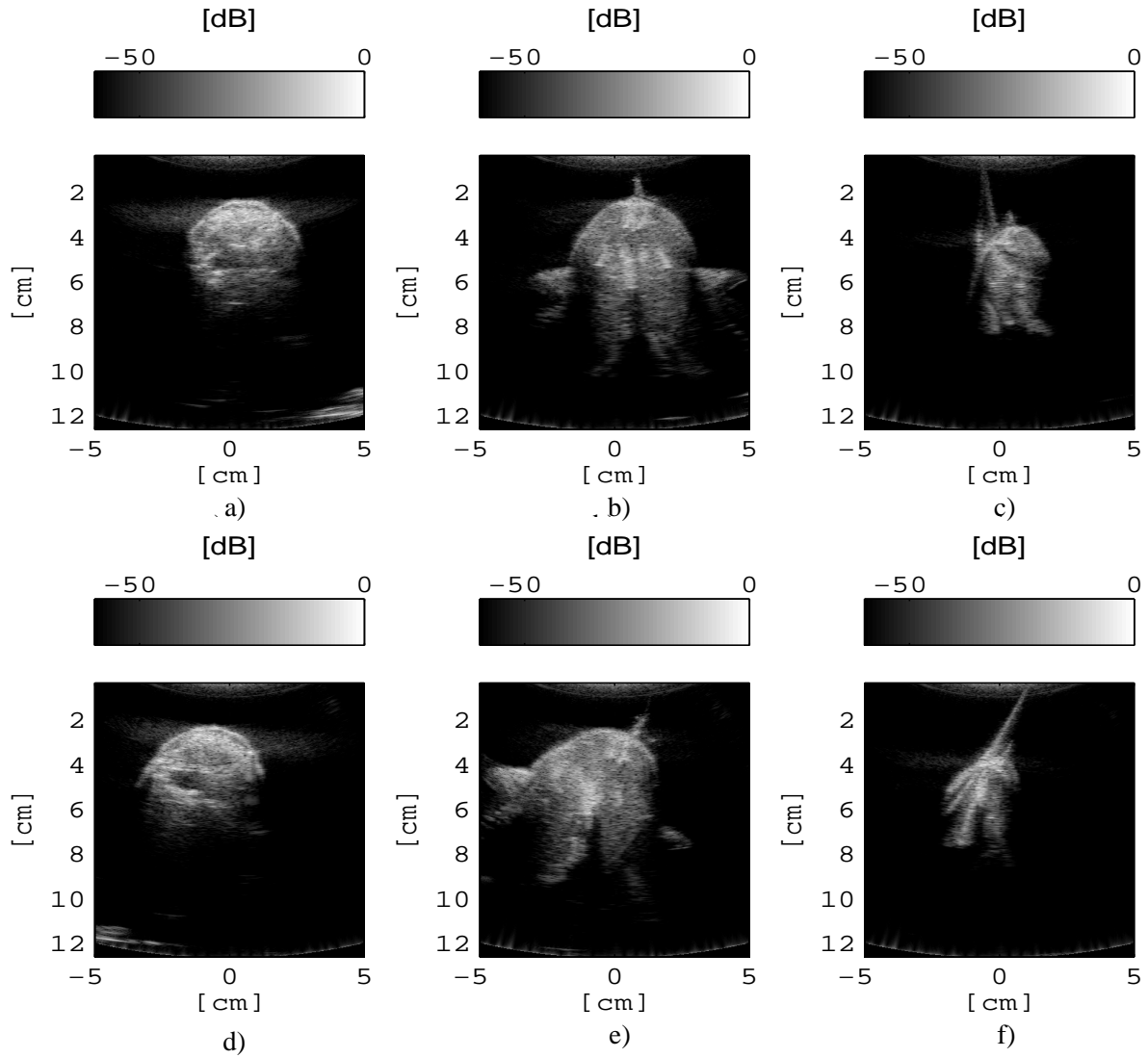


Figure C.21: Average cross section images of the saithe fish2. The transducer frequency is 6 MHz. The head with $\alpha = 15^\circ$ (a), $\alpha = -15^\circ$ (d). The body with $\alpha = 15^\circ$ (b), $\alpha = -15^\circ$ (e). The tail with $\alpha = 15^\circ$ (c), $\alpha = -15^\circ$ (f).

C.4.2 Average cross section images of the cod fish3

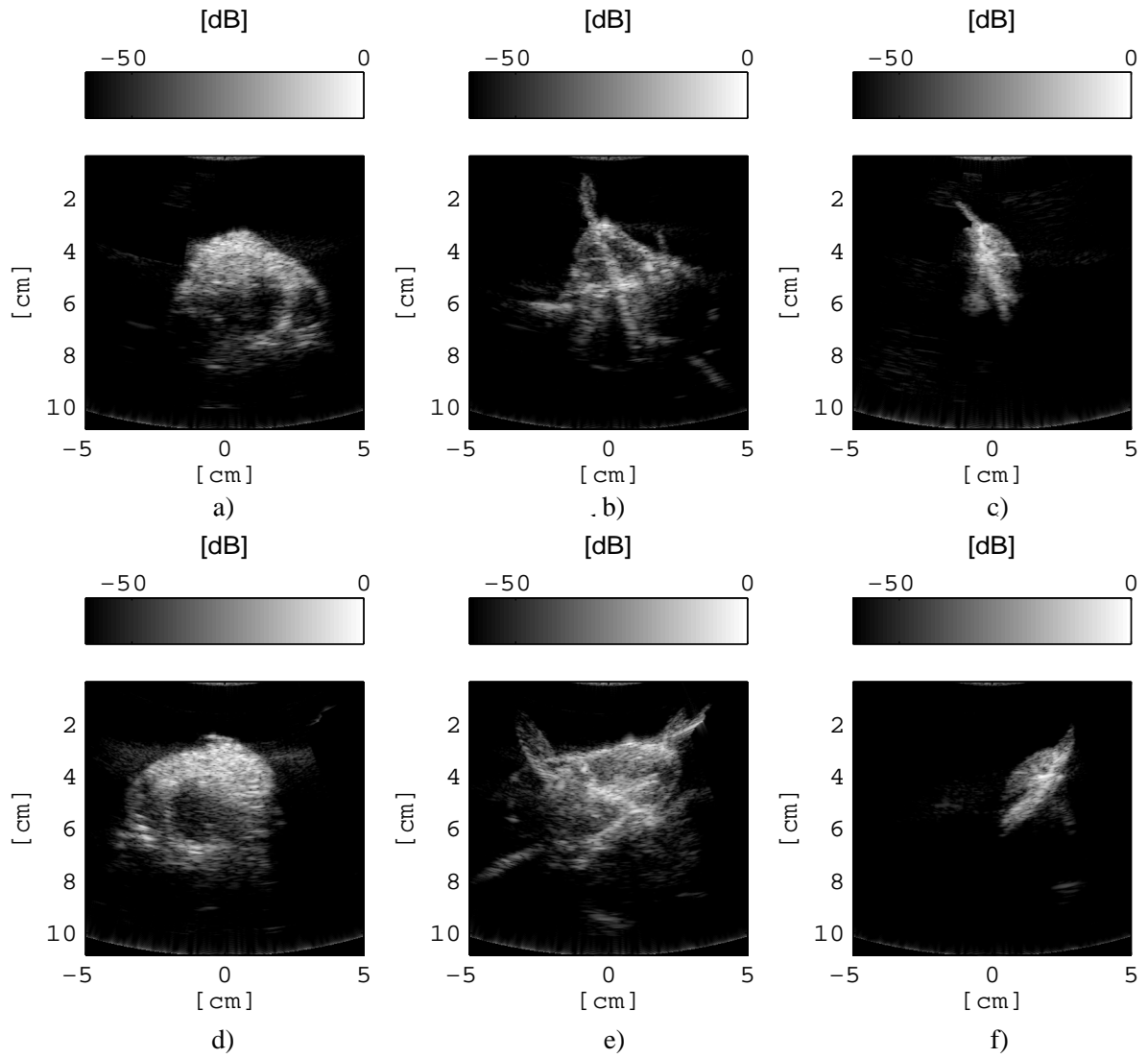


Figure C.22: Average cross section images of the cod fish3. The transducer frequency is 2.5 MHz. The head with $\alpha = 30^\circ$ (a), $\alpha = -30^\circ$ (d). The body with $\alpha = 30^\circ$ (b), $\alpha = -30^\circ$ (e). The tail with $\alpha = 30^\circ$ (c), $\alpha = -30^\circ$ (f).

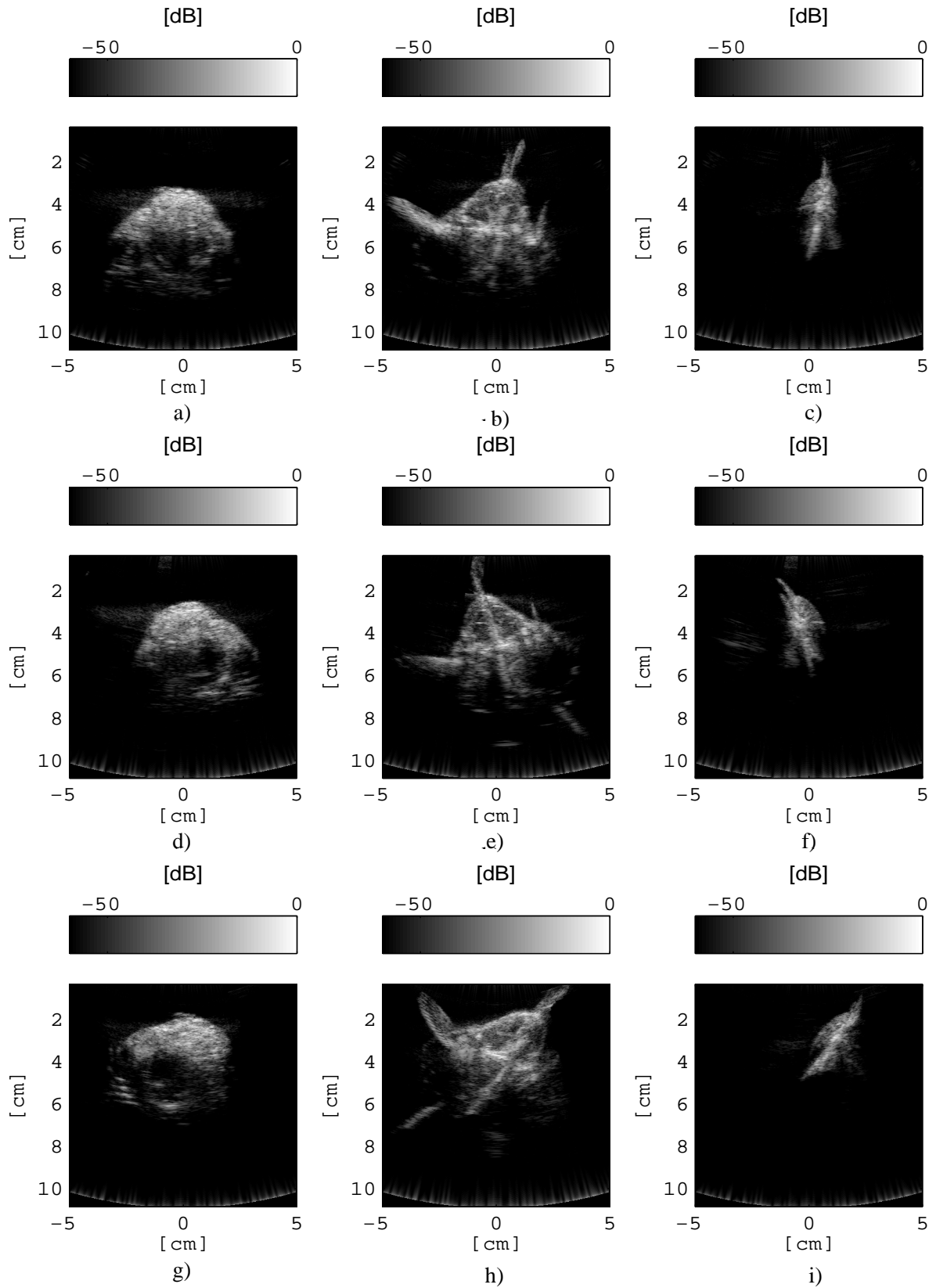


Figure C.23: Average cross section images of the cod fish3. The transducer frequency is 3.5 MHz. The head with $\alpha = 0^\circ$ (a), $\alpha = 30^\circ$ (d), and $\alpha = -30^\circ$ (g). The body with $\alpha = 0^\circ$ (b), $\alpha = 30^\circ$ (e), and $\alpha = -30^\circ$ (h). The tail with $\alpha = 0^\circ$ (c), $\alpha = 30^\circ$ (f), and $\alpha = -30^\circ$ (i).

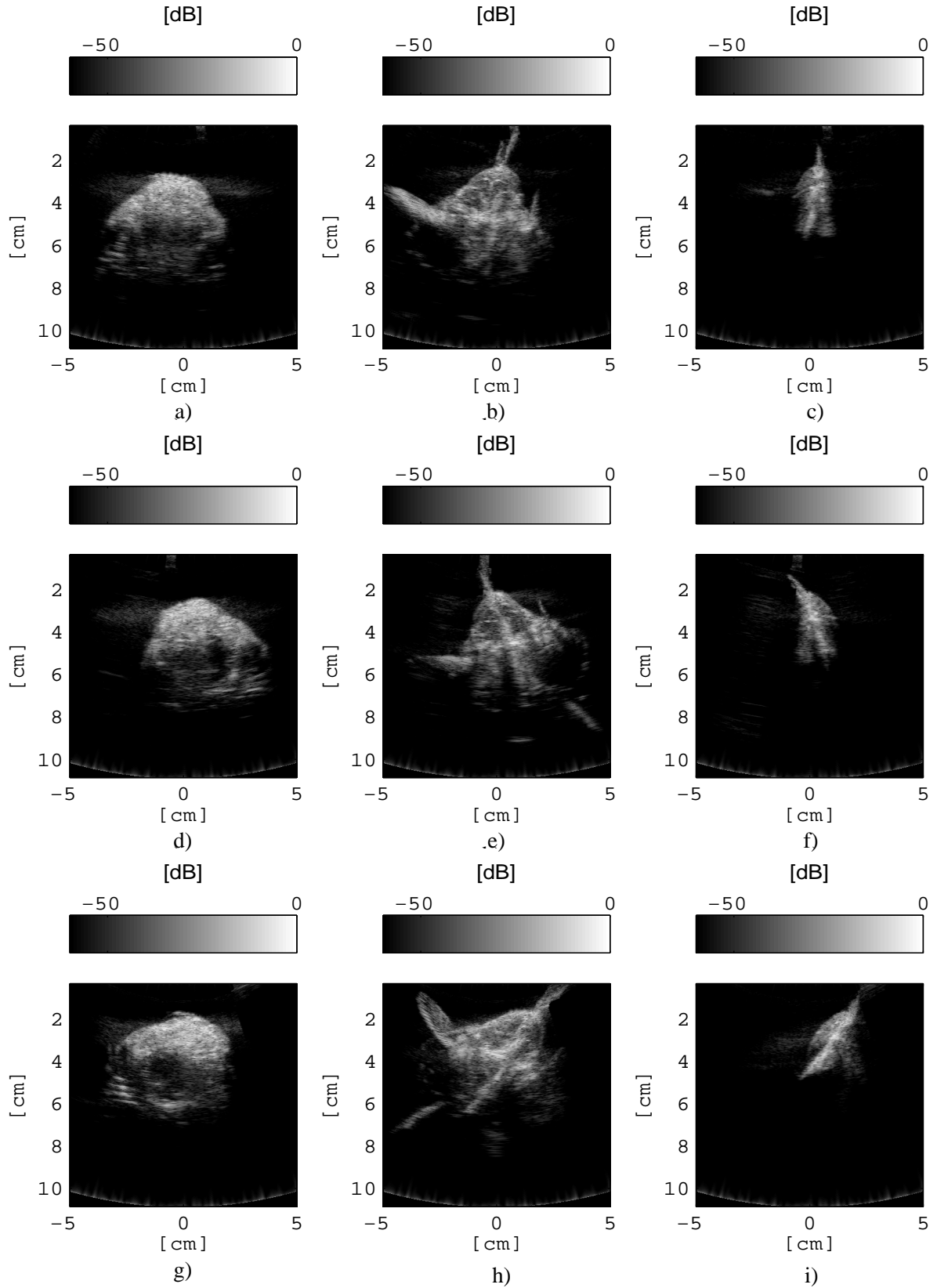


Figure C.24: Average cross section images of the cod fish3. The transducer frequency is 6 MHz. The head with $\alpha = 0^\circ$ (a), $\alpha = 30^\circ$ (d), and $\alpha = -30^\circ$ (g). The body with $\alpha = 0^\circ$ (b), $\alpha = 30^\circ$ (e), and $\alpha = -30^\circ$ (h). The tail with $\alpha = 0^\circ$ (c), $\alpha = 30^\circ$ (f), and $\alpha = -30^\circ$ (i).

C.5 Data of some other measurements of the study presented in chapter 4

This section presents results of some other measurements for the study presented in chapter 4.

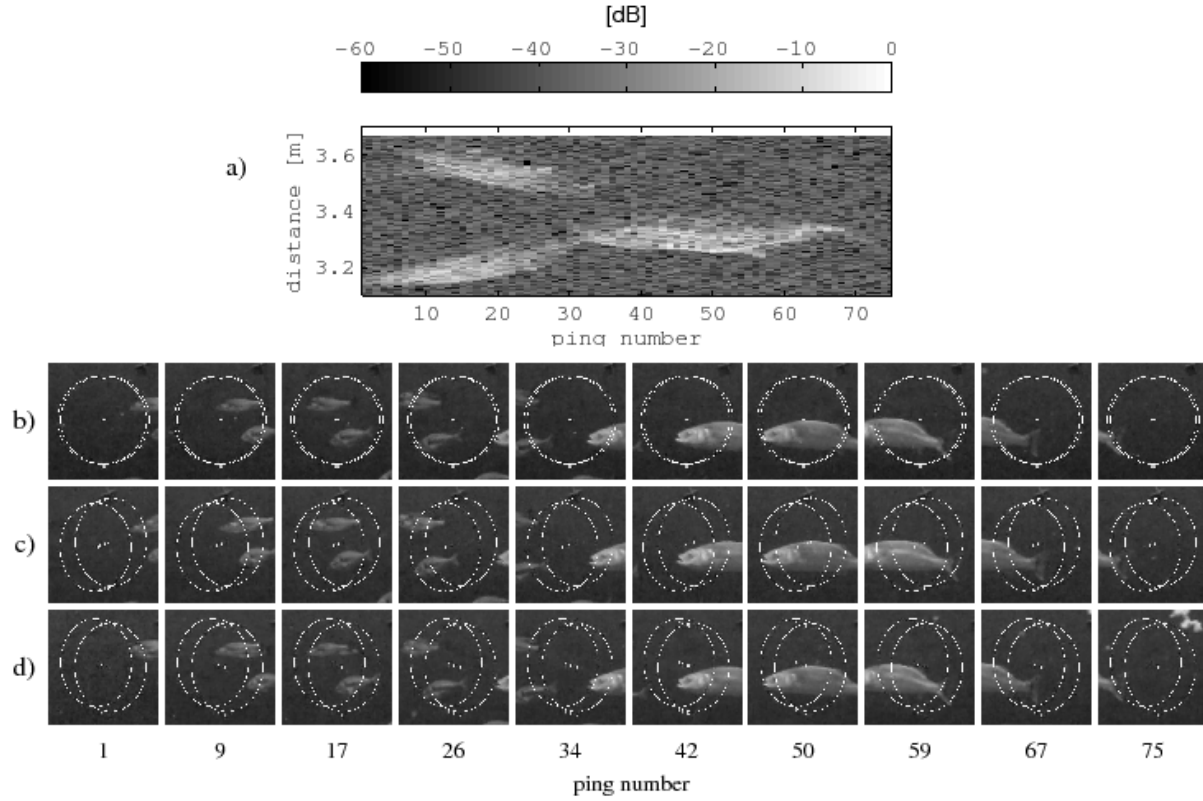


Figure C.25: Two small sea basses and a big sea bass swam from right to left. Range profiles of the sea basses (a), images from the center camera C1 (b), from the left-hand side camera C2 (c), from the right-hand side camera C3(d).

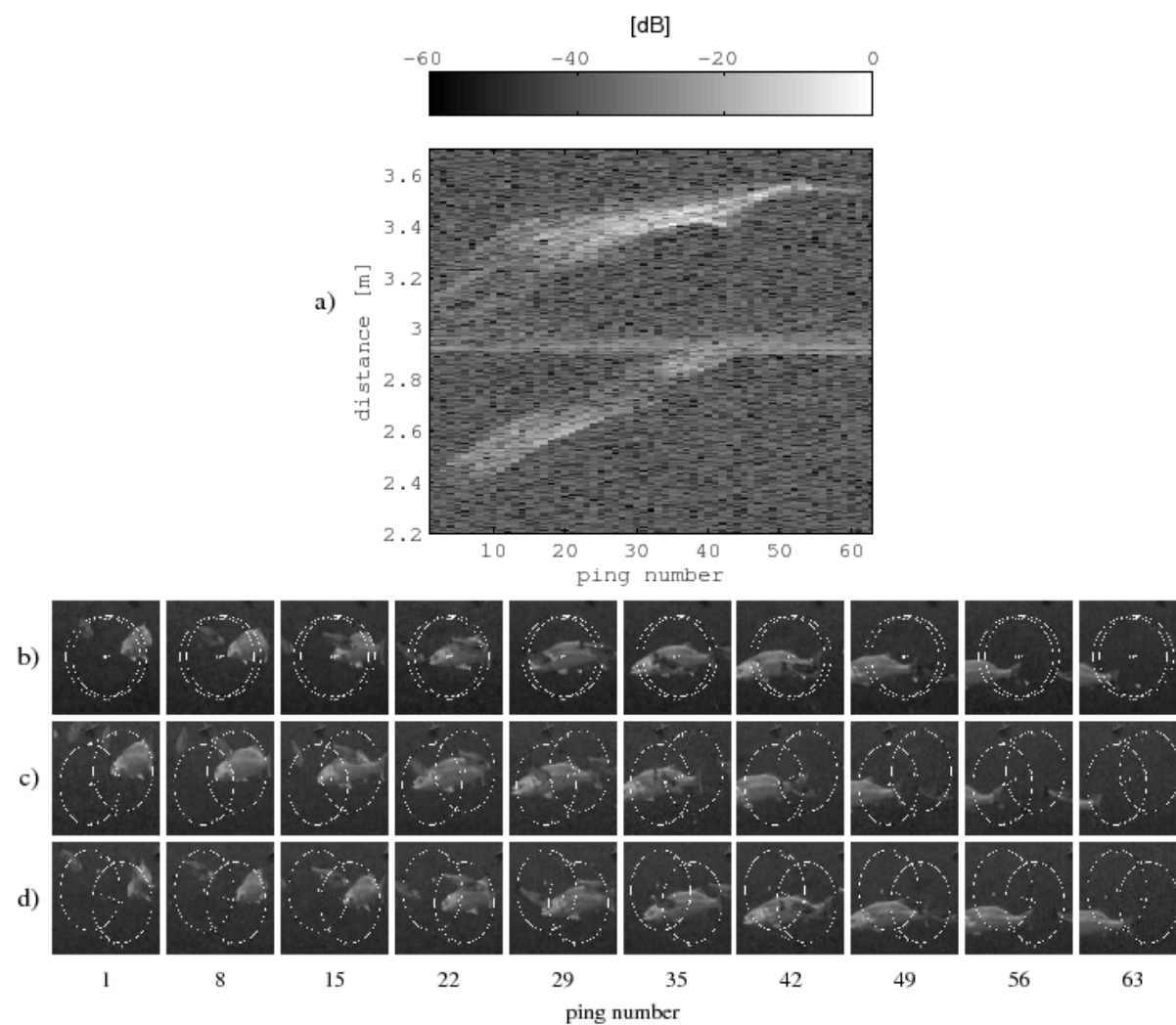


Figure C.26: Two small sea basses swam from left to right and a big sea bass turned and swam from right to left. Range profiles of the sea basses (a), images from the center camera C1 (b), from the left-hand side camera C2 (c), from the right-hand side camera C3(d).

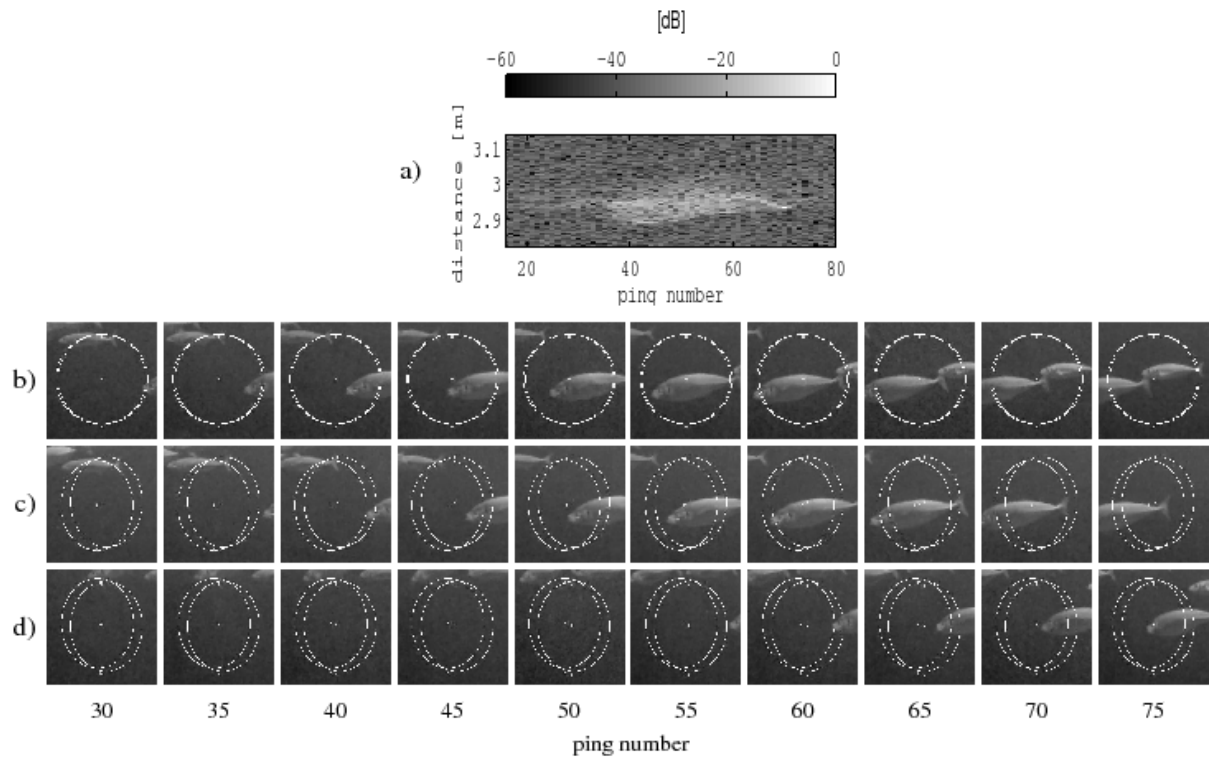


Figure C.27: A measurement using an Olympus 1 MHz single-element Videoscan transducer. A horse mackerel swam from right to left. Range profiles of the fish (a), images from the center camera C1 (b), from the left-hand side camera C2 (c), from the right-hand side camera C3(d).